UNIVERSITÀ DI PARMA

# UNIVERSITA' DEGLI STUDI DI PARMA

DOTTORATO DI RICERCA IN
SCIENZE DELLA TERRA

CICLO XXXI

# DIAGENETIC CONCRETIONS AS A TOOL TO CONSTRAIN PALAEO-FLUID CIRCULATION IN FAULT ZONES AND FOLDED STRATA

Coordinatore:
Chiar.mo Prof. Fulvio Celico

Tutore:
Chiar.mo Dott. Fabrizio Balsamo

Co-Tutore:
Chiar.ma Prof.ssa Paola Iacumin

Dottorando: Mattia Pizzati

Anni 2015/2018

*Dedicato ad un piccolo grande fiorellino...*

*...dedicato alla piccola Dalia...*

# PH. D THESIS ABSTRACT

This Ph. D Thesis is focused on the palaeo-fluid flow through fault zones and folded strata affecting poorly lithified siliciclastic sediments. Within deformed sediments, fluid flow is witnessed by the presence of selective cementation, often in the form of diagenetic concretions and mineral masses. These diagenetic alterations are of primary importance to study the interaction between fluids and deforming rocks in different hydrologic conditions, with implications for compartmentalization of geofluid reservoirs. During this 3-years project, we investigated the geometry, spatial distribution and growth mode of carbonate concretions hosted in both extensional fault zones and in syn-tectonic strata tilted during progressive folding. In such settings, concretions were used as markers of palaeo-fluid flow, and their shape allowed to infer the direction of flow. By integrating field and laboratory data, diagenetic environment in which selective cementation occurred was constrained, as well as the nature and the geochemical conditions of cementing fluids. A detailed analysis of the petrophysical properties of sediments involved in deformation, allowed to understand the impact of deformation upon the hydraulic behaviour. All the aspects previously described were aimed to investigate the hydrological role played by faulted and folded poorly cemented siliciclastic sediments, which is worth to be assessed especially for the exploration and exploitation of hydrocarbon reservoirs and groundwater reserves.

Three different field sites were selected:

(i) Enza River Valley, Northern Apennines, Italy, where concretions are associated with passively tilted strata along the forelimb of an active fault-related anticline.

(ii) Rocca di Neto fault zone, Crotone Basin, Southern Apennines, Italy, with selective cementation associated with soft-sediment deformation (deformation bands and gouges) characterizing an extensional fault zone.

(iii) Cotiella Massif, Spanish Pyrenees, Spain, fault-related soft-sediment deformation in low-porosity carbonate-rich rocks, affected by compressive tectonic.

To perform such a study a multidisciplinary approach was applied. It consisted of combined field work techniques and laboratory analyses. Field work was mainly aimed to the structural analysis of the selected sites, sample collection and *in situ* measurements (e.g., air-permeability). Laboratory analyses comprised grain size analysis, porosity measurements, petrographic-microstructural observations and C-O stable isotope analysis.

The Enza River Valley and the Rocca di Neto case studies benefited of contributions from Prof. Rudy Swennen from the Katholieke Universiteit of Leuven (Belgium). The Cotiella Massif case study is part of a scientific cooperation between the University Federico II of Naples (Italy), the University of Parma (Italy) and the University of Barcelona (Spain).

All the petrophysical, microstructural, petrographic-diagenetic and isotopic analyses were performed at the University of Parma. Micromill sampling needed for detailed stable isotope analysis was conducted at the Katholieke Universiteit of Leuven (Belgium).

The Thesis consists of a collection of two published papers and two manuscript drafts, almost ready to be submitted to international journals. Hence, its structure reflects the subdivision of the overall work in four distinct chapters, each of them corresponding to one manuscript.

The entire Thesis is written in English to ease the scientific distribution and visibility. A short summary of the main results of each chapter is provided also in Italian.

# THESIS CONTENTS

- **Short Summary of each Chapter (Italian)**

  Geological introduction, main results, discussion and conclusions of each case study briefly summarized in Italian.

- **General Introduction of the Research Topics**

  Introduction of the Ph. D project, literature background, importance of the research themes, implications for hydrocarbon and groundwater reservoir exploration and exploitation.

- **Palaeo-fluid Flow during Anticline Growth along the Enza River Valley**

  Carbonate concretions related to meteoric fluids, selectively cementing loose Pleistocene sandstone along the forelimb of the growing Quattro Castella Anticline. Concretions recorded the change of the direction of fluid flow in the framework of the lateral propagation of the anticline in its periclinal sector.

- **Structural and Diagenetic Evolution of the Rocca di Neto Fault Zone**

  Evolution of an extensional fault zone affecting Pleistocene age, loosely lithified sandstone and silty clay. The fault zone experienced a strain-hardening induced by both physical (tectonic compaction) and chemical (preferential cementation) processes.

- **Microstructures and Petrophysics of the Rocca di Neto Fault Zone**

  Microstructural features influencing the petrophysical (grain size, permeability and porosity) properties of deformed sandstone, leading to selective cementation along discrete fault and deformation band surfaces.

- **Deformation Bands of the Cotiella Massif**

  Soft-sediment deformation affecting low-porosity calcarenites, along the footwall of the Cotiella Thrust. Deformation bands are induced by a combination of solution of calcite cement and mechanical compaction of siliciclastic grains (mainly quartz and feldspar).

- **General Discussion and Conclusions**

  Discussion regarding each case study previously presented with final remarks and considerations.

- **Future Perspectives**

  Themes and topics deserving further investigations that were highlighted during this Ph. D project.

- **Acknowledgements**

- **Activities and Contributions**

  Courses, seminars, conference contributions, publications, didactic activity.

- **Reference List**

# RIASSUNTO DELLA TESI DI DOTTORATO

La presente Tesi di Dottorato è focalizzata allo studio dei paleo-flussi di fluidi all'interno di zone di faglia e strutture plicative che coinvolgono sedimenti silico-clastici a basso grado di litificazione. Il flusso di fluidi attraverso i sedimenti deformati è testimoniato dalla presenza di cementazione selettiva, spesso sottoforma di concrezioni diagenetiche e masse di minerali. Le alterazioni diagenetiche sono di primaria importanza nello studio delle interazioni tra fluidi e rocce-sedimenti deformati, per ricostruire le condizioni idrologiche ed il comportamento idraulico rivestito dai sedimenti coinvolti nella deformazione. Questo tipo di analisi è di particolare importanza nel valutare l'influenza sulla compartimentalizzazione dei *reservoir*. Durante il progetto triennale di Dottorato è stata studiata la modalità di crescita e di sviluppo delle concrezioni carbonatiche all'interno di zone di faglia o strati deformati all'interno di strutture plicative. All'interno di queste strutture, le concrezioni sono state impiegate come traccianti di paleo-flussi di fluidi e dalla loro forma è stata dedotta la direzione del flusso. Attraverso le analisi geochimiche è stato possibile vincolare l'ambiente diagenetico e sedimentario in cui è avvenuta la precipitazione dei cementi ed allo stesso tempo è stata identificata la natura dei fluidi responsabili della cementazione. L'analisi di dettaglio delle proprietà petrofisiche dei sedimenti coinvolti nella deformazione, ha permesso di valutare l'influenza della deformazione sul comportamento idraulico. Tutti gli aspetti menzionati precedentemente sono mirati al riconoscimento del ruolo idrologico di faglie e pieghe che interessano sedimenti silico-clastici debolmente litificati, le quali rivestono un ruolo fondamentale nel fase di esplorazione e sfruttamento dei *reservoir* di idrocarburi ed acquiferi.

Sono stati identificati tre differenti siti in cui condurre questa tipologia di studio:

(i) Val d'Enza, Appennino Settentrionale, Italia, in cui sono presenti concrezioni diagenetiche associate a strati deformati lungo il fianco esterno di una piega anticlinale legata a *thrust*.

(ii) Zona di faglia di Rocca di Neto, Bacino di Crotone, Appennino Meridionale, Italia, in cui è possibile studiare la cementazione selettiva che coinvolge strutture deformative *soft-sediment* (bande di deformazione e *gouge*) sviluppate all'interno di una zona di faglia estensionale.

(iii) Massiccio di Cotiella, Pirenei spagnoli, Spagna, dove si ha deformazione *soft-sediment* in rocce calcarenitiche a bassa porosità sottoposte a tettonica contrazionale.

Lo studio sopracitato è stato eseguito attraverso l'applicazione di un approccio multidisciplinare dato dall'unione di analisi di terreno e di laboratorio. Il rilevamento geologico-strutturale di terreno è stato mirato al riconoscimento degli elementi strutturali, all'analisi meso-strutturale dei

siti di interesse ed alla raccolta dei campioni necessari per le analisi di laboratorio ed analisi *in situ* (misure di permeabilità). Le tecniche analitiche di laboratorio comprendono analisi della granulometria, porosità, osservazioni petrografiche, diagenetiche e microstrutturali ed analisi degli isotopi stabili Carbonio-Ossigeno.

I casi di studio della Val d'Enza e della faglia di Rocca di Neto hanno visto la collaborazione del Prof. Rudy Swennen dell'Università Cattolica di Leuven (K.U.Leuven) (Belgio). Il caso di studio del Massiccio di Cotiella è nato come una collaborazione scientifica tra Università Federico II di Napoli (Italia), l'Università di Parma (Italia) e l'Università di Barcellona (Spagna).

Tutte le analisi petrofisiche, microstrutturali, petrografiche, diagenetiche ed isotopiche sono state eseguite presso i laboratori dell'Università di Parma. Il campionamento mediante *micromill* necessario per la campionatura di dettaglio prevista per le analisi isotopiche è stato eseguito presso l'Università Cattolica di Leuven (Belgio).

La presente Tesi si configura come una collezione di due articoli scientifici pubblicati ed altri due manoscritti in fase di sottomissione su riviste internazionali. La struttura della Tesi è suddivisa in capitoli, ognuno dei quali corrisponde alle suddette pubblicazioni.

L'intera Tesi di Dottorato è scritta in lingua inglese al fine di favorirne la visibilità e la diffusione nella comunità scientifica. Nella parte introduttiva è stato comunque inserito un riassunto esteso in lingua italiana dei risultati principali presentati in ciascun capitolo.

# CONTENUTI DELLA TESI

- **Riassunto Esteso (italiano)**

  Introduzione geologica, risultati principali, discussione e conclusioni di ciascun caso di studio, riassunti brevemente in italiano.

- **Introduzione Generale al Tema di Ricerca**

  Introduzione al progetto di Dottorato, letteratura esistente, importanza della tematica di ricerca, implicazioni per la fase di esplorazione e sfruttamento dei *reservoir* di idrocarburi ed acquiferi.

- **Paleo-circolazione di Fluidi Superficiali durante la Crescita di un'Anticlinale (Val d'Enza)**

  Concrezioni carbonatiche formate a partire da flussi di fluidi meteorici che cementano in modo selettivo arenarie Pleistoceniche debolmente litificate, deposte in corrispondenza del fianco esterno dell'anticlinale attiva di Quattro Castella. Le concrezioni hanno registrato un cambiamento nella direzione dei flussi di fluidi durante le ultime fasi di propagazione della piega nella zona periclinale.

- **Evoluzione Strutturale e Diagenetica della Zona di Faglia di Rocca di Neto**

  Evoluzione strutturale di una zona di faglia estensionale che interessa sedimenti poco litificati di età Pleistocenica. La zona di faglia è caratterizzata da un comportamento di tipo *strain-hardening* prodotto da una combinazione di processi fisici (compattazione tettonica) e chimici (cementazione selettiva).

- **Proprietà Microstrutturali e Petrofisiche della Faglia di Rocca di Neto**

  Controllo esercitato dalle caratteristiche microstrutturali sulle proprietà petrofisiche (granulometria, permeabilità e porosità) dei sedimenti deformati, sulla cementazione preferenziale lungo le superfici di faglie e lungo le bande di deformazione.

- **Bande di Deformazione del Massiccio di Cotiella**

  Deformazione *soft-sediment* di calcareniti in prossimità del *thrust* di Cotiella. Le bande di deformazione risultano dall'azione combinata di dissoluzione della calcite e compattazione meccanica dei clasti di quarzo e feldspato.

- **Discussione Generale e Conclusioni**

  Discussione comprensiva dei risultati mostrati in ogni caso di studio e considerazioni finali.

- **Studi Successivi e Prospettive Future**

  Tematiche evidenziate durante il percorso di Dottorato che meritano un successivo approfondimento.

- **Ringraziamenti**

- **Attività Svolte durante il Dottorato**

  Corsi, seminari, presentazioni a conferenze, pubblicazioni, attività didattica.

- **Referenze Bibliografiche**

# INDEX OF CONTENTS

# VERSIONE IN ITALIANO

# CAPITOLO 1

# Introduzione alla Tematica di Ricerca

## 1.1. Introduzione Generale

Il presente Dottorato di ricerca ha come obiettivo lo studio della cementazione selettiva che interessa i sedimenti silico-clastici ad alta porosità deformati lungo zone di faglie oppure all'interno di pieghe. L'importanza di questa tipologia di studio risiede nel valutare l'influenza che i processi diagenetici esercitano sul meccanismo deformativo. La relazione tra i processi diagenetici e deformativi è stata studiata in tre differenti località che presentano caratteristiche peculiari. In prima istanza, ci si è occupati dello studio di concrezioni carbonatiche sviluppate all'interno di sedimenti poco cementati, deformati lungo in fianco esterno di un'anticlinale attiva (caso di studio della Val d'Enza). Questo primo studio ha permesso la redazione di un approccio metodologico per l'analisi dei paleo-flussi di fluidi in un contesto strutturale e deformativo relativamente semplice. La metodologia messa a punto è stata poi applicata in contesti strutturali più complessi, cercando di indagare l'effetto dei flussi di fluidi superficiali attraverso una zona di faglia estensionale e valutarne l'influenza sul meccanismo deformativo (caso di studio della zona di faglia di Rocca di Neto). Infine, l'ultimo caso di studio preso in analisi riguarda l'analisi della deformazione *soft-sediment* che caratterizza rocce di natura calcarenitica a bassa porosità esposte nel *footwall* del Cotiella *Thrust* (Massiccio di Cotiella, Pirenei spagnoli). Questa Tesi di Dottorato cerca di fornire un maggiore dettaglio in merito al processo di cementazione selettiva ad opera di fluidi superficiali in corrispondenza di anticlinali attive ed in merito alla relazione tra cementazione e deformazione di sedimenti poco litificati. Di seguito vengono introdotti brevemente gli argomenti e le tematiche che sono trattate e discusse nei vari capitoli che compongono la Tesi.

## 1.2. Alterazioni Diagenetiche

Le alterazioni diagenetiche possono essere presenti sottoforma di cementazioni selettive, masse di minerali, croste di alterazione con differente composizione mineralogica in funzione della natura dei fluidi e dell'ambiente diagenetico in cui la precipitazione è avvenuta (e.g., Todd, 1903; Jacob, 1973; Theakstone, 1981; Boles et al., 1985; Pirrie, 1987; Mozley e Wersin, 1992; Wilkinson, 1993; Mozley, 1996; Morad et al., 2000; Abdel-Wahab e McBride, 2001; Aiello et al., 2001; Hendry et al., 2006; Cavazza et al., 2009; Balsamo et al., 2013; Dale et al., 2014; Angeletti et al., 2015; Oppo et al., 2015). I corpi diagenetici sono caratterizzati da diverse geometrie e dimensioni in funzione del tipo di fluidi cementanti, meccanismo di crescita (advezione vs

diffusione) e proprietà petrofisiche del sedimento-roccia in cui sono ospitate (Bjorkum e Walderhaug, 1990; Sellés-Martínez, 1996; Seilacher, 2001; Raiswell e Fisher, 2004; Mozley e Davis, 2005; Msharrafieh e Sultan, 2006; Chan et al., 2007; Parry, 2011).

Le concrezioni e la cementazione preferenziale si possono sviluppare in diversi contesti diagenetici che spaziano da condizioni di seppellimento profondo fino ad ambienti sub-superficiali (McBride, 1988; Bjorkum e Walderhaug, 1990; Cibin et al., 1993; Morad et al., 2000; Hudson et al., 2001; Seilacher, 2001; McBride e Milliken, 2006; Balsamo et al., 2012, 2013; Lash, 2015; Loyd e Berelson, 2016; Zamanian et al., 2016; Li et al., 2018) e sono stati riconosciuti anche sulla superficie di altri pianeti mediante analisi di immagini satellitari (Sefton-Nash e Catling, 2008; Potter et al., 2011; Chan et al., 2012). La disposizione spaziale delle concrezioni diagenetiche fornisce informazioni relative alla modalità di deflusso dei fluidi e diversi autori utilizzano le alterazioni come traccianti per dedurre la direzione dei fluidi (McBride et al., 1994; Mozley e Davis, 1996; Cavazza et al., 2009; Balsamo et al., 2012). In particolare, nel caso di concrezioni formate da flussi di fluidi advettivi, l'anisotropia di forma dei corpi cementati può fornire informazioni in merito al percorso preferenziale dei fluidi in sottosuolo (McBride e Parea, 2001; Mozley e Davis, 2005).

L'analisi petrografica dei cementi che compongono i corpi diagenetici fornisce vincoli per dedurre l'ambiente diagenetico e la massima profondità di seppellimento a cui la roccia incassante è stata sottoposta (Dix e Mullins, 1987; Wilkinson, 1993; Abdel-Wahab e McBride, 2001; Hendry e Poulsom, 2006; Wanas, 2008; Van Den Bril e Swennen, 2009; Viola et al., 2015).

Alcuni autori impiegano l'analisi degli isotopi stabili per vincolare l'origine dei fluidi responsabili della cementazione e per comprendere il contesto diagenetico-sedimentario in cui è avvenuta la precipitazione dei minerali (e.g., Hudson, 1977; Boles et al., 1985; Hays e Grossman, 1991; Bjorkum e Walderhaug, 1993; Nelson e Smith, 1996; Muchez et al., 1998; Van Den Bril e Swennen, 2009; Dale et al., 2014). All'interno di sedimenti e rocce di natura silico-clastica il cemento più diffuso è la calcite e conseguentemente i corpi diagenetici più ricorrenti sono le concrezioni carbonatiche (Morad, 1998; Morad et al., 2000). All'interno di rocce e sedimenti ad alta porosità, lo sviluppo delle concrezioni carbonatiche promuove una diminuzione delle proprietà petrofisiche attraverso la cementazione selettiva (Houseknecht, 1987; Dutton et al., 2002; McBride and Milliken, 2006). Questo può indurre lo sviluppo di percorsi di migrazione dei fluidi più complessi e può favorire la compartimentalizzazione di un potenziale *reservoir* nel caso di cementazioni ad elevata estensione e continuità laterale (Bjorkum e Walderhaug, 1990; Taylor et al., 1995; Klein et al., 1999; Davis et al., 2006; Boutt et al., 2014). Il riconoscimento di queste caratteristiche diagenetiche risulta di primaria importanza nel campo della geologia del petrolio e dell'idrogeologia (Dutton et al., 2002; Hall et al., 2004; Davis et al., 2006). Diversi autori hanno sottolineato la possibile influenza dell'attività microbica nel promuovere la cementazione selettiva (Folk, 1993; McBride et al., 1994; Mozley e Davis, 2005; Hendry et al., 2006; Oppo et al., 2015; Viola et al., 2015; Yoshida et al., 2015), ma il processo di

cementazione nel complesso spesso coinvolge sia processi abiotici che biotici (Bjorkum e Walderhaug, 1990; Morad et al., 2000; Nyman et al., 2010).

### 1.3. Deformazione *Soft-Sediment*

Con il termine deformazione *soft-sediment* in letteratura è descritta una vasta gamma di strutture deformative che interessano i sedimenti e le rocce ad elevata porosità. In generale, questo stile deformativo si verifica all'interno dei sedimenti durante la loro deposizione (deformazione sin-deposizionale), oppure dopo la deposizione se la porosità primaria viene sufficientemente preservata nel tempo.

La deformazione *soft-sediment* può essere legata a diversi fenomeni che comprendono inversioni di densità dei sedimenti che inducono la formazione di strutture non deposizionali (ad esempio *load cast* nelle torbiditi) (Tinterri et al., 2016), terremoti o impatti di meteoriti che producono liquefazioni, sismiti e deformazione fragile (Rodrigues-Pascua et al., 2000; Montenat et al., 2007; Okubo e Schultz, 2007; Alfaro et al., 2010; Boukhedimi et al., 2017) ed attività tettonica con la formazione di bande di deformazione e faglie (e.g., Aydin, 1978; Mair et al., 2000; Balsamo et al., 2010; Fossen, 2010; Schultz et al., 2010; Nicol et al., 2013; Ballas et al., 2014; Soliva et al., 2016; Fossen et al., 2017; Philit et al., 2018). Dato che uno dei requisiti fondamentali per la formazione di strutture da deformazione *soft-sediment* è la presenza di litotipi ad elevata porosità, essa caratterizza frequentemente arenarie o sabbie, in cui la porosità è tendenzialmente elevata (può attestarsi al 35-40% in volume nel caso di arenarie eoliche ben classate) (Aydin, 1978). Nonostante ciò, la presenza di deformazione *soft-sediment* è stata documentata anche all'interno di litologie diverse rispetto alle arenarie, ad esempio in calcari (Cilona et al., 2012; Tondi et al., 2012; Antonellini et al., 2014) e rocce vulcano-clastiche (Wilson et al., 2003; Cavailhes e Rotevatn, 2018).

La presente Tesi di Dottorato è focalizzata allo studio delle relazioni tra deformazione e cementazione all'interno di sedimenti silico-clastici ad elevata porosità, in cui la deformazione *soft-sediment* si verifica sottoforma di bande di deformazione e superfici di faglia. Le bande di deformazione sono strutture deformative tabulari descritte in prima istanza nella letteratura scientifica come "piccole faglie" oppure "bande di Luder" (Friedman e Logan, 1973; Aydin, 1978; Olsson, 2000). Le bande di deformazione possono essere presenti come singoli elementi oppure come *cluster* di bande ravvicinate (Aydin e Johnson, 1978, 1983; Antonellini e Aydin, 1994; Nicol et al., 2013; Soliva et al., 2016; Fossen et al., 2017; Philit et al., 2018). Il comportamento *strain-hardening* conferisce alla singola banda una maggiore resistenza alla deformazione, promuovendo la delocalizzazione della deformazione all'interno della roccia indeformata circostante, piuttosto che localizzarla lungo discontinuità pre-esistenti (Aydin e Johnson, 1978; Eichhubl et al., 2010; Deng e Aydin, 2012). Con il progressivo aumento della deformazione, possono svilupparsi spessi *cluster* di bande di deformazione in cui appena i sedimenti deformati raggiungono una elevata rigidità e coesione, la deformazione può essere localizzata lungo distinte superfici di faglia (Aydin e Johnson, 1978; Shipton e Cowie, 2001; Davatzes et al., 2005). Il

comportamento *strain-hardening* alla base dello sviluppo delle faglie in sedimenti poco cementati è il risultato del meccanismo deformativo. Spesso il meccanismo deformativo dominante si compone di flusso particellare e cataclasi, i quali inducono una diminuzione della porosità, riduzione di granulometria e del *sorting* della sabbia deformata (Antonellini et al., 1994; Menéndez et al., 1996; Zhu e Wong, 1997; Rawling e Goodwin, 2003; Fossen et al., 2007; Torabi et al., 2007; Balsamo e Storti, 2010, 2011; Soliva et al., 2013; Rodrigues e Alves da Silva, 2018). Tutte queste condizioni conferiscono una maggiore resistenza alla deformazione del sedimento deformato (Mair et al., 2002). Il meccanismo deformativo alla micro-scala determina anche le proprietà petrofisiche dei sedimenti deformati che generalmente registrano una diminuzione della porosità e permeabilità efficace (Zhang et al., 1990; Antonellini et al., 1999; Wong and Zhu, 1999; Shipton et al., 2005; Torabi e Fossen, 2009; Balsamo e Storti, 2010; Ballas et al., 2012), sottolineando l'importanza che riveste l'analisi della deformazione s*oft-sediment* per lo studio dei *reservoir* e degli analoghi di terreno.

### 1.4. Comportamento Idrologico delle Rocce e dei Sedimenti Deformati

Il ruolo idrologico rivestito dalle rocce di faglia che interessano rocce coesive è caratterizzato da un dualismo indotto dalla presenza di due distinti domini strutturali con caratteristiche peculiari. La zona di danneggiamento in generale presenta un denso sistema di fratture legato al rigetto accomodato lungo la superficie di faglia principale (Kim et al., 2004; Choi et al., 2015). All'interno di questo dominio strutturale l'interconnessione delle fratture può conferire un comportamento da condotto preferenziale nei confronti dei fluidi, con valori di permeabilità più elevati parallelamente alla direzione della superficie di faglia piuttosto che ortogonalmente ad essa (Caine et al., 1996; Evans et al., 1997; Caine and Forster, 1999; Billi et al., 2003; Faulkner et al., 2010; Farrell et al., 2014). Al contrario, il nucleo della faglia presenta un comportamento da barriera a causa della presenza di superfici di taglio con elevata comminuzione della granulometria, volumi di roccia cataclastica e *gouge* di faglia (Engelder, 1974; Caine et al., 1996; Storti et al., 2011; Bense et al., 2013). All'interno di rocce o sedimenti ad elevata porosità il ruolo idrologico delle zone di faglia può essere più complesso da decifrare. Questo aspetto è legato alla differenza tra le strutture deformative delle zone di faglia che interessano rocce coesive rispetto alle rocce ad elevata porosità. In particolare, all'interno di materiali granulari ad elevata porosità, le zone di faglia si compongono di un dominio che presenta una pronunciata delocalizzazione della deformazione con la presenza di bande di deformazione, il quale corrisponde alla zona di danneggiamento all'interno di rocce coesive e ben litificate (e.g., Person et al., 2000; Fisher e Knipe, 2001; Rawling et al., 2001; Wilson et al., 2003; Balsamo e Storti, 2010; Eichhubl et al., 2010; Loveless et al., 2011; Schueller et al., 2013). All'interno di questo dominio strutturale a causa della scarsa cementazione-litificazione del materiale deformato, non si possono formare fratture tensili o *joint*. La maggior parte del rigetto viene accomodato lungo una zona di taglio

che presenta una elevata densità di bande di deformazione e diverse superfici di faglia secondarie (Aydin e Johnson, 1978; Shipton e Cowie, 2001; Davatzes et al., 2005). Questo dominio ad elevata deformazione può essere assimilato al nucleo della faglia. In alcuni casi specifici, se il rigetto complessivo supera lo spessore massimo della stratificazione si può formare un terzo dominio, definito zona di mescolamento tettonico da diversi autori, che si compone di sedimenti altamente deformati e marca la transizione tra la zona di danneggiamento ed il nucleo della faglia (Heynekamp et al., 1999; Rawling e Goodwin, 2006; Loveless et al., 2011). Lungo le singole bande di deformazione che compongono la zona di faglia, la permeabilità può descrivere una riduzione da 1 a 6 ordini di grandezza rispetto ai sedimenti indeformati, mentre la diminuzione può essere anche maggiore all'interno del nucleo della faglia (Antonellini e Aydin, 1994; Taylor e Pollard, 2000; Bense et al., 2003; Johansen et al., 2005; Balsamo e Storti, 2010; Ballas et al., 2015; Fossen et al., 2015, 2017). Ne consegue che le zone di faglia che interessano sedimenti ad elevata porosità vadano a costituire delle barriere nei confronti dei fluidi circolanti anche all'interno della zona di danneggiamento, diversamente dal comportamento da condotto preferenziale che si ha nelle rocce litificate. All'interno del nucleo di faglia il comportamento da barriera è maggiormente pronunciato anche se in alcuni casi l'aumento della coesione mostrato da parte dei sedimenti deformati può promuovere lo sviluppo di fratture tensili beanti, aumentando localmente la permeabilità e la trasmissibilità (Tindall e Eckert, 2015). Diversi autori hanno preso in analisi il comportamento da barriera alla scala della singola banda di deformazione ed hanno posto enfasi sull'importanza delle variazioni laterali dello spessore e della densità del sistema di bande (Shipton et al., 2005; Rotevatn et al., 2013, 2017). Tutto ciò, ha permesso di valutare l'influenza che le strutture deformative a scala sub-sismica hanno durante la fase di sfruttamento dei *reservoir* (Main et al., 2000; Sample et al., 2006; Sternlof et al., 2004, 2006; Kolyukhin et al., 2010). A questo scopo, la presenza di deformazione *soft-sediment* che interessa strutture plicative e faglie all'interno di rocce ad elevata porosità è un fattore di cruciale importanza nel valutare la capacità di compartimentalizzare trappole sotterranee e *reservoir* (Tueckmantel et al., 2010; Bretan, 2016; Wibberley et al., 2017; Fisher et al., 2018).

### 1.5. Relazione tra Deformazione e Processi Diagenetici

I processi diagenetici che interessano le rocce ed i sedimenti deformati sono intimamente connessi alle proprietà petrofisiche degli stessi. All'interno dei materiali granulari ad elevata porosità la presenza di zone di faglia può indurre una canalizzazione dei flussi a lato dei domini deformati che sono caratterizzati dalla presenza di strutture deformative a bassa permeabilità. In questo caso, i fluidi possono interagire con i sedimenti indeformati o debolmente deformati senza coinvolgere direttamente i domini a deformazione maggiore. La paleo-circolazione di fluidi può essere dedotta e studiata a partire dalla distribuzione spaziale delle alterazioni diagenetiche attraverso l'intera zona di faglia (ad esempio, la presenza di fronti di ossidazione-riduzione, cementazione selettiva e dissoluzione) (e.g.,

Sample et al., 1993; Mozley e Goodwin, 1995; Chan et al., 2000; Eichhubl et al., 2004; Beitler et al., 2005; De Boever et al., 2009; Caine et al., 2010; Balsamo et al., 2012). La distribuzione delle alterazioni diagenetiche può dipendere anche dall'ambiente diagenetico-sedimentario, dal momento che il comportamento idrologico delle zone di faglia cambia a seconda delle condizioni di saturazione dei fluidi. In particolare, in condizioni di sovra-saturazione di fluidi, le faglie possono comportarsi come barriere impedendo o rallentando il percorso dei fluidi, soprattutto in direzione ortogonale alla superficie degli elementi deformativi (Fossen e Bale, 2007; Ballas et al., 2015). Al contrario, in condizioni di sotto-saturazione di fluidi i sedimenti deformati possono agire da condotti parziali a causa degli elevati tempi di ritenzione (Sigda et al., 1999; Sigda e Wilson, 2003; Wilson et al., 2003; Balsamo et al., 2012). Questo dualismo nel comportamento idrologico porta ad una differente distribuzione delle alterazioni diagenetiche e può influenzare l'evoluzione del meccanismo deformativo e delle proprietà petrofisiche dei sedimenti deformati (Bense et al., 2013; Philit et al., 2015; Williams et al., 2016; Wibberley et al., 2017; Fisher et al., 2018).

# Riassunti dei Capitoli

## 1.6. Anticlinale di Quattro Castella, Val d'Enza (Appennino Settentrionale)

Viene di seguito riportato un breve riassunto organizzato in paragrafi dei contenuti illustrati all'interno del Capitolo 2, che si compone di un articolo scientifico dal titolo "From axial parallel to orthogonal groundwater flow during fold amplification: insights from carbonate concretion development during the growth of the Quattro Castella Anticline, Northern Apennines, Italy", autori, Mattia Pizzati, Fabrizio Balsamo, Fabrizio Storti, Mahtab Mozafari, Paola Iacumin, Roberto Tinterri e Rudy Swennen, pubblicato sulla rivista *Journal of the Geological Society of London* 175, 806–819. https://doi.org/10.1144/jgs2018-031.

Questo studio ha permesso di analizzare il cambiamento nella direzione del flusso di fluidi superficiali durante le ultime fasi di propagazione laterale dell'anticlinale di Quattro Castella, registrato dal pattern delle concrezioni diagenetiche. Il risultato è stato reso possibile grazie all'adozione di una metodologia multidisciplinare che prevede il rilevamento geologico-strutturale, analisi petrografiche e diagenetico-isotopiche delle concrezioni carbonatiche ed analisi petrofisiche dei sedimenti interessati dalla cementazione preferenziale.

### 1.6.1. Introduzione

L'area di studio si trova in corrispondenza del fronte topografico appenninico lungo il corso del fiume Enza, dove affiora una successione silico-clastica di età Pleistocenica che registra il passaggio da un ambiente marino di acque basse ad un contesto fluvio-continentale. La successione è stata deposta lungo la zona periclinale del fianco esterno dell'anticlinale di Quattro Castella. L'anticlinale ha una geometria asimmetrica con il fianco esterno più inclinato rispetto a quello interno ed è stata prodotta da un sistema di *thrust* ciechi che scollano all'interno delle unità di avanfossa di età Miocenica. La piega si è nucleata nell'*hangingwall* del *thrust* a partire dalla fine del Miocene ed è attiva tuttora. In questo contesto la successione stratigrafica presa in analisi si configura come una sequenza di crescita della piega ed a causa della sua posizione può avere registrato i flussi di fluidi superficiali indotti dalle ultime fasi di propagazione dell'anticlinale.

### 1.6.2. Risultati Principali

L'affioramento preso in analisi ha uno spessore stratigrafico massimo misurato di 300 m e si compone di diverse formazioni, partendo dalla base si ha: (i) Formazione delle Argille Azzurre deposte in ambiente marino di acque basse (prodelta); (ii) Formazione delle Sabbie di Imola, che denota il passaggio ad ambienti di spiaggia; (iii) Sintema Emiliano-Romagnolo inferiore che si compone di sedimenti continentali-fluviali. L'intera successione mostra evidenze di sedimentazione sin-cinematica rispetto allo sviluppo della piega, come testimoniato dalla diminuzione dell'inclinazione degli strati dalla base al tetto dell'affioramento analizzato. L'affioramento lungo il fiume Enza è stato

studiato da altri autori per la presenza di concrezioni a "camino" metano-geniche ospitate all'interno della Formazione delle Argille Azzurre. Il contributo presentato in questa sezione si focalizza sullo studio di corpi diagenetici mai presi in analisi che sono presenti in corrispondenza della transizione tra le Formazioni delle Argille Azzurre e delle Sabbie di Imola ed all'interno dei corpi sabbiosi che compongono quest'ultima. Le concrezioni diagenetiche sono comprese all'interno di circa 30 m di successione e possono essere suddivise in diverse tipologie a seconda della morfologia e delle dimensioni: (i) concrezioni allungate singole di piccole dimensioni; (ii) concrezioni allungate coalescenti, composte da diversi elementi singoli cementati a formare corpi metrici; (iii) concrezioni tabulari parallele alla stratificazione ad elevata estensione laterale; (iv) concrezioni nodulari con forme circa sferiche. Mentre le concrezioni tabulari presentano un'orientazione parallela alla stratificazione, i corpi diagenetici allungati mostrano diverse orientazioni dell'asse maggiore attraverso l'intervallo stratigrafico preso in analisi (transizione che marca il passaggio dalle Argille Azzurre alle Sabbie di Imola). In particolare, le concrezioni allungate sono caratterizzate da una direzione media dell'asse maggiore verso Ovest alla base dell'intervallo in analisi, mentre essa subisce una rotazione progressiva prima verso NW ed infine verso NNE risalendo la stratigrafia presa in analisi. La direzione media delle concrezioni subisce una rotazione oraria di circa 110°. La ricostruzione della paleo-immersione degli strati che ospitano le concrezioni è stata effettuata mediante la retro-deformazione della sezione stratigrafica, riportando all'orizzontale in modo progressivo gli strati deformati. Ciò ha permesso di ricostruire paleo-immersioni verso Ovest alla base del *log* stratigrafico preso in analisi, mentre risalendo la stratigrafia gli strati mostrano una rotazione oraria che segue lo stesso andamento messo in luce dall'analisi della direzione delle concrezioni allungate.

L'analisi delle proprietà petrofisiche eseguite lungo l'intervallo stratigrafico indica che le concrezioni sono presenti all'interno di strati di sabbia caratterizzati da granulometrie comprese tra 90 e 290 μm e permeabilità tra $7\times10^{2}$ e $7\times10^{4}$ mD.

L'analisi petrografica delle concrezioni ha mostrato un pattern di cementazione composto da 4 distinte generazioni di cemento carbonatico: (i) calcite con cristalli isotropi (dimensione dei cristalli < 10-20 μm) organizzata in accrescimenti concentrici lungo la superficie esterna dei bioclasti o calcite detritica con luminescenza scura; (ii) calcite sparitica fine (dimensione dei cristalli < 25 μm) con tessitura a mosaico che compone menischi lungo la superficie dei clasti. La risposta in catodoluminescenza è quasi sempre scura anche se raramente questi cementi possono avere luminescenza arancione; (iii) calcite *blocky* con cristalli di dimensioni superiori a 300-400 μm, con una peculiare zonatura visibile in catodoluminescenza composta da accrescimenti concentrici non luminescenti alternati ad altri con tonalità arancione-giallo; (iv) calcite sparitica con cristalli di dimensioni < 50 μm, con colori in catodoluminescenza molto accesi che tendono al giallo. Le quattro generazioni di cemento sono state ritrovate in tutte le quattro tipologie di concrezioni. Le concrezioni allungate singole mostrano un *pattern* di cementazione composto da cementi di tipo (iii) e (iv) in uguali proporzioni, mentre all'interno delle

concrezioni tabulari il cemento (iii) diventa dominante.

Le analisi isotopiche eseguite su campioni di cemento carbonatico estratti dalle concrezioni mostrano un intervallo di variazione degli isotopi del carbonio compresa tra -10.7‰ e -2.5‰ V-PDB, mentre gli isotopi dell'ossigeno mostrano una variazione più contenuta tra -7.6‰ e -5.5‰ V-PDB. Le concrezioni nodulari con forma circa sferica sono caratterizzate dai valori meno impoveriti (meno negativi), mentre i corpi tabulari o allungati coalescenti di grandi dimensioni hanno valori isotopici più impoveriti (più negativi) sia per quanto riguarda gli isotopi del carbonio che dell'ossigeno. All'interno delle singole concrezioni il nucleo registra valori di $\delta^{13}C$ e $\delta^{18}O$ meno impoveriti, mentre lungo il bordo esterno tendono a diventare progressivamente più impoveriti. Considerando le generazioni di cemento più ricorrenti, i cementi composti da calcite *blocky* (iii) hanno composizioni isotopiche più impoverite rispetto alla calcite sparitica fine (iv).

### 1.6.3. Discussione dei Risultati

Le analisi degli isotopi stabili indicano un ambiente di precipitazione molto superficiale che corrisponde alla zona meteorica freatica e vadosa. La cementazione è avvenuta a cavallo della tavola d'acqua che delimita l'ambiente freatico saturo, da quello vadoso parzialmente saturo. La sequenza di cementazione suggerisce un progressivo approfondimento dell'ambiente diagenetico con un incremento delle condizioni riducenti all'interno del paleo-acquifero (approfondimento relativo rispetto alla tavola d'acqua). La cementazione preferenziale è avvenuta in condizioni di limitato seppellimento come è confermato dai dati isotopici che indicano una possibile influenza nella cementazione di fluidi di origine meteorica che hanno attraversato i suoli e dai dati stratigrafici che indicano una profondità massima di seppellimento inferiore a 120 m.

La geometria dei corpi diagenetici è in funzione della distribuzione iniziale dei nuclei di cementazione, ossia dei volumi di sedimento in cui la cementazione ha avuto origine. Un altro fattore di controllo è la modalità di deflusso delle acque in sottosuolo attraverso i sedimenti porosi: flussi di fluidi laminari che si dispongono parallelamente alla stratificazione promuovono la cementazione di corpi tabulari ad elevata continuità ed estensione laterale, mentre flussi più focalizzati portano alla formazione di concrezioni allungate coalescenti. La modalità di deflusso è influenzata dalla struttura di granulometria e permeabilità alla scala dell'intero affioramento, mentre l'organizzazione interna delle facies sedimentarie non sembra giocare un ruolo importante nel determinare la geometria finale delle concrezioni.

In questo contesto le concrezioni possono essere utilizzate come traccianti per dedurre la paleo-circolazione di fluidi e la rotazione della direzione dell'asse lungo delle concrezioni allungate può essere messa in relazione ad un cambiamento nella direzione di deflusso dei fluidi. Come indicato anche dai dati relativi alle paleo-inclinazioni degli strati, durante la deposizione della parte basale dell'intervallo stratigrafico preso in analisi, gli strati erano immergenti verso Ovest. Allo stesso modo le concrezioni diagenetiche che si ritrovano in prossimità della stessa altezza

stratigrafica sono caratterizzate da direzioni dell'asse maggiore rivolte verso Ovest. Ciò significa che la propagazione laterale dell'anticlinale di Quattro Castella in prossimità della chiusura periclinale, può avere indotto dei gradienti topografici ed idraulici diretti da Est verso Ovest. Durante le successive fasi di propagazione della piega, dopo che l'affioramento esposto lungo il fiume Enza è stato incluso all'interno del fianco esterno della piega, i flussi hanno registrato una rotazione prima verso NW ed infine verso NNE. Ciò si verifica in risposta ad una contestuale rotazione del gradiente topografico ed idraulico da direzioni Est-Ovest a Sud-Nord. Negli ultimi stadi deformativi della piega i flussi di fluidi sono diretti verso NNE, circa ortogonali all'asse della piega che ha direzione WNW-ESE.

### 1.6.4. Conclusioni

Gli strati sin-cinematici che compongono la sequenza di crescita dell'anticlinale di Quattro Castella hanno registrato paleo-flussi di fluidi che possono essere ricostruiti dallo studio delle concrezioni diagenetiche. I paleo-flussi di fluidi sono responsabili della cementazione preferenziale sottoforma di concrezioni con diverse geometrie e forme che spaziano da elementi allungati singoli a coalescenti fino a corpi tabulari. Le concrezioni si sono nucleate in un ambiente di transizione tra il meteorico vadoso e freatico. La cementazione è proseguita all'interno di un ambiente meteorico freatico con il contributo di fluidi che hanno interagito con i suoli. Le concrezioni si sono sviluppate mediante il processo di crescita verso l'esterno con il cemento di neo-formazione che precipita lungo la superficie esterna della proto-concrezione.

I corpi diagenetici allungati e tabulari si sono formati a partire da flussi advettivi, mentre le concrezioni nodulari-sferiche sono il risultato di un trasporto di massa dominato da fenomeni diffusivi. Le concrezioni si trovano all'interno di strati di sabbia con granulometria compresa tra 90 e 290 μm, e permeabilità tra $7\times10^{2}$ e $7\times10^{4}$ mD. La rotazione oraria della direzione dell'asse maggiore delle concrezioni allungate suggerisce una variazione nella direzione di deflusso dei fluidi meteorici durante le ultime fasi di propagazione dell'anticlinale. Le concrezioni registrano una rotazione oraria di circa 110° che è in relazione ad un cambiamento nel gradiente topografico ed idraulico da Est-Ovest a circa Sud-Nord.

## 1.7. Evoluzione Strutturale e Processi Diagenetici della Zona di Faglia di Rocca di Neto (Bacino di Crotone)

Viene di seguito riportato un breve riassunto organizzato in paragrafi dei contenuti illustrati all'interno del Capitolo 3, che si compone di un manoscritto intitolato "Physical and chemical strain-hardening, kinematically-induced stress, and strain delocalization-localization stages during faulting in poorly lithified sandstones (Crotone Basin, Southern Apennines, Italy)", autori Mattia Pizzati, Fabrizio Balsamo, Fabrizio Storti e Paola Iacumin, che verrà sottomesso a breve alla rivista *Geological Society of America Bulletin*.

Questo caso di studio ha permesso di valutare l'impatto e l'influenza dei processi diagenetici sul meccanismo deformativo che caratterizza una zona di faglia estensionale

che interessa sedimenti debolmente litificati e cementati all'interno del Bacino di Crotone. Lo studio dell'evoluzione strutturale e diagenetica della zona di faglia è stato effettuato mediante rilevamento geologico-strutturale della zona di faglia, tecniche analitiche-petrografiche per analizzare la tipologia dei cementi ed analisi degli isotopi stabili carbonio-ossigeno per vincolare la natura dei fluidi che hanno interagito con i sedimenti deformati.

### 1.7.1. Introduzione

La zona di faglia estensionale presa in analisi si trova all'interno del Bacino di Crotone, che si configura come un bacino di avan-arco riempito a partire dal Miocene Medio, di sedimenti provenienti in gran parte dal basamento metamorfico della Sila esumato e soggetto ad erosione. La successione stratigrafica completa si compone di circa 2500 m di sedimenti. Il bacino fa parte del complesso sistema geodinamico dell'Arco Calabro ed a causa della sua posizione ha subito diversi eventi tettonici durante la sua evoluzione, in prevalenza con componente estensionale e trascorrente. La zona di faglia presa in analisi fa parte di un sistema di faglie estensionali con direzione NE-SW che si sono sviluppate a partire dal Pleistocene Inferiore-Medio in risposta al sollevamento tettonico a cui il bacino è stato sottoposto durante le ultime fasi evolutive.

### 1.7.2. Risultati Principali

La zona di faglia studiata si trova in corrispondenza del paese di Rocca di Neto, ha componente estensionale ed interessa sedimenti poco litificati. In particolare, vengono coinvolti nella deformazione le arenarie di Scandale nel *footwall* e le argille di Cutro nell'*hangingwall*. La zona di faglia presenta un rigetto stimato tra 80 e 90 m e lungo il *footwall* mostra una diffusa deformazione sottoforma di bande di deformazione e *gouge*. La zona di faglia può essere distinta in quattro domini deformativi principali sulla base delle caratteristiche e densità delle strutture deformative: (i) zona a bassa deformazione, caratterizzata dalla presenza di bande di deformazione e faglie antitetiche e sintetiche rispetto alla faglia principale. All'interno di questa zona le bande e le faglie sono molto spaziate ed accomodano rigetti limitati; (ii) zona di danneggiamento, che si compone di un elevato numero di bande di deformazione organizzate in un sistema coniugato inclinato ed un terzo *set* orientato parallelamente alle faglie principali; (iii) zona di mescolamento tettonico con forte compattazione e mescolamento di sedimenti a differente granulometria; (iv) nucleo della faglia, dove viene accomodata la maggior parte del rigetto attraverso superfici di faglia e *gouge*. I limiti spaziali dei vari domini strutturali identificati sono stati definiti attraverso una *scanline* lineare lungo il *footwall* della zona di faglia in cui è stata misurata la densità delle bande di deformazione. Differenti *trend* lineari della densità cumulativa delle bande di deformazione corrispondono ai differenti domini di cui si compone la zona di faglia. Attraverso il *footwall* della zona di faglia sono presenti evidenze di cementazione preferenziale associata alle faglie ed alle bande di deformazione. In particolare, le discontinuità sono spesso interessate da cementazioni selettive con geometria tabulare composte da calcite. Le concrezioni mostrano spessori limitati (pochi cm) in

corrispondenza di bande e faglie a basso rigetto, mentre le faglie a rigetto elevato all'interno della zona di danneggiamento sono caratterizzate da corpi diagenetici con spessori maggiori (pochi dm). Sono presenti anche rare concrezioni parallele alla stratificazione, ma mostrano una scarsa continuità laterale e spessori nell'ordine di pochi cm.

I dati di resistenza a compressione uniassiale all'interno della sabbia inconsolidata sono al di sotto del limite inferiore di rilevabilità del martello di Schmidt, mentre le misure effettuate sulle superfici delle bande di deformazione mostrano aumenti consistenti. Infine, le misure condotte sulle bande di deformazione e sulle faglie cementate selettivamente dalle concrezioni registrano valori di compressione uniassiale molto elevati.

Dalle osservazioni petrografiche è stato possibile vincolare la natura dei cementi che compongono i corpi diagenetici. In particolare, le concrezioni poste all'interno della zona a bassa deformazione sono caratterizzate da cementi composti da calcite sparitica con tessitura granulare (dimensione dei cristalli < 70-80 μm) ed elevata intensità dei colori in catodoluminescenza (colore arancione-giallo). All'interno delle bande e delle faglie il cemento subisce una riduzione di granulometria. Le concrezioni che cementano le faglie e le bande all'interno della zona di danneggiamento sono caratterizzate da calcite con tessitura a mosaico (dimensione dei cristalli 90-100 μm), con luminescenza marrone scuro in prossimità del nucleo della concrezione e colori che virano a tonalità arancione-giallo lungo il bordo esterno. Infine, le concrezioni all'interno del nucleo della faglia presentano cemento a base di calcite con dimensioni dei cristalli variabili tra 30 e 200 μm e luminescenza arancione molto scura.

La differenza nella tipologia dei cementi è sottolineata anche dai dati isotopici degli isotopi stabili della calcite. Le concrezioni associate alle faglie ed alle bande di deformazione campionate nella zona a bassa deformazione mostrano valori di $\delta^{13}C$ che variano in un ampio intervallo compreso tra -23.08‰ e -8.98‰ V-PDB, mentre l'ossigeno mostra variazioni più contenute tra -8.45‰ V-PDB e -4.12‰ V-PDB. Le concrezioni che interessano le faglie all'interno della zona di danneggiamento hanno un intervallo di variazione degli isotopi del carbonio compreso tra -10.35‰ e -0.02‰ V-PDB, mentre l'ossigeno spazia tra -5.39‰ e -1.25‰ V-PDB. Le concrezioni all'interno della zona di mescolamento tettonico presentano valori isotopici meno impoveriti tra -3.26‰ e -0.16‰ V-PDB per il $\delta^{13}C$ e tra -3.99‰ e -1.32‰ V-PDB per il $\delta^{18}O$. Infine, le concrezioni lungo la superficie di faglia principale all'interno del nucleo della faglia presentano valori degli isotopi del carbonio compresi tra -8.09‰ e -0.49‰ V-PDB ed una variazione dell'ossigeno tra -7.51‰ e -2.09‰ V-PDB. Valutando gli andamenti dei risultati isotopici sulle singole concrezioni si nota che le concrezioni campionate nel nucleo della faglia presentano valori circa costanti dal nucleo al bordo. Al contrario le concrezioni all'interno della zona di danneggiamento mostrano i valori isotopici più arricchiti in prossimità del nucleo e più impoveriti in corrispondenza del bordo esterno. Infine, i corpi diagenetici all'interno della zona a bassa deformazione hanno valori isotopici molto impoveriti soprattutto vicino al nucleo.

### 1.7.3. Discussione dei Risultati

L'analisi strutturale dell'orientazione delle bande di deformazione ha permesso di identificare un doppio campo di stress che caratterizza i diversi settori della zona di faglia. In particolare, all'interno della zona a bassa deformazione il campo di stress dedotto presenta un asse di stress principale $\sigma_1$ orientato circa verticalmente (modello Andersoniano classico). All'interno del dominio di faglia (zona di danneggiamento, zona di mescolamento e nucleo della faglia) l'asse di stress principale è inclinato e descrive un angolo di circa 44° rispetto all'inclinazione della superficie di faglia. Questa differente orientazione suggerisce che la faglia, durante il suo sviluppo abbia indotto la formazione di un campo di stress locale.

La componente fisica del processo *strain-hardening* osservata alla scala dell'intera faglia è data dall'azione del campo di stress locale che induce la formazione di un denso sistema di bande di deformazione e faglie. La componente chimica dello *strain-hardening* è invece data dalla cementazione sin-cinematica che è particolarmente accentuata in prossimità della superficie di faglia principale. Le analisi isotopiche, combinate con le osservazioni meso-strutturali permettono di definire l'evoluzione della zona di faglia nel tempo. Durante le prime fasi deformative, la faglia si è nucleata come un sistema di bande di deformazione in un ambiente marino di acque basse subito dopo la deposizione della sabbia. In questo primo stadio di deformazione non si verificano cementazioni selettive, a causa di condizioni di sottosaturazione rispetto al carbonato di calcio dell'acqua marina, oppure a causa del ruolo da barriera efficace che caratterizza le bande di deformazione in condizioni di completa saturazione di acqua. Durante il sollevamento tettonico a cui il bacino è stato sottoposto, la deformazione si è propagata verso la zona indeformata a causa della cementazione progressiva lungo le discontinuità pre-esistenti. In questo stadio le concrezioni registrano cementi precipitati a partire da fluidi composti da un mescolamento di acque marine e meteoriche. Il progressivo sviluppo della zona di faglia induce la formazione di un campo di stress locale che produce il sistema di bande di deformazione coniugato inclinato. Le concrezioni all'interno della zona di danneggiamento registrano l'influenza di fluidi meteorici nella cementazione. Infine, durante gli ultimi stadi di evoluzione della faglia la deformazione si propaga verso la zona indeformata dove le concrezioni si sono formate sotto l'influenza di fluidi meteorici molto superficiali. Durante questo ultimo stadio la deformazione non viene più accomodata lungo la superficie principale della faglia a causa dell'aumento della resistenza a deformazione che caratterizza i sedimenti deformati e cementati in modo selettivo nei domini strutturali più interni.

### 1.7.4. Conclusioni

L'approccio multidisciplinare adottato ha permesso di ricostruire l'evoluzione strutturale e diagenetica della zona di faglia studiata. Lo sviluppo della faglia ha promosso la formazione di un campo di stress aggiuntivo locale che risulta nella formazione del sistema di bande di deformazione coniugate. La cementazione selettiva ha indotto la formazione di concrezioni diagenetiche durante le diverse fasi di attività della faglia. La cementazione è quindi sin-cinematica e registra il passaggio da ambienti

con mescolamenti di acque marine e meteoriche ad ambienti dominati da fluidi meteorici. L'azione combinata di compattazione e deformazione tettonica e la cementazione selettiva ha promosso lo spostamento della deformazione verso la zona indeformata, a causa di un comportamento *strain-hardening* sia alla scala della singola banda che dell'intera zona di faglia.

## 1.8. Meccanismi Deformativi e Proprietà Petrofisiche della Zona di Faglia di Rocca di Neto (Bacino di Crotone)

Viene di seguito riportato un breve riassunto organizzato in paragrafi dei contenuti illustrati all'interno del Capitolo 4, che si compone di un manoscritto intitolato "Displacement-dependent microstructural and petrophysical properties of deformation bands and gouges within poorly lithified sandstone deformed at shallow burial depth (Crotone Basin, Italy)", autori Mattia Pizzati, Fabrizio Balsamo e Fabrizio Storti, che verrà sottomesso a breve alla rivista *Journal of Structural Geology*.

Questo studio ha permesso di descrivere e vincolare il meccanismo deformativo che caratterizza le bande di deformazione, i *gouge* e le faglie presenti all'interno della zona di faglia di Rocca di Neto, la cui evoluzione strutturale e diagenetica è stata descritta all'interno del Capitolo 3. L'analisi del meccanismo deformativo è stata effettuata mediante tecniche analitiche petrografiche ed attraverso metodi di analisi di immagine per quantificare il *fabric* delle strutture deformative. Le proprietà petrofisiche dei sedimenti deformati sono state caratterizzate attraverso misure *in situ* e mediante analisi di laboratorio.

### 1.8.1. Introduzione

Lo studio è stato effettuato lungo la zona di faglia di Rocca di Neto descritta precedentemente all'interno del paragrafo 1.7. Per una breve descrizione dell'assetto geologico del Bacino di Crotone si rimanda il lettore al paragrafo 1.7.1.

### 1.8.2. Risultati Principali

Lo studio è stato condotto valutando le strutture da deformazione *soft-sediment* che sono presenti all'interno del *footwall* della faglia di Rocca di Neto. Le strutture deformative prese in analisi comprendono bande di deformazione che presentano differente entità di rigetto ($d < 1$ cm a $d > 20$ cm), campionate in diverse posizioni all'interno della zona di faglia, livelli di *gouge* ($5 \text{ cm} < d < 10 \text{ cm}$) all'interno del nucleo della faglia e faglie secondarie ($d > 20$ cm). Le proprietà petrofisiche (granulometria, permeabilità e porosità) dei sedimenti deformati sono state confrontate con la controparte indeformata.

I sedimenti indeformati sono sabbie medio-fini e più raramente mostrano granulometria medio-grossolana. Le bande di deformazione con rigetti inferiori ad 1 cm inducono una riduzione della granulometria con un significativo aumento nel numero di particelle nell'intervallo tra 10 e 100 µm. Le bande a rigetto maggiore all'interno della zona di danneggiamento sono caratterizzate da granulometrie medie di 125 µm ed un marcato aumento delle particelle tra 0.7 e 70 µm con una contestuale diminuzione di

quelle che ricadono tra 100 e 500 µm. I livelli di *gouge* e sabbia foliata all'interno del nucleo della faglia sono i campioni che presentano le granulometrie più fini. La deformazione all'interno del nucleo di faglia induce una riduzione di granulometria di 7-8 volte rispetto alla sabbia medio-fine indeformata. La diminuzione di granulometria avviene contestualmente alla diminuzione di permeabilità. In particolare, lungo le bande di deformazione la permeabilità risulta da 0.5 a 2 volte inferiore rispetto al sedimento indeformato. I *gouge*, i nuclei delle faglie secondarie e la sabbia foliata nel *fault core*, sono caratterizzate da una diminuzione di permeabilità di 3-4 ordini di grandezza rispetto alla sabbia medio-fine. La porosità 2-D calcolata mediante analisi di immagine restituisce un valore medio di 37% per la sabbia medio-fine, mentre all'interno delle bande di deformazione si riduce tra 5.8% e 1.3%. I *gouge* neri hanno valori di porosità primaria inferiori ad 1%.

Dalle analisi petrografiche la composizione modale della sabbia indeformata risulta compresa tra le arkose litiche ed arkose. All'interno dei campioni deformati l'analisi micro-strutturale mostra differenti caratteristiche a seconda del rigetto totale accumulato. Le bande con rigetti contenuti (d < 1 cm) presentano una limitata riduzione di granulometria ed una riorganizzazione del *fabric* con una leggera rotazione dei clasti. Tutto ciò induce una riduzione della porosità e promuove una maggiore compattazione del sedimento deformato. All'aumentare del rigetto le bande di deformazione mostrano una maggiore riduzione della granulometria che avviene attraverso lo sviluppo di fratture intra-granulari (soprattutto lungo i punti di contatto trai i clasti) e mediante rotolamento dei clasti. Le bande di deformazione più deformate sono caratterizzate da nuclei ultra-comminuti. I *gouge* sono costituiti da sottili livelli con ultracomminuzione della sabbia medio-fine localizzata lungo superfici di taglio discrete.

L'analisi dei parametri di forma indica che i clasti deformati si presentano meno anisotropi, più circolari e con bordi più regolari rispetto ai clasti indeformati. La differenza tra i parametri di forma tende ad essere più marcata all'aumentare del rigetto accomodato lungo il singolo elemento deformativo. L'analisi dei parametri di forma eseguita sulle specie mineralogiche più frequenti (quarzo, feldspato e frammenti litici), consente di valutare in dettaglio il meccanismo deformativo. All'aumentare del rigetto i clasti di quarzo si presentano più anisotropi (elevato rapporto tra asse maggiore e minore), meno circolari e con bordi esterni più irregolari rispetto ai clasti di feldspato. La differenza diventa più pronunciata all'aumentare del rigetto. I frammenti litici hanno andamenti più complessi rispetto al quarzo ed al feldspato a causa di una maggiore varietà composizionale (clasti di origine sedimentaria, ignea o metamorfica). All'interno dei domini deformati i clasti tendono ad allineare l'asse maggiore rispetto alla direzione dell'elemento deformativo. Al contrario nei campioni di controllo i clasti mostrano orientazioni dell'asse maggiore casuali. All'aumentare dell'anisotropia di forma dei clasti, essi tendono ad allinearsi entro un intervallo angolare di 20-30° rispetto all'elemento deformativo presente (banda di deformazione o *gouge*).

### 1.8.3. Discussione dei Risultati

La limitata riduzione di granulometria e la riorganizzazione del *fabric* che caratterizza le bande di deformazione con rigetto inferiore ad 1 cm sono interpretati come il risultato di un meccanismo deformativo dominato dal flusso particellare non distruttivo. Anche per entità di deformazione molto basse si ha una diminuzione significativa di porosità che all'aumentare del rigetto si traduce in un elevata frammentazione dei clasti. La frammentazione e rotolamento dei clasti vengono interpretati come evidenze di processi cataclastici, che localmente possono indurre una estrema riduzione di granulometria. All'interno dei *gouge* la cataclasi è estrema e produce una localizzata ultra-comminuzione della granulometria.

La deformazione agisce in modo differente a seconda della mineralogia dei clasti coinvolti. In particolare, i clasti di feldspato anche per basse entità di deformazione sono interessati da fratture intra-granulari che si impostano lungo i piani di geminazione. Al contrario, i clasti di quarzo sono meno soggetti alla formazione di fratture intra-granulari e la loro deformazione avviene prevalentemente attraverso processi di abrasione delle asperità. I sub-clasti che si formano sono più anisotropi, meno circolari e con bordi più irregolari. Una maggiore intensità della cataclasi accentua la differenza tra i parametri di forma dei clasti di quarzo rispetto al feldspato.

Il meccanismo deformativo riveste un ruolo fondamentale nel determinare la diminuzione di granulometria e del *sorting* della sabbia deformata, inducendo una marcata caduta di permeabilità. La ridotta permeabilità dei sedimenti deformati si può tradurre in un ruolo da barriera esercitato dalla faglia in condizioni di completa saturazione dei fluidi, e da parziale condotto in condizioni insature o parzialmente sature. La presenza di cementazioni preferenziali lungo le bande di deformazione e le faglie suggerisce che i sedimenti deformati abbiano agito da parziale condotto a causa di tempi di ritenzione dei fluidi molto lunghi.

### 1.8.4. Conclusioni

Il meccanismo deformativo responsabile della deformazione si compone di flusso particellare seguito da cataclasi che si instaura a seguito di una diminuzione di porosità al di sotto del 5-6%. La cataclasi ha agito in modo differente a seconda della mineralogia dei clasti coinvolti: il feldspato tende a sviluppare fratture intra-granulari lungo i piani di geminazione, mentre il quarzo si deforma principalmente attraverso processi di abrasione delle asperità. Ciò comporta una differenza nella forma dei clasti, con il quarzo che è caratterizzato da forme più anisotrope (allungate), minore circolarità e bordi più irregolari rispetto al feldspato. La deformazione induce una riduzione della granulometria con una caduta di permeabilità massima di 3-4 ordini di grandezza rispetto al sedimento indeformato. La presenza di cementazioni selettive lungo le discontinuità suggerisce un comportamento da parziale condotto della zona di faglia avvenuto in ambienti parzialmente saturi di fluidi.

## 1.9. Deformazione *Soft-Sediment* lungo il Cotiella Thrust (Pirenei spagnoli)

Viene di seguito riportato un breve riassunto organizzato in paragrafi dei contenuti illustrati all'interno del Capitolo 5, che si compone di un articolo intitolato "Shear-

enhanced compaction-solution bands in quartz-rich calcarenites of the Cotiella Massif (Spanish Pyrenees)", autori Stefano Tavani, Pablo Granado, Fabrizio Balsamo, Mattia Pizzati, Irene Cantarero, Amerigo Corradetti e Josep Anton Muñoz, pubblicato sulla rivista *Journal of Structural Geology* 114, 274–279. https://doi.org/10.1016/j.jsg.2017.11.018

Questo studio ha permesso di documentare la presenza di bande di deformazione ibride con componente di compattazione e dissoluzione preferenziale all'interno di calcareniti che affiorano nel *footwall* del Cotiella *Thrust*. La descrizione è stata eseguita attraverso l'analisi meso-strutturale ed osservazioni petrografiche combinate con l'analisi di immagine.

### 1.9.1. Introduzione

Le bande di deformazione studiate si trovano in corrispondenza del *footwall* del Cotiella *Thrust* che pone in contatto rocce con età compresa tra Triassico e Cretaceo Superiore nell'*hangingwall* con rocce di età che vanno dal Cretaceo Superiore al Paleogene nel *footwall*. Le bande si sono sviluppate all'interno di rocce calcarenitiche con componente mista carbonatica e silico-clastica, deposte nell'avampaese della catena pirenaica e sepolte a 2-3 km di profondità.

### 1.9.2. Risultati Principali

Le bande di deformazione studiate sono organizzate in due distinti sistemi coniugati che formano un angolo di 45° e 135° rispetto alla stratificazione. Alcune bande sono organizzate in un terzo sistema orientato perpendicolarmente rispetto alla stratificazione, ma sono minoritarie rispetto a quelle precedentemente descritte. Le bande si intersecano tra loro, ma non mostrano rigetti significativi. Dalle osservazioni petrografiche, la roccia che ospita le bande di deformazione si caratterizza come una calcarenite bioclastica, con cemento a base di calcite micro-sparitica e minore componente silico-clastica. La componente carbonatica è assimilabile ad un *grainstone* peloidale, mentre quella silico-clastica è data da quarzo, feldspato, plagioclasio e miche. Le bande di deformazione si caratterizzano come zone in cui i clasti di quarzo e feldspato sono densamente concentrati e presentano frammentazione.

Attraverso l'analisi di immagine è possibile definire la percentuale della componente carbonatica che si attesta tra 60-80% dell'area totale nei domini indeformati e tra 30-40% all'interno delle bande. Ciò corrisponde ad una deformazione per compattazione che spazia da 32% a 59%. In corrispondenza delle bande i clasti sono caratterizzati da una frammentazione eterogenea e localmente si possono avere delle riduzioni di granulometria del 50% rispetto alla roccia indeformata. La frammentazione dei clasti produce un leggero aumento della circolarità. All'interno delle bande si ritrovano superfici stilolitiche in cui si è verificata la dissoluzione della componente carbonatica, mentre i clasti di quarzo presentano contatti suturati. Lungo le superfici stilolitiche è presente una elevata densità di minerali insolubili come ossidi di ferro-titanio e minerali argillosi tra cui illite, montmorillonite e muscovite.

### 1.9.3. Discussione dei Risultati

L’assenza di rigetti visibili alla meso-scala supporta l’ipotesi che lungo le bande la deformazione di taglio sia stata molto blanda. Questa considerazione è ulteriormente supportata dall’assenza di un *fabric* cataclastico bel sviluppato: i clasti di natura silico-clastica sono deformati mediante un processo di frammentazione, ma non presentano evidenze di rotolamento, come confermato dai parametri di forma che indicano solo una leggera variazione della circolarità dei clasti. La dissoluzione è ben evidente prendendo in considerazione la diminuzione della quantità di calcite all’interno delle bande. La profondità di deformazione compresa tra 2 e 3 km può avere favorito la dissoluzione della calcite ed allo stesso tempo la frammentazione dei clasti di quarzo e feldspato. La disposizione geometrica dei due sistemi di bande di deformazione, e la presenza di un terzo sistema perpendicolare alla stratificazione, supporta l'ipotesi di una deformazione indotta da raccorciamento parallelo alla stratificazione.

### 1.9.4. Conclusioni

All'interno di rocce a bassa porosità, caratterizzate da una composizione poli-mineralica con componente mista carbonatica e silicoclastica, sepolte a profondità di 2-3 km la deformazione può avvenire mediante la combinazione di dissoluzione dei componenti più solubili (calcite) e frammentazione dei clasti più resistenti e meno solubili (quarzo e feldspato). La deformazione risultante produce bande di deformazione formate in un regime di stress compressivo che presentano una componente ibrida di dissoluzione e compattazione.

# ENGLISH VERSION

# CHAPTER 1

# Introduction to the Research Themes

## 1.1. General Introduction

The present Ph. D project is aimed to the study of the selective cementation affecting faulted and folded siliciclastic high-porosity sediments. The importance of such study resides in the evaluation of the impact that diagenetic processes exert on petrophysical properties of siliciclastic sediments and on the influence upon the deformation mechanism. Relationship between diagenesis and deformation was studied in three different sites showing peculiar characteristics. First, we focused on carbonate concretions developed within loose sandstone affected by tilting along the forelimb of an active anticline (Enza River Valley case study). This first case study allowed us to set up a methodological approach to efficiently investigate the effect of fluid flow in relatively simple structural setting. The same kind of approach was subsequently applied to a more complex structural setting trying to constrain the effect of shallow fluid flow within an extensional fault zone, and on the deformation mechanism affecting loosely lithified sandstones (Rocca di Neto fault zone case study). Eventually, the last case study (Cotiella Massif) is aimed to unravel the soft-sediment deformation involving low-porosity calcarenites in the footwall of the Cotiella Thrust. This Thesis attempts to provide further details concerning the selective cementation operated by shallow fluids along propagating anticline and on the relationship between cementation and deformation inside fault zones. Hereafter is presented a brief introduction of the major topics that will be investigated and discussed along the chapters composing the Thesis.

## 1.2. Diagenetic Alterations

Diagenetic alterations may be present in the form of selective cementation, mineral masses, alteration crusts with different compositions depending on the nature of the fluids and on the diagenetic-sedimentary environment in which mineral precipitation occurred (e.g., Todd, 1903; Jacob, 1973; Theakstone, 1981; Boles et al., 1985; Pirrie, 1987; Mozley and Wersin, 1992; Wilkinson, 1993; Mozley, 1996; Morad et al., 2000; Abdel-Wahab and McBride, 2001; Aiello et al., 2001; Hendry et al., 2006; Cavazza et al., 2009; Balsamo et al., 2013; Dale et al., 2014; Angeletti et al., 2015; Oppo et al., 2015). Diagenetic bodies display different shape and size related to the type of cementing fluids, growth mode, dominant mass transfer mechanism (advection vs diffusion) and petrophysical properties of the host rocks or sediments (Bjorkum and Walderhaug, 1990; Sellés-Martínez, 1996; Seilacher, 2001; Raiswell and Fisher, 2004; Mozley and Davis, 2005; Msharrafieh and Sultan, 2006; Chan et

al., 2007; Parry, 2011). Concretions and preferential cementation are present in different diagenetic settings, spanning from the deep burial to the shallow-near surface environment (McBride, 1988; Bjorkum and Walderhaug, 1990; Cibin et al., 1993; Morad et al., 2000; Hudson et al., 2001; Seilacher, 2001; McBride and Milliken, 2006; Balsamo et al., 2012, 2013; Lash, 2015; Loyd and Berelson, 2016; Zamanian et al., 2016; Li et al., 2018), and have been recognized also from satellite imaging on the surface of other planets (Sefton-Nash and Catling, 2008; Potter et al., 2011; Chan et al., 2012). The spatial arrangement of diagenetic alterations provides information concerning the fluid flow pattern and several authors used them as proxy and marker to infer the flow direction (McBride et al., 1994; Mozley and Davis, 1996; Cavazza et al., 2009; Balsamo et al., 2012). Especially, in the case of concretions forming by advective fluid flow the shape anisotropy of the cemented bodies can be seen as evidence of the preferential pathways of fluids (McBride and Parea, 2001; Mozley and Davis, 2005).

Detailed petrographic analysis of the cement composing the concretionary bodies provides clues to unravel the diagenetic setting and maximum burial depth experienced by the hosting rocks (Dix and Mullins, 1987; Wilkinson, 1993; Abdel-Wahab and McBride, 2001; Hendry and Poulsom, 2006; Wanas, 2008; Van Den Bril and Swennen, 2009; Viola et al., 2015).

Authors commonly use stable isotope analysis to constrain the origin of the cementing fluid and therefore the diagenetic setting in which mineral precipitation occurred (e.g., Hudson, 1977; Boles et al., 1985; Hays and Grossman, 1991; Bjorkum and Walderhaug, 1993; Nelson and Smith, 1996; Muchez et al., 1998; Van Den Bril and Swennen, 2009; Dale et al., 2014). Within siliciclastic sediments the most common type of cement is calcite, hence the most frequent diagenetic bodies are carbonate concretions (Morad, 1998; Morad et al., 2000). Inside high-porosity siliciclastic rocks and sediments, the occurrence of carbonate concretions is responsible for the diminishing of the petrophysical properties of the host rock by selective cementation (Houseknecht, 1987; Dutton et al., 2002; McBride and Milliken, 2006). This may promote the development of different pathways of migration of fluids and also the compartmentalization of a potential reservoir in the case of pervasive and laterally persistent cementation (Bjorkum and Walderhaug, 1990; Taylor et al., 1995; Klein et al., 1999; Davis et al., 2006; Boutt et al., 2014). Thus the recognition of such diagenetic features is of primary importance in the field of the petroleum geology and hydrogeology (Dutton et al., 2002; Hall et al., 2004; Davis et al., 2006). Many contributions were made concerning the influence of bacterial activity upon the development of selective cementation (Folk, 1993; McBride et al., 1994; Mozley and Davis, 2005; Hendry et al., 2006; Oppo et al., 2015; Viola et al., 2015; Yoshida et al., 2015), but the overall cementation often involves both in-organic as well as organic processes (Bjorkum and Walderhaug, 1990; Morad et al., 2000; Nyman et al., 2010).

### 1.3. Soft-Sediment Deformation

With the term soft-sediment deformation in literature is described a vast occurrence of deforming features involving sediments and

rocks characterized by high-porosity. Typically, such deformation style occurs inside sediments during deposition (syn-depositional deformation), or after deposition if porosity is preserved enough to allow deformation.

Soft-sediment deformation may be triggered by several factors including, density inversion leading to non-depositional features and fluid escape structures (i.e., load cast of turbidity current) (Tinterri et al., 2016), syn-depositional earthquakes or impacts producing liquefaction, seismites and faulting (Rodrigues-Pascua et al., 2000; Montenat et al., 2007; Okubo and Schultz, 2007; Alfaro et al., 2010; Boukhedimi et al., 2017) and tectonic activity responsible for the development of deformation bands and faults (Aydin, 1978; Mair et al., 2000; Balsamo et al., 2010; Fossen, 2010; Schultz et al., 2010; Nicol et al., 2013; Ballas et al., 2014; Soliva et al., 2016; Fossen et al., 2017; Philit et al., 2018). Since one of the fundamental requirements for the onset of soft-sediment deformation is the presence of high-porosity, it often occurs inside sandstones or sands where typically porosity is high (porosity exceeds 35-40% of volume in well-sorted aeolian sandstones) (Aydin, 1978). However, the occurrence of soft-sediment deformation structures was reported also in lithologies apart from the sandstone, such as limestone (Cilona et al., 2012; Tondi et al., 2012; Antonellini et al., 2014) and volcaniclastic rocks (Wilson et al., 2003; Cavailhes and Rotevatn, 2018).

The present Thesis is focused on the relationship between deformation and cementation in high-porosity siliciclastic sediments where soft-sediment deformation occurs in the form of deformation bands and fault. Deformation bands are tabular deforming structures that were first reported as “small-faults” or “Luders’ bands” (Friedman and Logan, 1973; Aydin, 1978; Olsson, 2000). Deformation bands can be present both as single structures or arranged in clusters of closely spaced bands (Aydin and Johnson, 1978, 1983; Antonellini and Aydin, 1994; Nicol et al., 2013; Soliva et al., 2016; Fossen et al., 2017; Philit et al., 2018). The strain-hardening behaviour provides to the single deformation band an increasing strength during progressive strain accommodation, promoting the delocalization of the deformation in the surrounding undeformed rock rather than leading to the slip localization along pre-existing discontinuity (Aydin and Johnson, 1978; Eichhubl et al., 2010; Deng and Aydin, 2012). With further displacement accommodation, a thick cluster of deformation bands may develop a discrete slip surface, as soon as the overall deformed sediments reach enough stiffness (Aydin and Johnson, 1978; Shipton and Cowie, 2001; Davatzes et al., 2005). The overall strain-hardening behaviour is induced by the deformation mechanism responsible for deformation band nucleation and development. In particular, the combination of particulate flow and cataclasis leads to pore collapse, porosity decrease, grain size reduction and decrease of sorting of the deformed sand (Antonellini et al., 1994; Menéndez et al., 1996; Zhu and Wong, 1997; Rawling and Goodwin, 2003; Fossen et al., 2007; Torabi et al., 2007; Balsamo and Storti, 2010, 2011; Soliva et al., 2013; Rodrigues and Alves da Silva, 2018). All these conditions promote a higher strength with respect to shear stress and strain (Mair et al., 2002). The micro-mechanics of deformation bands determines also the petrophysical properties

which usually record a decrease in porosity and effective permeability (Zhang et al., 1990; Antonellini et al., 1999; Wong and Zhu, 1999; Shipton et al., 2005; Torabi and Fossen, 2009; Balsamo and Storti, 2010; Ballas et al., 2012), thus highlighting their importance during reservoir and field analogue study.

### 1.4. Hydrological Role of Deformed Rocks and Sediments

The hydrological role of fault zones affecting cohesive rocks is characterized by a dualism given by the presence of two distinct structural domains with peculiar deforming features. The damage zone, is typically affected by a dense network of fractures related to the strain accommodation along the master slip surface (Kim et al., 2004; Choi et al., 2015). Within this domain the interconnected fractures may behave as an efficient conduit towards fluids, with higher permeability values parallel to the fault strike rather than orthogonal to the fault surface (Caine et al., 1996; Evans et al., 1997; Caine and Forster, 1999; Billi et al., 2003; Faulkner et al., 2010; Farrell et al., 2014). On the contrary, the fault core domain is characterized by a barrier behaviour due to the presence of ultra-comminute slip surfaces, cataclastic fault rocks and gouges (Engelder, 1974; Caine et al., 1996; Storti et al., 2011; Bense et al., 2013). Within high-porosity rocks or sediments the hydrological role of fault zones can be slightly more complex. This feature is linked to the difference between the structure of a fault zone affecting cohesive rocks with respect to loose or high-porosity sediments. In particular, in high-porosity granular materials the fault zone consists of a domain with delocalized deformation in the form of deformation bands which corresponds to the damage zone in fully lithified and cohesive rocks (e.g., Person et al., 2000; Fisher and Knipe, 2001; Rawling et al., 2001; Wilson et al., 2003; Balsamo and Storti, 2010; Eichhubl et al., 2010; Loveless et al., 2011; Schueller et al., 2013). Due to the loose nature of the deformed material, joints or tensile fractures cannot form. The majority of the displacement is mostly accommodated along a shear zone with a high-density of deformation bands and discrete slip surfaces (Aydin and Johnson, 1978; Shipton and Cowie, 2001; Davatzes et al., 2005). This high-deformation domain can be considered as the fault core of the fault. In some cases, when the displacement exceeds the bedding thickness a third domain can develop, namely the mixed zone as defined by several authors, which consists of highly deformed sediments, marking the transition between the damage zone and the fault core (Heynekamp et al., 1999; Rawling and Goodwin, 2006; Loveless et al., 2011). Along deformation bands composing the fault zone, the permeability shows a reduction from 1 to 6 orders of magnitude with respect to the pristine rock, while the drop can be even more pronounced considering sediments deformed inside the fault core (Antonellini and Aydin, 1994; Taylor and Pollard, 2000; Bense et al., 2003; Johansen et al., 2005; Balsamo and Storti, 2010; Ballas et al., 2015; Fossen et al., 2015, 2017). Thus, fault zones deforming loose sediments display a barrier role towards fluid flow even inside the damage zone domain, conversely to the conduit behaviour shown by fully lithified rocks. Inside the fault core the barrier role is enhanced even if in some cases the increase in mechanical strength of the deformed

sediments may lead to the formation of tensile fractures locally enhancing the effective permeability and transmissibility (Tindall and Eckert, 2015). Authors evaluated the sealing potential at the scale of the single deformation band and pointed out the importance of along strike thickness variation and density of the band network (Shipton et al., 2005; Rotevatn et al., 2013, 2017). This allowed to estimate the impact of sub-seismic deformation features on reservoir exploitation (Main et al., 2000; Sample et al., 2006; Sternlof et al., 2004, 2006; Kolyukhin et al., 2010). Thus the occurrence of soft-sediment deformation structures affecting folds and faults in high-porosity rocks is therefore a critical parameter to be evaluated in studying the sealing potential of subsurface traps or reservoirs (Tueckmantel et al., 2010; Bretan, 2016; Wibberley et al., 2017; Fisher et al., 2018).

### 1.5. Relationship between Deformation and Diagenesis

Diagenetic processes affecting deformed rocks or sediments are related to the intrinsic petrophysical properties of the faulted domains. Inside high-porosity granular media the presence of fault zones may induce a channelization of fluids aside of the deformed domain due to the presence of low-permeability structural features. In this case, fluids may interact with undeformed or weakly deformed sediments without directly affecting the faulted domains. Fluid circulation pattern can be inferred from the spatial distribution of diagenetic alterations through the entire fault zone (e.g., oxidation fronts and deposition of oxides, bleaching, selective cementation and dissolution) (e.g., Sample et al., 1993; Mozley and Goodwin, 1995; Chan et al., 2000; Eichhubl et al., 2004; Beitler et al., 2005; De Boever et al., 2009; Caine et al., 2010; Balsamo et al., 2012). The distribution of diagenetic alterations depends also on the diagenetic-sedimentary environment, since the hydrological behaviour of fault zones changes according to the water-saturation conditions. In particular, under water-saturated conditions, faults may act as affective barriers impeding and hampering fluids directed orthogonal to fault strike (Fossen and Bale, 2007; Ballas et al., 2015). Conversely, in under-saturated conditions deformed sediments can play a partial conduit role provided by high retention time of fluids within deformed domains (Sigda et al., 1999; Sigda and Wilson, 2003; Wilson et al., 2003; Balsamo et al., 2012). This double behaviour can lead to different distribution of diagenetic alterations and can contribute to the evolution of deformation mechanism and to the modification of the petrophysical properties of the faulted sediments (Bense et al., 2013; Philit et al., 2015; Williams et al., 2016; Wibberley et al., 2017; Fisher et al., 2018).

# CHAPTER 2

## Palaeo-fluid Flow during Anticline Growth along the Enza River Valley

This chapter deals with carbonate concretions related to shallow meteoric fluids, affecting loosely lithified Pleistocene siliciclastic sediments deposited along the forelimb of the active Quattro Castella fault-related anticline, along the topographic front of the Northern Apennines. Detailed study of these concretionary bodies revealed the change of fluid flow direction induced by the lateral propagation of the anticline along the periclinal zone and the nature of the cementing fluids in the framework of a palaeo-aquifer environment.

*From axial parallel to orthogonal groundwater flow during fold amplification: insights from carbonate concretion development during the growth of the Quattro Castella Anticline, Northern Apennines, Italy.*

Pizzati, M., Balsamo, F., Storti, F., Mozafari, M., Iacumin, P., Tinterri, R., Swennen, R.

Published on the *Journal of the Geological Society of London*, 175, 806–819. https://doi.org/10.1144/jgs2018-031

# From axial parallel to orthogonal groundwater flow during fold amplification: insights from carbonate concretion development during the growth of the Quattro Castella Anticline, Northern Apennines, Italy

Mattia Pizzati[1], Fabrizio Balsamo[1], Fabrizio Storti[1], Mahtab Mozafari[1], Paola Iacumin[2], Roberto Tinterri[2] & Rudy Swennen[3]

[1] Natural and Experimental Tectonics Research Group, Department of Chemistry, Life Sciences, and Environmental Sustainability, University of Parma, 43124 Parma, Italy

[2] Department of Chemistry, Life Sciences, and Environmental Sustainability, University of Parma, 43124 Parma, Italy

[3] Department of Earth and Environmental Sciences, KU Leuven, B-3001 Leuven, Belgium

## Abstract

This paper is based on a multidisciplinary field and laboratory study of carbonate concretions developed in poorly lithified Quaternary, syn-kinematic sediments along the Quattro Castella Anticline, Northern Apennines, Italy. The studied concretions consist of both tabular (parallel to bedding) and elongate single to coalescent concretionary bodies oriented at different angles to the bedding throughout the exposed stratigraphic succession. The dimensions of the concretions range from a few centimetres for single elongate concretions up to several metres for tabular to coalescent concretions. Field observations and petrophysical data indicate that the concretions developed preferentially in sediments characterized by mean grain sizes of 90–290 μm and a permeability ranging from $7 \times 10^2$ to $7 \times 10^4$ mD. Carbon and oxygen stable isotope analyses in conjunction with the petrographic investigations indicate that the precipitation of concretionary calcite occurred in a meteoric vadose realm during early eogenesis and subsequently in a meteoric phreatic environment. Diagenetic data and concretion patterns in syn-tectonic sediments suggest they formed during the lateral propagation of the anticline, which, in turn, promoted a change in the local topographic–hydraulic gradient from fold axial parallel to fold orthogonal. The integrated analysis of carbonate concretions provides a useful tool with which to unravel the palaeo-fluid flow history and therefore to predict fluid circulation patterns in folded siliciclastic rocks.

### 2.1. Introduction

Unravelling fluid flow pathways within exposed rocks and sediments leads to a

better understanding of the processes affecting oil and gas reservoir quality and facilitates hydrocarbon exploitation and the preservation of groundwater reserves (Taylor et al., 2000; Dutton et al., 2002; Hall et al., 2004). Diagenetic concretions and mineral masses can provide a useful tool with which to reconstruct palaeo-fluid flow patterns within transforming porous media involved in deformation (e.g. Johnson, 1989; McBride et al., 1994; Mozley and Davis, 1996; McBride and Parea, 2001; Balsamo et al., 2012, 2013). Moreover, selective cementation plays a key part in modifying the petrophysical properties of sediments, such as porosity and permeability (Houseknecht, 1987; Davis et al., 2006; Boutt et al., 2014). Pervasive cementation can eventually lead to the formation of laterally extensive, bedding-parallel, low-permeability layers, which can compartmentalize reservoirs (Morad et al., 2000; Dutton et al., 2002; Hall et al., 2004). Diagenetic concretions within siliciclastic sediments are characterized by different shapes and sizes (e.g. Sellés-Martínez, 1996; Seilacher, 2001) depending on the fluid flow patterns and the spatial distribution of sediments (McBride et al., 1994; Davis, 1999; McBride and Parea, 2001; Cavazza et al., 2009; Balsamo et al., 2012).

The arrangement of concretions has been used as marker of fluid flow and to recognize the diagenetic setting in which precipitation occurred (Pirrie, 1987; McBride et al., 1994; Mozley and Davis, 1996; Davis, 1999; South and Talbot, 2000). Different modes of growth have been identified based on the type of concretion (Mozley, 1996; Abdel-Wahab and McBride, 2001; Mozley and Davis, 2005). A significant amount of research has been carried out on the relationship between diagenetic concretions and fault zones within siliciclastic sediments with different degrees of lithification (Mozley and Goodwin, 1995; Hendry and Poulsom, 2006; Balsamo et al., 2012, 2013; Philit et al., 2015; Williams et al., 2016). However, comparable information is lacking on the presence and patterns of carbonate concretions hosted in syn-kinematic sediments deformed in growing folds, where the pattern of fluid flow may change during fold amplification.

We present here the results of a multidisciplinary study on diagenetic concretions developed within poorly lithified Quaternary syn-kinematic sediments exposed in the Quattro Castella Anticline at the mountain front of the Northern Apennines. The petrophysical and sedimentological properties of the sediments hosting the concretions were studied by laboratory analyses (grain size distribution, two-dimensional porosity) and in situ measurements (permeability). We inferred the diagenetic environment and the nature of the fluids responsible for the formation of concretions using stable isotope analysis combined with petrographic observations of carbonate cements. The integration of field and laboratory data allowed us to constrain the control of the lateral propagation and growth of the anticline on the palaeo-fluid flow pathways.

### 2.2. Geological Framework

The Apennines fold–thrust belt developed from early Oligocene times as a consequence of the subduction of the Adria plate below the European plate (Boccaletti et al., 1971; Doglioni, 1991). Subduction was responsible for the emplacement of remnants of oceanic crust and the related sedimentary cover of

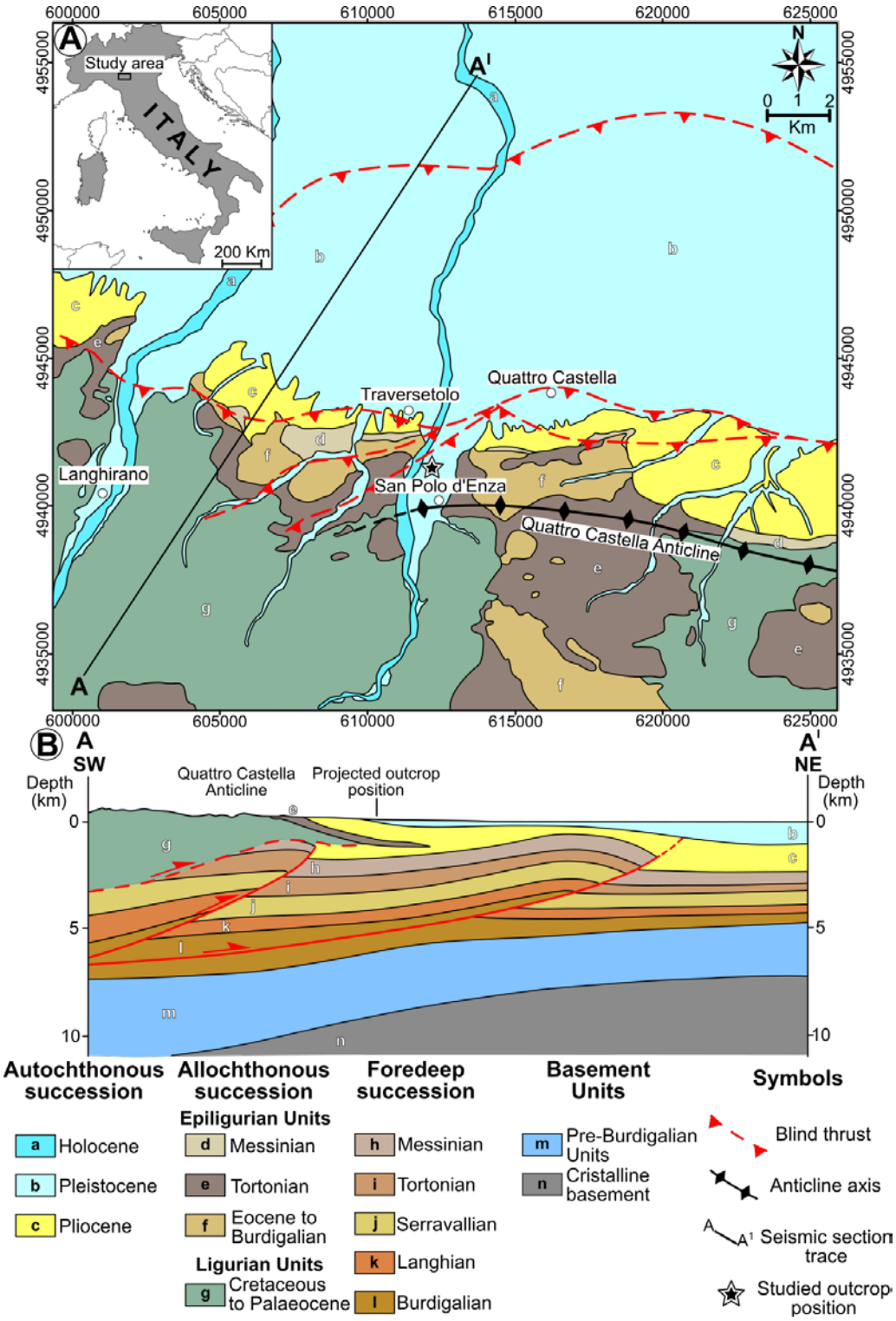


**Fig. 2.1.** (**a**) Simplified geological map of the topographic front of the Northern Apennines showing the position of the study area along the Enza River valley (modified after Oppo et al. 2015). (**b**) Reflection seismic section with line drawing interpretation of the main structural features in the vicinity of the studied field site (modified after Oppo et al. 2015).

the Ligurian–Piedmont ocean (Ligurian Units) onto the inverted Adria passive margin successions (Doglioni, 1991). The Epiligurian wedge-top basin successions (Eocene to Late Miocene) formed on top of the Ligurian thrust sheets during their northeastwards migration (Zattin et al., 2002; Remitti et al., 2011; Piazza et al., 2016). The study site is

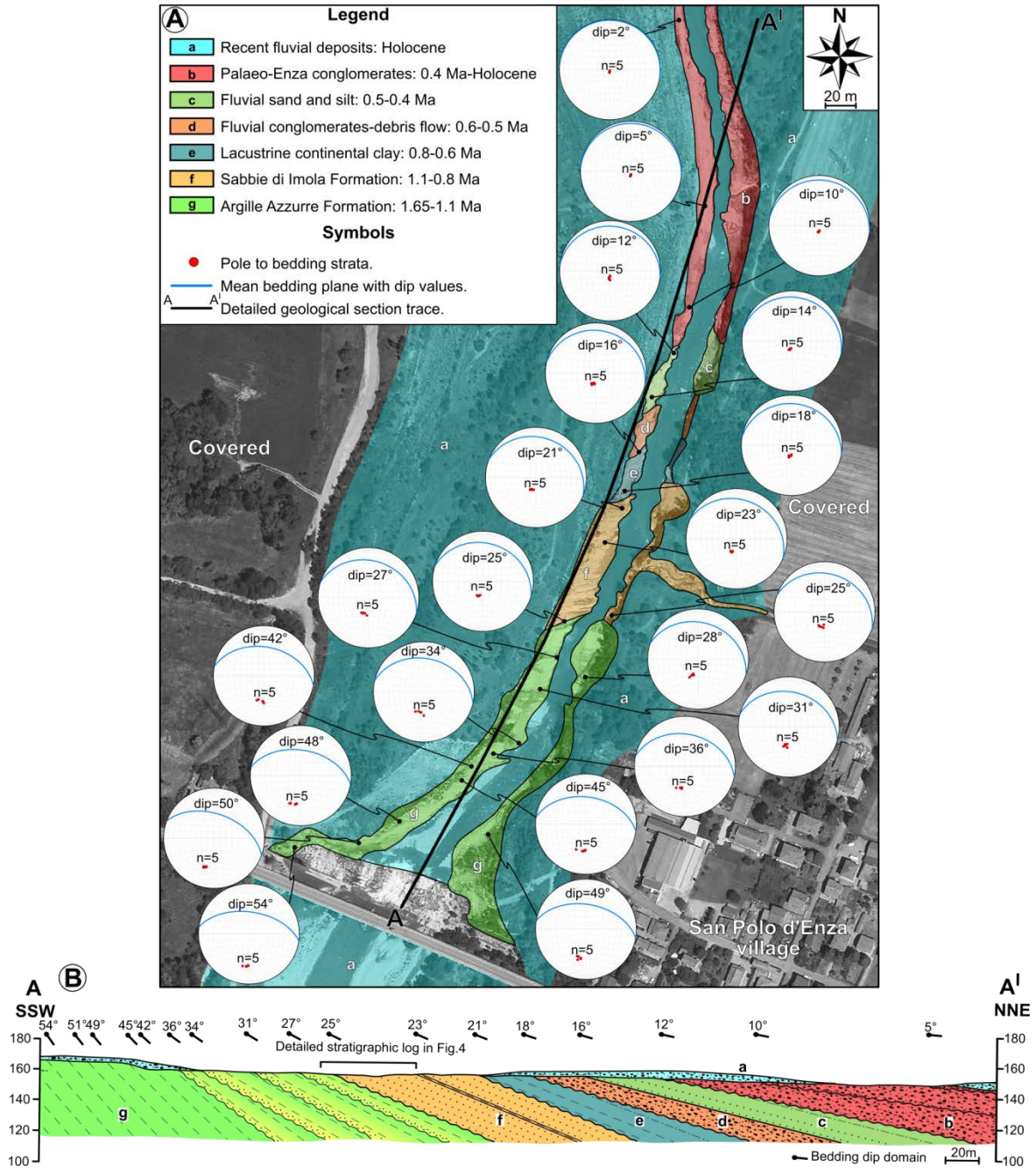


**Fig. 2.2.** (**a**) Detailed geological map of the Enza River outcrop. Stereonets (Schmidt equal area projection lower hemisphere) report the mean bedding planes with dip angles and poles to bedding measured at different sites along the outcrop. (**b**) Detailed geological section across the entire Enza River outcrop. Bedding dip domains are also reported and show a progressive decrease in dip from the base to the top of the succession.

located at the mountain front of the Northern Apennines (Fig. 2.1a) and is characterized by Ligurian and Epiligurian rocks, which were overthrust onto Miocene siliciclastic foredeep turbiditic sediments during Middle Pliocene times (Oppo et al., 2013, 2015; Gunderson et al., 2014).

The Quattro Castella Anticline formed in the hanging wall of a blind thrust ramp cutting through the foredeep strata, which were

previously overthrust by a Ligurian thrust sheet and the associated Epiligurian sediments (Fig. 2.1b). Such a blind thrust has been active since Late Miocene times and is still active today (Ponza et al., 2010; Boccaletti et al., 2011; Gunderson et al., 2014). The stratigraphic succession investigated in this work lies in the forelimb of the WNW–ESE-striking Quattro Castella Anticline, a regional-scale fold that deforms the Ligurian and Epiligurian rocks and part of the Po plain autochthonous succession (Fig. 2.1a, b). In particular, remarkable and continuous exposure is provided by the erosional incision of the Enza River (Fig. 2.2a). The outcrop consists of Pleistocene and Holocene sediments belonging to the Po plain succession that were deposited in the western periclinal termination during the late stage of fold growth. The outcrop may have recorded a different pattern of fluid flow induced by the anticline lateral amplification. From the base, it is composed of the silty clay Argille Azzurre Formation deposited in a shallow prodelta environment. It is followed by the fluvio-deltaic sand of the Sabbie di Imola Formation, overlain by the Lower Emilia–Romagna synthem, which is mainly characterized by fluvio-continental deposits (Gunderson et al., 2014).

### 2.3. Analytical Methods

A total of 620 structural data values were collected to construct the geological cross-section through the outcrop (Fig. 2.2). A c. 300 m thick stratigraphic succession was logged, excluding the uppermost 70–80 m thick fluvial conglomerates. A 30 m thick stratigraphic log was measured in greater detail to investigate the typology and arrangement of carbonate concretions. Within this interval, the petrophysical properties of the sediments hosting concretions were measured. In particular, 40 grain size samples were analysed using a Malvern Instruments Mastersizer 3000 laser diffraction particle size analyser with an operating range from 0.1 to 3500 μm, equipped with a Hydro EV wet dispersion unit using de-ionized water as the dispersant fluid. Detailed information about the adopted standard operating procedures are provided in the Supplementary Material. The sediment permeability corresponding to the 40 grain size sampling sites was measured using a New England Research Tiny Perm II air permeameter. The instrument has a rubber nozzle with a central hole of 0.5 cm diameter and the data were calibrated according to the method used by Balsamo et al. (2012). We performed 900 in situ permeability measurements throughout the 30 m thick detailed log. A set of 780 permeability measurements was also measured on the outer surface of the concretionary bodies (see Supplementary Material).

A total of 12 concretions of different sizes and shapes were sampled in different stratigraphic positions along the section. Eleven of the concretions were from the sandy strata of the Sabbie di Imola Formation, whereas only one was sampled within the Argille Azzurre Formation, in the same interval studied by Oppo et al. (2015), and was used for comparative purposes. Hand specimens of the concretions were cut to obtain 14 thin sections impregnated with a blue-dyed resin to calculate the two-dimensional porosity and intergranular volume (IGV) from scanned high-resolution images using ImageJ image analysis software. Polished rock slabs and thin sections were

stained with Alizarin Red S and potassium ferricyanide to identify the cement mineralogy (dolomite v. calcite) (Dickson, 1966). Cold cathodoluminescence (CITL CL Mk5-2 with operating settings of 250 µA and 10–12 kV) was used to better describe the texture and spatial distribution of the cement. A JEOL JSM 6400 scanning electron microscope (operating settings 240 µA and 20 kV) was used to acquire detailed photomicrographs of the cement.

The bulk rock carbon and oxygen stable isotopes were analysed from powder samples extracted from fresh section cuts with a dental drill along two orthogonal transects with different sample spacings (1 cm for the horizontal trace and 0.5 cm for the vertical trace). A total of 184 samples was collected. The concretion cements were also sampled in 45 different spots identified from thin sections using a New Wave Research micromill with a 300 µm diameter drill bit. Micromill sampling was performed at the Department of Earth and Environmental Sciences, KU Leuven, Belgium. All samples were analysed with a Thermo Finnigan DELTA plus XP mass spectrometer coupled with a Thermo Finnigan GasBench II gas preparation and introduction system. All isotopic analyses were carried out at the Department of Chemistry, Life Sciences and Environmental Sustainability of the University of Parma, Italy. Both $\delta^{13}C$ and $\delta^{18}O$ are referred to the international standard V-PDB (Pee Dee Belemnite). The analytical precision for the carbon isotope determination was 0.10‰ V-PDB and that for the oxygen isotopes was 0.15‰, whereas the prediction uncertainty was c. 0.15‰ for carbon and c. 0.20‰ for the oxygen isotopes.

## 2.4. Stratigraphic and Structural Description

### 2.4.1. Outcrop Features

The stratigraphic interval recorded in the 300 m long exposure spans a time period from 1.65 Ma at the base to Holocene deposits at the top (Gunderson et al., 2014). From the base to the top, two different synthems can be identified: (1) the Marine Quaternary synthem; and (2) the Lower Emilia–Romagna synthem (see Gunderson et al. 2014). From a lithostratigraphic point of view, the Marine Quaternary synthem is composed of two formations: the Argille Azzurre Formation and the Sabbie di Imola Formation.

The Argille Azzurre Formation consists of a grey–cyan silt to silty clay, organized in metre-thick strata with weakly defined stratification. The age covered by the formation ranges from 1.65 to 1.1 Ma (Gunderson et al., 2014) with a total thickness of 121 m. It can be further subdivided in two distinct units. The lower unit is a 70 m thick unit composed of relatively uniform silty clay with thin, very fine-grained sand layers containing sparse marine fossils and fossilized methane expulsion vents. The upper unit of the Argille Azzurre Formation has a total thickness of 51 m and includes three distinct fine sand units, each composed of 8–10 m thick fine-grained laminated sand, in which asymmetrical to symmetrical ripples are present, separated by thick silty clay bodies (Fig. 2.2b). The uppermost part of the second unit shows a progressive increase in the sand fraction. Consequently, the Argille Azzurre Formation is characterized by a general coarsening upwards and the upper coarse-grained interval marks the transition to the overlying Sabbie di Imola Formation.

The Sabbie di Imola Formation is located almost in the middle part of the investigated succession (Fig. 2.2b). It consists of yellow–orange, medium- to fine-laminated sand with a total thickness of 28 m. The age spans from 1.1 to 0.8 Ma (Gunderson et al., 2014). This formation is composed of two distinct sand units separated by a 2 m thick, grey–blue fossil-rich clay. The basal sand body is made of medium- to fine-grained sand organized in amalgamated strata with hummocky cross-stratification. The total thickness of this unit is 13 m. The second depositional unit of the Sabbie di Imola Formation shows an increase in grain size and is mainly composed of an alternation of medium-grained sand and pebble–cobble orthoconglomerates for a total thickness of 12 m (Fig. 2.2b). The Lower Emilia–Romagna synthem unconformably overlies the Sabbie di Imola Formation with an age between 0.8 and 0.4 Ma (Gunderson et al., 2014). At the base, it shows an 11 m thick green to grey clay with faint stratification characterized by abundant plant roots and extensive orange–red colour mottling. These deposits are overlain, with a sharp erosive surface, by a pebble to cobble conglomerate, followed by a 4 m thick conglomeratic mudstone. The uppermost portion of this synthem is formed by a sandy unit with a thickness of c. 15 m. The Lower Emilia–Romagna synthem passes upwards, through a well-defined erosional unconformity, into the 70–80 m thick conglomerates body of the Upper Emilia–Romagna synthem (Fig. 2.2b). Consequently, the stratigraphic succession is characterized by a coarsening and shoaling upwards facies sequence that records a transition from an offshore marine environment (Argille Azzurre Formation) to an alluvial environment (the Lower and Upper Emilia–Romagna synthem) (Gunderson et al., 2014).

### 2.4.2. Sedimentary Wedging

The entire outcrop displays a wedge-shaped geometry with strata pinching towards the south and opening basinwards to the north. The investigated succession was deposited along the forelimb of the growing anticline, thus showing a progressive decrease in the bedding dip angle from the base to the top of the outcrop. In the first few metres of the succession, within the Argille Azzurre Formation, the bedding dip has a maximum value of 55°; going upsection through the basal unit of this formation (i.e. within the first 70 m of the measured stratigraphic log), it decreases to 36° (Fig. 2.2a, b). This decrease occurs progressively and no sharp unconformity is visible in the field. Within the second unit of the Argille Azzurre Formation, the bedding dip continue to decrease from 36 to 25° at the top of the transition between the Argille Azzurre and Sabbie di Imola formations. In this interval, the variation in the bedding dip is no longer gradual, but occurs along the erosive surfaces at the base of the three fining-up sedimentary cycles. The base of the Sabbie di Imola Formation has an average dip of 25°, which decreases to 23° within the 2 m thick clay layer separating the two sand units (Fig. 2.2b). Throughout the second sandy unit, the bedding dip remains almost constant at 22–23°. The Lower Emilia–Romagna synthem shows a bedding dip decreasing from 18° in the continental clay to almost horizontal at the top of the sedimentary succession (Fig. 2.2b). The dip direction of the strata remains almost

constant throughout the entire section, with values spanning from N 2° to N 25°.

## 2.5. Carbonate Concretions

### 2.5.1. Concretion Types and Patterns

The stratigraphic interval in which the diagenetic concretions are densely concentrated includes the transition between the Argille Azzurre and the Sabbie di Imola formations and the first sand body of the latter formation (Fig. 2.2b). Based on their shape, size and spatial distribution, the concretions can be classified into four categories as follows.

(1) Single elongate, cigar- to blade-shaped concretions occur within the medium–fine sand strata of the first body of the Sabbie di Imola Formation (Fig. 2.3a). In some sand layers, these concretions are clustered and closely spaced, without merging together.

(2) Elongate coalescent concretions, which make up metre-scale wide bodies, can be found within the basal sand strata of the transition from the Argille Azzurre to the Sabbie di Imola formations and at the top of the first sand unit of the latter formation. These concretions are massive and emerge by their strong positive relief with respect to the host sand due to differential weathering. Concretionary bodies are formed by the joining of several single elongate bodies (Fig. 2.3b).

(3) Tabular concretions are often distributed within the first sand body of the Sabbie di Imola Formation. They appear as laterally extensive layers, oriented parallel to the sand strata bedding, showing a variable thickness from 2 to 20 cm (Fig. 2.3c). The degree of cementation is high, even if a few tabular bodies are friable in hand specimen. The majority of these concretionary bodies display a clear elongation direction and they seem to be formed by several single, small-sized elongate concretions merged together. The merging aspect is clearly visible on the basal and upper surfaces of the tabular

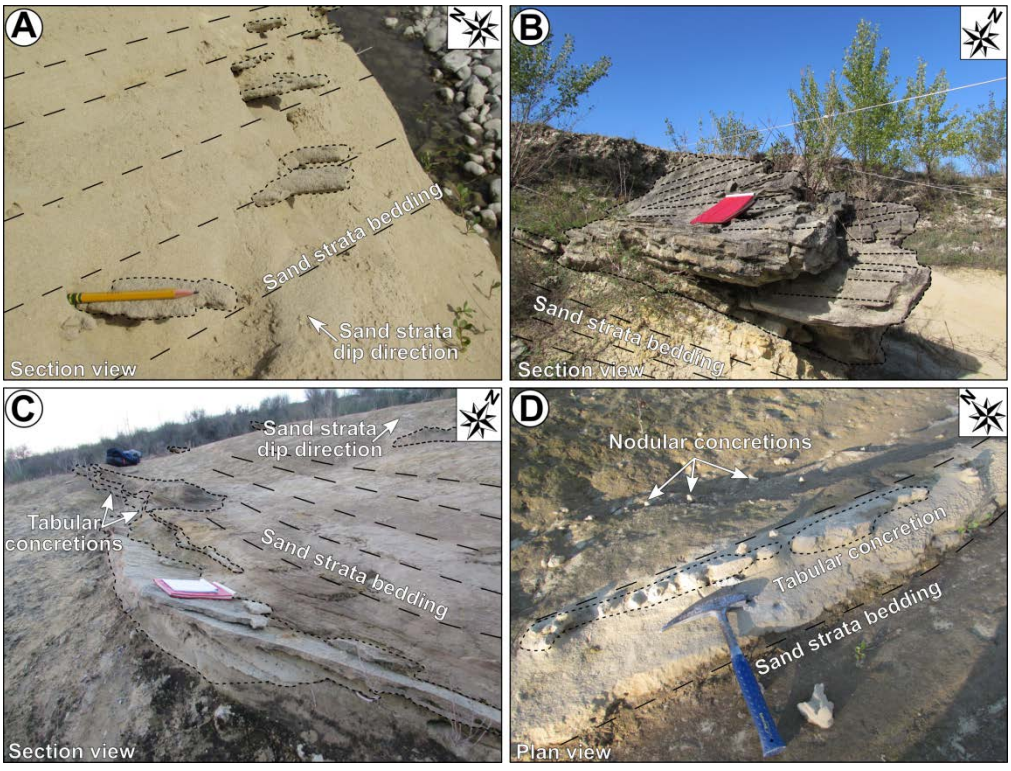


**Fig. 2.3.** Types of concretion hosted within the stratigraphic succession. (**a**) Elongate single cigar-or blade-shaped concretions emerging from loose sand at the base of the Sabbie di Imola Formation. (**b**) Coalescent elongate concretion displaying elongation traces on the top surface. (**c**) Tabular metre-wide bedding-parallel concretions. (**d**) Nodular and tabular bedding-parallel concretions.

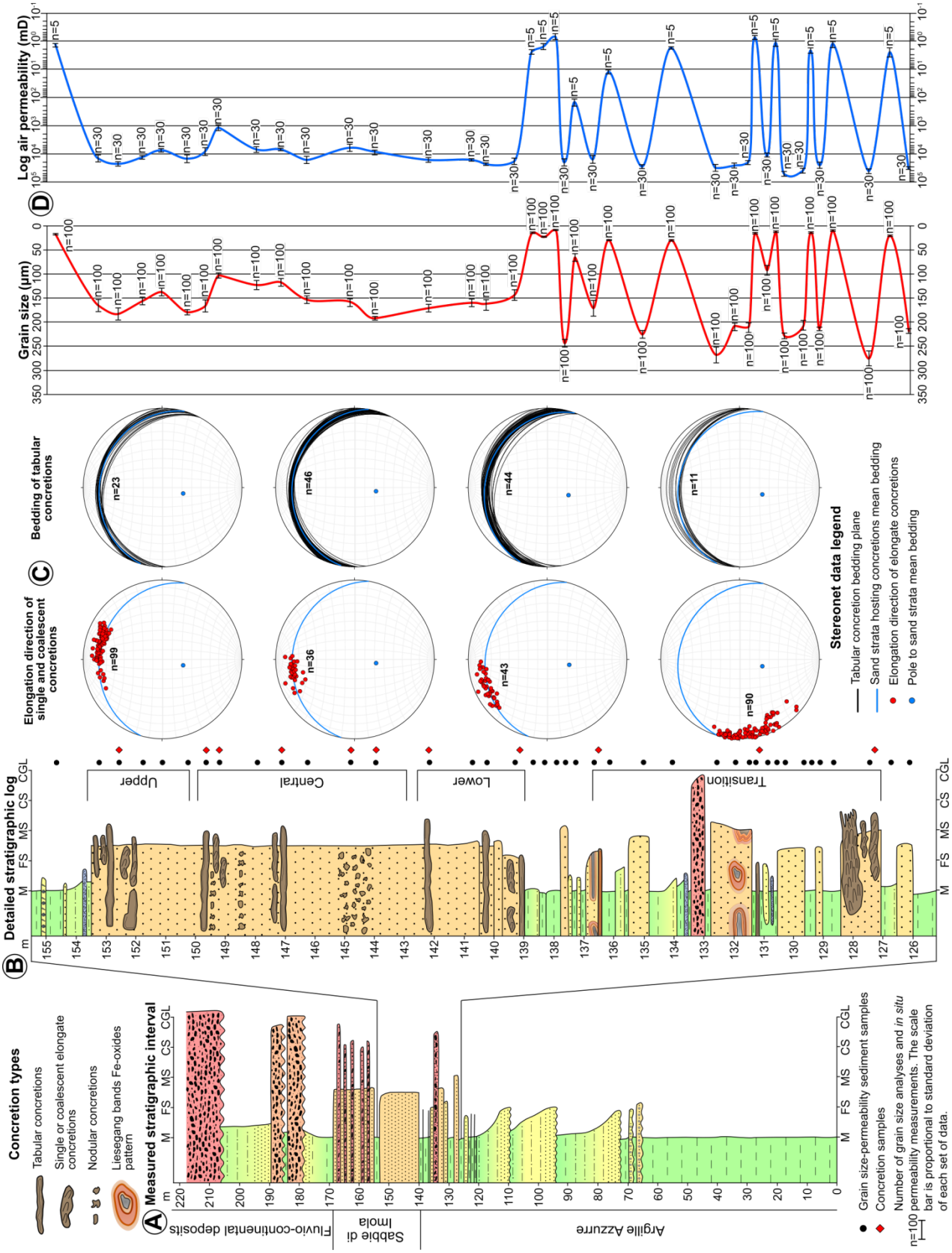


**Fig. 2.4.** Stratigraphic, structural and petrophysical properties of the investigated succession. (**a**) Stratigraphic log of the entire exposed succession. (**b**) 30 m thick detailed log showing the transition between the Argille Azzurre and Sabbie di Imola formations and the first sand unit of the latter formation. (**c**) Concretion structural data through the detailed log (Schmidt equal area projection lower hemisphere). (**d**) Grain size and permeability variation curves.

concretions, but it is not distinguishable in cross-section.

(4) Nodular concretions display almost spherical shapes with diameters from 4 to 15 cm. They are densely clustered in three different layers near the middle of the first sand unit of the Sabbie di Imola Formation. The degree of cementation varies inside each nodule, with some small sand volumes strongly cemented and others almost non-cemented (Fig. 2.3d).

The geometrical relationship between the orientation of the concretions, marked by their longest axis, and the bedding of the host sediment varies along the investigated stratigraphic succession (Fig. 2.4b, c). In particular, at the transition between the Argille Azzurre and Sabbie di Imola formations, the measured elongation direction, both on single and coalescent concretions, shows a mean trend pointing towards the west. The concretion plunge is not parallel to the bedding dip direction (which is towards the NNE) and is roughly oriented along the strike direction of the strata. The plunge values vary from 1 to 19°. Moving upsection to the base of the first sand unit of the Sabbie di Imola Formation, the mean elongation direction displays a NNW orientation (Fig. 2.4c). Even in this interval, the concretion plunge is not parallel to the bedding dip direction, but describes a narrower angle to it compared with the underlying concretions. The plunge values are similar to the strata dip angle (23°). Near the middle of the first sand unit, elongate concretions show a mean direction pointing almost to the north (Fig. 2.4c). The concretion plunge is constant and almost parallel to the strata dip direction. At the top of the basal sand unit, elongate concretions plunge towards the NNE, i.e. parallel to the bedding dip direction (21°). From the base to the top of the detailed log (Fig. 2.4b) (c. 25 m in stratigraphic height), the direction of the elongate concretions describes a 110° clockwise rotation (Fig. 2.4c).

To recognize the changes in bedding and

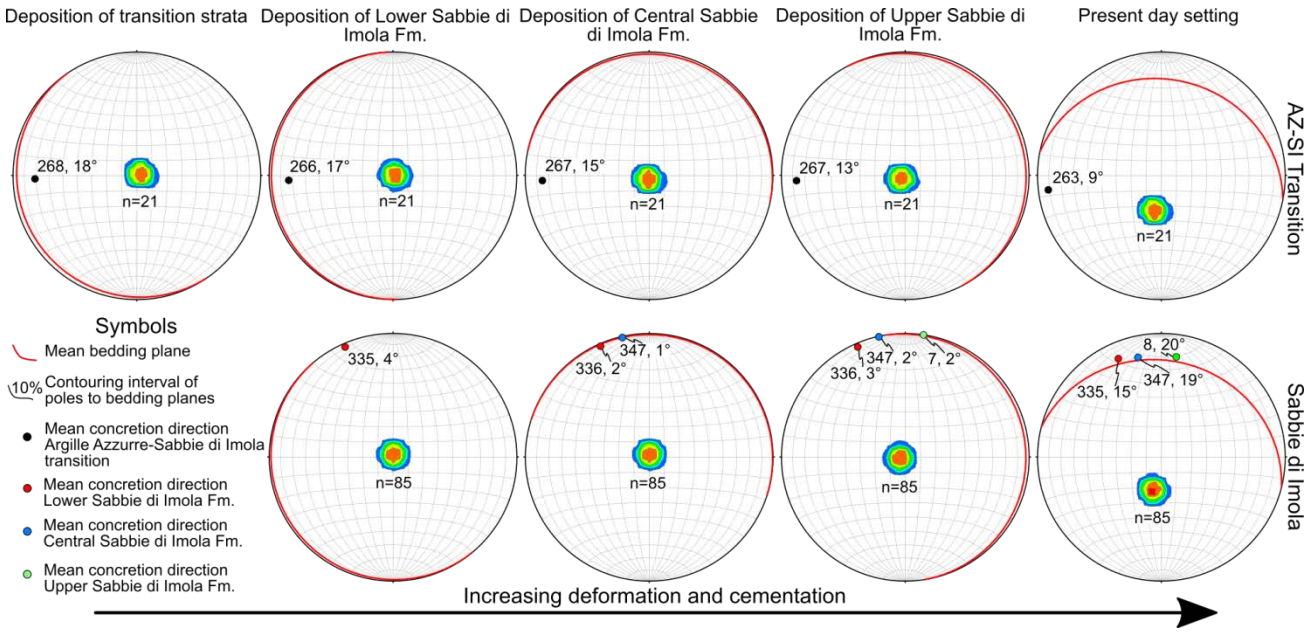


**Fig. 2.5.** Progressive tilting of the strata calculated from the unfolding of the dip domains shown in Figure 2.2b within the stratigraphic interval consisting of the Argille Azzurre–Sabbie di Imola (transition AZ–SI) and the Sabbie di Imola Formation. The mean direction of the elongate concretions was calculated in the same deformation stages and is displayed as the azimuth and dip angles (Schmidt equal area projection lower hemisphere).

concretion orientation during sedimentation, unfolding of tilted strata was performed considering the dip domains illustrated in the geological cross-section (Fig. 2.2b). During the deposition of the strata marking the transition between the Argille Azzurre and Sabbie di Imola formations, the bedding was almost sub-horizontal, with a slight dip towards the west (Fig. 2.5). With ongoing sedimentation, the bedding dip direction recorded a progressive clockwise rotation from the west to the NE. The same rotation is also displayed by the sand strata of the Sabbie di Imola Formation (Fig. 2.5). Unfolding of the mean direction of elongate concretions indicates that the diagenetic bodies were only affected by a coaxial rotation during the tilting of the strata. This is confirmed by the increase in dip values and by the almost constant strike direction characterizing the longest axis of the concretions during the deposition and tilting of the host strata.

### 2.5.2. Petrophysical Properties

Within the transition from the Argille Azzurre to the Sabbie di Imola formations, the sand strata hosting the concretions have a mean grain size varying between 145 and 290 µm with moderate sorting. The mean permeability of these strata spans from $1.6 \times 10^4 \pm 3.4 \times 10^3$ to $4.2 \times 10^4 \pm 5.6 \times 10^3$ mD. By contrast, the grain size and permeability show a reduced variability range within the Sabbie di Imola Formation. The sediments hosting the concretions have a narrow grain size range varying between 103 and 188 µm with high sorting, whereas the permeability ranges from $1.2 \times 10^3 \pm 2.3 \times 10^2$ to $2.3 \times 10^4 \pm 3.1 \times 10^3$ mD (Fig. 2.4d). Concretions did not develop below a grain size of 90 µm and a permeability of 600–700 mD.

| Sample name | Concretion type | Cement type | Porosity (%) | Cement (%) | IGV (%) |
|---|---|---|---|---|---|
| SP1.3C | Single elongate | C2 | 16.9 | 33.5 | 50.4 |
| SP1.18C | Tabular | C1, C2 | 4.1 | 46.7 | 50.8 |
| SP1.24C | Tabular | C1, C2 | 1.7 | 43.2 | 44.9 |
| SP1.27C | Tabular | C1, C2 | 3.1 | 43.3 | 46.4 |
| SP1.28C | Single elongate | C2 | 2.1 | 45.7 | 47.8 |
| SP1.29C | Single elongate | C2 | 2.2 | 44.3 | 46.5 |
| SP1.31C | Tabular | C1, C2 | 4.1 | 42.9 | 47 |
| SP1.33C | Nodular | C2 | 1.9 | 47.2 | 49.1 |
| SP1.34C | Coalescent elongate | C1, C2 | 2.8 | 42.8 | 45.6 |
| SP1.38C | Coalescent elongate | C1, C2 | 1.9 | 52.9 | 54.8 |

**Table 2.1.** Morphology, main cement types, percentage porosity, cement and intergranular volume of the sampled concretions.

The porosity is almost completely interparticle, showing a patchy distribution with rare intraparticle and partial mouldic porosity characterizing only fossil shells affected by partial dissolution. The two-dimensional concretion porosity ranges between 1.7 and 4.2% (Table 2.1). Only one elongate concretionary body displays an anomalously higher porosity of 16.9%, which lies outside the range identified by other concretions (Table 2.1). The IGV in the sampled concretions varies from 44.9 to 54.8% (Table 2.1).

### 2.5.3. Concretion Petrography

The sampled concretions are composed of abundant quartz, K-feldspar and plagioclase grains, with minor amounts of opaque iron oxides, a few biotite and muscovite micas, rare lithic fragments and pyrite (Fig. 2.6a, c, e and g). Apart from the calcite cement, the carbonate phases are mostly represented by several species of foram, mollusc and

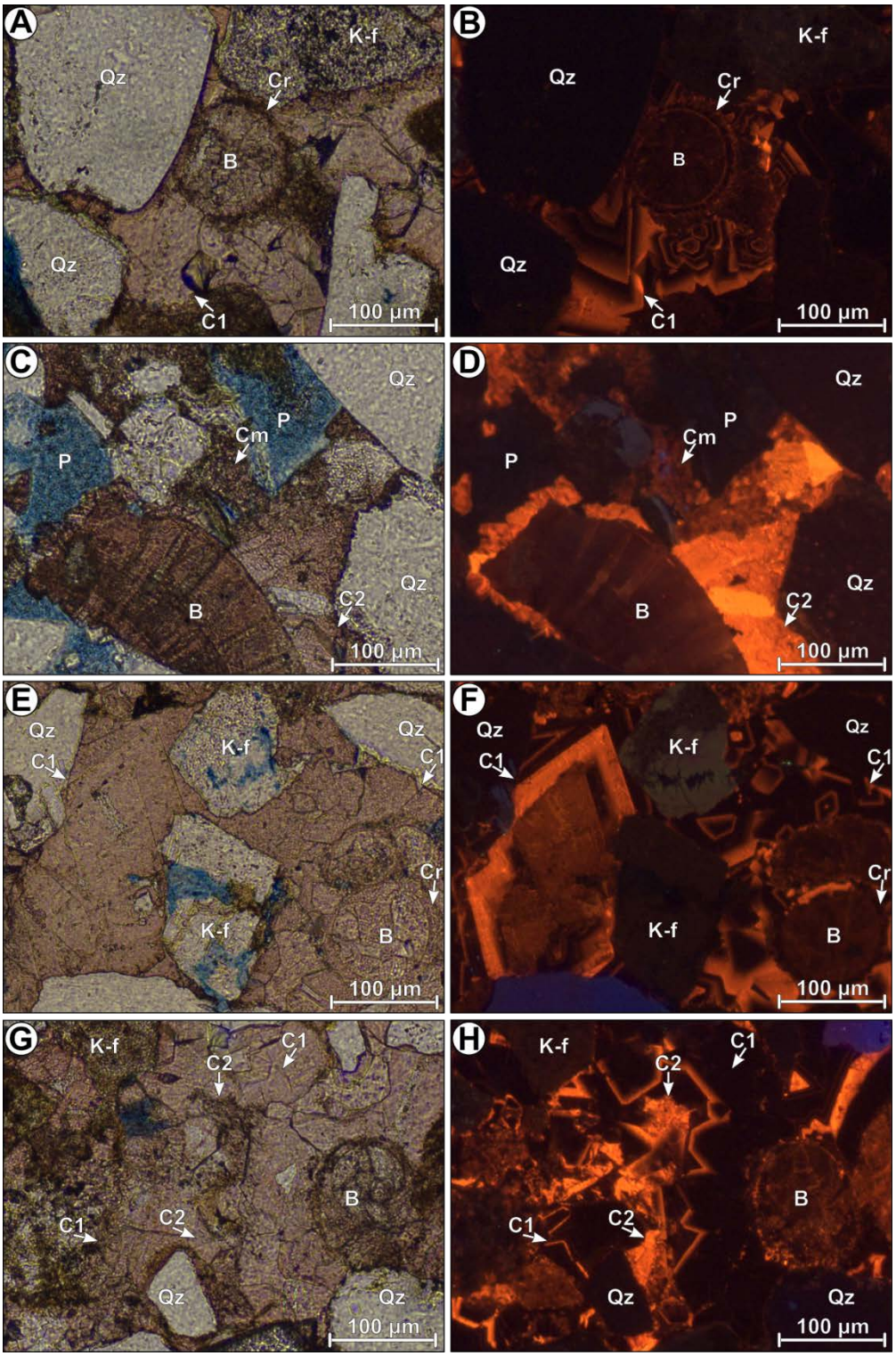


**Fig. 2.6.** Photomicrographs of the cement on stained thin sections under transmitted light and under cathodoluminescence. (**a**, **b**) Circumgranular rim of equant calcite (Cr) around bioclast followed by blocky zoned calcite (C1) with several zonations inside a tabular concretion sample. (**c**, **d**) Rare meniscus dully luminescent calcite (Cm) and fine equant sparitic calcite (C2) surrounding bioclast inside single elongate concretion. (**e**, **f**) Syntaxial overgrowth around crinoid fragments and blocky zoned calcite (C1) in tabular concretion. Circumgranular-isopachous rim of equant calcite (Cr) is also present around bioclast. (**g**, **h**) Fine equant sparite (C2) post-dating blocky zoned calcite (C1) inside elongate coalescent concretion. B, bioclast; K-f, feldspar; P, porosity; Qz, quartz.

gastropod shell fragments, as well as crinoids, peloids and a few detrital calcite grains.

The carbonate cement inside the concretions is made of nonferroan calcite (pink staining colour) (Fig. 2.6a, c, e and g). The majority of the cement is pore-filling, with a lesser amount being a grain-lining and coating cement; the cement therefore reduces the interparticle porosity.

Based on the petrographic analysis, four main cement types can be distinguished.

(1) Cr: circumgranular–isopachous rims of small-sized equant calcite (crystal size < 10–20 µm) around bioclasts and fossil shells. This cement has a dark cathodoluminescence

response (Fig. 2.6b, f) and does not contain fluid inclusions.

(2) Cm: pore-lining and pore-filling fine sparitic calcite (crystal size < 25 μm) with a mosaic texture, located around quartz and feldspar grains and forming a meniscus cement. It is dominantly non-luminescent, but in a few areas a bright orange luminescence occurs (Fig. 2.6d). No fluid inclusion is present inside this cement.

(3) C1: coarse–blocky sparite with a drusy texture (the size of the cement crystals increases towards the centre of the pore), together with syntaxial overgrowths around crinoid fragments, biogenic and detrital calcite (Fig. 2.6f). This cement is characterized by crystal sizes up to 200–300 μm and the majority show a zoned cathodoluminescence pattern consisting of alternating non-luminescent and bright sub-zones (Fig. 2.6b, h). The sub-zone number and width vary according to the type of concretion. Tabular concretions display the highest number of sub-zones with smaller widths, whereas elongate single concretions have just a few, thick, less-defined sub-zones. Other crystals belonging to the same cement pattern do not display any zonation and are non-luminescent. Syntaxial overgrowths may develop crystals up to 400 μm. They are characterized by less bright sub-zones than the blocky calcite and the crystal cores are usually non-luminescent (Fig. 2.6f). A few small (5–7 μm) mono-phase, all-liquid fluid inclusions are present within this cement type.

(4) C2: fine pore-filling equant sparitic calcite (crystal size < 50 μm) with a constant bright orange–yellow cathodoluminescence response (Fig. 2.6d, h). No fluid inclusion has been found inside this cement type.

Scanning electron microscopy images showed the presence of clustered spherical bodies (1–2 μm in diameter) located around the Cm and Cr cements, which could represent bacteria. Details of the cement morphology and timing based on scanning electron microscopy photomicrographs are given in the Supplementary Material.

Cement types Cm, C1 and C2 are pore-filling and often prevent contact between quartz and feldspar clasts, giving rise to a floating fabric, which explains the high IGV. Tabular, elongate single, coalescent and nodular concretions show different amounts of these calcite cements. In particular, in elongate single and coalescent concretions, the pores are filled by almost equal proportions of C1 and C2 cements, whereas in the tabular bodies C1 becomes prevalent. Cr and Cm are rare and subordinate to C1 and C2 in all concretion types. Eventually, the cement within the nodular concretions is almost completely composed of C2 in a scattered pattern. Zoned C1 cement is subordinate and occurs as small crystals relative to those found in the tabular and coalescent concretions.

### 2.5.4. Stable Carbon and Oxygen Isotopes

Bulk isotopic analyses (n = 184) on concretions from the Sabbie di Imola Formation show $\delta^{13}C$ spanning from −10.7 to −2.5‰, whereas $\delta^{18}O$ covers a narrower interval from −7.6 to −5.5‰ VPDB (Fig. 2.7a). The isotopic data show a near-vertical alignment in a cross-plot (Fig. 2.7b). Nodular and small elongate single concretions have the least depleted $\delta^{13}C$ values (−2.5‰), whereas tabular and elongate coalescent bodies usually show the most depleted

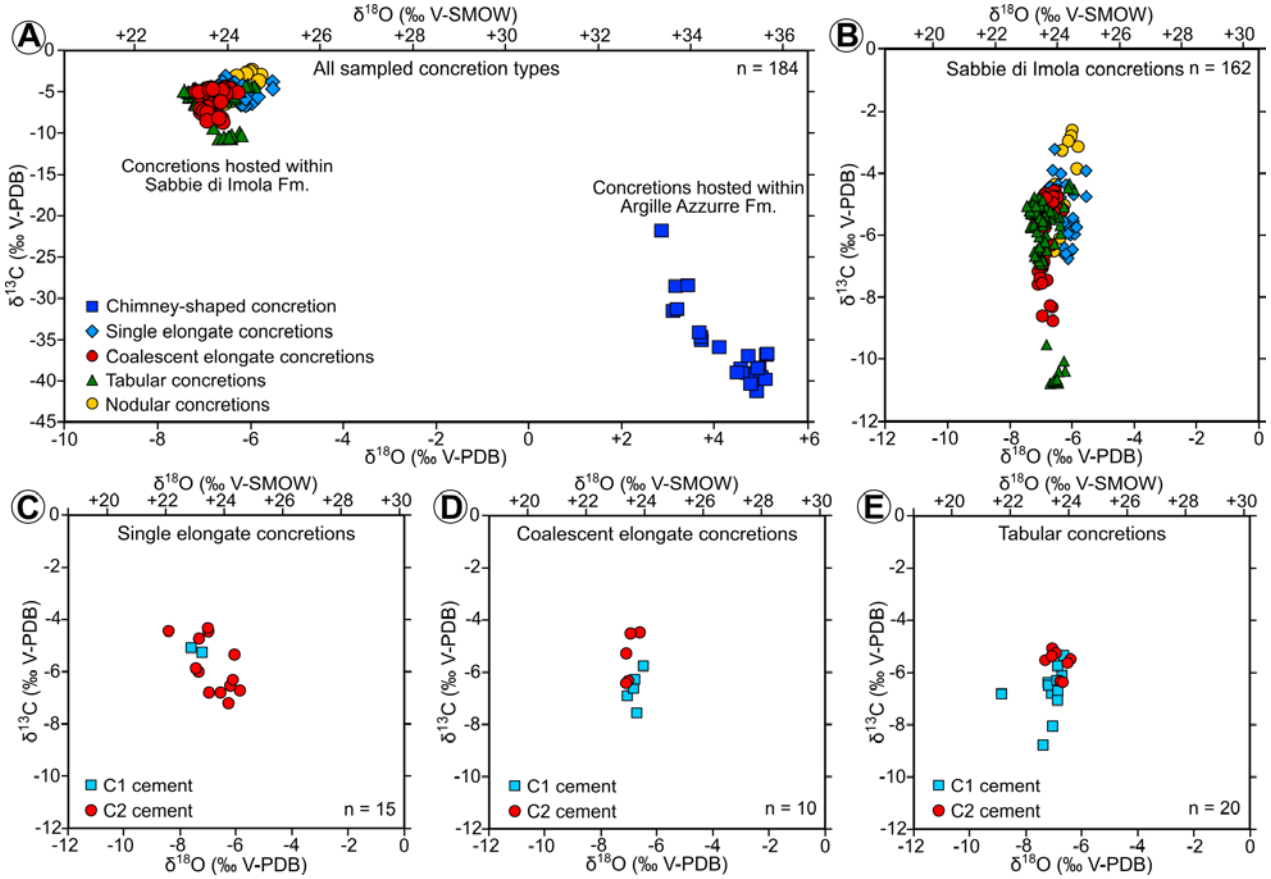


**Fig. 2.7.** Isotopic data collected on (**a**, **b**) hand specimens and (**c**–**e**) on thin sections with micromill technique. (**a**) Cumulative isotopic data characterizing the concretions inside the Sabbie di Imola and the Argille Azzurre formations. (**b**) Detailed isotopic trend shown by concretions hosted within the Sabbie di Imola Formation. Isotopic data gained from (**c**) single elongate, (**d**) coalescent elongate and (**e**) tabular concretions with micromill technique.

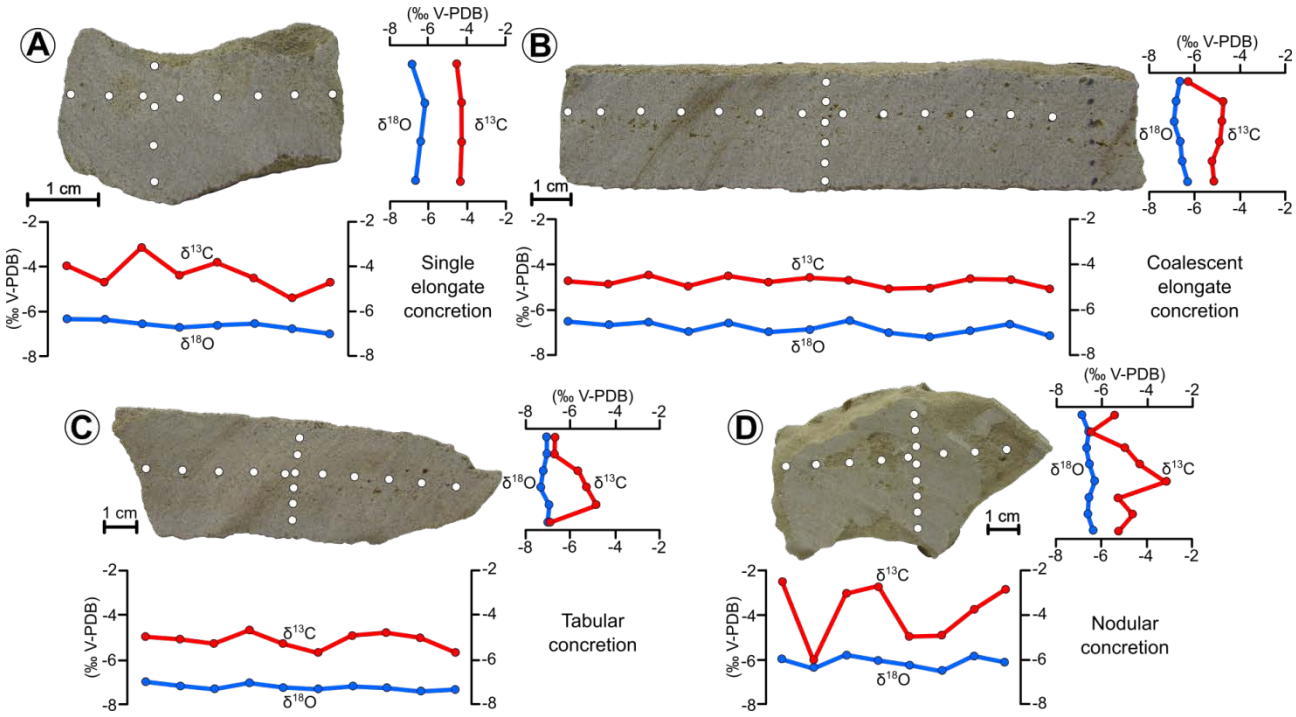


**Fig. 2.8.** Sampling methods and isotopic trends on representative concretion hand specimens. (**a**) Single elongate, (**b**) elongate coalescent, (**c**) tabular and (**d**) nodular concretions.

isotopic response (−10.7‰). Data from a chimney-shaped concretion collected within the Argille Azzurre Formation for comparative purposes displays extremely depleted $\delta^{13}C$ (−41.2 to −21.8‰) and slightly enriched $\delta^{18}O$ (+2.8 to +5.1‰ V-PDB) values (Fig. 2.7a). Isotopic data obtained with the micromill (n = 45) allow a more precise evaluation of the isotopic signature of the main cement types (Fig. 2.7c–e). In single elongate concretions, the C2 cement has an isotopic signature similar to C1: $\delta^{13}C$ ranges from −7.2 to −4.4‰, whereas $\delta^{18}O$ spans from −8.5 to −5.9‰ V-PDB (Fig. 2.7c). Conversely, in the tabular and coalescent concretions, the C2 cement has less depleted $\delta^{13}C$ (−6.4 to −4.5‰) than the C1 cement (−8.8 to −5.5‰), whereas the $\delta^{18}O$ spans from −8.8 to −6.0‰ V-PDB (Fig. 2.7d, e). Statistical analysis to assess the difference in isotopic signature of the C1 and C2 cements can be found in the Supplementary Material. No sample from Cr and Cm could be isolated due to their size, which were below the sampling resolution of the micromill device.

Along the isotopic sampling lines, single elongate concretions show slightly less depleted $\delta^{13}C$ values near the centre along the horizontal transects, whereas $\delta^{18}O$ remains almost constant. Both $\delta^{13}C$ and $\delta^{18}O$ are almost constant on vertical transects (Fig. 2.8a). Coalescent concretions display less depleted $\delta^{13}C$ and more depleted $\delta^{18}O$ values around the centre. Approaching the outer margin, $\delta^{13}C$ shifts towards the more depleted values, whereas $\delta^{18}O$ displays slightly less depleted signatures (Fig. 2.8b). Tabular concretions record oscillating $\delta^{13}C$ and $\delta^{18}O$ values along the horizontal transects. On vertical transects, moving away from the centre, $\delta^{13}C$ becomes more depleted, whereas $\delta^{18}O$ shows less depleted values (Fig. 2.8c). Nodular concretions are characterized by an alternation of less depleted and more depleted $\delta^{13}C$ values and stable $\delta^{18}O$ values of c. −6.0‰ V-PDB along the horizontal transect. On the vertical sampling lines, $\delta^{13}C$ shows less depleted values in the central part, decreasing towards the outer margin. The $\delta^{18}O$ values show only small oscillations around −6.5‰ V-PDB (Fig. 2.8d).

## 2.6. Discussion

### 2.6.1. Carbonate Concretion Diagenetic History

According to the petrographic observations and stable isotope data, four cementation stages are proposed (Fig. 2.9a).

(1) The first cement is Cr (Fig. 2.9b). The isopachous texture and dark cathodoluminescence pattern possibly suggest an oxidizing (high $pO_2$) meteoric phreatic environment (Moore, 1989; Budd and Land, 1990; Hiatt and Pufhal, 2014).

(2) The second cement to precipitate is Cm (Fig. 2.9b). The dominant dark cathodoluminescence response suggests an environment with stable oxidizing geochemical conditions. The mosaic texture and the presence of meniscus cement around quartz and feldspar clasts support cementation in a meteoric vadose zone above the water table (Moore, 1989) (Fig. 2.9a).

(3) The third, more pervasive, cementation stage consists of C1 (Fig. 2.9b). The zonation is induced by changes in the water geochemistry (Habermann et al., 1996, 1998; Hiatt and Pufhal, 2014), possibly caused by Eh and pH oscillations. It testifies to shifts from fully oxidizing to partially reducing to

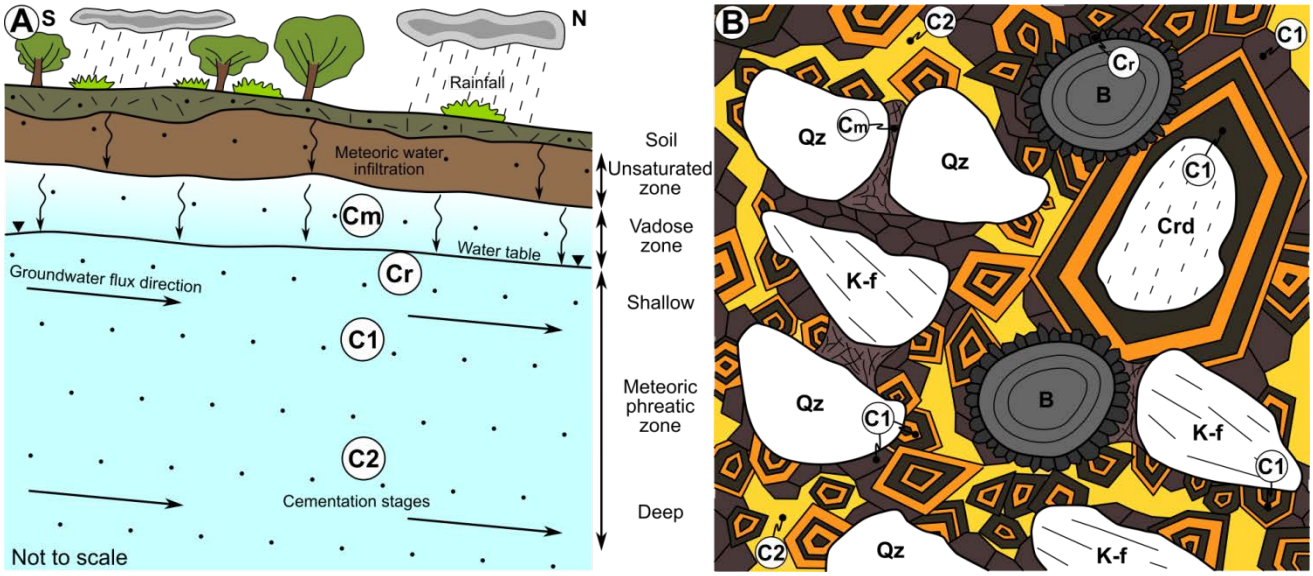


**Fig. 2.9.** (**a**) Diagenetic environments inferred from the four identified cementation stages. (**b**) Schematic cementation sequence deduced from petrographic and cathodoluminescence observations. Cement colours refer to the cathodoluminescence response. Cr, isopachous rim of equant calcite; Cm, meniscus mosaic sparitic calcite; C1, blocky zoned calcite; C2, fine equant sparitic calcite; B, bioclast; Crd, crinoid; K-f, feldspar; Qz, quartz.

suboxic conditions and vice versa (Barnaby and Rimstidt, 1989). This feature is common in meteoric phreatic environments with increasing reducing conditions moving away from the water table with depth (Li et al., 2017). The presence of zoned crystals could be related to cementation occurring within the meteoric phreatic zone in a deeper vertical position with respect to the Cr and Cm cements (Fig. 2.9a, b). The depleted $\delta^{13}C$ and $\delta^{18}O$ values of this cement support a meteoric origin of fluid with a contribution from soil-derived $CO_2$ (Hudson, 1977). The mono-phase fluid inclusions also support the hypothesis that C1 precipitated in the temperature range < 40–50°C (Goldstein and Reynolds, 1994).

(4) The fourth cementing stage consists of C2 (Fig. 2.9b). The homogeneous bright orange cathodoluminescence response could be related to an environment with stable reducing conditions (low $pO_2$) (Barnaby and Rimstidt, 1989; Hiatt and Pufhal, 2014). The $\delta^{13}C$ is less depleted than C1, probably due to a lower contribution from soil-derived $CO_2$ caused by the deeper conditions (Fig. 2.9a). The reconstructed diagenetic sequence reflects the vertical variation of the diagenetic settings, with a progressive deepening trend (Fig. 2.9a, b). This could be due to the growth of the anticline southwards of the study site, causing a steepening of the hydraulic gradient or an increase in rainfall related to climate change during the diagenetic history.

The studied concretions developed in a shallow diagenetic setting, as confirmed by the limited thickness of the overlying strata, the presence of floating grains surrounded by cement and the high values of IGV (Table 2.1), which collectively indicate a maximum burial depth of c. 100–120 m (Houseknecht, 1987; Cibin et al., 1993). The Sabbie di Imola Formation sand strata were deposited in a shallow marine setting along proximal fluvial lobes close to the shore. However, no evidence of marine cement has been found. This could mean that the sediments underwent a rapid change in sedimentary environment caused by a period of sea-level

fall, in agreement with Gunderson et al. (2014), or uplift induced by the growth of the Quattro Castella Anticline (Ponza et al., 2010; Gunderson et al., 2014; Oppo et al., 2015). An alternative hypothesis is that the onset of topography-driven meteoric flow affected the permeable fluvial sand lobes after their deposition in a shallow marine setting (Chafetz et al., 1988).

### 2.6.2. Concretion Growth Mode

The size and arrangement of concretions depend on several factors, such as: (1) the spatial distribution of cementation nuclei; (2) the sedimentary facies; (3) the grain size–permeability structure; and (4) the fluid flow pattern.

(1) Cementation nuclei are the sites where calcite precipitation starts (Bjorkum and Walderhaug, 1990; Abdel-Wahab and McBride, 2001). Within the studied concretions, the early cement generations (Cr and Cm in Fig. 2.6b, d) are often associated with fossil shells and detrital calcite grains, the limited dissolution of which probably influenced the fluid saturation conditions.

(2) Several researchers have linked the presence of carbonate concretions to peculiar sedimentary facies (Cavazza et al., 2009; Van Den Bril and Swennen, 2009; Arribas et al., 2012). Along the Enza River section, the occurrence of concretions is not strictly constrained to specific facies. However, the outcrop-scale three dimensional facies distribution and geometry influenced the development of the concretions. At the lamina scale, the concretions cut lamina sets of ripple and hummocky cross-stratification with different

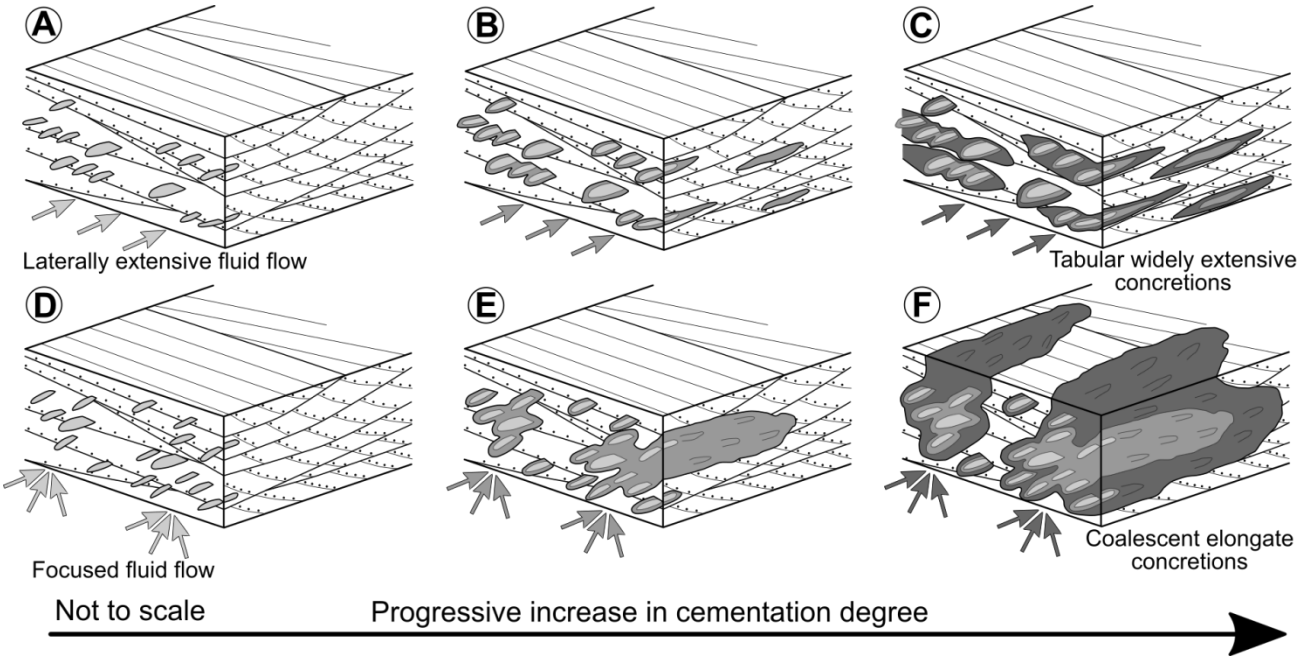


**Fig. 2.10.** Concretion development modality for (**a**–**c**) tabular and (**d**–**f**) coalescent elongate concretions. (**a**) Alignment of cementation nuclei leads to the formation of single elongate concretions in a pattern parallel to the strike of strata. (**b**) With a laterally spread fluid flow pattern (parallel to the bedding surface), single elements may merge together forming tabular bodies. (**c**) Pervasive cementation eventually allows the development of widely extensive tabular concretions. (**d**) The scattered and sparse arrangement of cementation nuclei is responsible for the formation of densely clustered arrays of single elongate concretions. (**e**) Focused fluid flow pattern induces the cementation of larger elongate bodies. (**f**) Coalescent elongate concretions increase their size until the fluid flow is able to carry the solutes necessary for cementation.

angles, implying that the internal organization of facies did not exert a direct control on the development of concretions. This could be due to a low-permeability contrast between the different lamina sets or to fast advective flow forcing the fluids to neglect the internal structure of the facies.

(3) Grain size and permeability distributions associated with the host sediments were the main drivers for the development of concretions (Mozley and Davis, 1996; Davis et al., 2006). The studied concretions developed in sediments characterized by a mean grain size > 90 μm and a permeability > 700 mD. Concretions did not develop below these two threshold values, possibly because the limited fluid flow through the sediments was unable to provide the constituents needed for cementation.

(4) Single elongate concretionary bodies represent the first stage of concretion growth (Fig. 2.10a, d). Such elongate bodies (Fig. 2.3a) preferentially develop parallel to the advective fluid flow direction (McBride et al., 1994; McBride and Parea, 2001; Balsamo et al., 2012). Their occurrence suggests that, after the early cementation, the system was no longer saturated with respect to calcite locally and was unable to promote any further broadening of the concretionary bodies (Bjorkum and Walderhaug, 1990). Cementation continued at other sites where the system was still saturated and closely spaced blade-shaped concretions merged together via newly formed cement bridges (Fig. 2.10b). Persistent and laterally extensive fluid flow eventually allowed the cementation of many elongate concretions to form tabular bodies parallel to the surfaces of the basal and upper strata (Fig. 2.10c). Conversely, elongate coalescent concretions originated from the focused advective fluid flow caused by the three-dimensional outcrop-scale facies distribution (Fig. 2.10d). Single elongate bodies progressively merged together (Fig. 2.10e) and eventually formed metre-wide concretions (Fig. 2.10f). Nodular concretions with a spherical shape are probably related to a steady, diffusion-dominated fluid flow regime (Theakstone, 1981; Bjorkum and Walderhaug, 1990; Wanas, 2008).

The proposed evolutionary pathways is consistent with the outward propagation of the cementation front (Bjorkum and Walderhaug, 1990, 1993; Klein et al., 1999; Abdel-Wahab and McBride, 2001; Mozley and Davis, 2005), which agrees with the observed outward-depletion concentric pattern of $\delta^{13}C$ values. The along-strike oscillatory pattern of $\delta^{13}C$ values indicates the non-cylindrical, three-dimensionally complex outward propagation of cementation fronts and the possible interference among multiple growing cementation sites.

### 2.6.3. Sources of Carbonate Cement

The depleted $\delta^{13}C$ values and the vertical alignment in the $\delta^{18}O$– $\delta^{13}C$ cross-plot of cement isotopic data shown by concretions within the Sabbie di Imola Formation are consistent with a carbonate source mainly provided by the infiltration of $CaCO_3$-saturated meteoric fluids carrying soil-derived $CO_2$ (Fig. 2.7a, b) (Hudson, 1977; Nelson and Smith, 1996) facilitated by the shallow burial depth (< 120 m). Further evidence of the meteoric origin of the fluids comes from the back-calculated $\delta^{18}O$ composition of the cementing fluid. Assuming a superficial temperature of 12°C, a

normal geothermal gradient (25°C $km^{-1}$) and 120 m of maximum burial, the Friedman and O'Neil (1977) fractionation formula for the water–calcite system gives $\delta^{18}O$ from −9.2 to −6.1‰ V-SMOW. These values are in accordance with the expected isotopic composition of meteoric water at the mountain front of the Northern Apennines (Giustini et al., 2016). Additional carbonate could be provided by the partial dissolution of detrital calcite and foram and mollusc shells (Bjorkum and Walderhaug, 1990; Wanas, 2008; Van Den Bril and Swennen, 2009). The limited presence of bacterial cells inside fossil shells and the occurrence of framboidal pyrite suggest that bacterial activity may have influenced the distribution of nucleation sites during early cementation (Folk, 1993; McBride et al., 1994; Abdel-Wahab and McBride, 2001; McBride and Parea, 2001).

Methane-rich fluids responsible for the formation of chimney concretions did not contribute to the cementation of the studied concretions inside the Sabbie di Imola Formation, as confirmed by the difference in the isotopic signatures (Fig. 2.7a).

### 2.6.4. Anticline Growth and Related Fluid Flow Pathways

The growth-wedge geometry of the studied succession (Fig. 2.2b) and the clockwise rotation of the bedding dip direction indicate sedimentation during the growth of the anticline (Figs 2.4 and 2.5). In particular, during the deposition of the transition between the Argille Azzurre and the Sabbie di Imola formations, the strata were dipping towards the west. The carbonate concretions in this stratigraphic interval are aligned along the same westwards direction (Fig. 2.4b, c). The bedding dip direction shifted during the deposition of the Sabbie di Imola Formation from NW at the base to NNE at the top; the same trend is shown by the concretions (Fig. 2.4b, c). We therefore propose that the palaeo-groundwater flow recorded by the concretions was controlled by changes in the topographic gradient induced by the lateral propagation of the anticline (Fig. 2.11). This is also confirmed by the nearby streams changing flow direction from parallel to orthogonal with respect to the Apennines topographic front during fold amplification (Maestrelli et al., 2018). In particular, during the early lateral propagation stage of the anticline, the higher topography was positioned to the east of the studied outcrop (Fig. 2.11a), thus promoting a topographic and hydraulic gradient towards the west. After the incorporation of the studied outcrop within the fold forelimb, the topography increased rapidly in the crestal region of the fold (Fig. 2.11b), forcing groundwater fluxes towards the NW (Fig. 2.11c) and eventually to the NNE during further fold amplification (Fig. 2.11d). The evidence that the older concretions do not record the growth direction of the younger concretions implies that the geometry of the concretions only recorded the first fluid flow direction within the host sediments. This means that the first fluid flow direction imprinted the shape of the early concretions, whereas later groundwater flow probably increased the size of the concretions without affecting the original shape and elongation direction. The outer layer of the pre-cemented bodies acted as a nucleation surface (Bjorkum and Walderhaug, 1990) for the new calcite precipitation provided by later fluid flow.

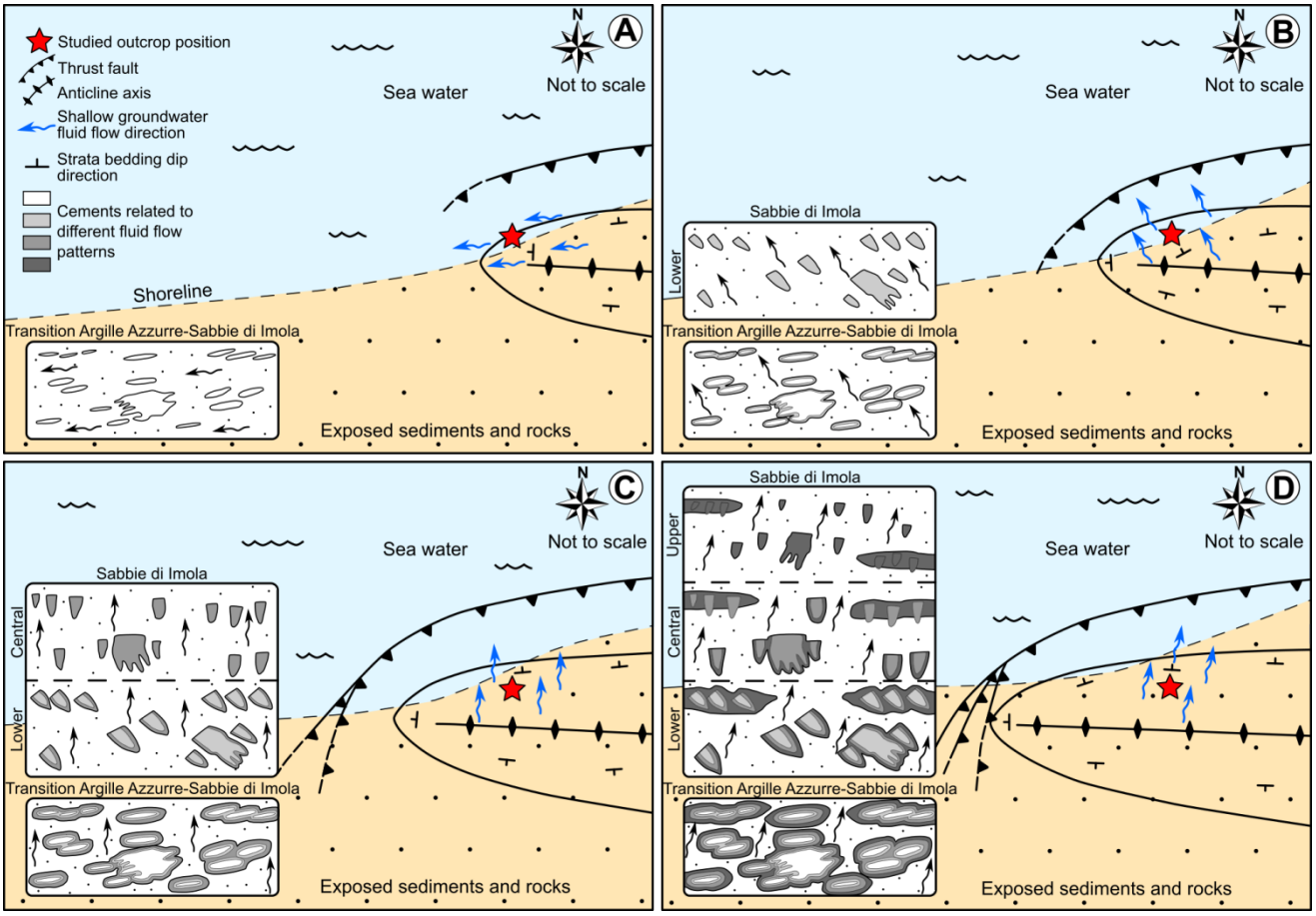


**Fig. 2.11.** Conceptual sketch with inferred fluid flow patterns induced by anticline growth from the carbonate concretion data. (**a**) In the first stage of fold growth, the anticline was propagating near the study site and hence the fluid flow and sediment supply were directed parallel to the fold axis from east to west. (**b**) With an increase in topography southward from the Enza River, the fluid flow direction started to rotate clockwise towards the NW. (**c**) The westward propagation of the fold axis led to shallow fluxes towards the north. (**d**) During the late stage of fold growth, shallow fluid flow was mainly directed to the NNE following the hydraulic and topographic gradient induced by the growing anticline.

## 2.7. Conclusions

The studied concretions within the Pleistocene syn-kinematic sediments of the Sabbie di Imola Formation exposed along the Enza River stratigraphic section are interpreted to record different past patterns of groundwater fluid flow.

Four major conclusions can be drawn from our results.

(1) Fossil fluid flow through weakly lithified sediments is still recognizable in the form of the selective cementation of tabular, elongate and nodular carbonate concretions and the flow direction can be inferred from the long axis of the concretions.

(2) The carbonate concretions nucleated just after the deposition of sand in a transitional environment between meteoric vadose and meteoric phreatic. Cementation continued in a meteoric phreatic environment with the contribution of fluids percolating through soils. Concretions developed according to the concentric growth model, with advective flow forming elongate and tabular concretions, whereas nodular to spherical bodies grew under diffusion-dominated mass transfer conditions.

(3) Concretionary bodies are selectively hosted in sediments with a permeability

between $7 \times 10^2$ and $7 \times 10^4$ mD and a mean grain size from 90 to 290 µm, regardless of the internal structure of the sedimentary facies.

(4) The clockwise rotation shown by the elongation direction of the concretions indicates that the lateral propagation of the Quattro Castella Anticline promoted a change in the topographic and hydraulic gradient along its western periclinal termination. The mean groundwater fluid flow direction locally changed from east–west (axial parallel) to south–north (axial orthogonal).

**Acknowledgements**

The reviewers R.T. Williams and G. Rawling and the Editor V. Vandeginste are warmly acknowledged for their suggestions and constructive criticisms, which helped to improve the final version of this paper. The authors thank E.M. Selmo and A. Di Matteo (University of Parma) for the stable isotope data. A. Comelli and L. Barchi (University of Parma) are thanked for thin section preparation and support during the scanning electron microscopy observations, respectively. S. Boullion, D. Vanhove and Z. Kelemen (KU Leuven) are kindly acknowledged for their support during micromill sampling.

M. Pizzati collected field and laboratory data and wrote the paper; F. Balsamo participated in fieldwork and data interpretation; F. Storti took part in data interpretation; M. Mozafari and R. Swennen participated in the interpretation of diagenetic data; P. Iacumin contributed to the interpretation of the stable isotope data; R. Tinterri participated in the facies interpretation.

**Supplementary Material 1: Stable Isotope Analysis**

Carbonate powder extracted both with the dental drill (table 2.A1) and by micromill (table 2.A2) were reacted with 100% phosphoric acid (at 25°C) at a constant temperature of 70-75°C. An additional $CO_2$ reference gas (pure Carrara marble) with known isotopic ratio was analysed during the measurements to determine the $\delta^{13}C$ and $\delta^{18}O$ values. Table 2.A1 contains also isotopic data gained from one "chimney" concretion hosted within the Argille Azzurre Fm. that was used as a comparison with concretions located in the Sabbie di Imola Fm. Statistical analysis was performed to assess possible difference in isotopic composition of C1 and C2 cement using the data extracted with the micromill (table 2.A3). The Shapiro-Wilkinson test was performed to assess the normality of the data distributions. T-Student test was used to evaluate the probability to gain the same mean from the two considered data distribution. Probability data allowed to assess the difference between C1 and C2 cements. In particular, inside single elongate concretions the probability to have the same $\delta^{13}C$ mean for C1 and C2 cements is 17.8%, while for $\delta^{18}O$ is 2.2%. In coalescent elongate concretions the probability to have the same $\delta^{13}C$ value is 5.2%, and 19.3% for $\delta^{18}O$. Eventually, in tabular concretions the probability on $\delta^{13}C$ is 0.3% and 17.4% for $\delta^{18}O$ (table 2.A3).

Concretions hosted inside the Sabbie di Imola Fm., show isotopic data gained both from hand samples and from micromill on thin sections which plot inside the meteoric cement field deduced from literature data (Fig. 2.A1). Data cover a wide range of $\delta^{13}C$

while $\delta^{18}O$ has a narrower interval of variation. The most depleted $\delta^{13}C$ values are close to the soil calcites field due to the pronounced influence of $CO_2$ derived from decaying organic matter inside soils (Hudson, 1977). Isotopic data from "chimney" concretion are aligned close to the methane-derived cements. The relative enrichment shown by $\delta^{18}O$ could be related to the presence of dolomite cement precipitating in a marine environment (Nelson and Smith, 1996).

TABLE 2.A1: DATA FROM CONCRETION HAND SPECIMEN

| Sample n° | Sample name | Stratigraphic position | Concretion type | $d^{13}C$ (‰ VPDB) | $d^{18}O$ (‰ VPDB) |
|---|---|---|---|---|---|
| 1 | SP1.MT C1 | Argille Azzurre Fm. | Chimney methane-related | -21,82 | 2,82 |
| 2 | SP1.MT C2 | Argille Azzurre Fm. | Chimney methane-related | -31,51 | 3,07 |
| 3 | SP1.MT C3 | Argille Azzurre Fm. | Chimney methane-related | -35,08 | 3,68 |
| 4 | SP1.MT C4 | Argille Azzurre Fm. | Chimney methane-related | -38,48 | 4,52 |
| 5 | SP1.MT C5 | Argille Azzurre Fm. | Chimney methane-related | -39,03 | 4,66 |
| 6 | SP1.MT C6 | Argille Azzurre Fm. | Chimney methane-related | -38,98 | 4,44 |
| 7 | SP1.MT C7 | Argille Azzurre Fm. | Chimney methane-related | -36,84 | 5,07 |
| 8 | SP1.MT C8 | Argille Azzurre Fm. | Chimney methane-related | -39,19 | 4,84 |
| 9 | SP1.MT C9 | Argille Azzurre Fm. | Chimney methane-related | -38,36 | 4,92 |
| 10 | SP1.MT C10 | Argille Azzurre Fm. | Chimney methane-related | -35,89 | 4,06 |
| 11 | SP1.MT C11 | Argille Azzurre Fm. | Chimney methane-related | -31,28 | 3,15 |
| 12 | SP1.MT R1 | Argille Azzurre Fm. | Chimney methane-related | -28,53 | 3,13 |
| 13 | SP1.MT R2 | Argille Azzurre Fm. | Chimney methane-related | -34,67 | 3,67 |
| 14 | SP1.MT R3 | Argille Azzurre Fm. | Chimney methane-related | -41,25 | 4,87 |
| 15 | SP1.MT R4 | Argille Azzurre Fm. | Chimney methane-related | -39,44 | 4,96 |
| 16 | SP1.MT R5 | Argille Azzurre Fm. | Chimney methane-related | -39,81 | 5,05 |
| 17 | SP1.MT R6 | Argille Azzurre Fm. | Chimney methane-related | -36,69 | 5,09 |
| 18 | SP1.MT R7 | Argille Azzurre Fm. | Chimney methane-related | -40,32 | 4,73 |
| 19 | SP1.MT R8 | Argille Azzurre Fm. | Chimney methane-related | -38,41 | 4,88 |
| 20 | SP1.MT R9 | Argille Azzurre Fm. | Chimney methane-related | -36,98 | 4,68 |
| 21 | SP1.MT R10 | Argille Azzurre Fm. | Chimney methane-related | -34,10 | 3,63 |
| 22 | SP1.MT R11 | Argille Azzurre Fm. | Chimney methane-related | -28,45 | 3,38 |
| 23 | SP1.3C R1 | Transition AZ-SI Fms. | Single elongate | -4,63 | -5,93 |
| 24 | SP1.3C R2 | Transition AZ-SI Fms. | Single elongate | -3,85 | -5,54 |
| 25 | SP1.3C R3 | Transition AZ-SI Fms. | Single elongate | -5,60 | -6,18 |
| 26 | SP1.3C R4 | Transition AZ-SI Fms. | Single elongate | -6,35 | -6,23 |
| 27 | SP1.3C R5 | Transition AZ-SI Fms. | Single elongate | -5,51 | -6,23 |
| 28 | SP1.3C R6 | Transition AZ-SI Fms. | Single elongate | -5,49 | -5,94 |
| 29 | SP1.3C R7 | Transition AZ-SI Fms. | Single elongate | -5,94 | -6,04 |
| 30 | SP1.3C R8 | Transition AZ-SI Fms. | Single elongate | -5,91 | -5,90 |
| 31 | SP1.3C R9 | Transition AZ-SI Fms. | Single elongate | -5,38 | -5,96 |
| 32 | SP1.3C R10 | Transition AZ-SI Fms. | Single elongate | -6,50 | -6,06 |
| 33 | SP1.3C C1 | Transition AZ-SI Fms. | Single elongate | -6,59 | -6,22 |
| 34 | SP1.3C C2 | Transition AZ-SI Fms. | Single elongate | -6,39 | -5,97 |
| 35 | SP1.3C C3 | Transition AZ-SI Fms. | Single elongate | -6,69 | -6,11 |
| 36 | SP1.3C C4 | Transition AZ-SI Fms. | Single elongate | -6,53 | -6,19 |

| | | | | | |
|---|---|---|---|---|---|
| 37 | SP1.3C C5 | Transition AZ-SI Fms. | Single elongate | -5,88 | -6,12 |
| 38 | SP1.3C C6 | Transition AZ-SI Fms. | Single elongate | -6,25 | -6,66 |
| 39 | SP1.3C C7 | Transition AZ-SI Fms. | Single elongate | -5,68 | -5,85 |
| 40 | SP1.3C C8 | Transition AZ-SI Fms. | Single elongate | -4,69 | -5,53 |
| 41 | SP1.11C R1 | Transition AZ-SI Fms. | Tabular | -10,02 | -6,23 |
| 42 | SP1.11C R2 | Transition AZ-SI Fms. | Tabular | -10,34 | -6,20 |
| 43 | SP1.11C R3 | Transition AZ-SI Fms. | Tabular | -10,68 | -6,48 |
| 44 | SP1.11C R4 | Transition AZ-SI Fms. | Tabular | -10,72 | -6,57 |
| 45 | SP1.11C R5 | Transition AZ-SI Fms. | Tabular | -10,73 | -6,68 |
| 46 | SP1.11C R6 | Transition AZ-SI Fms. | Tabular | -10,69 | -6,57 |
| 47 | SP1.11C R7 | Transition AZ-SI Fms. | Tabular | -10,72 | -6,42 |
| 48 | SP1.11C R8 | Transition AZ-SI Fms. | Tabular | -10,65 | -6,46 |
| 49 | SP1.11C R9 | Transition AZ-SI Fms. | Tabular | -10,67 | -6,46 |
| 50 | SP1.11C R10 | Transition AZ-SI Fms. | Tabular | -10,60 | -6,46 |
| 51 | SP1.11C C1 | Transition AZ-SI Fms. | Tabular | -9,49 | -6,80 |
| 52 | SP1.11C C2 | Transition AZ-SI Fms. | Tabular | -10,36 | -6,41 |
| 53 | SP1.11C C3 | Transition AZ-SI Fms. | Tabular | -10,66 | -6,57 |
| 54 | SP1.11C C4 | Transition AZ-SI Fms. | Tabular | -10,60 | -6,46 |
| 55 | SP1.18C R1 | Base Sabbie di Imola Fm. | Tabular | -4,48 | -5,91 |
| 56 | SP1.18C R2 | Base Sabbie di Imola Fm. | Tabular | -5,90 | -6,35 |
| 57 | SP1.18C R3 | Base Sabbie di Imola Fm. | Tabular | -5,38 | -6,37 |
| 58 | SP1.18C R4 | Base Sabbie di Imola Fm. | Tabular | -5,38 | -6,64 |
| 59 | SP1.18C R5 | Base Sabbie di Imola Fm. | Tabular | -5,23 | -6,65 |
| 60 | SP1.18C R6 | Base Sabbie di Imola Fm. | Tabular | -5,45 | -6,64 |
| 61 | SP1.18C R7 | Base Sabbie di Imola Fm. | Tabular | -5,04 | -6,24 |
| 62 | SP1.18C R8 | Base Sabbie di Imola Fm. | Tabular | -4,28 | -6,05 |
| 63 | SP1.18C R9 | Base Sabbie di Imola Fm. | Tabular | -5,24 | -6,54 |
| 64 | SP1.18C R10 | Base Sabbie di Imola Fm. | Tabular | -5,63 | -6,36 |
| 65 | SP1.18C C1 | Base Sabbie di Imola Fm. | Tabular | -6,22 | -6,54 |
| 66 | SP1.18C C2 | Base Sabbie di Imola Fm. | Tabular | -6,02 | -6,89 |
| 67 | SP1.18C C3 | Base Sabbie di Imola Fm. | Tabular | -5,95 | -6,81 |
| 68 | SP1.18C C4 | Base Sabbie di Imola Fm. | Tabular | -5,60 | -6,95 |
| 69 | SP1.18C C5 | Base Sabbie di Imola Fm. | Tabular | -5,41 | -6,81 |
| 70 | SP1.18C C6 | Base Sabbie di Imola Fm. | Tabular | -4,42 | -6,10 |
| 71 | SP1.24C R1 | Base Sabbie di Imola Fm. | Tabular | -5,01 | -6,96 |
| 72 | SP1.24C R2 | Base Sabbie di Imola Fm. | Tabular | -5,08 | -7,15 |
| 73 | SP1.24C R3 | Base Sabbie di Imola Fm. | Tabular | -5,25 | -7,30 |
| 74 | SP1.24C R4 | Base Sabbie di Imola Fm. | Tabular | -4,73 | -7,02 |
| 75 | SP1.24C R5 | Base Sabbie di Imola Fm. | Tabular | -5,28 | -7,21 |
| 76 | SP1.24C R6 | Base Sabbie di Imola Fm. | Tabular | -5,70 | -7,30 |
| 77 | SP1.24C R7 | Base Sabbie di Imola Fm. | Tabular | -4,94 | -7,16 |
| 78 | SP1.24C R8 | Base Sabbie di Imola Fm. | Tabular | -4,80 | -7,23 |
| 79 | SP1.24C R9 | Base Sabbie di Imola Fm. | Tabular | -5,01 | -7,42 |
| 80 | SP1.24C R10 | Base Sabbie di Imola Fm. | Tabular | -5,66 | -7,31 |
| 81 | SP1.24C C1 | Base Sabbie di Imola Fm. | Tabular | -6,89 | -6,99 |
| 82 | SP1.24C C2 | Base Sabbie di Imola Fm. | Tabular | -4,83 | -6,91 |
| 83 | SP1.24C C3 | Base Sabbie di Imola Fm. | Tabular | -5,25 | -7,29 |

| | | | | | |
|---|---|---|---|---|---|
| 84 | SP1.24C C4 | Base Sabbie di Imola Fm. | Tabular | -5,61 | -7,20 |
| 85 | SP1.24C C5 | Base Sabbie di Imola Fm. | Tabular | -6,69 | -7,04 |
| 86 | SP1.24C C6 | Base Sabbie di Imola Fm. | Tabular | -6,67 | -7,04 |
| 87 | SP1.27C R1 | Base Sabbie di Imola Fm. | Tabular | -5,22 | -7,13 |
| 88 | SP1.27C R2 | Base Sabbie di Imola Fm. | Tabular | -4,72 | -7,19 |
| 89 | SP1.27C R3 | Base Sabbie di Imola Fm. | Tabular | -5,09 | -6,80 |
| 90 | SP1.27C R4 | Base Sabbie di Imola Fm. | Tabular | -5,17 | -6,67 |
| 91 | SP1.27C R5 | Base Sabbie di Imola Fm. | Tabular | -5,26 | -6,87 |
| 92 | SP1.27C R6 | Base Sabbie di Imola Fm. | Tabular | -5,55 | -6,79 |
| 93 | SP1.27C R7 | Base Sabbie di Imola Fm. | Tabular | -5,15 | -7,34 |
| 94 | SP1.27C R8 | Base Sabbie di Imola Fm. | Tabular | -4,94 | -7,23 |
| 95 | SP1.27C R9 | Base Sabbie di Imola Fm. | Tabular | -5,16 | -7,32 |
| 96 | SP1.27C R10 | Base Sabbie di Imola Fm. | Tabular | -5,37 | -6,91 |
| 97 | SP1.27C R11 | Base Sabbie di Imola Fm. | Tabular | -5,32 | -6,86 |
| 98 | SP1.27C R12 | Base Sabbie di Imola Fm. | Tabular | -5,00 | -7,14 |
| 99 | SP1.27C R13 | Base Sabbie di Imola Fm. | Tabular | -5,51 | -6,86 |
| 100 | SP1.27C R14 | Base Sabbie di Imola Fm. | Tabular | -5,55 | -6,84 |
| 101 | SP1.27C R15 | Base Sabbie di Imola Fm. | Tabular | -5,39 | -7,02 |
| 102 | SP1.27C C1 | Base Sabbie di Imola Fm. | Tabular | -6,01 | -7,03 |
| 103 | SP1.27C C2 | Base Sabbie di Imola Fm. | Tabular | -5,84 | -7,11 |
| 104 | SP1.27C C3 | Base Sabbie di Imola Fm. | Tabular | -5,01 | -7,43 |
| 105 | SP1.27C C4 | Base Sabbie di Imola Fm. | Tabular | -5,62 | -6,92 |
| 106 | SP1.27C C5 | Base Sabbie di Imola Fm. | Tabular | -5,50 | -6,92 |
| 107 | SP1.28C R1 | Middle Sabbie di Imola Fm. | Single elongate | -3,95 | -6,35 |
| 108 | SP1.28C R2 | Middle Sabbie di Imola Fm. | Single elongate | -4,71 | -6,36 |
| 109 | SP1.28C R3 | Middle Sabbie di Imola Fm. | Single elongate | -3,16 | -6,55 |
| 110 | SP1.28C R4 | Middle Sabbie di Imola Fm. | Single elongate | -4,38 | -6,72 |
| 111 | SP1.28C R5 | Middle Sabbie di Imola Fm. | Single elongate | -3,84 | -6,61 |
| 112 | SP1.28C R6 | Middle Sabbie di Imola Fm. | Single elongate | -4,50 | -6,55 |
| 113 | SP1.28C R7 | Middle Sabbie di Imola Fm. | Single elongate | -5,44 | -6,76 |
| 114 | SP1.28C R8 | Middle Sabbie di Imola Fm. | Single elongate | -4,74 | -6,99 |
| 115 | SP1.28C C1 | Middle Sabbie di Imola Fm. | Single elongate | -4,37 | -6,68 |
| 116 | SP1.28C C2 | Middle Sabbie di Imola Fm. | Single elongate | -4,30 | -6,44 |
| 117 | SP1.28C C3 | Middle Sabbie di Imola Fm. | Single elongate | -4,30 | -6,18 |
| 118 | SP1.28C C4 | Middle Sabbie di Imola Fm. | Single elongate | -4,55 | -6,85 |
| 119 | SP1.31C R1 | Middle Sabbie di Imola Fm. | Tabular | -7,39 | -6,92 |
| 120 | SP1.31C R2 | Middle Sabbie di Imola Fm. | Tabular | -5,70 | -6,86 |
| 121 | SP1.31C R3 | Middle Sabbie di Imola Fm. | Tabular | -5,34 | -6,50 |
| 122 | SP1.31C R4 | Middle Sabbie di Imola Fm. | Tabular | -7,39 | -6,79 |
| 123 | SP1.31C R5 | Middle Sabbie di Imola Fm. | Tabular | -7,52 | -7,08 |
| 124 | SP1.31C R6 | Middle Sabbie di Imola Fm. | Tabular | -6,80 | -6,89 |
| 125 | SP1.31C R7 | Middle Sabbie di Imola Fm. | Tabular | -7,00 | -6,95 |
| 126 | SP1.31C R8 | Middle Sabbie di Imola Fm. | Tabular | -6,53 | -6,84 |
| 127 | SP1.31C R9 | Middle Sabbie di Imola Fm. | Tabular | -6,91 | -6,94 |
| 128 | SP1.31C R10 | Middle Sabbie di Imola Fm. | Tabular | -6,25 | -6,67 |
| 129 | SP1.31C C1 | Middle Sabbie di Imola Fm. | Tabular | -5,48 | -7,11 |
| 130 | SP1.31C C2 | Middle Sabbie di Imola Fm. | Tabular | -7,10 | -7,08 |

| | | | | | |
|---|---|---|---|---|---|
| 131 | SP1.31C C3 | Middle Sabbie di Imola Fm. | Tabular | -7,31 | -7,02 |
| 132 | SP1.31C C4 | Middle Sabbie di Imola Fm. | Tabular | -7,49 | -6,95 |
| 133 | SP1.31C C5 | Middle Sabbie di Imola Fm. | Tabular | -8,26 | -6,63 |
| 134 | SP1.31C C6 | Middle Sabbie di Imola Fm. | Tabular | -8,70 | -6,61 |
| 135 | SP1.31C C7 | Middle Sabbie di Imola Fm. | Tabular | -8,54 | -6,94 |
| 136 | SP1.31C C8 | Middle Sabbie di Imola Fm. | Tabular | -8,21 | -6,69 |
| 137 | SP1.33C R1 | Middle Sabbie di Imola Fm. | Nodular | -2,55 | -5,97 |
| 138 | SP1.33C R2 | Middle Sabbie di Imola Fm. | Nodular | -6,05 | -6,37 |
| 139 | SP1.33C R3 | Middle Sabbie di Imola Fm. | Nodular | -3,09 | -5,78 |
| 140 | SP1.33C R4 | Middle Sabbie di Imola Fm. | Nodular | -2,74 | -6,01 |
| 141 | SP1.33C R5 | Middle Sabbie di Imola Fm. | Nodular | -4,98 | -6,23 |
| 142 | SP1.33C R6 | Middle Sabbie di Imola Fm. | Nodular | -4,94 | -6,50 |
| 143 | SP1.33C R7 | Middle Sabbie di Imola Fm. | Nodular | -3,80 | -5,82 |
| 144 | SP1.33C R8 | Middle Sabbie di Imola Fm. | Nodular | -2,91 | -6,10 |
| 145 | SP1.33C C1 | Middle Sabbie di Imola Fm. | Nodular | -5,25 | -6,34 |
| 146 | SP1.33C C2 | Middle Sabbie di Imola Fm. | Nodular | -4,63 | -6,60 |
| 147 | SP1.33C C3 | Middle Sabbie di Imola Fm. | Nodular | -5,26 | -6,56 |
| 148 | SP1.33C C4 | Middle Sabbie di Imola Fm. | Nodular | -3,20 | -6,29 |
| 149 | SP1.33C C5 | Middle Sabbie di Imola Fm. | Nodular | -4,29 | -6,52 |
| 150 | SP1.33C C6 | Middle Sabbie di Imola Fm. | Nodular | -4,92 | -6,67 |
| 151 | SP1.33C C7 | Middle Sabbie di Imola Fm. | Nodular | -6,46 | -6,56 |
| 152 | SP1.33C C8 | Middle Sabbie di Imola Fm. | Nodular | -5,43 | -6,84 |
| 153 | SP1.34C R1 | Top Sabbie di Imola Fm. | Coalescent elongate | -6,69 | -7,07 |
| 154 | SP1.34C R2 | Top Sabbie di Imola Fm. | Coalescent elongate | -6,67 | -6,92 |
| 155 | SP1.34C R3 | Top Sabbie di Imola Fm. | Coalescent elongate | -6,49 | -7,10 |
| 156 | SP1.34C R4 | Top Sabbie di Imola Fm. | Coalescent elongate | -6,87 | -6,97 |
| 157 | SP1.34C R5 | Top Sabbie di Imola Fm. | Coalescent elongate | -6,44 | -6,78 |
| 158 | SP1.34C R6 | Top Sabbie di Imola Fm. | Coalescent elongate | -6,43 | -7,11 |
| 159 | SP1.34C R7 | Top Sabbie di Imola Fm. | Coalescent elongate | -6,61 | -7,16 |
| 160 | SP1.34C R8 | Top Sabbie di Imola Fm. | Coalescent elongate | -6,77 | -6,91 |
| 161 | SP1.34C R9 | Top Sabbie di Imola Fm. | Coalescent elongate | -6,78 | -7,03 |
| 162 | SP1.34C R10 | Top Sabbie di Imola Fm. | Coalescent elongate | -6,48 | -7,19 |
| 163 | SP1.34C C1 | Top Sabbie di Imola Fm. | Coalescent elongate | -6,16 | -6,84 |
| 164 | SP1.34C C2 | Top Sabbie di Imola Fm. | Coalescent elongate | -6,34 | -7,02 |
| 165 | SP1.34C C3 | Top Sabbie di Imola Fm. | Coalescent elongate | -6,62 | -7,17 |
| 166 | SP1.38C R1 | Top Sabbie di Imola Fm. | Coalescent elongate | -4,74 | -6,49 |
| 167 | SP1.38C R2 | Top Sabbie di Imola Fm. | Coalescent elongate | -4,87 | -6,67 |
| 168 | SP1.38C R3 | Top Sabbie di Imola Fm. | Coalescent elongate | -4,48 | -6,52 |
| 169 | SP1.38C R4 | Top Sabbie di Imola Fm. | Coalescent elongate | -4,97 | -6,95 |
| 170 | SP1.38C R5 | Top Sabbie di Imola Fm. | Coalescent elongate | -4,51 | -6,57 |
| 171 | SP1.38C R6 | Top Sabbie di Imola Fm. | Coalescent elongate | -4,78 | -6,97 |
| 172 | SP1.38C R7 | Top Sabbie di Imola Fm. | Coalescent elongate | -4,59 | -6,85 |
| 173 | SP1.38C R8 | Top Sabbie di Imola Fm. | Coalescent elongate | -4,70 | -6,46 |
| 174 | SP1.38C R9 | Top Sabbie di Imola Fm. | Coalescent elongate | -5,07 | -6,98 |
| 175 | SP1.38C R10 | Top Sabbie di Imola Fm. | Coalescent elongate | -5,04 | -7,18 |
| 176 | SP1.38C R11 | Top Sabbie di Imola Fm. | Coalescent elongate | -4,67 | -6,92 |
| 177 | SP1.38C R12 | Top Sabbie di Imola Fm. | Coalescent elongate | -4,68 | -6,59 |

| | | | | | |
|---|---|---|---|---|---|
| 178 | SP1.38C R13 | Top Sabbie di Imola Fm. | Coalescent elongate | -5,07 | -7,12 |
| 179 | SP1.38C C1 | Top Sabbie di Imola Fm. | Coalescent elongate | -5,11 | -6,28 |
| 180 | SP1.38C C2 | Top Sabbie di Imola Fm. | Coalescent elongate | -5,22 | -6,54 |
| 181 | SP1.38C C3 | Top Sabbie di Imola Fm. | Coalescent elongate | -4,88 | -6,62 |
| 182 | SP1.38C C4 | Top Sabbie di Imola Fm. | Coalescent elongate | -4,79 | -6,89 |
| 183 | SP1.38C C5 | Top Sabbie di Imola Fm. | Coalescent elongate | -4,73 | -6,82 |
| 184 | SP1.38C C6 | Top Sabbie di Imola Fm. | Coalescent elongate | -6,25 | -6,65 |

**Table 2.A1.** Isotopic data acquired from concretion hand samples collected in different positions along the investigated succession. Data are referred to the international standard V-PDB. The analytical precision upon carbon isotopes determination is 0.10‰ V-PDB, while on oxygen isotopes is 0.15‰.

TABLE 2.A2: ISOTOPIC DATA FROM MICROMILL SAMPLING ON THIN SECTIONS

| Sample n° | Sample name | Stratigraphic position | Concretion type | Cement type | $d^{13}C$ (‰ VPDB) | $d^{18}O$ (‰ VPDB) |
|---|---|---|---|---|---|---|
| 1 | SP1.3C 1 | Transition AZ-SI Fms. | Single elongate | C2 | -6,60 | -6,29 |
| 2 | SP1.3C 2 | Transition AZ-SI Fms. | Single elongate | C2 | -6,37 | -6,20 |
| 3 | SP1.3C 3 | Transition AZ-SI Fms. | Single elongate | C2 | -5,41 | -6,14 |
| 4 | SP1.3C 4 | Transition AZ-SI Fms. | Single elongate | C2 | -6,78 | -5,95 |
| 5 | SP1.3C 5 | Transition AZ-SI Fms. | Single elongate | C2 | -7,26 | -6,35 |
| 6 | SP1.18C 1 | Base Sabbie di Imola Fm. | Tabular | C1 | -6,86 | -7,31 |
| 7 | SP1.18C 2 | Base Sabbie di Imola Fm. | Tabular | C1 | -6,45 | -7,44 |
| 8 | SP1.18C 3 | Base Sabbie di Imola Fm. | Tabular | C2 | -6,41 | -7,00 |
| 9 | SP1.18C 4 | Base Sabbie di Imola Fm. | Tabular | C1 | -8,13 | -7,27 |
| 10 | SP1.18C 5 | Base Sabbie di Imola Fm. | Tabular | C2 | -6,45 | -6,91 |
| 11 | SP1.24C 1 | Base Sabbie di Imola Fm. | Tabular | C1 | -5,15 | -7,30 |
| 12 | SP1.24C 2 | Base Sabbie di Imola Fm. | Tabular | C2 | -6,55 | -7,42 |
| 13 | SP1.24C 3 | Base Sabbie di Imola Fm. | Tabular | C1 | -5,60 | -7,55 |
| 14 | SP1.24C 4 | Base Sabbie di Imola Fm. | Tabular | C1 | -6,78 | -7,08 |
| 15 | SP1.24C 5 | Base Sabbie di Imola Fm. | Tabular | C1 | -6,18 | -6,93 |
| 16 | SP1.27C 1 | Base Sabbie di Imola Fm. | Tabular | C2 | -5,56 | -6,62 |
| 17 | SP1.27C 2 | Base Sabbie di Imola Fm. | Tabular | C2 | -5,71 | -6,74 |
| 18 | SP1.27C 3 | Base Sabbie di Imola Fm. | Tabular | C1 | -5,42 | -6,87 |
| 19 | SP1.27C 4 | Base Sabbie di Imola Fm. | Tabular | C1 | -5,81 | -7,09 |
| 20 | SP1.27C 5 | Base Sabbie di Imola Fm. | Tabular | C2 | -6,36 | -7,12 |
| 21 | SP1.29C 1 | Middle Sabbie di Imola Fm. | Single elongate | C2 | -4,52 | -6,64 |
| 22 | SP1.29C 2 | Middle Sabbie di Imola Fm. | Single elongate | C2 | -4,39 | -7,05 |
| 23 | SP1.29C 3 | Middle Sabbie di Imola Fm. | Single elongate | C1 | -5,13 | -7,68 |
| 24 | SP1.29C 4 | Middle Sabbie di Imola Fm. | Single elongate | C2 | -4,80 | -7,07 |
| 25 | SP1.29C 5 | Middle Sabbie di Imola Fm. | Single elongate | C1 | -5,31 | -7,29 |
| 26 | SP1.31C 1 | Middle Sabbie di Imola Fm. | Tabular | C1 | -6,96 | -7,39 |
| 27 | SP1.31C 2 | Middle Sabbie di Imola Fm. | Tabular | C1 | -7,62 | -7,04 |
| 28 | SP1.31C 3 | Middle Sabbie di Imola Fm. | Tabular | C1 | -6,66 | -7,16 |
| 29 | SP1.31C 4 | Middle Sabbie di Imola Fm. | Tabular | C2 | -6,39 | -7,36 |
| 30 | SP1.31C 5 | Middle Sabbie di Imola Fm. | Tabular | C2 | -6,49 | -7,44 |
| 31 | SP1.33C 1 | Middle Sabbie di Imola Fm. | Nodular | C2 | -4,50 | -7,09 |

| | | | | | | |
|---|---|---|---|---|---|---|
| 32 | SP1.33C 2 | Middle Sabbie di Imola Fm. | Nodular | C2 | -6,06 | -7,40 |
| 33 | SP1.33C 3 | Middle Sabbie di Imola Fm. | Nodular | C2 | -5,93 | -8,49 |
| 34 | SP1.33C 4 | Middle Sabbie di Imola Fm. | Nodular | C2 | -4,85 | -7,42 |
| 35 | SP1.33C 5 | Middle Sabbie di Imola Fm. | Nodular | C2 | -5,56 | -7,52 |
| 36 | SP1.34C 1 | Top Sabbie di Imola Fm. | Coalescent elongate | C1 | -8,86 | -7,62 |
| 37 | SP1.34C 2 | Top Sabbie di Imola Fm. | Coalescent elongate | C1 | -7,13 | -7,09 |
| 38 | SP1.34C 3 | Top Sabbie di Imola Fm. | Coalescent elongate | C2 | -5,33 | -7,16 |
| 39 | SP1.34C 4 | Top Sabbie di Imola Fm. | Coalescent elongate | C2 | -5,44 | -7,31 |
| 40 | SP1.34C 5 | Top Sabbie di Imola Fm. | Coalescent elongate | C1 | -6,89 | -9,14 |
| 41 | SP1.38C 1 | Top Sabbie di Imola Fm. | Coalescent elongate | C1 | -5,81 | -6,79 |
| 42 | SP1.38C 2 | Top Sabbie di Imola Fm. | Coalescent elongate | C2 | -4,52 | -6,94 |
| 43 | SP1.38C 3 | Top Sabbie di Imola Fm. | Coalescent elongate | C1 | -6,33 | -7,12 |
| 44 | SP1.38C 4 | Top Sabbie di Imola Fm. | Coalescent elongate | C2 | -4,57 | -7,28 |
| 45 | SP1.38C 5 | Top Sabbie di Imola Fm. | Coalescent elongate | C2 | -5,34 | -7,43 |

**Table 2.A2.** Isotopic data gained with the micromill sampling on thin sections. Data are referred to the international standard V-PDB. The analytical precision upon carbon isotopes determination is 0.10‰ V-PDB, while on oxygen isotopes is 0.15‰. C1, blocky zoned calcite; C2, fine equant sparitic calcite.

TABLE 2.A3: STATISTICAL ANALYSIS ON CEMENT C1 AND C2 FROM MICROMILL

Single elongate concretions

| | C1 $\delta^{13}C$ (‰ VPDB) | C2 $\delta^{13}C$ (‰ VPDB) | C1 $\delta^{18}O$ (‰ VPDB) | C2 $\delta^{18}O$ (‰ VPDB) |
|---|---|---|---|---|
| Data N | 3 | 13 | 3 | 13 |
| Mean | -5,23 | -5,62 | -7,49 | -5,95 |
| Standard Error | 0,053 | 0,266 | 0,113 | 0,2 |
| Standard Deviation | 0,092 | 0,965 | 0,195 | 0,72 |
| Shapiro-Wilk p(normal) | 0,64 (64%) | 0,39 (39%) | 0,91 (91%) | 0,35 (35%) |
| F test p(same var) | 0,018 (1,8%) | | 0,14 (14%) | |
| t test p(same mean) | 0,178 (17,8%) | | 0,022 (2,2%) | |

Coalescent elongate concretions

| | C1 $\delta^{13}C$ (‰ VPDB) | C2 $\delta^{13}C$ (‰ VPDB) | C1 $\delta^{18}O$ (‰ VPDB) | C2 $\delta^{18}O$ (‰ VPDB) |
|---|---|---|---|---|
| Data N | 5 | 5 | 5 | 5 |
| Mean | -6,67 | -5,46 | -7,1 | -7,29 |
| Standard Error | 0,302 | 0,425 | 0,097 | 0,092 |
| Standard Deviation | 0,678 | 0,951 | 0,217 | 0,206 |
| Shapiro-Wilk p(normal) | 0,99 (99%) | 0,18 (18%) | 0,9 (90%) | 0,08 (8%) |
| F test p(same var) | 0,53 (53%) | | 0,92 (92%) | |
| t test p(same mean) | 0,05 (5%) | | 0,19 (19%) | |

Tabular concretions

| | C1 $\delta^{13}C$ (‰ VPDB) | C2 $\delta^{13}C$ (‰ VPDB) | C1 $\delta^{18}O$ (‰ VPDB) | C2 $\delta^{18}O$ (‰ VPDB) |
|---|---|---|---|---|
| Data N | 12 | 8 | 12 | 8 |

| | | | | |
|---|---|---|---|---|
| Mean | -6,78 | -5,7 | -7,36 | -7,07 |
| Standard Error | 0,272 | 0,169 | 0,172 | 0,111 |
| Standard Deviation | 0,943 | 0,478 | 0,6 | 0,313 |
| Shapiro-Wilk p(normal) | 0,32 (32%) | 0,13 (13%) | 0,0004 (0,04%) | 0,93 (93%) |
| F test p(same var) | 0,082 (8,2%) | | 0,096 (9,6%) | |
| t test p(same mean) | 0,003 (0,3%) | | 0,174 (17,4%) | |

**Table 2.A3.** Statistical analysis to assess difference or similarities of C1 and C2 cement isotopic data obtained by micromill sampling. Difference between dataset was assessed evaluating the probability to gain the same mean value with the t-Student test p(same mean) comparing $\delta^{13}C$ and $\delta^{18}O$ in both cement patterns.

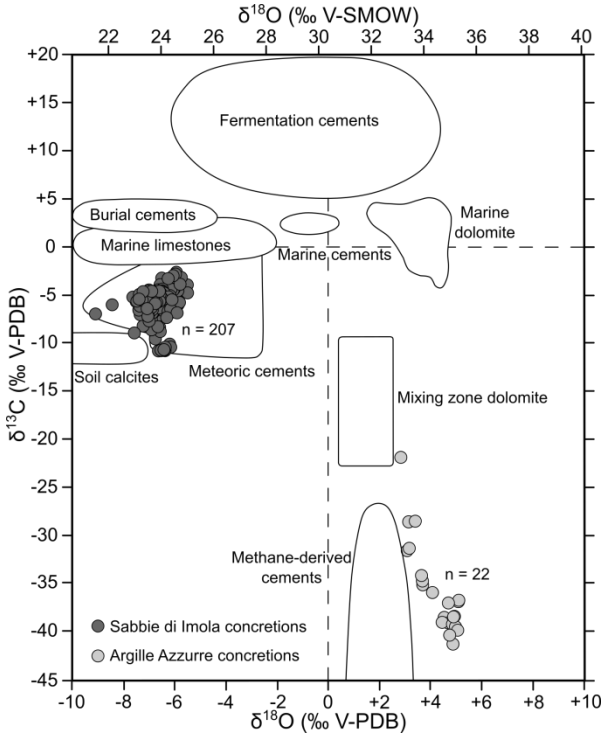


**Fig. 2.A1.** Overview of $\delta^{18}O$ and $\delta^{13}C$ values obtained from studied concretions and their comparison with major carbonate cement fields introduced by Nelson & Smith (1996). Carbonate concretions within the Sabbie di Imola Fm. are located in the meteoric cement field, while chimneys inside the Argille Azzurre Fm. are close to the methane-derived cement field.

## Supplementary Material 2: Cement SEM Images

SEM images help in better defining and understanding the cementation sequence recorded inside concretions. The complete diagenetic history can be reconstructed where fossil shells occur (Fig. 2.A2a). On the outer edge of the shells isopachous equant calcite rim typically occurs (Cr). This first cement is then followed by the pore-lining and pore-filling fine-grained mosaic sparite (Cm). Third cementation stage is characterized by the blocky-coarse sparitic calcite and syntaxial overgrowths (C1), while fine sparite (C2) composing the last cement seems to postdate C1. Within calcite cement crystals inside foraminifera and mollusc shells it is locally possible to recognize clusters of almost spherical bodies, 1-2 µm in diameter, which could represent cells of bacteria (Fig. 2.A2a). Bacteria hosted close to Cr and Cm cements could have partially influenced the cementation during the early stages of the diagenetic history. However, their occurrence is sparse and not widespread so that bacteria likely played a minor role in facilitating cementation. The acquired images allow to better constrain the cementation sequence between C1 and C2 cements within tabular (Fig. 2.A2b), elongate coalescent (Fig. 2.A2c), and elongate single (Fig. 2.A2d) concretions. In all samples cement type C1 seems to predate C2.

## Supplementary Material 3: Grain Size Analysis

All the 40 grain size analyses were performed with a Mastersizer 3000 laser particle analyser (Malvern Instruments) equipped with a Hydro EV wet dispersion unit. The

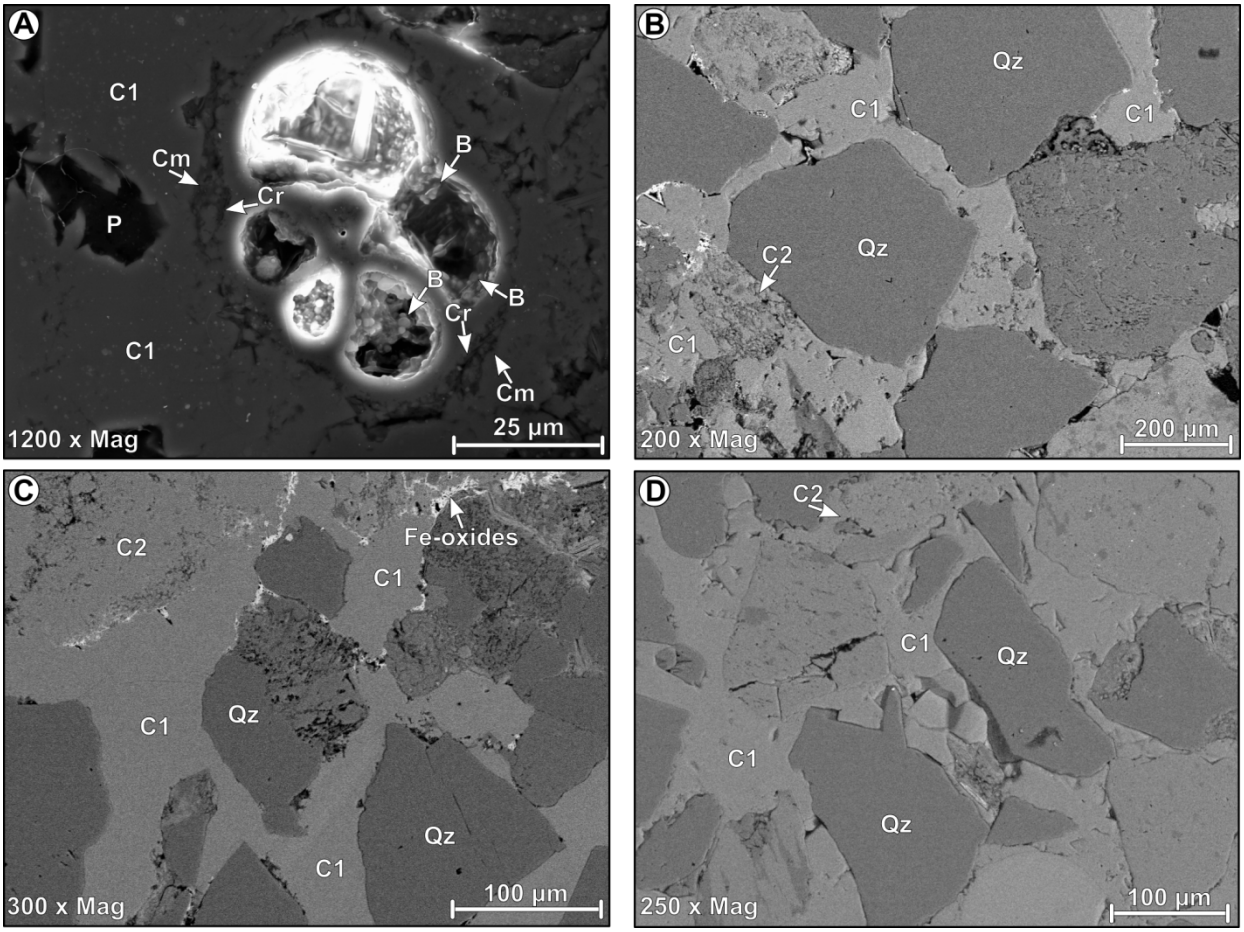


**Fig. 2.A2.** (**a**) Secondary electrons photomicrograph of the cementation sequence with equant rim (Cr), meniscus (Cm) and blocky calcite (C1) around foraminifera shell. Inside foraminifera chambers, clusters of spherical bodies with diameter of 1-2 µm similar to bacteria are present. (**b**) Backscatter image of blocky (C1) and fine sparitic (C2) calcite cements inside a tabular concretion sample. (**c**) Backscatter image of fine equant sparitic calcite (C2) postdating blocky calcite (C1) inside an elongate coalescent concretion. (**d**) Backscatter image of blocky (C1) and fine sparitic calcite (C2) within an elongate single concretion. Qz, quartz; P, porosity; B, bacteria; Fe-oxides, Fe-Ti oxides and hydroxides grain coating.

analytical range spans from 0.1 to 3500 µm. De-ionized water was used as dispersant fluid. All samples were previously dried in an oven with a constant temperature of 40°C for 48 hours to completely remove moisture. Sediment samples were subdivided in two sets according to their lithology: (1) medium-fine sand and (2) silty clay. For each lithology, a specific standard operative procedure (SOP) was developed with the aim of providing the best final grain size distribution (GSD) by minimizing sample alteration during the analysis. Medium-fine sand samples were first sieved at 2000 µm to remove coarser particles and impurities and then were split with Quantachrome macro and micro rifflers to gain the proper aliquot necessary to run the analysis. Cohesive silty clay samples were dissolved in de-calcified water for 24 hours to allow the chemical disaggregation of clay assemblages.

Several tests were performed to investigate the influence of analytical settings on final grain size distribution according to the method proposed by Storti and Balsamo (2010). The first test consisted in defining the proper stirrer speed necessary to efficiently analyse all size classes. To this end, we started with the lowest pump speed (500 rpm) and then increased it up to the

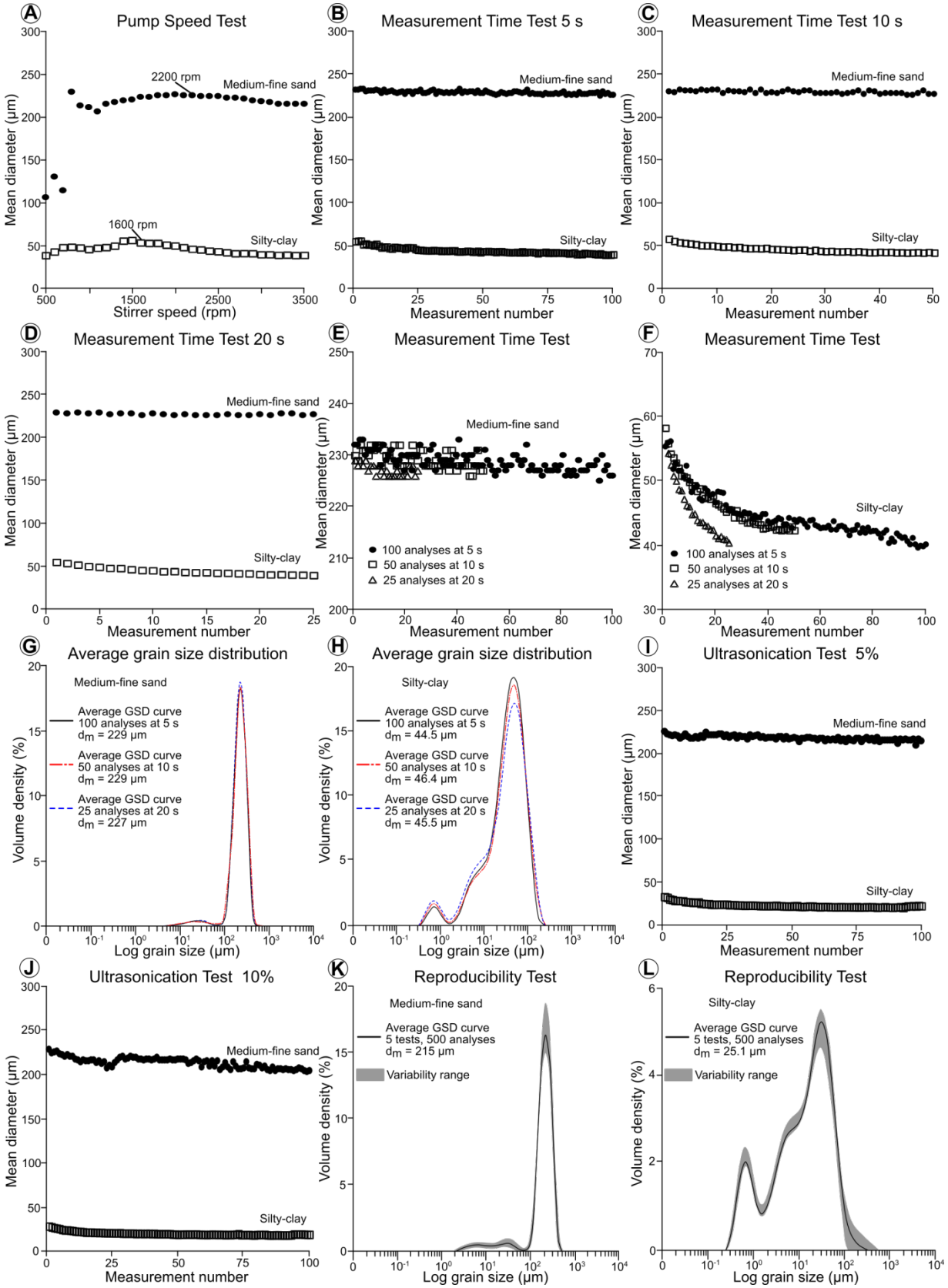


**Fig. 2.A3.** Grain size analysis standard operative procedures (SOP) and performed tests. (**a**) Stirrer speed test for sand and silty clay samples. Measurement time test at 5 s (**b**), 10 s (**c**) and 20 s (**d**). Comparison of the measurement time tests regarding sand (**e**) and silty clay samples (**f**). Average grain size distribution for sand (**g**) and silty clay samples (**h**). Ultrasonication test performed at 5% (**i**) and 10% intensity (**j**). Reproducibility test showing the grain size distribution of medium-fine sand (**k**) and silty clay samples (**l**).

maximum achievable (3500 rpm), by progressive incremental steps of 100 rpm. At low pump speed, grain size distributions are shifted towards finer particles, because the stirrer is not able to mobilize coarser particles remaining on the bottom of the beacker. With gradual pump speed increase, grain size distributions show a shift towards coarser particles, which abruptly occurs at 700-800 rpm for medium-fine sand and, more gradually around 1400 rpm in silty clay samples. Further stirrer speed increase leads to stable plateau of mean diameters from 1900 rpm to 2500 rpm in the case of medium-fine sand, and from 1600 rpm to 1800 rpm for silty clay. With extremely high pump speed, mean diameters slightly decrease from plateau values. The optimal stirrer speed was selected inside the mean diameters stable plateau, thus avoiding the fine-ward and coarse-ward biases. In particular, the pump speed adopted in analyzing medium to fine sand was 2200 rpm, while the one used for silty clay was 1600 rpm (Fig. 2.A3a). The second test was aimed to determine the measurement time required for each analysis. We tested three different configurations: (1) 100 measurements, each of them with a duration of 5 s (Fig. 2.A3b); (2) 50 measurements at 10 s (Fig. 2.A3c); (3) 25 measurements at 20 s (Fig. 2.A3d). In this way samples were kept inside the beacker for the same duration of time. Graph comparison shows that measurement time did not influence the final sand and silty clay GSDs (Fig. 2.A3e-f-g-h), hence we proceeded performing 100 analyses at 5 s. The possible influence of ultrasonication was tested at two different intensities: 5% (Fig. 2.A3i) and 10% (Fig. 2.A3j). Ultrasonication helps keeping separated clay minerals, but at the same time, can induce severe biasing of particle size by opening pre-existing fractures and decreasing mean diameters. Silty clay samples show a rapid decrease in mean diameters at the beginning of the ultrasonication test and then it stabilizes to constant values. Conversely, sand samples are characterized by a progressive decrement of mean diameters throughout all the test. Such a decrease is more evident at 10% of ultrasonication intensity. Therefore, we decided to use 2% ultrasonication intensity for sand samples, just to remove the fine oxide coating around clasts, and 25% intensity for 10 minutes to stabilize mean diameter of silty clay samples and then lowering it to 2% during the analysis in order to prevent clay flocculation. The last test consisted in verifying the reproducibility of the identified SOPs by repeating 5 different analyses with the same settings. Medium-fine sand samples were tested with a stirrer speed of 2200 rpm, 100 measurements at 5 s with 2% of ultrasonication intensity (Fig. 2.A3k). Silty clay SOP reproducibility test was performed with a pump speed of 1600 rpm, 100 measurements at 5 s, ultrasonication at 2% throughout all the analysis after 10 minutes with 25% intensity to stabilize the mean diameter (Fig. 2.A3l). Graphs show that both SOPs are characterized by small variation range around the mean diameter thus testifying the quality of the adopted procedures.

**Supplementary Material 4: Permeability Measurements**

30 permeability measurements were recorded on each medium-fine grained sand strata, while on silt and clay rich strata only 5

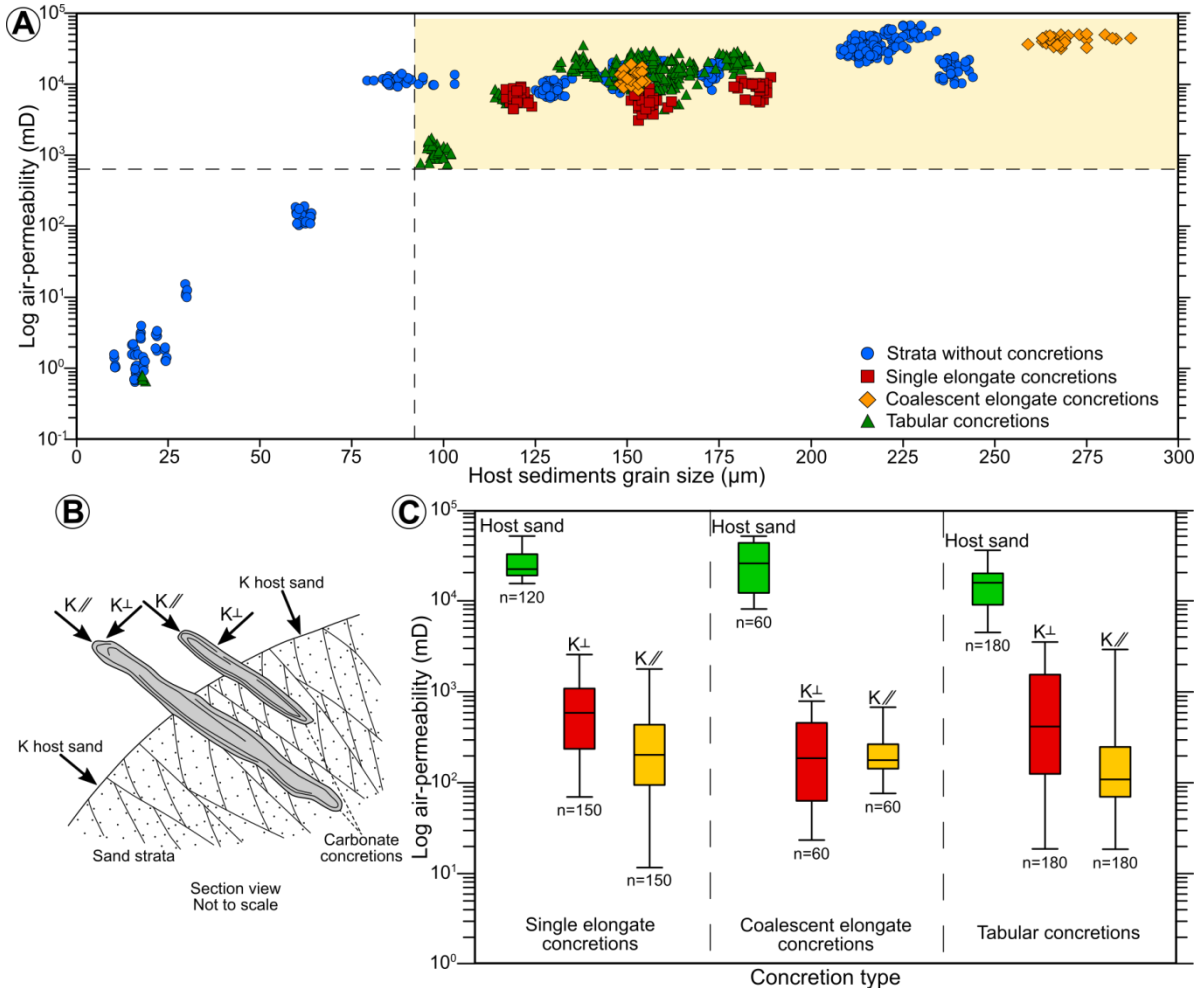


**Fig. 2.A4.** (**a**) Grain size (μm) vs Log permeability (mD) graph based on the petrophysical data measured on the host sediments. Several fields can be identified corresponding to different concretion types and morphologies. Permeability and grain size lower thresholds are also shown as dashed lines. (**b**) Simplified sketch showing the adopted permeability measurement directions upon concretionary bodies and loose sediments. (**c**) Permeability comparison between host sand and different types of carbonate concretions (elongate single, coalescent and tabular bodies).

measurements were collected due to their consistency, as indicated by the low standard deviation characterizing all measurements. Permeability measurements were performed upon relatively unaltered strata, trying to avoid any secondary alterations such as the presence of Fe-hydroxides which may alter permeability values. Generally, in the analysed section (Fig. 2.4d), as expected, there is a strong correlation between grain size and permeability with silty clay strata having the lowest mean grain size and permeability values, while medium-fine sand showing a coarse grain size and higher permeability. Grain size and permeability data plotted versus concretion types allow identifying clusters corresponding to the different types of concretions (Fig. 2.A4a, b). Tabular concretions occur over a slightly wider range of grain size with respect to single elongate ones. It is also possible to recognize grain size and permeability thresholds below which diagenetic concretions basically did not develop (i.e. grain size of 90 μm and a permeability value of about 600-700 mD) (Fig. 2.A4a). Permeability measured within the diagenetic bodies parallel to the concretion dip direction and perpendicular to it (Fig. 2.A4a) shows a drop of 2-3 orders of magnitude with respect

to the weakly cemented hosting sand (Fig. 2.A4c).

# CHAPTER 3

## Structural and Diagenetic Evolution of the Rocca di Neto Fault Zone

This chapter describes the structural evolution of the extensional Rocca di Neto fault zone, Crotone Basin. The fault zone affects poorly cemented Pleistocene siliciclastic sediments and is characterized by occurrence of soft-sediment deformation in the form of deformation bands, clusters of bands and gouges. The evolution of the fault zone is determined by the combination of tectonic compaction and selective cementation leading to a pronounced strain-hardening behaviour at the scale of the entire fault zone. The relative timing of deformation has been constrained by the study of the cementation pattern along the structural domains composing the fault zone.

*Physical and chemical strain-hardening, kinematically-induced stress, and strain delocalization-localization stages during faulting in poorly lithified sandstone (Crotone Basin, Southern Apennines, Italy)*

Pizzati, M., Balsamo, F., Storti, F., Iacumin, P.

This manuscript is currently in preparation for submission to the *Geological Society of America Bulletin*.

# Physical and chemical strain-hardening, kinematically-induced stress, and strain delocalization-localization stages during faulting in poorly lithified sandstone (Crotone Basin, Southern Apennines, Italy)

Mattia Pizzati[1], Fabrizio Balsamo[1], Fabrizio Storti[1], and Paola Iacumin[2]

[1] NEXT, Natural and Experimental Tectonics Research Group, Department of Chemistry, Life Sciences, and Environmental Sustainability, University of Parma, 43124 Parma, Italy.

[2] Department of Chemistry, Life Sciences, and Environmental Sustainability, University of Parma, 43124 Parma, Italy.

## Abstract

In this work, we report the results of a multidisciplinary study describing the structural architecture and diagenetic evolution of the Rocca di Neto extensional fault zone developed in the poorly lithified sediments of the Crotone Basin, Southern Italy. The studied fault zone has an estimated displacement of about 90 m and consists of: (1) a low-deformation zone with subsidiary faults and widely spaced deformation bands; (2) a ~ 10 m-thick damage zone, characterized by a dense network of conjugate deformation bands; (3) a ~ 3 m-thick mixed zone produced by tectonic mixing of sediments with different grain size; (4) a ~ 1 m-thick fault core with bedding transposed into foliation and ultra-comminuted black gouge layers. Microstructural investigations indicates that particulate flow was the dominant early-stage deformation mechanism, while cataclasis became predominant after porosity loss, shallow burial, and selective calcite cementation. The combination of tectonic compaction and preferential cementation led to a strain-hardening behavior inducing the formation of "inclined conjugate deformation band sets" inside the damage zone, caused by the kinematic stress field associated with fault activity. Conversely, conjugate deformation band sets with a vertical bisector formed outside the damage zone, in response to the regional extensional stress field. Stable isotope analysis helped constraining the diagenetic environment of deformation, which is characterized by mixed marine-meteoric signatures for cements hosted inside the damage zone, while it progressively becomes more meteoric moving outside the fault zone. This evidence supports the outward propagation of fault-related deformation in the footwall damage zone.

### 3.1. Introduction

Understanding the mechanical behavior of faulted sediments and high porosity

sandstones has a primary impact on the improvement of conceptual models of faulting at very shallow depth, including both coseismic rupture propagation and slow earthquakes (Scholz, 1998; Gratier et al., 2011; Ozawa et al., 2011; Yamaguchi et al., 2011; Imanishi et al., 2012; Kodaira et al., 2012; Fagereng et al., 2014). This is particularly true for the response of materials to incremental deformation, i.e. whether sediments have a strain-hardening behavior with shearing and what are the controlling factors. Strain-hardening characterizes materials that show an increasing resistance to deformation with progressive increments of stress and strain (e.g., Fossen, 2010). It occurs within the inelastic deformation field and is responsible for the shift to higher stress-strain values of the yield point of the deforming material (Mair et al., 2000). Strain-hardening in granular materials such as high-porosity sandstones and poorly lithified sediments, promotes the switch of deformation in the surrounding undeformed sediments, rather than persisting on pre-existing deformation structures, which become stronger and less easy to be re-activated (Aydin and Johnson, 1978; Mair et al., 2000; Fossen et al., 2017). Such deformation structures typically consist of deformation bands of different type and geometry (e.g., Friedman and Logan, 1973; Aydin, 1978; Antonellini et al., 1994; Cashman and Cashman, 2000; Wilson et al., 2003; Torabi and Fossen, 2009; Fossen et al., 2017).

Progressive strain-hardening behavior commonly leads to the formation of clusters of closely-spaced deformation bands that, after reaching a threshold thickness, eventually fail internally to develop preferential slip surfaces that accommodate additional strain (Aydin and Johnson, 1978, 1983; Antonellini et al., 1994; Nicol et al., 2013; Soliva et al., 2016). Strain-hardening is therefore responsible for early-stage delocalization of deformation, and late-stage localization on discrete slip surfaces. Shear localization in loose material is expected to increase the kinematically-induced shear stress field (e.g., Davis et al., 2012) along the fault zone to eventually overcome the strength of sediments and produce shear-related deformation structure arrays (Logan et al., 1979; Hancock, 1985; Sylvester, 1988).

Fault damage zones can form at this stage, where stratigraphic features are preserved and deformation bands are abundant, surrounding thin fault cores, where most fault slip is accommodated (Shipton and Cowie, 2001, 2003; Davatzes et al., 2005; Williams et al., 2016). When fault displacement exceeds bedding thickness, mixed zones may form between fault cores and damage zones (Heynekamp et al., 1999; Rawling and Goodwin, 2006; Loveless et al., 2011).

Transition from shear delocalization to localization may correspond to a switch from dominant aseismic slip and possibly slow earthquakes, typically associated with deformation banding (Fossen et al., 2017), to coseismic slip producing thin layers of black gouge (Balsamo et al., 2014; Ujiie and Kimura, 2014). However, in some cases, black gouges can form in pristine sediments without the strain-hardening effect caused by deformation bands in damage zones (Balsamo and Storti, 2011).

Deformation bands and fault zones strongly influence the hydrological behavior of poorly lithified sediments and high porosity sandstones, typically providing barriers to fluid flow (e.g., Antonellini and Aydin, 1994;

Main et al., 2000; Ogilvie and Glover, 2001; Sternlof et al., 2004; Balsamo and Storti, 2010; Ballas et al., 2012). Porosity collapse produced by both failure of sedimentary grain packing and grain size reduction by cataclasis, can favor selective cementation along deformation bands and fault cores (Balsamo et al., 2012). Such a preferential structural diagenesis can dramatically alter the mechanical behavior of deformation bands and fault zones. It follows that, in many cases, a combination of physical and chemical processes drives the evolution of strain-hardening in high-porosity sediments during faulting and, hence, the evolution of fault frictional properties.

To obtain further information on the somehow poorly constrained interaction between deformation and selective cementation at very shallow depth, we studied in detail the cross-sectional architecture of the Rocca di Neto extensional fault zone, developed in quartz-feldspathic high-porosity sandstone of the Crotone Basin, in Southern Italy. The basin provides very good exposures of extensional fault zones affecting loose sandstone, and many of them are characterized by abundant carbonate concretions both in damage zones and fault cores (Balsamo et al., 2012). The structure of the Rocca di Neto fault was described by mesoscopic and microscopic investigations, whereas the cementation history was constrained by petrographic and stable isotope analysis, to determine the overall evolution of the fault zone during slip and exhumation.

### 3.2. Geological Framework

The Rocca di Neto extensional fault zone is located in the Crotone forearc basin, which developed since Middle Miocene times during the SE-ward migration of the Calabrian Arc, in the Southern Apennines of Italy (Knott and Turco, 1991; Van Dijk and Scheepers, 1995; Van Dijk et al., 2000; Zecchin et al., 2004, 2012) (Fig. 3.1a, b). The interaction between subduction of the Adria-Ionian plate underneath the European plate, and back-arc spreading in the Tyrrhenian sea, was responsible for the onset of different tectonic regimes during basin formation and infilling (Polonia et al., 2011; Reitz and Seeber, 2012; Massari and Prosser, 2013). Since Lower Pliocene times, the basin underwent at least five subsidence-uplift cycles, induced by the interplay between subduction-related contraction and back-arc extension, being the latter the dominant tectonic regime (Van Dijk, 1994; Van Dijk and Scheepers, 1995; Ferranti et al., 2009; Zecchin et al., 2012; Massari and Prosser, 2013), particularly since Middle Pleistocene times (Antonioli et al., 2006; Zecchin et al., 2012).

The Crotone Basin is bounded to the north and to the south by the NW-SE-trending Rossano-San Nicola and Petilia-Policastro left-lateral strike-slip fault zones (Van Dijk, 1994; Zecchin et al., 2004; Galli and Scionti, 2006) (Fig. 3.1b). In the central part of the basin, several NE-SW-trending extensional fault zones are interpreted to be formed during the last extensional event (Antonioli et al., 2006; Massari and Prosser, 2013). Basin infilling started with deposition of the San Nicola dell'Alto conglomerates in an alluvial setting. They are overlain by the deep-marine Ponda clay (Fig. 3.1c). Olistostrome and radiolarite deposits (Tripoli Formation) preceded the deposition of the Lower and

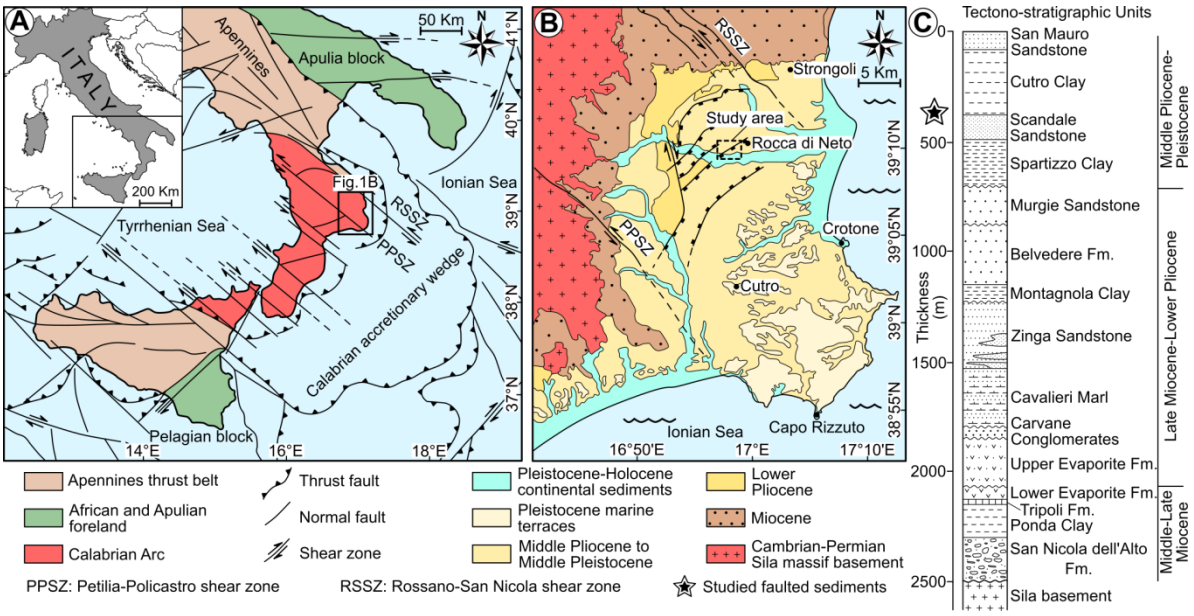


**Fig. 3.1**. (**a**) Regional setting of the calabrian arc and related accretionary wedge (after Van Dijk et al., 2000). (**b**) Geological map of the Crotone Basin (modified after Zecchin et al., 2012). (**c**) Stratigraphic succession of the entire Crotone Basin (modified from Balsamo et al., 2012).

Upper Evaporite Formation, unconformably overlain by the Carvane continental conglomerates (Fig. 3.1c). An abrupt change of the depositional environment is indicated by the overlying Cavalieri deep-water marls, followed up-section by the Zinga sandstone, which testifies to a shoaling upward evolution. The Zinga sandstone is overlain by the lagoon Montagnola clay, passing to the sandstone-dominated, shallow-water Belvedere and Murgie Formations. Further up, the Spartizzo clay deposited again in a lagoon environment, is laterally interfingered with the Scandale shoreface sandstone, which is in turn overlain by the offshore deep-marine Cutro clay (Fig. 3.1c). The latest basin infill is provided by the San Mauro sandstone, recording tectonic uplift and the consequent shift from a shallow-marine to a continental depositional environment. During the entire infilling history of the Crotone Basin, sediment supply was mainly provided by the erosion of the metamorphic basement rocks exposed in the adjacent Sila massif since the first stages of basin formation (Van Dijk et al., 2000; Zecchin et al., 2004, 2012). The Rocca di Neto fault zone juxtaposes the Cutro clay in the hangingwall, against the poorly lithified Scandale sandstone in the footwall. In particular, we focused on deformation structures well exposed in the fault footwall. The Scandale sandstone is mainly composed of quartz, K-feldspar, plagioclase and lithic fragments. Lithics mainly consist of gneiss and granitic rock fragments; biotite and muscovite micas also occur. Other accessory minerals are Fe-Ti oxides, and detrital and biogenic calcite (shell fragments). Cement is generally absent and interparticle porosity is high.

### 3.3. Analytical Methods

To investigate on the type and density of deformation bands and faults exposed in the footwall of the Rocca di Neto extensional fault zone, we constructed a 64 m-long, detailed geological cross-section throughout the entire fault footwall. The CF parameter was used to quantify deformation band

density (Soliva et al., 2016). It is defined as follows:

$$CF = \sqrt{\frac{\sum f_i^2}{\sum f_i} - f_{av}}. \quad (1)$$

where *CF* stands for clustering factor, $f_i$ is the density of bands per meter at the $i^{th}$ meter of the scan-line, and $f_{av}$ is the average band density along the entire scan-line.

Hand samples were collected in different positions along the fault zone to obtain 55 polished thin sections impregnated with blue-dyed resin to facilitate porosity estimations. Among them, 25 thin sections were obtained from carbonate concretion samples and stained with a solution of Alizarin Red S and potassium ferricyanide to determine the nature of carbonate cement (calcite vs dolomite; Dickson, 1966). Petrographic investigations on thin sections were performed with a standard petrography microscope (Zeiss Axioplan 2) and on scanned high-resolution images of the entire thin section areas (Nikon SuperCoolScan 5000). A cold cathodoluminescence apparatus (CITL CL Mk5-2 operating setting 250 µA and 10 kV) was used to investigate in detail generations and spatial distribution of cements. Detailed photomicrographs of cement and microstructures were acquired with a JEOL JSM 6400 Scanning Electron Microscope (SEM) (with operating setting 240 nA and 20 kV).

Carbon and oxygen stable isotope analysis was performed on small powder amounts extracted from concretion fresh cuts using a dental drill. Two sampling transects were made on each concretionary body, parallel and orthogonal to the basal surface, respectively. Sampling distance was 1.0 cm for surface-parallel transects and 1.0 or 0.5 cm for surface-orthogonal ones, depending on concretion thickness. A total of 324 isotopic pair data was obtained. Carbonate powders were reacted with 100% phosphoric acid at a constant temperature of 70°C. An additional $CO_2$ reference gas (pure Carrara marble) with known isotopic ratio was analyzed during the measurements to determine the $\delta^{13}C$ and $\delta^{18}O$ values. Samples were analyzed with a Thermo Finnigan DELTA plus XP mass spectrometer coupled with a Thermo Finnigan GasBench II gas preparation and sample introduction device. Both $\delta^{13}C$ and $\delta^{18}O$ values are referred to the international standard V-PDB (Vienna Pee Dee Belemnite). The analytical precision upon $\delta^{13}C$ determination was 0.10‰ V-PDB, while on $\delta^{18}O$ it was 0.15‰. The prediction uncertainty was 0.15‰ for carbon and 0.20‰ for oxygen isotopes, respectively.

The relative rock strength was measured with a Schmidt hammer (Proceq Instruments, N-type configuration hammer, with an impact energy of 2.207 Nm). The instrument provides the Q rebound value calculated as follows:

$$Q = 100 \times \frac{Energy\ (recovered)}{Energy\ (impact)}. \quad (2)$$

where *Q* indicates the output rebound value, $Energy_{(recovered)}$ is the remaining after the elastic rebound and $Energy_{(impact)}$ is the input impact strength. A total of 30 rebound values were collected on each deformation band or concretionary body. To ensure measure accuracy, selected areas were deeply polished with a corundum abrasive tool in order to remove alteration haloes and reduce surface roughness (Katz and Reches, 2000; Demirdag et al., 2009). Measurements were made keeping the Schmidt hammer orthogonal to the reference surface, being the instrument equipped with an automatic

correction tool for inclination. Analysis of Q value was made after discarding the lower half of data distribution (Katz and Reches, 2000).

### 3.4. Fault Zone Structure

The NE-SW-trending Rocca di Neto extensional fault zone is located ~ 1 km south-westward from the homonymous village and is exposed in a dismissed quarry area and along a road cut (Fig. 3.2a). These outcrops provide an excellent exposure of the footwall of the fault, while the hangingwall side is almost completely covered by debris. The Scandale sandstone is poorly lithified and mainly medium to fine-grained, but frequent thin coarse-grained layers occur. The maximum displacement of the Rocca di Neto fault can be estimated in 80-90 m, on the basis of stratigraphic constraints. The entire fault zone shows evidence for soft-sediment deformation,

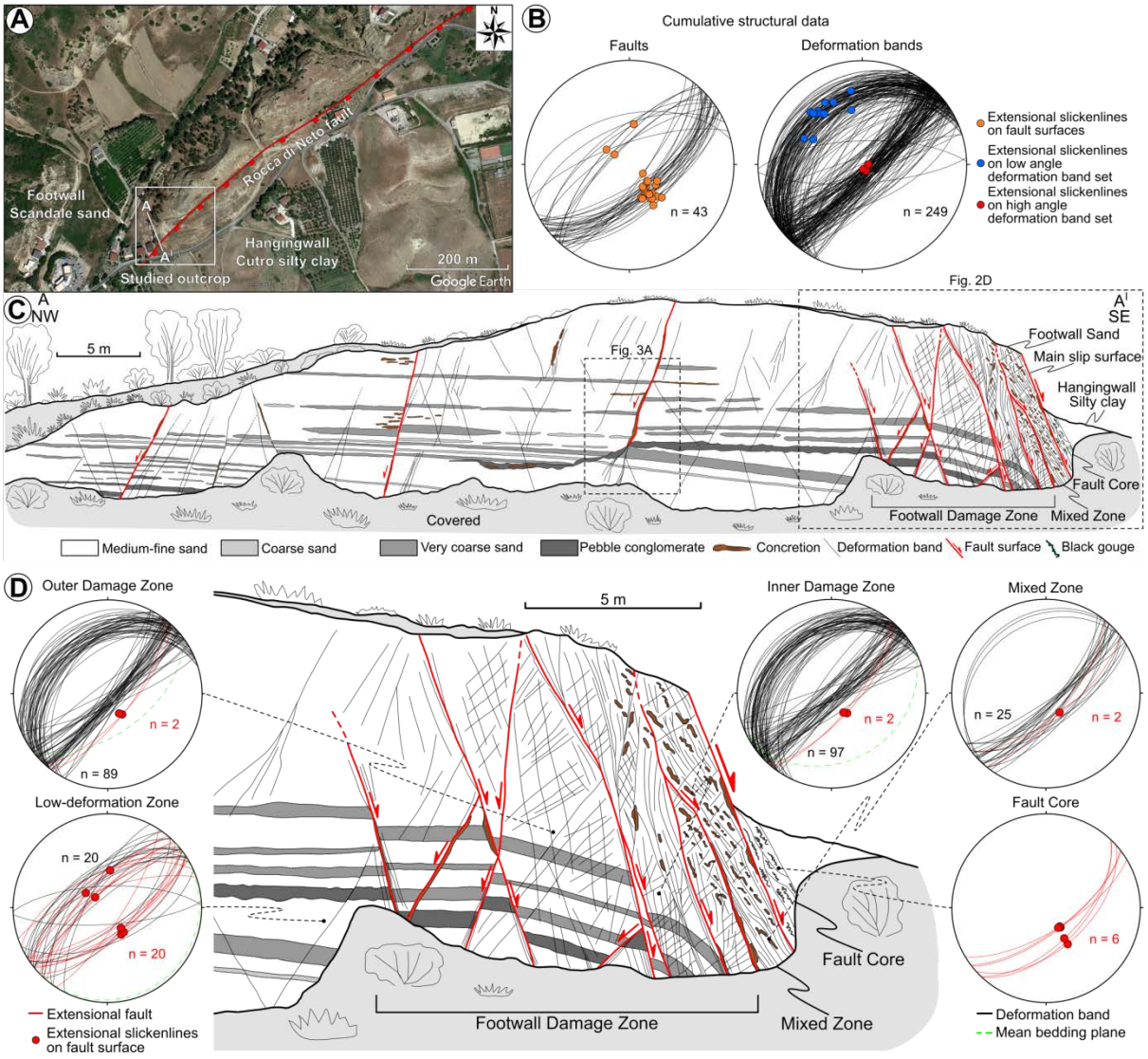


**Fig. 3.2**. (**a**) Satellite image (Google Earth) of the investigated fault zone with the trace of the master fault. (**b**) Cumulative structural data regarding faults and deformation bands. (**c**) Detailed geological cross-section of the fault zone with the identified structural domains. (**d**) Detail of the fault domains, with stereonets plotting the structural data (Schmidt lower hemisphere projection).

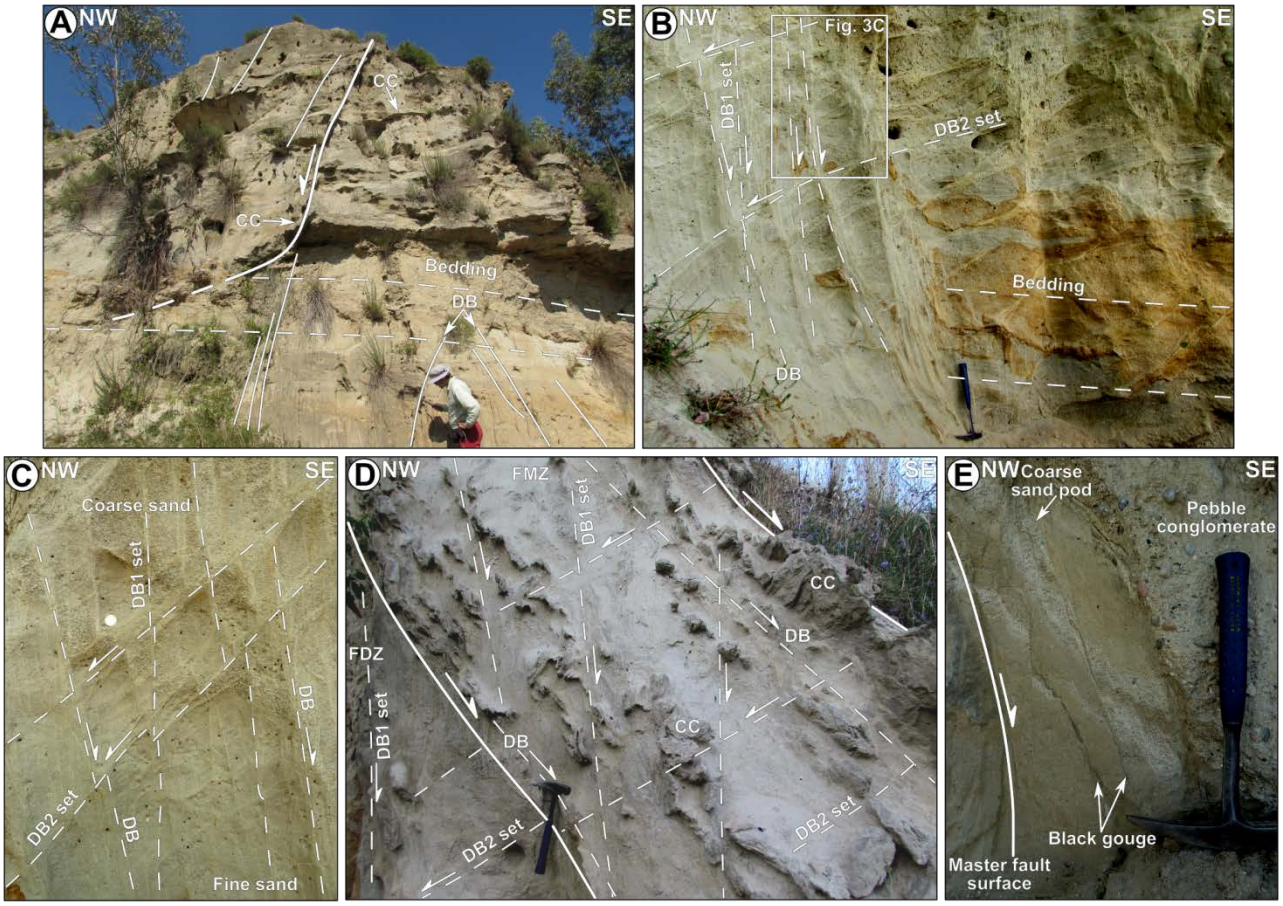


**Fig. 3.3**. Main structural features of the fault domains. (**a**) Low-displacement fault within the low-deformation zone. A few, widely spaced deformation bands are also present. Carbonate concretions are present both along minor faults and parallel to bedding. (**b**) Conjugate deformation bands within the footwall damage zone. (**c**) Detail of the deformation band sets with mutual cross-cut relationship. (**d**) Boundary between the damage zone (FDZ) and mixed zone (FMZ). (E) Fault core with the main slip surface, foliated sand and black gouges. DB, fault-parallel deformation bands; DB1, high-angle band set; DB2, low-angle band set; CC, carbonate concretions.

provided by widespread occurrence of deformation bands, deformation band clusters, and slip surfaces (Fig. 3.2b, c). Deformation bands far from the master slip surface mainly occur in scattered conjugate pairs with vertical bisectors (Fig. 3.2c, d). Low-displacement antithetic faults also occur (Figs. 3.2 and 3.3a). In the outer and inner damage zone, and in the mixed zone, deformation bands form dense networks of conjugate pairs (DB1 and DB2) with inclined bisectors (Fig. 3.2d). Approaching the master slip surface, a third set of deformation bands (DB), oriented parallel to subsidiary faults, also occurs (Fig. 3.3b-d).

### 3.4.1. Low-Deformation Zone

By low-deformation zone (LDZ) we refer to the sector outside the footwall damage zone, affected by background deformation. There, bedding has a slight dip (~ 5°) towards SE (Figs. 3.2c and 3.3a). According to the scan-line, this domain is about 48 m-thick as indicated by the gentle slope of the best-fit line of the cumulated deformation band frequency (Fig. 3.4). The LDZ is characterized by the presence of widely spaced conjugate deformation bands with displacement generally < 1-2 cm, and minor conjugate faults, with displacement < 15-20 cm (Fig.

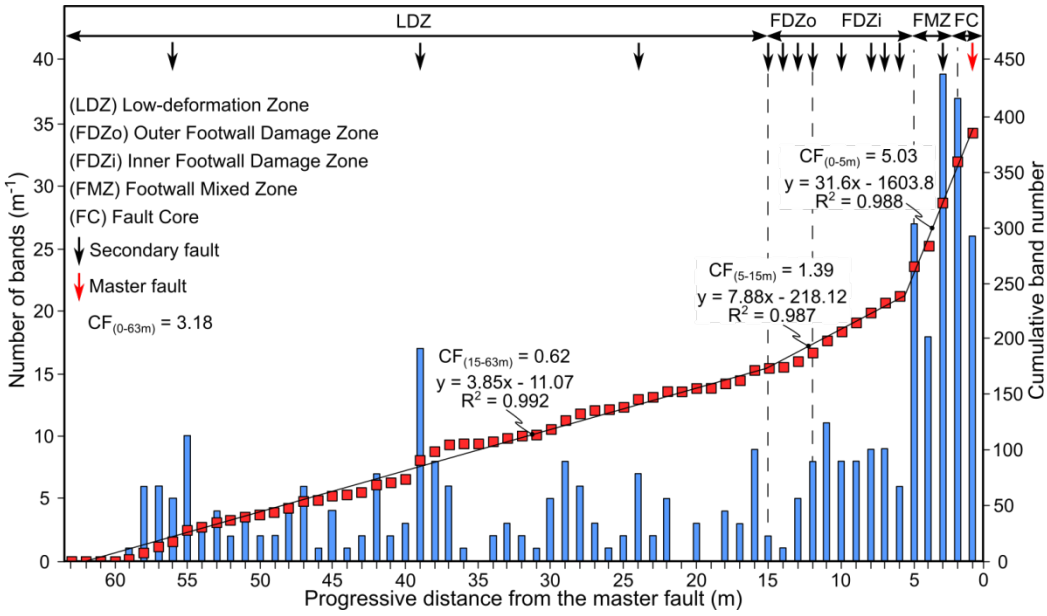


**Fig. 3.4**. Linear scan-line along the footwall side of the fault zone. Number of deformation bands is reported as cumulative and non-cumulative number. The cumulative band number of the structural domains is fitted by linear functions with different slope. CF, cluster factor (Soliva et al., 2016).

3.2c). Deformation bands and subsidiary faults are arranged in conjugate patterns making a mean acute dihedral angle of 48° (α in Fig. 3.5). The antithetic and synthetic sets describe an angle of 47° and 2° with the master fault, respectively (Fig. 3.5). The density of deformation bands is 3.5 $m^{-1}$, with a peak value of 17 $m^{-1}$ (Fig. 3.4). Higher values are measured in the vicinity of three antithetic faults cutting through the entire quarry wall and characterized by sharp surfaces and displacement values between 0.5 and 1.5 m (Fig. 3.3a). Locally, slip surfaces show preferential cementation and slickenlines. The deformation band clustering factor (CF) calculated for the LDZ yields a value of 0.62 (Fig. 3.4).

### 3.4.2. Footwall Damage Zone

In the footwall damage zone (FDZ) bedding is still recognizable, but is locally displaced by faults (Fig. 3.2c). Within the innermost part of the damage zone, bedding is tilted in fault blocks, and steeply dragged (dip value of ~ 50°) by a high-displacement fault located at the footwall damage zone-mixed zone boundary (Fig. 3.2d). The transition from the low-deformation domain occurs as a progressive increase of conjugate deformation band and fault density. Subsidiary faults zones are 10 to 30 cm-thick, with well-developed slip surfaces and a set of sub-parallel deformation bands adjacent to them (DB in Fig. 3.3c, d). These fault zones have greater displacement approaching the master slip surface.

The total width of the FDZ is about 10 m, as constrained by the linear fit of cumulated deformation band frequency showing steeper slope compared to the low-deformation zone (Fig. 3.4). In particular, the mean density of deformation bands is 6.7 $m^{-1}$, with a maximum value of 11 $m^{-1}$. The deformation band clustering factor yields a value of 1.39, i.e. more than twice that in the LDZ. Based on deformation band density, an inner (~7 m-wide) and outer (~3 m-wide) footwall damage zone can be identified (Fig. 3.4).

Deformation bands are organized in two conjugate sets (Fig. 3.3b). The first set (DB1), at high-angle to bedding, is synthetic with respect to the master slip surface, while the second one (DB2), at low-angle to bedding,

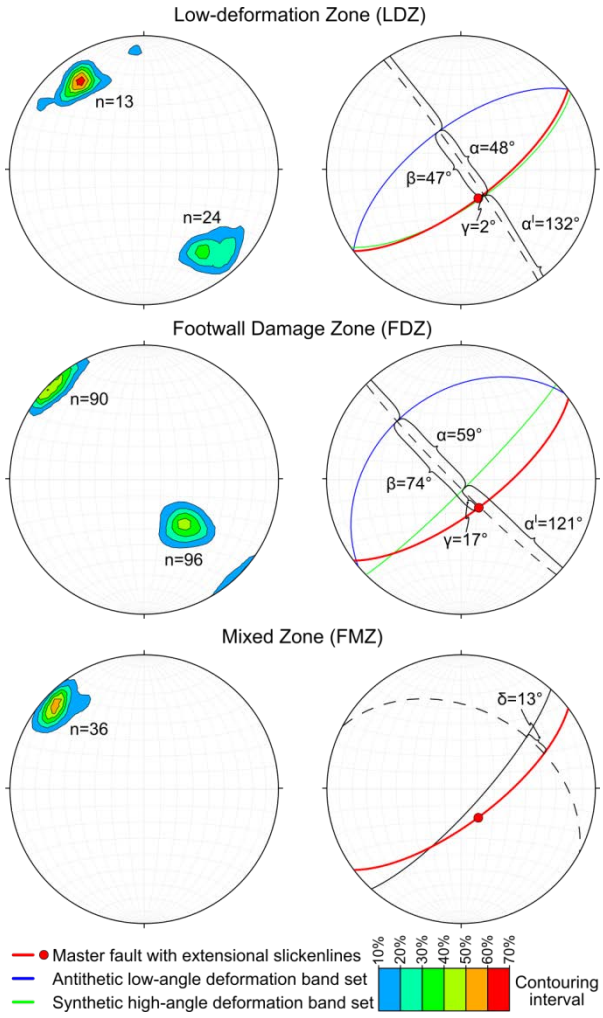


**Fig. 3.5**. Stereonet (Schmidt lower hemisphere projection) with contouring of poles to deformation band planes performed on data collected from the low-deformation, damage zone and mixed zone domains. Mean deformation band planes are calculated from the maximum pole density. Relationships between bands and main fault are reported as angles. $\alpha$-$\alpha^{I}$, acute and obtuse dihedral angles described by conjugate deformation bands; $\beta$, angle between the master fault and antithetic bands; $\gamma$, angle between the master fault and synthetic bands; $\delta$, angle between the master fault and fault-parallel bands.

has antithetic shear sense (Figs. 3.2d and 3.3d). Deformation bands show mutually cross-cut relationship and occur as single elements or as clusters of anastomosing bands (Fig. 3.3c). Along single deformation bands, displacement rarely exceeds a few centimeters, while thick clusters of bands may show an offset up to 20-25 cm. Conjugate deformation bands form an acute dihedral angle of 59° (Fig. 3.5). The antithetic and synthetic sets describe an angle of 74° and 17° with the trace of the master slip surface, respectively (Fig. 3.5).

### 3.4.3. Footwall Mixed Zone

In the footwall mixed zone (FMZ), bedding is almost completely transposed into foliation, and only locally it is still recognizable and displays a high-angle dip. The FMZ consists of a 2 to 3 m-thick domain bounded by a synthetic fault zone both on the damage zone and on the fault core side (Figs. 3.2d and 3.3d). It is characterized by closely spaced, fault-parallel deformation bands with a mean density of 28 $m^{-1}$, with a peak value of 39 $m^{-1}$ (Fig. 3.4). Close to the bounding fault zones, deformation bands are characterized by greenish colors and are thicker compared to those far away from the two fault zones. In this structural domain the deformation band clustering factor value is 5.03 and the mean angle that deformation bands form with the master slip surface is 13° (Fig. 3.5).

### 3.4.4. Fault Core

The fault core (FC) is a 1 to 2 m-thick body where most displacement is accommodated and deformation intensity is higher (Figs. 3.2d and 3.3e). It is composed of foliated medium-fine sand layers, alternating with coarse sand pods as remnants of the transposed original bedding (Fig. 3.3e). The footwall side of the fault core is bounded by the master slip surface showing extensional slickenlines, whereas the hangingwall side is mostly covered by debris. Close to the master

slip surface, numerous black-dark green gouge layers are present. Many of them have a straight geometry, parallel to the master slip surface. Fault-parallel deformation bands also occur, as well as conjugate sets. The mean band density is 31.5 $m^{-1}$, with a maximum value of 39 $m^{-1}$ (Fig. 3.4). Deformation bands and gouge layers mutually cross-cut each other.

### 3.5. Microstructural Analysis

Deformation bands developed within the low-deformation zone, outside the fault footwall, usually show grain packing re-organization and incipient fragmentation of coarse grains, without evidence of significant grain rotation and cataclasis (Fig. 3.6a). Conjugate deformation bands inside the damage zone display evidence for grain rotation and grain size reduction (Fig. 3.6b), even for millimetric displacements. Fault-parallel deformation bands are characterized by significant grain size reduction (Fig. 3.6c). Within the mixed zone, fault-parallel deformation bands are thicker than those in the damage zone and show extremely sharp boundaries at the thin section scale (Fig. 3.6d). Grain size reduction is not uniform, but is enhanced in ~ 250 µm-thick slip zones located in the central sectors of the deformation bands (Fig. 3.6d). Such crushed cores show a fine-grained brown matrix surrounding survivor quartz grains. The matrix is almost completely composed of crushed feldspar and plagioclase grains, fine particles of former calcite cement, and less abundant quartz chips.

High-strain fault-parallel deformation bands locally include ultra-comminute layers. They are typically asymmetric and show discontinuous gradients of grain size reduction organized in thin domains

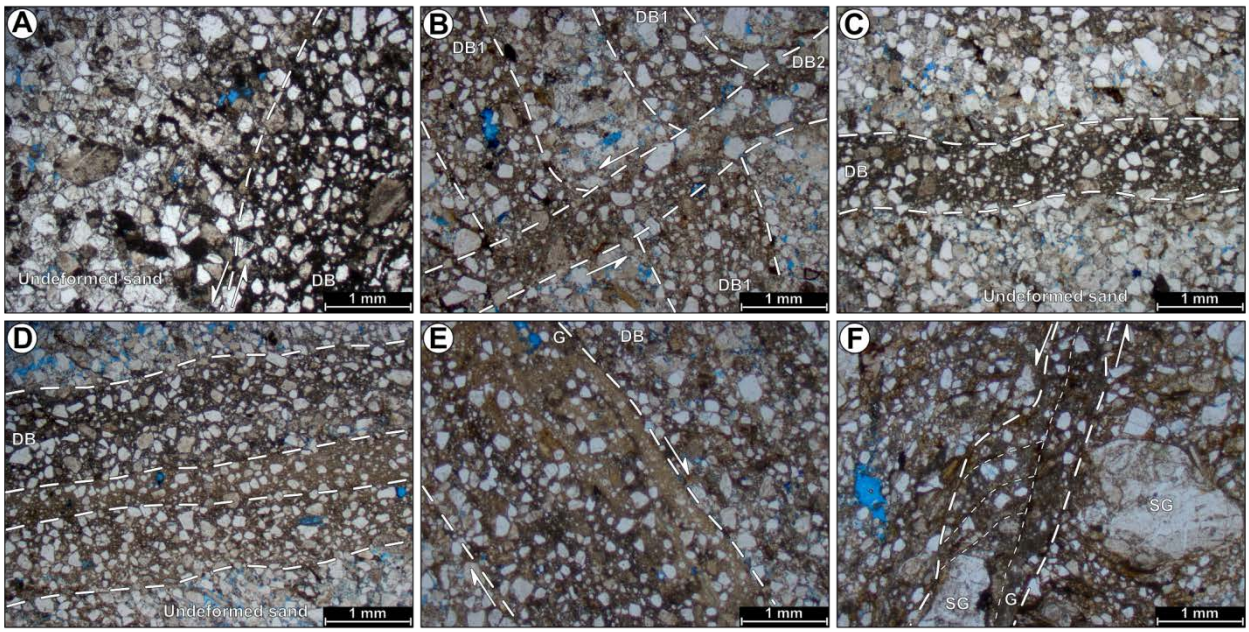


**Fig. 3.6**. Petrographic characterization of different types of deformation bands. (**a**) Low-displacement band (DB) in the low-deformation zone showing incipient fragmentation of grains. (**b**) Conjugate deformation bands (DB1 and DB2) within the damage zone. (**c**) Fault-parallel, low-displacement band (DB) inside the footwall damage zone. (**d**) Fault-parallel, high-displacement band (DB) showing an ultra-comminute core and less deformed outer zone. (**e**) High-displacement band (DB) with asymmetric gradient of grain size comminution and thin gouge layer (G). (**f**) Black gouge layer (**g**) with extreme grain size reduction forming a fine-grained matrix surrounding a few survivor grains (SG). S-C structures are frequent inside foliated sand.

paralleling the deformation band boundaries, and are characterized by the preferential alignment of grains to produce a foliation (Fig. 3.6e). Some deformation bands, especially inside the mixed zone and fault core, host calcite micro-veins located within their strongly comminuted cores. These veins originated from tensile fractures arranged in two patterns: (1) fault-parallel geometry, which is the most frequent one and is characterized by veins with a maximum width of 800 µm; (2) tiny veins (maximum width < 100 µm) arranged in left-stepping *en-échelon* array forming clockwise angles of 40-50° with slip surfaces, i.e. coherent geometry with extensional shearing.

In the fault core, foliated sands host thin black gouge layers consisting of a very fine-grained, dark-colored ultra-comminuted matrix and a few survivor grains. Immediately outside the gouge layers, S-C type structures indicating extensional shear frequently occur (Fig. 3.6f). As observed at the mesoscale, also at the microscale gouge layers show mutual cross-cut relationships with conjugate deformation band sets.

### 3.6. Cementation Pattern

Preferential cementation occurs throughout the investigated outcrop in the form of diagenetic concretions locally cementing the loose host sandstone. The vast majority of concretions are associated with deformation bands and faults. Bedding-parallel concretions are rare and usually show a limited lateral continuity and thickness typically lower than 5 cm (Fig. 3.3a). Inside the low-deformation domain, concretions hosted within faults and deformation bands display a tabular geometry with thickness varying between 5 and 10 cm, typically increasing in deformation band clusters and subsidiary faults. Almost all subsidiary faults and fault zones in the footwall damage zone are characterized by tightly cemented bodies (Fig. 3.3d). Here, concretions encase deformation bands and thick deformation band clusters to form cemented bodies as thick as 15-20 cm. The mixed zone is characterized by an abrupt increase in concretion number, which are offset along conjugate deformation band sets and show limited thickness (< 10 cm) and lateral continuity (Fig. 3.3d). Concretion development along conjugate deformation bands resulted in geometric arrays resembling folds (Fig. 3.7). Axes of such pseudo-folds, i.e. intersection lineations between concretions with different dip, plot almost parallel to the strike of the master slip surface. Inside the fault core, only one laterally continuous, 30-40 cm-thick tabular concretion occurs along the master slip surface.

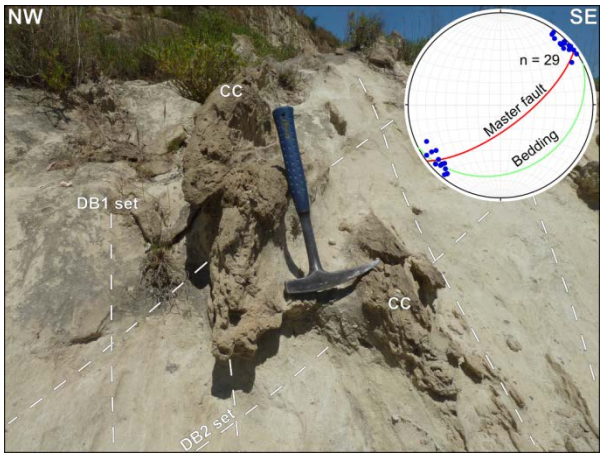


**Fig. 3.7**. Outcrop photo of a concretion located within the mixed zone, at a distance of 2 m from the master fault, showing a pseudo-fold geometry along the intersection with the two conjugate deformation band sets. DB1, high-angle set; DB2, low-angle set; CC, carbonate concretions.

#### 3.6.1. Concretion Petrography

Cement petrography was investigated both on the undeformed as well as on the deformed sand inside deformation bands along the same concretions.

Concretionary bodies developed in undeformed loose sandstone of the low-deformation zone are made up of sparitic calcite with mosaic texture and crystal size up to 70-80 µm (Fig. 3.8a). The size of the crystals tends to increase where the pore space is wider. Locally, calcite cement forms also syntaxial overgrowths around peloids, fossil shells and detrital calcite grains. Under cathodoluminescence (CL), this cement displays very bright yellow-orange luminescence, with a few and thin dull sub-zones (Fig. 3.8a). Concretions developed by preferential cementation along deformation bands and subsidiary faults within the low-deformation zone are characterized by cementation patterns similar to those developed in the undeformed sands, with bright-yellow luminescence (Fig. 3.9a-c). The main difference is the crystal size of calcite, which is typically < 10-20 µm (Fig. 3.10a). Locally, grain boundaries have a 10 µm-thick fringe of undeformed equant calcite (Fig. 3.9a). Calcite cement infilling intergranular pores includes both crushed and undeformed calcite crystals, the latter still preserving the original shapes (Fig. 3.10a). Intergranular pores are frequently partially filled by grain fragments and have very fine-grained sparitic calcite cement (Fig. 3.9c).

Concretions developed in undeformed sandstone within the damage zone are characterized by a more complex cementation pattern. The dominant cement is still sparitic mosaic calcite, but with coarser size, up to 90-100 µm (Fig. 3.8b). Under CL, this calcite displays a dull dark-brown color in the core of the crystals, followed by growth zonations with a bright-yellow luminescence (Fig. 3.8b). The observed CL-pattern varies according to the position inside concretions: concretion cores have a dominant dark-brown cement, while moving to the outer edges bright-yellow sub-zones typically occur and eventually become the dominant cement type (Fig. 3.8b). Concretions developed along deformation bands within the footwall damage zone commonly encase a high number of closely spaced deformation bands. In these cases, deformation bands located close to concretion nuclei display very fine-grained calcite crystals (Fig. 3.10b) with

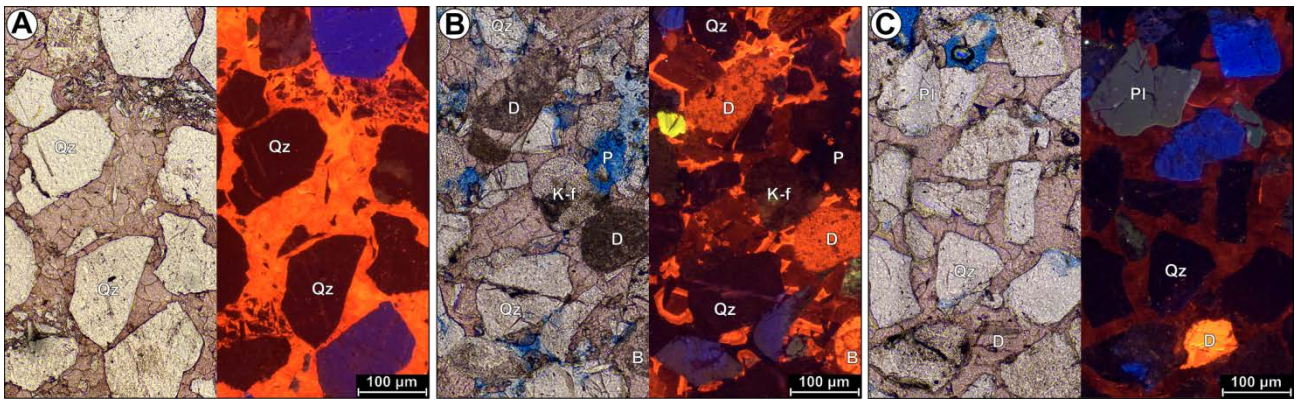


**Fig. 3.8**. Petrographic characteristic of cement in the undeformed concretion volume. (**a**) Sparitic equant calcite with mosaic texture and yellow CL color inside concretions from the low-deformation zone. (**b**) Sparitic calcite with dark-brown luminescence followed by bright-yellow one, characterizing concretions from the damage zone. (**c**) Concretions along the fault core show dull brown-colored coarse sparitic calcite. Qz, quartz; K-f, feldspar; Pl, plagioclase; D, detrital calcite; B, bioclast; P, porosity.

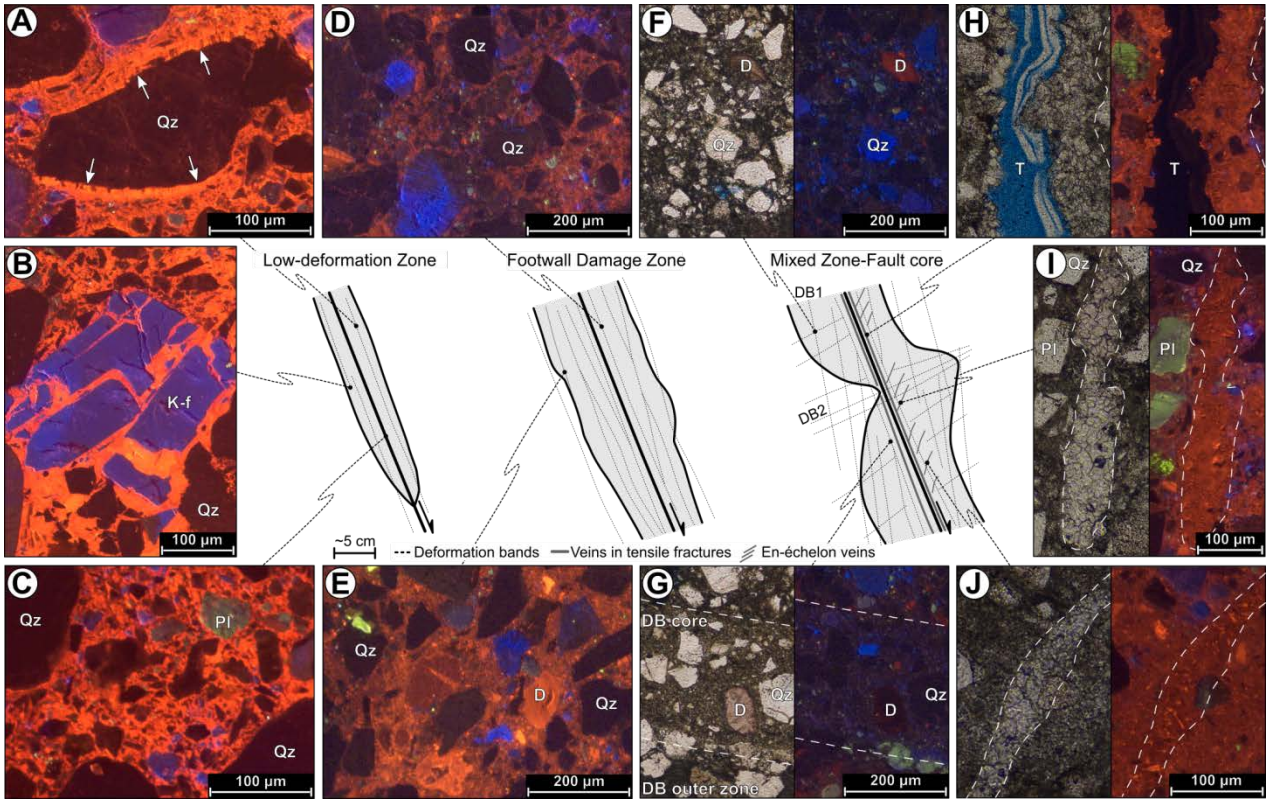


**Fig. 3.9**. Petrographic features of cement inside deformation bands and faults. (**a**) Fine-grained calcite cementing a deformation band located in the low-deformation zone. White arrows indicate a fringe of undeformed equant calcite along the outer rim of quartz grain. (**b**) Detail of calcite cementing a fractured feldspar grain within a band inside the low-deformation zone: cement is coarser where pore space in higher. (**c**) Core of a band inside the low-deformation zone displaying finely grained sparitic calcite. (**d**) Dully luminescent crushed calcite inside a deformation band close to the core of a concretion hosted in the damage zone. (**e**) Crushed bright-orange cement found in a deformation band along the outer edge of a concretion within the damage zone. (**f**) Conjugate deformation bands showing low amount of dull brown crushed cement within concretion from the mixed zone. (**g**) Fault-parallel high-displacement band inside the mixed zone with highly crushed dull cement both in the core and in the outer zone of the band. (**h**) Fault-parallel tensile fracture developed within concretion from the mixed zone, with partial infilling. (**i**) Vein composing the *en-échelon* array, filled by equant mosaic calcite. (**j**) *En-échelon* vein slightly sheared within a concretion from the fault core. Qz, quartz; K-f, feldspar; Pl, plagioclase; D, detrital calcite; DB, fault-parallel deformation band; DB1, high-angle band set; DB2, low-angle band set; T, tensile fracture.

brownish CL colors (Fig. 3.9d). Deformation bands located in proximity of concretion outer edges are cemented by almost equal proportions of brown and yellow-luminescent fine-grained calcite (Fig. 3.9e).

Concretions developed in undeformed sands within the mixed zone and fault core have a prevalent cement composed of sparitic calcite with crystal size ranging from 30 to 200 µm (Fig. 3.8c). Analysis under CL reveals dark-brown luminescence similar to the one characterizing cements from concretions sampled in the damage zone (Fig. 3.8b). However, no bright-yellow luminescence was found. Concretions developed along deformation bands in the mixed zone and fault core show a dark cement under CL. In particular, deformed fine-grained cement is mixed with the fine matrix made up of crushed feldspar and to less extent, quartz grains (Fig. 3.9f). Concretions encasing fault-parallel deformation bands show dark comminute cement inside cores, and less deformed, dark-brown calcite in the outer sectors (Figs. 3.9g and 3.10c).

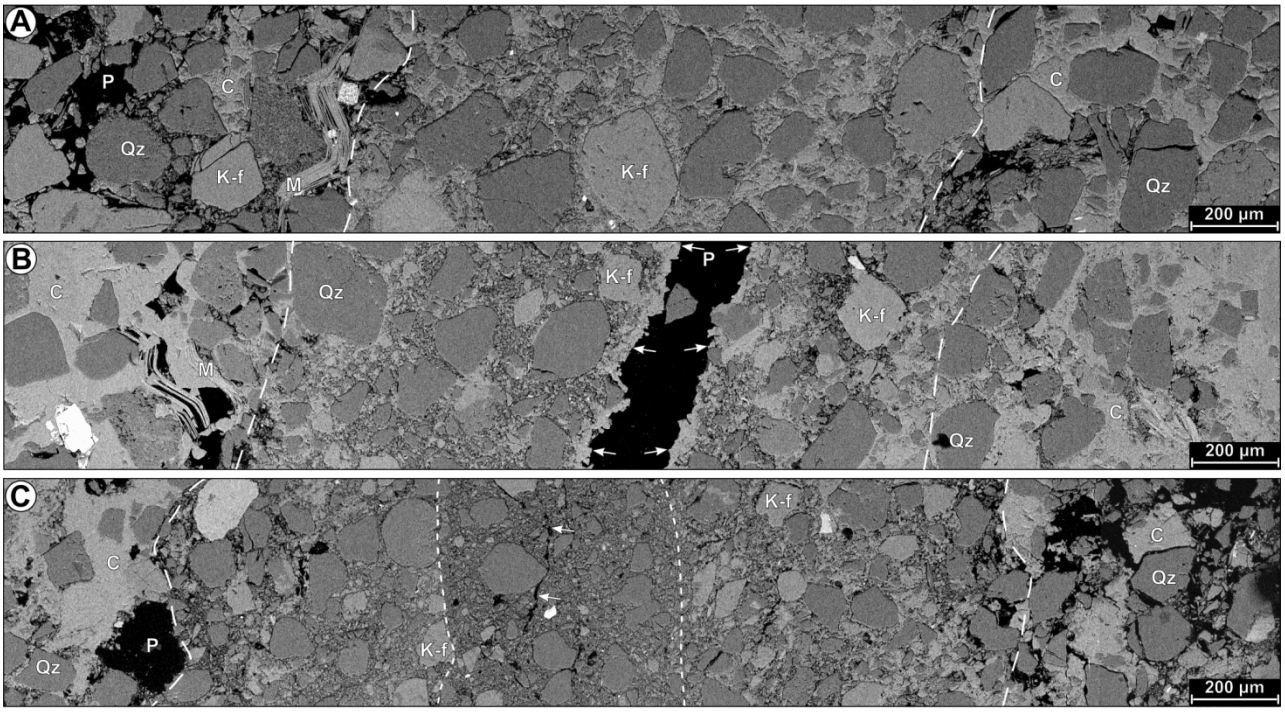


**Fig. 3.10**. Backscattered scanning electron microscope photomicrographs of representative samples of deformation bands. (**a**) Band with low-displacement within the low-deformation zone, cemented by a coarse equant calcite outside and fine-grained one inside band boundary. (**b**) Medium-displacement band from the damage zone showing the same cement pattern, with a tensile fracture in the middle partially filled by cement (white arrows). (**c**) High-displacement band close to the main fault with almost no cement in the core zone, while it is sparsely distributed in the outer zone of the band. A tiny tensile fracture developed in the middle of the core of the band. Qz, quartz; K-f, feldspar; M, mica; C, calcite; P, porosity.

### 3.6.2. Vein Petrography

Most of the veins pertaining to the fault-parallel pattern are partially filled by mosaics of equant to elongate (dogtooth) calcite (Figs. 3.9h and 3.10b), while only a few are completely filled. The CL color is brown dull-orange, similar to that shown by calcite cementing concretions outside the veins (Fig. 3.9h). *En-échelon* veins have a limited lateral continuity and are completely filled by mosaic calcite with brown CL color (Fig. 3.9i, J). Some of these veins display little drag and shearing in the vicinity of deformation bands.

### 3.6.3. Cement Stable Isotope Geochemistry

Stable isotope data acquired from concretions in different structural positions plot in well-defined fields in a $\delta^{18}O$-$\delta^{13}C$ cross-plot (Fig. 3.11a). In particular, concretions associated with deformation bands and subsidiary faults from the low-deformation zone, are characterized by $\delta^{13}C$ spanning in a wide range of values (from -23.08 to -8.98‰) and $\delta^{18}O$ with a narrow span (from -8.45 to -4.12‰ V-PDB). A concretion formed along an erosive surface has different isotopic signature, with less depleted $\delta^{13}C$ (from -9.3 to -0.08‰) and $\delta^{18}O$ (from -6.66 to -1.55‰ V-PDB) (Fig. 3.11a). Data from diagenetic bodies sampled inside the footwall damage zone show only a limited overlap with those from concretions in the low-deformation zone. In particular, $\delta^{13}C$ values range from -10.35 to -0.02‰ while $\delta^{18}O$ values span from -5.39 to -1.25‰ V-PDB (Fig. 3.11a). Concretions within the mixed zone have less depleted isotopic signatures, with $\delta^{13}C$ values spanning from -3.26 to -0.16‰ and $\delta^{18}O$ values in the -3.99

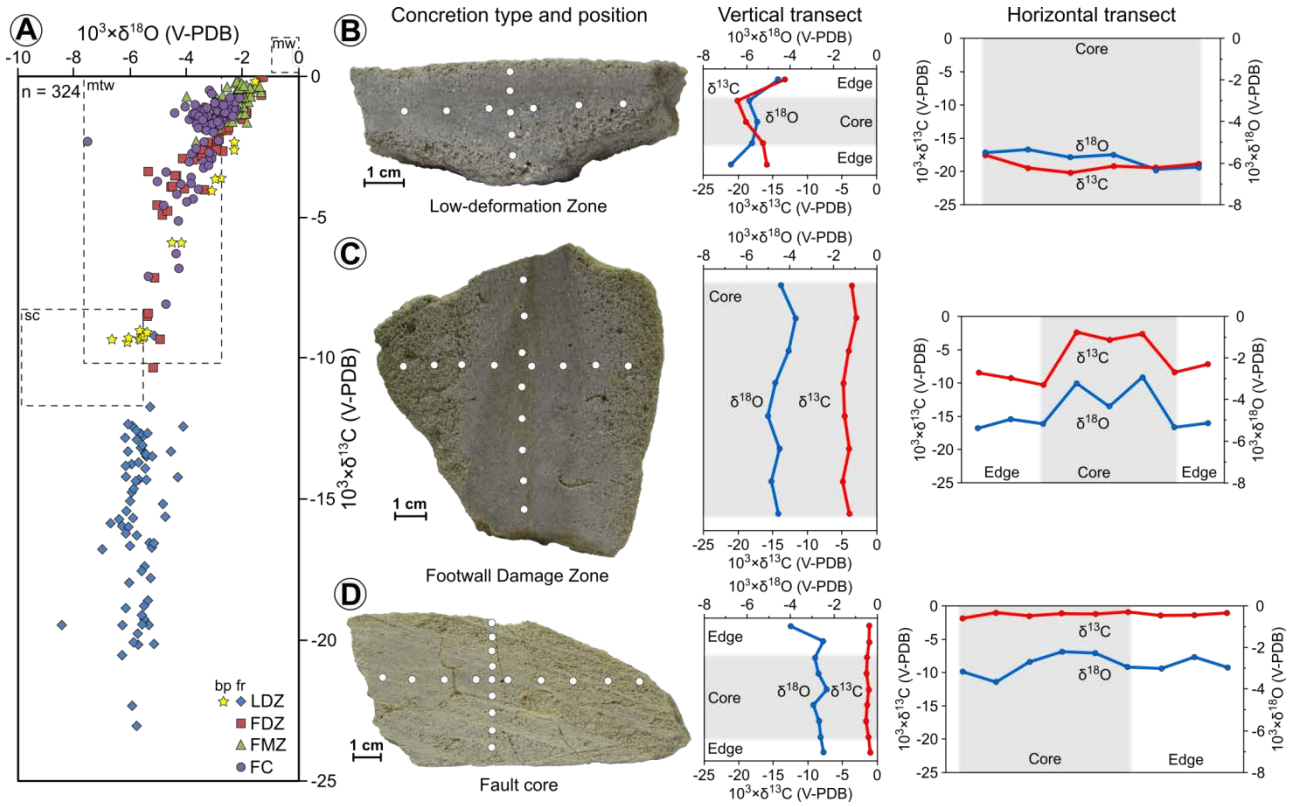


**Fig. 3.11**. Stable isotope data extracted from concretionary bodies. (**a**) $\delta^{18}O$-$\delta^{13}C$ cross-plot of the cumulative data gained from all sampled concretions. (**b**) Concretion sampled in the low-deformation zone displays the most depleted $\delta^{18}O$ and $\delta^{13}C$ values. (**c**) Concretion sampled within the damage zone shows least depleted isotopic response close to the core, while the outer edge has the more depleted ones. (**d**) Concretion from fault core has roughly constant and scarcely depleted $\delta^{18}O$ and $\delta^{13}C$ isotopic signature. LDZ, low-deformation zone; FDZ, footwall damage zone; FMZ, footwall mixed zone; FC, fault core; V-PDB, Vienna Pee Dee Belemnite; fr, fault-related concretion; bp, bedding-parallel concretion; mw, marine water cement; mtw, meteoric water cement; sc, soil-derived cements.

to -1.32‰ V-PDB range. Eventually, concretions sampled from the fault core have isotopic values of $\delta^{13}C$ spanning from -8.09 to -0.49‰, while $\delta^{18}O$ values vary from -7.51 to -2.09‰ V-PDB (Fig. 3.11a).

Data from sampling transects along and across concretions show peculiar isotopic signatures. Concretions from the low-deformation zone are characterized by the most depleted $\delta^{13}C$ values (-20.18‰) located in the central parts of the cemented cores, while outer edges have less depleted isotopic signatures (-13.31‰) (Fig. 3.11b). $\delta^{18}O$ values describe asymmetrical variations, being the most depleted sector located close to one boundary (-6.71‰ V-PDB), whereas less depleted signatures characterize concretion cores (around -5.51‰ V-PDB) and least depleted values occur close to the other boundary (-4.56‰ V-PDB) (Fig. 3.11b). Concretions from the damage zone show symmetric variations in isotopic values with respect to their geometry. The most depleted $\delta^{13}C$ values (-10.35‰) are recorded along the outer zones, while cores have the least depleted values (-2.34‰) (Fig. 3.11c). $\delta^{18}O$ data follow the same trend described by carbon, with the most depleted values located close to cores (-5.39‰ V-PDB) and the least depleted ones pertaining to the outer edges (-2.92‰ V-PDB) (Fig. 3.11c). The fault core hosts concretions with more stable isotopic signatures in comparison with data from the damage zone. From the core to the

outer edge, $\delta^{13}C$ values display a variability between -1.89 and -0.9‰, whereas $\delta^{18}O$ values span from -4.03 to -2.2‰ V-PDB (Fig. 3.11d).

### 3.7. Uniaxial Strength Data

Undeformed and uncemented sediments are characterized by Schmidt hammer rebound values lower than the detection limit of the instrument (8.5 Q). Within the damage zone, deformation bands pertaining to set DB1 are characterized by a mean Q value of 12.03, while deformation bands pertaining to set DB2 have a mean value of 11.43 (Fig. 3.12).

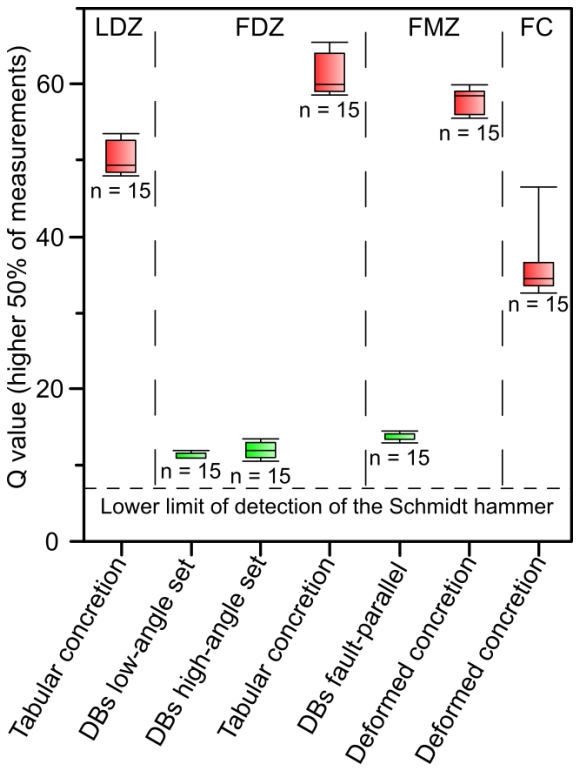


**Fig. 3.12**. Schmidt hammer rock relative strength (Q value) measurements for different type of deformation bands and diagenetic bodies along the fault zone. DBs, deformation bands; LDZ, low-deformation zone; FDZ, footwall damage zone; FMZ, footwall mixed zone; FC, fault core.

Fault-parallel deformation bands (DB) hosted within the mixed zone are characterized by a mean Q value of 13.7. A tabular concretion cementing a low-displacement fault in the low-deformation zone displays a mean Q value of 50.13, while inside the damage zone a similar body has a mean Q value of 61.7. Deformed concretions in the mixed zone and fault core have mean rebound values of 58.06 and 35.76, respectively (Fig. 3.12).

### 3.8. Discussion

#### 3.8.1. Regional and Kinematically-Induced Stress Fields from Conjugate Deformation Bands

The presence, only within the fault zone, of conjugate deformation band arrays with inclined bisectors is a peculiar feature that, to our knowledge, was never described before in extensional fault zones affecting poorly lithified sediments. By applying basic fault mechanics (e.g., Mandl, 2000), conjugate deformation bands offer the possibility to determine the orientation of the principal axes of the stress ellipsoid both inside and outside the Rocca di Neto footwall damage zone (Fig. 3.13). In the low-deformation domain, outside the fault zone, the intersection line between DB1 and DB2 deformation band sets yields the orientation 234°,4° for the $\sigma_2$ axis. The bisector of the angle between the two conjugate sets yields a $\sigma_1$ oriented almost vertical, with a slight plunge towards the north (8°,86°). The pole of the $\sigma_1$-$\sigma_2$ plane yields the orientation of $\sigma_3$ (145°,3°), which is consistent with the extension direction inferred from slickenlines (Fig. 3.13a). In the footwall damage zone, mixed zone and fault core the bisector of the average angle between the two DB1 and DB2 conjugate deformation band sets provides a NW-plunging $\sigma_1$ axis (306°,65°), making an angle of 44° with the trace of the master slip

surface. The intersection line between DB1 and DB2 yields an almost horizontal $\sigma_2$ axis, with a slight plunge towards NE (45°,3°). The pole of the $\sigma_1$-$\sigma_2$ plane yields the orientation of the $\sigma_3$ axis (137°,25°) (Fig. 3.13b).

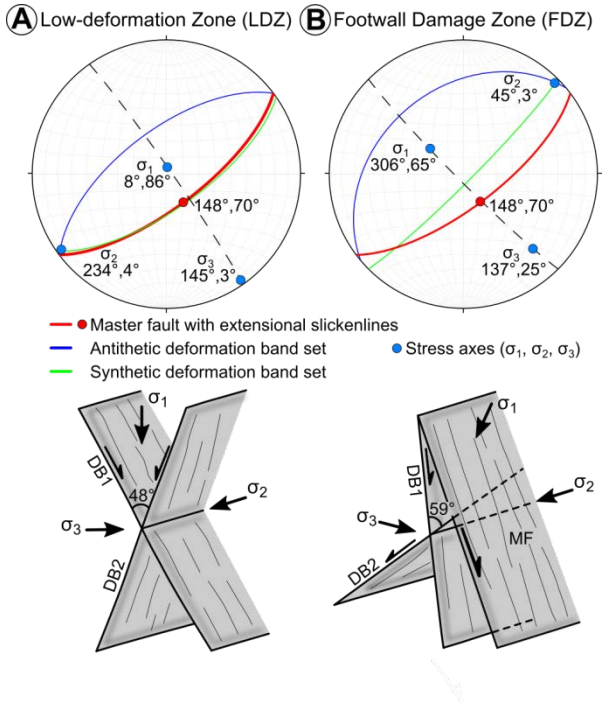


**Fig. 3.13**. Orientation of stress field deduced from conjugate deformation bands found in the low-deformation zone and within the damage zone, based on geometrical relationships shown in Figure 3.5. Schmidt lower hemisphere projection. (**a**) Stress field inferred from conjugate deformation band sets inside the low-deformation domain. (**b**) Stress field inferred from inclined conjugate deformation band sets inside the footwall damage zone. DB1, high-angle band set; DB2, low-angle band set; MF, master fault.

Results from inversion of deformation band data indicate that: (i) two different palaeo-stress fields occurred in the study area, outside and inside the Rocca di Neto fault footwall damage zone, respectively; (ii) the palaeo-stress field inferred from the low-deformation zone is typical of "Andersonian extensional faulting" (i.e. with vertical $\sigma_1$; e.g., Mandl, 2000) (Fig. 3.13a). This can be assumed to represent the regional stress field affecting the Crotone Basin from Middle Pleistocene times (Zecchin et al., 2012), because the orientation of the principal axes of the stress ellipsoid fits well the mean NE-SW trend of extensional fault zones involving Pleistocene sediments; (iii) the palaeo-stress field inferred from the footwall damage zone and mixed zone is not compliant with the classic "Andersonian faulting", rather the inclination of $\sigma_1$ to the master slip surface fits extremely well with a kinematically-induced stress field (e.g., Davis et al., 2012) produced by fault activity in a 8 to 10 m-thick belt from the master slip surface (Fig. 3.13b). In this view, conjugate high and low-angle deformation band sets can be interpreted as Riedel shears (Davis et al., 2000; Ahlgren, 2001; Katz et al., 2004; Olsson et al., 2004). In particular, DB1 deformation band set can be interpreted as synthetic R shears (at ~17° to the master slip surface), while DB2 set can be interpreted as antithetic $R^1$ shears (at ~74° to the master slip surface) (Davis et al., 2000). The orientation of the $\sigma_1$ axis of the kinematically-induced stress field with respect to the master slip surface, as well as that of R and $R^1$ shears, indicates that slip on the master fault itself occurred by simple shear, without any dilational component.

### 3.8.2. Deformation Mechanisms and Physical Strain-Hardening

Deformation in the Rocca di Neto fault occurred at very shallow burial depth (< 1 Km), by a combination of particulate flow and cataclasis (Fig. 3.6). In particular, outside the footwall damage zone, non-destructive particulate flow (Rawling and Goodwin, 2003) was the dominant deformation mechanism in deformation bands, characterized by grain reorganization with negligible sliding and limited fragmentation. Evidence of cataclasis are found only inside thick clusters of

deformation bands or along subsidiary faults (Fig. 3.14a). Conversely, cataclasis and wear processes (Engelder, 1974; Rawling and Goodwin, 2003; Balsamo and Storti, 2010, 2011) occurred in the footwall damage zone, where they overprinted early particulate flow, as indicated by the severe fragmentation and comminution affecting the grains (Fig. 3.6b-f). The switch between the two deformation mechanisms was likely facilitated by: (1) significant loss of sediment porosity by tectonic compaction within the fault zone (Antonellini et al., 1994; Shipton et al., 2005); (2) early selective cementation localized along deformation bands and faults (Mozley and Goodwin, 1995; Caine and Minor, 2009; Philit et al., 2015; Skurtveit et al., 2015; Williams et al., 2016); (3) increase of fault displacement locally accommodated within deformation bands (Torabi et al., 2007; Kaproth et al., 2010); (4) increasing stress-strain condition near the master slip surface (Cashman and Cashman, 2000; Mair et al., 2000).

The strain-hardening behavior of deformation mechanisms in the fault zone (Aydin and Johnson, 1978; Mair et al., 2000; Nicol et al., 2013; Fossen et al., 2017) is supported by the abrupt increase of deformation band density occurring in the footwall damage zone, mixed zone and fault core (Fig. 3.4). Moreover, cataclasis shows a pronounced gradient approaching the master fault, thus indicating that its intensity is linked to the stress-strain conditions associated with the fault activity. Strain-hardening is also supported by the presence of ultra-comminute layers in the central cores of deformation bands (Figs. 3.6d-e and 3.14b), and by micro-veins developed within these layers, testifying to late-stage shear and strain localization processes (Aydin and Johnson, 1978; Davatzes et al., 2005; Fossen et al., 2017) that eventually produced cohesive material suitable to fail by Coulomb shear (Fossen, 2010; Davis et al., 2012) (Fig. 3.14c). The slightly positive trend of Q values moving from deformation bands in the lower deformation zone towards the mixed zone (Fig. 3.12) is associated with the corresponding increase of comminution intensity due to higher displacement along single bands.

### 3.8.3. Syn-Kinematic Cementation and Chemical Strain-Hardening

Cement started to form within deformation bands and subsidiary faults possibly enhanced by the presence of crushed detrital fossil shell fragments acting as cementation nuclei for successive calcite precipitation (Bjorkum and Walderhaug, 1990). The lower porosity and permeability within faulted sediments could have caused an increase of fluid retention time regardless of the water-saturation conditions, leading to a continuous cementation through time (Antonellini et al., 1994; Sigda and Wilson, 2003; Wilson et al., 2003). Moreover, the presence of black thin gouge layers in the fault core supports coseismic slip (Balsamo and Storti, 2011; Balsamo et al., 2014), which might have caused rapid drops of $CO_2$ pressure, causing fast calcite precipitation within deformation bands located close to the master fault (Hendry and Poulsom, 2006). The isotopic signature of cements records different diagenetic environments during calcite precipitation in different fault sectors. The marine water end-member was assumed from mollusk shells sampled from other nearby faults by Balsamo et al. (2012) and is

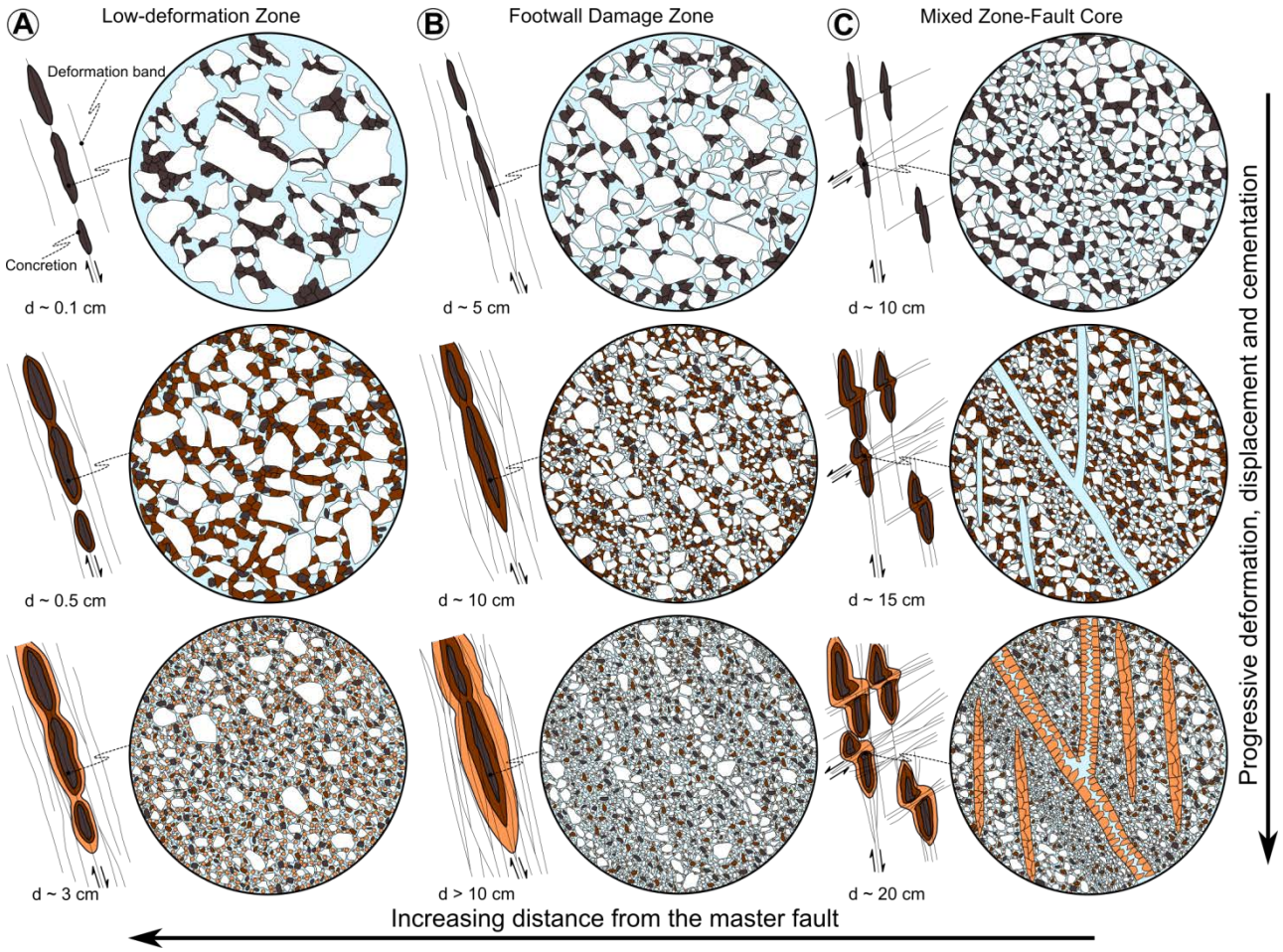


**Fig. 3.14**. Schematic evolution of microstructures and syn-kinematic cementation in different structural domains along the fault zone. (**a**) Progressive cementation and deformation characterizing array of fault-parallel deformation bands to form tabular-shaped concretionary bodies inside the low-deformation domain. (**b**) Syn-kinematic cementation of dense cluster of deformation bands within the footwall damage zone. The resulting concretion is typically thicker compared to the ones characterizing the low-deformation domain. (**c**) Cementation coeval with deformation along the conjugate deformation band sets inside the mixed zone and fault core, close to the master fault. The shape of the resulting concretions features "pseudo-fold" geometry given by the intersection and mutual cross-cut relationship between the two deformation band sets. Note the micro-veins, both parallel and with *en-échelon* pattern characterizing these concretions, as a result of the both chemical and physical strain-hardening achieved in the nearest vicinity of the master fault.

characterized by a $\delta^{13}C$ of +0.3‰ and a $\delta^{18}O$ of -0.5‰ V-PDB. Concretions located within the fault core and mixed zone show isotopic data characteristic of the mixing zone between marine and meteoric water (Hudson, 1977; Nelson and Smith, 1996) (Fig. 3.11a, d). This is testified also by the dull-brown CL-response of cements and veins, suggesting suboxic Eh conditions (Barnaby and Rimstidt, 1989). Concretions from the damage zone recorded the shift from a mixed marine-meteoric environment to a markedly meteoric one (Hudson, 1977). This is confirmed by the depletion of both $\delta^{13}C$ and $\delta^{18}O$ and by the relative increase of yellow-bright cement with respect to the dull one moving from the core to the outer edge of the concretion (Hudson, 1977; Hiatt and Pufhal, 2014) (Figs. 3.9d, 3.11a, c). Concretions from the low-deformation zone formed from meteoric fluids (Hudson, 1977) (Fig. 3.11a, b). The bright CL pattern with minor dull sub-zones can be related to dominant highly reducing conditions alternated with short suboxic-oxic ones (Barnaby and Rimstidt, 1989; Hiatt and

Pufhal, 2014) (Fig. 3.8a-c). The most depleted $\delta^{13}C$ values (from -23 to -15‰ in Fig. 3.11a) could be explained by a combination of $CO_2$ coming from fluids percolating through soils and organic matter alteration mediated by bacteria (Nelson and Smith, 1996).

The presence of both undeformed and crushed fine-grained cement inside deformation bands, as well as slickenlines formed by mechanical striations, suggest that partial cementation started during deformation and was then completed by younger undeformed cement (Fig. 3.9a-e). In high-displacement deformation bands close to the fault core, the very limited free pore volume due to strong tectonic compaction, prevented any significant early stage cementation (Skurtveit et al., 2015) (Fig. 3.9f, g).

Development of syn-kinematic carbonate concretions along two cross-cutting orientations progressively created a network of much stronger material compared also to cohesive deformation bands (see Fig. 3.12). Accordingly, the overall strength of the footwall damage zone likely increased through time. Moreover, the presence of a network of cohesive material within poorly lithified sand is supposed to trigger a complex pattern of stress concentration beams as highlighted by the striations shown by concretions close to the master fault.

### 3.8.4. Fault Zone Evolution

The multidisciplinary dataset collected in the footwall and core of the Rocca di Neto extensional fault zone, allowed us to obtain robust constraints on its structural evolution, framed within varying diagenetic environmental conditions. Deformation in the Scandale sandstone, which was deposited following a regional subsidence pulse (Zecchin et al., 2012), likely started in a marine-water dominated environment, under very shallow burial of about 400-500 m, on the basis of stratigraphic constraints. The extensional shear zone originated as a fault-parallel deformation band (DB) cluster, developed in response to a regional vertical $\sigma_1$ (Fig. 3.15a), similarly to what described in many other extensional settings worldwide (Aydin and Johnson, 1978; Shipton and Cowie, 2003; Ballas et al., 2015; Soliva et al., 2016) and in other fault zones affecting the loose sediments of the Crotone Basin (Balsamo and Storti, 2010, 2011). No concretions with clear marine isotopic signature were found in the studied exposures of the Rocca di Neto fault zone, thus suggesting that early structural diagenesis did not include selective cementation of deformation bands. This feature may relate to under-saturated condition of marine water with respect to carbonate species (Bjorkum and Walderhaug, 1990).

The well-known strain-hardening behavior of deformation bands (e.g., Aydin and Johnson, 1978; Mair et al., 2000; Fossen et al., 2017) caused progressive widening of the shear zone by outward migration of deformation, producing new fault-parallel deformation bands and a proto-damage zone during regional uplift and the transition from a marine-dominated environment to a mixing zone of marine and meteoric fluids (Fig. 3.15b). This inference is based on the isotopic signature of tabular to lens-shaped concretions that started to nucleate along deformation bands, deformation band clusters and faults, likely due to capillary suction and to high retention time of fluids

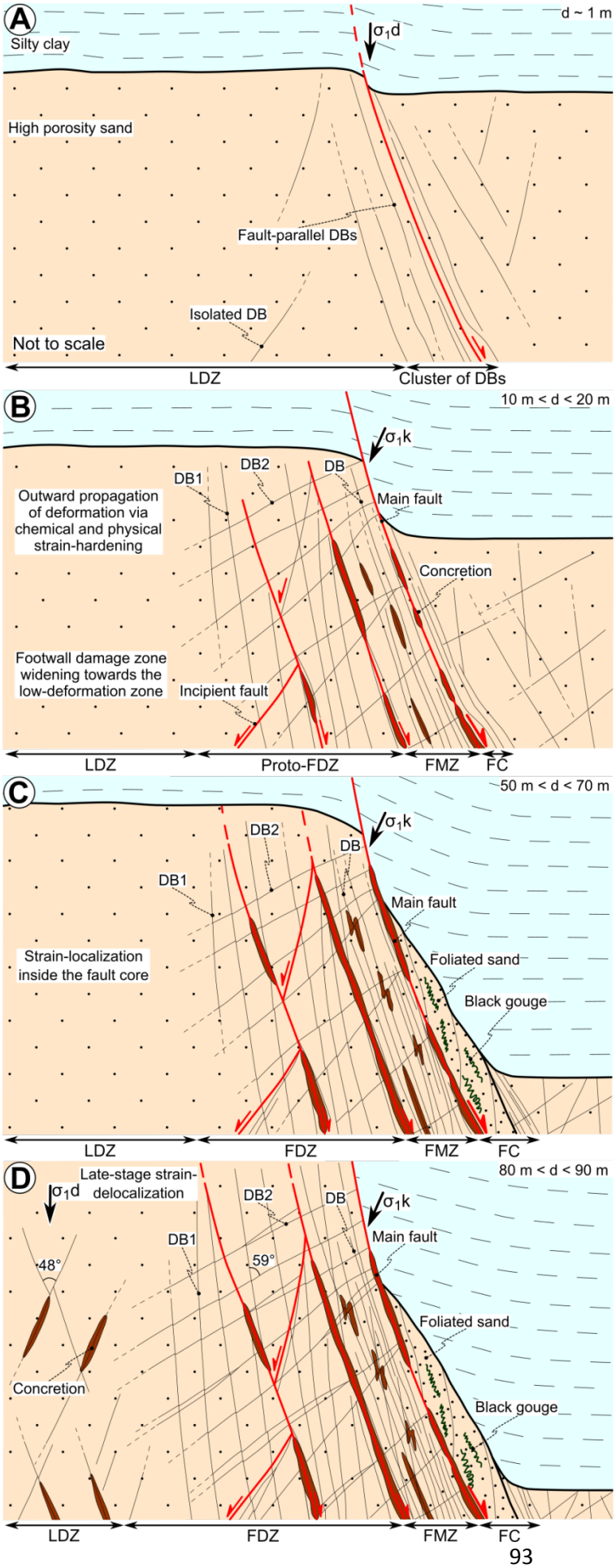


**Fig. 3.15**. Evolutionary model of the studied fault zone. (**a**) Early stage of deformation with nucleation of deformation bands in a marine water-dominated diagenetic environment. At this stage the fault zone consists of a cluster of deformation bands formed under the regional-dynamic stress field. (**b**) With progressive displacement the fault zone widened towards the undeformed domain due to the tectonic compaction and preferential cementation in a mixed marine-meteoric environment. The conjugate deformation bands formed under a kinematic stress field produced by the displacement accommodation along the fault core. During this stage the footwall damage zone formed, hosting conjugate deformation bands and subsidiary faults. (**c**) With continuing strain accommodation the fault zone reached a critical width that forced the localization of the deformation along the fault core. Displacement was likely accommodated by alternating coseismic and slow slip events affecting tectonically compacted sand producing gouge layers and deformation bands inside the fault core. At the same time inside the footwall damage zone, the conjugate deformation bands underwent clustering and contributed to the overall displacement partitioning. Some concretions were deformed along the deformation bands and recorded an isotopic signature shifting progressively from mixed marine-meteoric to meteoric fluids. (**d**) In the last stage of uplift the fault zone the deformation is delocalized towards the low-deformation zone, where widely spaced conjugate bands formed. Concretions hosted along these deformation bands and subsidiary faults are characterized by marked meteoric signature. LDZ, low-deformation zone; FDZ, footwall damage zone; FMZ, footwall mixed zone; FC, fault core; DBs, deformation bands; DB1, synthetic high-angle deformation bands; DB2, antithetic low-angle deformation bands; $\sigma_{1d}$, dynamic maximum stress axis; $\sigma_{1k}$, kinematic maximum stress axis; d, displacement.

inside faulted sandstone (Sigda et al., 1999; Sigda and Wilson, 2003; Wilson et al., 2003; Balsamo et al., 2012). The combination of tectonic compaction (Engelder, 1974; Mair et al., 2000; Kaproth et al., 2010; Fossen et al., 2017) and preferential cementation (Mozley and Goodwin, 1995; Caine and Minor, 2009; Balsamo et al., 2012) with continuing fault slip, further enhanced the overall strain-hardening behavior within the fault zone, which continued propagating outward into the undeformed sediments. Under the new kinematically induced stress field, dense clusters of fault-parallel deformation bands progressively developed around pre-existing faults as well as inclined conjugate sets (Fig. 3.15b). At this stage the mixed zone formed, next to the narrow fault core, and cementation started along deforming structures inside these domains. This is further confirmed by the isotopic signature shown by concretions close to the master fault, which suggests cementation acted by fluids with composition close to the marine water (Fig. 3.11c, d).

Eventually, the fault zone reached a critical width and a threshold value of overall strength, deformation delocalization ceased, and further slip was accommodated inside the fault core and along the master fault (Fig. 3.15c). According to isotopic data from concretions, this happened when fluids circulating within the Scandale sandstone were located in the mixing zone between marine and meteoric water. In the fault core, thin layers of black gouge formed, indicating occurrence of coseismic events (Balsamo et al., 2014). Seismic activity supports further increase of fault strength and this provides a mechanical explanation for the formation of conjugate R and $R^1$ shears (Davis et al., 2000; Ahlgren, 2001; Katz et al., 2004) at this stage, as a consequence of greater rock strength overcome by the kinematically-induced stress field within the fault zone. Development of R and $R^1$ shears might have helped dissipating coseismic other than interseismic slip. Isotopic signature of concretions formed along DB1 and DB2 deformation band sets and involved in deformation, indicates ongoing cementation and faulting in a diagenetic environment progressively shoaling upwards and shifting towards meteoric fluids.

Concomitant formation of DB1 and DB2 deformation band clusters overprinting the previously formed fault-parallel ones (DB), and preferential cementation along them during the last stage of uplift, eventually resulted in a complex network of intersecting, strain-hardening structures that progressively hampered the prosecution of deformation within the fault zone. Residual deformation was accommodated inside the low-deformation zone, outside the fault zone *sensu strictu*, during the last stage of strain delocalization (Fig. 3.15d). This process occurred at extremely shallow depth and lower confining pressure, as indicated by (i) the narrower conjugate angles between deformation bands and faults (Mair, Elphick, et al., 2002), (ii) the particulate flow and more immature cataclastic fabrics, and (iii) the isotopic signature of the corresponding syn-kinematic concretions, which indicates shallow meteoric fluid conditions with a possible contribution from plant-related organic matter fermentation inside soils (Hudson, 1977; Nelson and Smith, 1996) (Fig. 3.11a).

## 3.9. Conclusions

We described the deformation architecture and the structural-diagenetic evolution of the Rocca di Neto fault, a complex extensional fault zone affecting poorly lithified, high-porosity sediments in the Crotone Basin, Southern Apennines. The fault zone shows widespread evidence of soft-sediment deformation (deformation bands and gouges) and preferential cementation (carbonate concretions), which concurrently occurred during fault slip. Major results from the combination of field measurements, microstructural, petrographic, diagenetic and isotopic data can be summarized in the following points.

(1) Particulate flow and cataclasis are the dominant deformation mechanisms. The first one was active during the early stages of deformation, while with increasing burial and fault displacement, cataclasis became dominant in narrow slip zones and black gouges. The switch between the two mechanisms was favored by the porosity loss induced by tectonic compaction, little burial and selective cementation.

(2) Concretions developed during fault activity and recorded the shift from several diagenetic environments during the uplift history of the fault zone. Oldest concretions are located along the fault core and recorded mixed marine and meteoric isotopic signatures. Through the damage zone, concretions become progressively younger and are characterized by isotopic data shifting progressively from mixed marine-meteoric to meteoric environment. Outside the footwall damage zone, isotopic data show a marked meteoric signature, with contribution from fluids interacting with soils and organic matter alteration.

(3) Physical (tectonic compaction) and chemical (selective cementation) strain-hardening processes caused initial delocalization and outward propagation of deformation, followed by localization and onset of deformations triggered by the kinematically-induced stress field. Eventually, strain-hardening hampered further significant deformation within the damage zone and favored late-stage delocalization of low-displacement deformation banding and faulting in the low-deformation zone.

(4) Occurrence of a simple shear-related deformation fabric overprinting fault-parallel deformation bands and deformation band clusters, suggests that physical (and possibly chemical) strain-hardening is necessary to eventually increase the magnitude of the kinematically-induced stress field, up to values overcoming the yield strength of the tectonically compacted, poorly lithified sediments. Such a stress magnitude increase might have been favored by the onset of episodic coseismic activity.

(5) The overall deformation pattern suggests that activity of the Rocca di Neto fault zone occurred by aseismic creep and possibly slow slip (deformation bands), episodically overprinted by seismic slip (black gouges).

**Acknowledgements**

M. Mozafari is warmly thanked for fruitful discussion concerning diagenetic and isotopic data interpretation. F. Pessina is kindly acknowledged for the support during field work in the Crotone Basin. The authors wish also to thank E.M. Selmo and A. di Matteo for stable isotope analysis. A. Comelli and L. Barchi are acknowledged for thin section preparation and support during SEM image acquisition, respectively.

M. Pizzati collected field and laboratory data, provided their interpretations, and wrote the manuscript; F. Balsamo participated to fieldwork, contributed to data interpretation, and critically revised the manuscript; F. Storti participated to some fieldwork, contributed to data interpretation, and critically revised the manuscript; P. Iacumin contributed to the interpretation of isotopic data and critically revised the manuscript.

## Supplementary Material 1: Concretion Samples and Isotopic Dataset

TABLE 3.A1. CONCRETION SAMPLES AND POSITION ALONG THE FAULT ZONE

| n° | Sample name | Type and geometry | Thickness (cm) | Structural domain | Latitude | Longitude |
|---|---|---|---|---|---|---|
| 1 | RN1.C1 | Tabular fault-parallel | 4 | Low-deformation Zone | 39° 10' 55.13" N | 16° 59' 20.17" E |
| 2 | RN1.C1A | Tabular fault-parallel | 5 | Low-deformation Zone | 39° 10' 55.13" N | 16° 59' 20.17" E |
| 3 | RN1.C1B | Tabular fault-parallel | 9 | Low-deformation Zone | 39° 10' 54.65" N | 16° 59' 21.28" E |
| 4 | RN1.C2A | Tabular fault-parallel | 3 | Low-deformation Zone | 39° 10' 54.75" N | 16° 59' 20.63" E |
| 5 | RN1.C2B | Deformed fault-parallel | 3 | Footwall Mixed Zone | 39° 10' 54.07" N | 16° 59' 21.51" E |
| 6 | RN1.C3 | Tabular fault-parallel | 4 | Low-deformation Zone | 39° 10' 54.43" N | 16° 59' 20.89" E |
| 7 | RN1.C4 | Tabular erosive surface | 6 | Low-deformation Zone | 39° 10' 54.41" N | 16° 59' 20.89" E |
| 8 | RN1.C5 | Tabular fault-parallel | 7 | Footwall Damage Zone | 39° 10' 53.83" N | 16° 59' 21.25" E |
| 9 | RN1.C6 | Tabular fault-parallel | 3.5 | Footwall Mixed Zone | 39° 10' 53.66" N | 16° 59' 21.21" E |
| 10 | RN1.C7 | Deformed fault-parallel | 8 | Footwall Mixed Zone | 39° 10' 53.63" N | 16° 59' 21.19" E |
| 11 | RN1.C8 | Deformed fault-parallel | 4 | Fault Core | 39° 10' 53.50" N | 16° 59' 21.20" E |
| 12 | RN1.C8B | Deformed fault-parallel | 6.5 | Fault Core | 39° 10' 53.50" N | 16° 59' 21.20" E |
| 13 | RN1.C9 | Deformed fault-parallel | 6 | Fault Core | 39° 10' 54.06" N | 16° 59' 21.57" E |
| 14 | RN1.C10 | Tabular fault-parallel | 4 | Footwall Damage Zone | 39° 10' 54.25" N | 16° 59' 21.45" E |
| 15 | RN1.C11 | Dissected-displaced | 5 | Footwall Mixed Zone | 39° 10' 53.62" N | 16° 59' 21.12" E |
| 16 | RN1.C12 | Tabular fault-parallel | 9 | Footwall Damage Zone | 39° 10' 54.91" N | 16° 59' 22.31" E |
| 17 | RN1.C13 | Dissected-displaced | 7 | Footwall Mixed Zone | 39° 10' 54.19" N | 16° 59' 21.81" E |
| 18 | RN1.C14 | Dissected-displaced | 3 | Fault Core | 39° 10' 54.02" N | 16° 59' 21.85" E |
| 19 | RN1.C15 | Deformed fault-parallel | 4 | Fault Core | 39° 10' 54.06" N | 16° 59' 21.90" E |
| 20 | RN2.C1 | Tabular fault-parallel | 7 | Footwall Damage Zone | 39° 10' 54.84" N | 16° 59' 21.56" E |
| 21 | RN2.C2 | Dissected-displaced | 11 | Footwall Mixed Zone | 39° 10' 54.39" N | 16° 59' 22.28" E |
| 22 | RN3.C1 | Tabular fault-parallel | 5 | Footwall Damage Zone | 39° 10' 54.99" N | 16° 59' 21.63" E |
| 23 | RN3.C2 | Deformed fault-parallel | 8 | Footwall Mixed Zone | 39° 10' 54.75" N | 16° 59' 22.76" E |

**Table 3.A1.** Concretion sample name, morphology and type, maximum measured thickness, structural domain along the fault zone, geographical coordinates.

Table 3.A2. COMPLETE ISOTOPIC DATASET

| n° | Sample name | Type and geometry | Structural domain | $\delta^{13}C$ (‰ VPDB) | $\delta^{18}O$ (‰ VPDB) |
|---|---|---|---|---|---|
| 1 | RN1.C1 R1 | Tabular fault-parallel | Low-deformation Zone | -5,63 | -13,18 |
| 2 | RN1.C1 R2 | Tabular fault-parallel | Low-deformation Zone | -5,57 | -12,78 |

| | | | | | |
|---|---|---|---|---|---|
| 3 | RN1.C1 R3 | Tabular fault-parallel | Low-deformation Zone | -5,96 | -13,76 |
| 4 | RN1.C1 R4 | Tabular fault-parallel | Low-deformation Zone | -5,77 | -12,89 |
| 5 | RN1.C1 R5 | Tabular fault-parallel | Low-deformation Zone | -5,43 | -13,49 |
| 6 | RN1.C1 R6 | Tabular fault-parallel | Low-deformation Zone | -5,63 | -12,68 |
| 7 | RN1.C1 R7 | Tabular fault-parallel | Low-deformation Zone | -5,30 | -11,73 |
| 8 | RN1.C1 R8 | Tabular fault-parallel | Low-deformation Zone | -6,17 | -13,83 |
| 9 | RN1.C1 R9 | Tabular fault-parallel | Low-deformation Zone | -5,91 | -15,68 |
| 10 | RN1.C1 C1 | Tabular fault-parallel | Low-deformation Zone | -5,94 | -12,40 |
| 11 | RN1.C1 C2 | Tabular fault-parallel | Low-deformation Zone | -6,09 | -13,31 |
| 12 | RN1.C1 C3 | Tabular fault-parallel | Low-deformation Zone | -5,70 | -14,31 |
| 13 | RN1.C1 C4 | Tabular fault-parallel | Low-deformation Zone | -5,15 | -9,20 |
| 14 | RN1.C1A R1 | Tabular fault-parallel | Low-deformation Zone | -5,39 | -12,67 |
| 15 | RN1.C1A R2 | Tabular fault-parallel | Low-deformation Zone | -5,47 | -13,92 |
| 16 | RN1.C1A R3 | Tabular fault-parallel | Low-deformation Zone | -5,48 | -13,39 |
| 17 | RN1.C1A R4 | Tabular fault-parallel | Low-deformation Zone | -6,14 | -15,43 |
| 18 | RN1.C1A R5 | Tabular fault-parallel | Low-deformation Zone | -5,44 | -13,41 |
| 19 | RN1.C1A R6 | Tabular fault-parallel | Low-deformation Zone | -5,71 | -13,70 |
| 20 | RN1.C1A R7 | Tabular fault-parallel | Low-deformation Zone | -5,81 | -14,37 |
| 21 | RN1.C1A R8 | Tabular fault-parallel | Low-deformation Zone | -5,44 | -14,32 |
| 22 | RN1.C1A R9 | Tabular fault-parallel | Low-deformation Zone | -5,57 | -13,09 |
| 23 | RN1.C1A R10 | Tabular fault-parallel | Low-deformation Zone | -5,78 | -12,57 |
| 24 | RN1.C1A R11 | Tabular fault-parallel | Low-deformation Zone | -5,95 | -14,76 |
| 25 | RN1.C1A C1 | Tabular fault-parallel | Low-deformation Zone | -6,16 | -14,21 |
| 26 | RN1.C1A C2 | Tabular fault-parallel | Low-deformation Zone | -5,88 | -14,64 |
| 27 | RN1.C1A C3 | Tabular fault-parallel | Low-deformation Zone | -6,30 | -15,96 |
| 28 | RN1.C1A C4 | Tabular fault-parallel | Low-deformation Zone | -5,22 | -13,48 |
| 29 | RN1.C1A C5 | Tabular fault-parallel | Low-deformation Zone | -6,41 | -15,72 |
| 30 | RN1.C2 R1 | Tabular fault-parallel | Low-deformation Zone | -5,51 | -19,29 |
| 31 | RN1.C2 R2 | Tabular fault-parallel | Low-deformation Zone | -4,12 | -12,43 |
| 32 | RN1.C2 R3 | Tabular fault-parallel | Low-deformation Zone | -5,32 | -16,57 |
| 33 | RN1.C2 R4 | Tabular fault-parallel | Low-deformation Zone | -4,75 | -15,64 |
| 34 | RN1.C2 R5 | Tabular fault-parallel | Low-deformation Zone | -4,31 | -14,23 |
| 35 | RN1.C2 R6 | Tabular fault-parallel | Low-deformation Zone | -5,24 | -16,73 |
| 36 | RN1.C2 C1 | Tabular fault-parallel | Low-deformation Zone | -5,38 | -18,61 |
| 37 | RN1.C2 C2 | Tabular fault-parallel | Low-deformation Zone | -4,84 | -15,18 |
| 38 | RN1.C2 C3 | Tabular fault-parallel | Low-deformation Zone | -6,05 | -17,98 |
| 39 | RN1.C2 C4 | Tabular fault-parallel | Low-deformation Zone | -5,28 | -17,81 |
| 40 | RN1.C2 C5 | Tabular fault-parallel | Low-deformation Zone | -6,30 | -20,56 |
| 41 | RN1.C3 R1 | Tabular fault-parallel | Low-deformation Zone | -5,50 | -17,40 |
| 42 | RN1.C3 R2 | Tabular fault-parallel | Low-deformation Zone | -5,35 | -19,49 |
| 43 | RN1.C3 R3 | Tabular fault-parallel | Low-deformation Zone | -5,72 | -20,18 |
| 44 | RN1.C3 R4 | Tabular fault-parallel | Low-deformation Zone | -5,59 | -19,13 |
| 45 | RN1.C3 R5 | Tabular fault-parallel | Low-deformation Zone | -6,29 | -19,49 |
| 46 | RN1.C3 R6 | Tabular fault-parallel | Low-deformation Zone | -6,17 | -18,89 |
| 47 | RN1.C3 C1 | Tabular fault-parallel | Low-deformation Zone | -6,71 | -15,87 |
| 48 | RN1.C3 C2 | Tabular fault-parallel | Low-deformation Zone | -5,78 | -16,30 |
| 49 | RN1.C3 C3 | Tabular fault-parallel | Low-deformation Zone | -5,51 | -18,81 |

| | | | | | |
|---|---|---|---|---|---|
| 50 | RN1.C3 C4 | Tabular fault-parallel | Low-deformation Zone | -5,89 | -20,10 |
| 51 | RN1.C3 C5 | Tabular fault-parallel | Low-deformation Zone | -4,56 | -13,31 |
| 52 | RN1.C4 R1 | Tabular erosive surface | Low-deformation Zone | -6,66 | -9,30 |
| 53 | RN1.C4 R2 | Tabular erosive surface | Low-deformation Zone | -3,10 | -4,03 |
| 54 | RN1.C4 R3 | Tabular erosive surface | Low-deformation Zone | -2,31 | -2,58 |
| 55 | RN1.C4 R4 | Tabular erosive surface | Low-deformation Zone | -1,55 | -0,08 |
| 56 | RN1.C4 R5 | Tabular erosive surface | Low-deformation Zone | -2,77 | -3,57 |
| 57 | RN1.C4 R6 | Tabular erosive surface | Low-deformation Zone | -2,97 | -3,61 |
| 58 | RN1.C4 R7 | Tabular erosive surface | Low-deformation Zone | -4,18 | -5,86 |
| 59 | RN1.C4 R8 | Tabular erosive surface | Low-deformation Zone | -2,30 | -2,28 |
| 60 | RN1.C4 R9 | Tabular erosive surface | Low-deformation Zone | -4,52 | -5,86 |
| 61 | RN1.C4 R10 | Tabular erosive surface | Low-deformation Zone | -5,67 | -8,98 |
| 62 | RN1.C4 C1 | Tabular erosive surface | Low-deformation Zone | -6,11 | -9,39 |
| 63 | RN1.C4 C2 | Tabular erosive surface | Low-deformation Zone | -6,07 | -9,24 |
| 64 | RN1.C4 C3 | Tabular erosive surface | Low-deformation Zone | -5,64 | -9,31 |
| 65 | RN1.C4 C4 | Tabular erosive surface | Low-deformation Zone | -5,40 | -9,08 |
| 66 | RN1.C4 C5 | Tabular erosive surface | Low-deformation Zone | -5,69 | -9,28 |
| 67 | RN1.C4 C6 | Tabular erosive surface | Low-deformation Zone | -5,49 | -9,19 |
| 68 | RN1.C4 C7 | Tabular erosive surface | Low-deformation Zone | -5,55 | -9,23 |
| 69 | RN1.C5 R1 | Tabular fault-parallel | Footwall Damage Zone | -3,34 | -4,03 |
| 70 | RN1.C5 R2 | Tabular fault-parallel | Footwall Damage Zone | -1,35 | -0,03 |
| 71 | RN1.C5 R3 | Tabular fault-parallel | Footwall Damage Zone | -1,32 | -0,66 |
| 72 | RN1.C5 R4 | Tabular fault-parallel | Footwall Damage Zone | -3,20 | -2,40 |
| 73 | RN1.C5 R5 | Tabular fault-parallel | Footwall Damage Zone | -2,87 | -1,79 |
| 74 | RN1.C5 R6 | Tabular fault-parallel | Footwall Damage Zone | -2,54 | -1,39 |
| 75 | RN1.C5 C1 | Tabular fault-parallel | Footwall Damage Zone | -1,25 | -0,02 |
| 76 | RN1.C5 C2 | Tabular fault-parallel | Footwall Damage Zone | -2,39 | -1,09 |
| 77 | RN1.C5 C3 | Tabular fault-parallel | Footwall Damage Zone | -1,80 | -0,59 |
| 78 | RN1.C5 C4 | Tabular fault-parallel | Footwall Damage Zone | -2,74 | -1,82 |
| 79 | RN1.C5 C5 | Tabular fault-parallel | Footwall Damage Zone | -1,94 | -1,19 |
| 80 | RN1.C5 C6 | Tabular fault-parallel | Footwall Damage Zone | -1,84 | -1,30 |
| 81 | RN1.C5 C7 | Tabular fault-parallel | Footwall Damage Zone | -2,08 | -1,21 |
| 82 | RN1.C5 C8 | Tabular fault-parallel | Footwall Damage Zone | -1,98 | -1,52 |
| 83 | RN1.C5 C9 | Tabular fault-parallel | Footwall Damage Zone | -1,96 | -1,35 |
| 84 | RN1.C5 C10 | Tabular fault-parallel | Footwall Damage Zone | -1,86 | -1,27 |
| 85 | RN1.C6 R1 | Tabular fault-parallel | Footwall Mixed Zone | -2,25 | -1,27 |
| 86 | RN1.C6 R2 | Tabular fault-parallel | Footwall Mixed Zone | -2,30 | -1,44 |
| 87 | RN1.C6 R3 | Tabular fault-parallel | Footwall Mixed Zone | -2,17 | -1,02 |
| 88 | RN1.C6 R4 | Tabular fault-parallel | Footwall Mixed Zone | -2,44 | -1,18 |
| 89 | RN1.C6 R5 | Tabular fault-parallel | Footwall Mixed Zone | -2,56 | -0,91 |
| 90 | RN1.C6 R6 | Tabular fault-parallel | Footwall Mixed Zone | -2,04 | -1,33 |
| 91 | RN1.C6 R7 | Tabular fault-parallel | Footwall Mixed Zone | -2,86 | -1,24 |
| 92 | RN1.C6 C1 | Tabular fault-parallel | Footwall Mixed Zone | -1,89 | -1,32 |
| 93 | RN1.C6 C2 | Tabular fault-parallel | Footwall Mixed Zone | -2,69 | -1,49 |
| 94 | RN1.C6 C3 | Tabular fault-parallel | Footwall Mixed Zone | -2,59 | -1,26 |
| 95 | RN1.C6 C4 | Tabular fault-parallel | Footwall Mixed Zone | -2,89 | -0,92 |
| 96 | RN1.C6 C5 | Tabular fault-parallel | Footwall Mixed Zone | -2,86 | -1,30 |

| | | | | | |
|---|---|---|---|---|---|
| 97 | RN1.C6 C6 | Tabular fault-parallel | Footwall Mixed Zone | -2,61 | -1,20 |
| 98 | RN1.C6 C7 | Tabular fault-parallel | Footwall Mixed Zone | -2,89 | -0,77 |
| 99 | RN1.C6 C8 | Tabular fault-parallel | Footwall Mixed Zone | -3,98 | -0,71 |
| 100 | RN1.C7 R1 | Deformed fault-parallel | Footwall Mixed Zone | -1,83 | -1,62 |
| 101 | RN1.C7 R2 | Deformed fault-parallel | Footwall Mixed Zone | -2,47 | -0,95 |
| 102 | RN1.C7 R3 | Deformed fault-parallel | Footwall Mixed Zone | -2,12 | -0,82 |
| 103 | RN1.C7 R4 | Deformed fault-parallel | Footwall Mixed Zone | -2,44 | -1,21 |
| 104 | RN1.C7 R5 | Deformed fault-parallel | Footwall Mixed Zone | -2,34 | -1,45 |
| 105 | RN1.C7 R6 | Deformed fault-parallel | Footwall Mixed Zone | -1,78 | -0,89 |
| 106 | RN1.C7 R7 | Deformed fault-parallel | Footwall Mixed Zone | -2,03 | -1,01 |
| 107 | RN1.C7 R8 | Deformed fault-parallel | Footwall Mixed Zone | -2,12 | -0,92 |
| 108 | RN1.C7 R9 | Deformed fault-parallel | Footwall Mixed Zone | -2,14 | -0,92 |
| 109 | RN1.C7 R10 | Deformed fault-parallel | Footwall Mixed Zone | -2,85 | -1,84 |
| 110 | RN1.C7 R11 | Deformed fault-parallel | Footwall Mixed Zone | -2,50 | -1,59 |
| 111 | RN1.C7 C1 | Deformed fault-parallel | Footwall Mixed Zone | -1,95 | -1,07 |
| 112 | RN1.C7 C2 | Deformed fault-parallel | Footwall Mixed Zone | -2,15 | -0,88 |
| 113 | RN1.C7 C3 | Deformed fault-parallel | Footwall Mixed Zone | -2,19 | -1,12 |
| 114 | RN1.C7 C4 | Deformed fault-parallel | Footwall Mixed Zone | -2,35 | -1,60 |
| 115 | RN1.C7 C5 | Deformed fault-parallel | Footwall Mixed Zone | -2,20 | -1,00 |
| 116 | RN1.C7 C6 | Deformed fault-parallel | Footwall Mixed Zone | -2,65 | -1,38 |
| 117 | RN1.C7 C7 | Deformed fault-parallel | Footwall Mixed Zone | -3,04 | -1,78 |
| 118 | RN1.C8 R1 | Deformed fault-parallel | Fault Core | -2,74 | -1,35 |
| 119 | RN1.C8 R2 | Deformed fault-parallel | Fault Core | -2,62 | -1,29 |
| 120 | RN1.C8 R3 | Deformed fault-parallel | Fault Core | -2,50 | -1,45 |
| 121 | RN1.C8 R4 | Deformed fault-parallel | Fault Core | -2,42 | -1,34 |
| 122 | RN1.C8 R5 | Deformed fault-parallel | Fault Core | -3,33 | -1,88 |
| 123 | RN1.C8 R6 | Deformed fault-parallel | Fault Core | -2,93 | -1,41 |
| 124 | RN1.C8 R7 | Deformed fault-parallel | Fault Core | -3,00 | -1,89 |
| 125 | RN1.C8 R8 | Deformed fault-parallel | Fault Core | -3,16 | -1,79 |
| 126 | RN1.C8 R9 | Deformed fault-parallel | Fault Core | -2,79 | -1,65 |
| 127 | RN1.C8 R10 | Deformed fault-parallel | Fault Core | -2,59 | -1,41 |
| 128 | RN1.C8 C1 | Deformed fault-parallel | Fault Core | -2,75 | -1,44 |
| 129 | RN1.C8 C2 | Deformed fault-parallel | Fault Core | -3,13 | -1,82 |
| 130 | RN1.C8 C3 | Deformed fault-parallel | Fault Core | -2,88 | -1,68 |
| 131 | RN1.C8 C4 | Deformed fault-parallel | Fault Core | -2,73 | -1,60 |
| 132 | RN1.C8 C5 | Deformed fault-parallel | Fault Core | -3,25 | -1,73 |
| 133 | RN1.C8 C6 | Deformed fault-parallel | Fault Core | -2,84 | -1,29 |
| 134 | RN1.C8 C7 | Deformed fault-parallel | Fault Core | -3,29 | -1,44 |
| 135 | RN1.C8B R1 | Deformed fault-parallel | Fault Core | -3,17 | -1,89 |
| 136 | RN1.C8B R2 | Deformed fault-parallel | Fault Core | -3,67 | -1,00 |
| 137 | RN1.C8B R3 | Deformed fault-parallel | Fault Core | -2,68 | -1,43 |
| 138 | RN1.C8B R4 | Deformed fault-parallel | Fault Core | -2,20 | -1,16 |
| 139 | RN1.C8B R5 | Deformed fault-parallel | Fault Core | -2,25 | -1,23 |
| 140 | RN1.C8B R6 | Deformed fault-parallel | Fault Core | -2,96 | -0,90 |
| 141 | RN1.C8B R7 | Deformed fault-parallel | Fault Core | -3,01 | -1,45 |
| 142 | RN1.C8B R8 | Deformed fault-parallel | Fault Core | -2,43 | -1,31 |
| 143 | RN1.C8B R9 | Deformed fault-parallel | Fault Core | -2,94 | -1,10 |

| | | | | | |
|---|---|---|---|---|---|
| 144 | RN1.C8B C1 | Deformed fault-parallel | Fault Core | -2,46 | -0,96 |
| 145 | RN1.C8B C2 | Deformed fault-parallel | Fault Core | -2,58 | -1,18 |
| 146 | RN1.C8B C3 | Deformed fault-parallel | Fault Core | -2,67 | -1,54 |
| 147 | RN1.C8B C4 | Deformed fault-parallel | Fault Core | -2,94 | -1,46 |
| 148 | RN1.C8B C5 | Deformed fault-parallel | Fault Core | -2,30 | -1,16 |
| 149 | RN1.C8B C6 | Deformed fault-parallel | Fault Core | -2,71 | -1,48 |
| 150 | RN1.C8B C7 | Deformed fault-parallel | Fault Core | -2,86 | -1,40 |
| 151 | RN1.C8B C8 | Deformed fault-parallel | Fault Core | -2,51 | -1,10 |
| 152 | RN1.C8B C9 | Deformed fault-parallel | Fault Core | -4,03 | -1,07 |
| 153 | RN1.C9 R1 | Deformed fault-parallel | Fault Core | -5,02 | -3,73 |
| 154 | RN1.C9 R2 | Deformed fault-parallel | Fault Core | -4,33 | -4,18 |
| 155 | RN1.C9 R3 | Deformed fault-parallel | Fault Core | -3,82 | -3,58 |
| 156 | RN1.C9 R4 | Deformed fault-parallel | Fault Core | -3,74 | -4,35 |
| 157 | RN1.C9 R5 | Deformed fault-parallel | Fault Core | -3,07 | -2,76 |
| 158 | RN1.C9 R6 | Deformed fault-parallel | Fault Core | -4,18 | -3,83 |
| 159 | RN1.C9 R7 | Deformed fault-parallel | Fault Core | -3,09 | -2,93 |
| 160 | RN1.C9 R8 | Deformed fault-parallel | Fault Core | -3,20 | -3,00 |
| 161 | RN1.C9 R9 | Deformed fault-parallel | Fault Core | -3,18 | -2,70 |
| 162 | RN1.C9 R10 | Deformed fault-parallel | Fault Core | -3,56 | -4,01 |
| 163 | RN1.C9 R11 | Deformed fault-parallel | Fault Core | -3,38 | -3,02 |
| 164 | RN1.C9 C1 | Deformed fault-parallel | Fault Core | -4,25 | -6,82 |
| 165 | RN1.C9 C2 | Deformed fault-parallel | Fault Core | -4,35 | -6,30 |
| 166 | RN1.C9 C3 | Deformed fault-parallel | Fault Core | -4,27 | -5,13 |
| 167 | RN1.C9 C4 | Deformed fault-parallel | Fault Core | -3,97 | -4,45 |
| 168 | RN1.C9 C5 | Deformed fault-parallel | Fault Core | -3,37 | -3,25 |
| 169 | RN1.C9 C6 | Deformed fault-parallel | Fault Core | -3,20 | -3,16 |
| 170 | RN1.C9 C7 | Deformed fault-parallel | Fault Core | -3,89 | -3,03 |
| 171 | RN1.C10 R1 | Tabular fault-parallel | Footwall Damage Zone | -3,40 | -2,70 |
| 172 | RN1.C10 R2 | Tabular fault-parallel | Footwall Damage Zone | -2,52 | -1,91 |
| 173 | RN1.C10 R3 | Tabular fault-parallel | Footwall Damage Zone | -2,88 | -2,26 |
| 174 | RN1.C10 R4 | Tabular fault-parallel | Footwall Damage Zone | -3,34 | -2,56 |
| 175 | RN1.C10 R5 | Tabular fault-parallel | Footwall Damage Zone | -2,48 | -1,82 |
| 176 | RN1.C10 R6 | Tabular fault-parallel | Footwall Damage Zone | -2,82 | -2,22 |
| 177 | RN1.C10 R7 | Tabular fault-parallel | Footwall Damage Zone | -2,68 | -1,47 |
| 178 | RN1.C10 C1 | Tabular fault-parallel | Footwall Damage Zone | -3,23 | -1,16 |
| 179 | RN1.C10 C2 | Tabular fault-parallel | Footwall Damage Zone | -2,63 | -1,29 |
| 180 | RN1.C10 C3 | Tabular fault-parallel | Footwall Damage Zone | -3,42 | -2,83 |
| 181 | RN1.C10 C4 | Tabular fault-parallel | Footwall Damage Zone | -3,41 | -2,58 |
| 182 | RN1.C10 C5 | Tabular fault-parallel | Footwall Damage Zone | -2,69 | -2,65 |
| 183 | RN1.C11 R1 | Dissected-displaced | Footwall Mixed Zone | -2,55 | -1,06 |
| 184 | RN1.C11 R2 | Dissected-displaced | Footwall Mixed Zone | -2,36 | -0,85 |
| 185 | RN1.C11 R3 | Dissected-displaced | Footwall Mixed Zone | -2,93 | -1,31 |
| 186 | RN1.C11 R4 | Dissected-displaced | Footwall Mixed Zone | -2,29 | -1,06 |
| 187 | RN1.C11 R5 | Dissected-displaced | Footwall Mixed Zone | -2,13 | -1,06 |
| 188 | RN1.C11 R6 | Dissected-displaced | Footwall Mixed Zone | -2,25 | -0,97 |
| 189 | RN1.C11 C1 | Dissected-displaced | Footwall Mixed Zone | -2,40 | -1,15 |
| 190 | RN1.C11 C2 | Dissected-displaced | Footwall Mixed Zone | -2,66 | -1,40 |

| | | | | | |
|---|---|---|---|---|---|
| 191 | RN1.C11 C3 | Dissected-displaced | Footwall Mixed Zone | -2,86 | -1,04 |
| 192 | RN1.C11 C4 | Dissected-displaced | Footwall Mixed Zone | -2,32 | -0,92 |
| 193 | RN1.C11 C5 | Dissected-displaced | Footwall Mixed Zone | -2,22 | -0,99 |
| 194 | RN1.C11 C6 | Dissected-displaced | Footwall Mixed Zone | -2,12 | -0,92 |
| 195 | RN1.C12 R1 | Tabular fault-parallel | Footwall Damage Zone | -5,39 | -8,52 |
| 196 | RN1.C12 R2 | Tabular fault-parallel | Footwall Damage Zone | -4,92 | -9,34 |
| 197 | RN1.C12 R3 | Tabular fault-parallel | Footwall Damage Zone | -5,17 | -10,35 |
| 198 | RN1.C12 R4 | Tabular fault-parallel | Footwall Damage Zone | -3,22 | -2,34 |
| 199 | RN1.C12 R5 | Tabular fault-parallel | Footwall Damage Zone | -4,34 | -3,52 |
| 200 | RN1.C12 R6 | Tabular fault-parallel | Footwall Damage Zone | -2,92 | -2,60 |
| 201 | RN1.C12 R7 | Tabular fault-parallel | Footwall Damage Zone | -5,35 | -8,42 |
| 202 | RN1.C12 R8 | Tabular fault-parallel | Footwall Damage Zone | -5,12 | -7,16 |
| 203 | RN1.C12 C1 | Tabular fault-parallel | Footwall Damage Zone | -4,54 | -3,92 |
| 204 | RN1.C12 C2 | Tabular fault-parallel | Footwall Damage Zone | -4,84 | -4,91 |
| 205 | RN1.C12 C3 | Tabular fault-parallel | Footwall Damage Zone | -4,49 | -3,91 |
| 206 | RN1.C12 C4 | Tabular fault-parallel | Footwall Damage Zone | -5,03 | -4,57 |
| 207 | RN1.C12 C5 | Tabular fault-parallel | Footwall Damage Zone | -4,66 | -4,77 |
| 208 | RN1.C12 C6 | Tabular fault-parallel | Footwall Damage Zone | -4,06 | -3,99 |
| 209 | RN1.C12 C7 | Tabular fault-parallel | Footwall Damage Zone | -3,73 | -2,96 |
| 210 | RN1.C12 C8 | Tabular fault-parallel | Footwall Damage Zone | -4,39 | -3,53 |
| 211 | RN1.C13 R1 | Dissected-displaced | Footwall Mixed Zone | -3,28 | -1,18 |
| 212 | RN1.C13 R2 | Dissected-displaced | Footwall Mixed Zone | -1,70 | -0,55 |
| 213 | RN1.C13 R3 | Dissected-displaced | Footwall Mixed Zone | -1,69 | -0,41 |
| 214 | RN1.C13 R4 | Dissected-displaced | Footwall Mixed Zone | -1,32 | -0,54 |
| 215 | RN1.C13 R5 | Dissected-displaced | Footwall Mixed Zone | -1,52 | -0,36 |
| 216 | RN1.C13 R6 | Dissected-displaced | Footwall Mixed Zone | -1,38 | -0,34 |
| 217 | RN1.C13 R7 | Dissected-displaced | Footwall Mixed Zone | -1,70 | -0,70 |
| 218 | RN1.C13 R8 | Dissected-displaced | Footwall Mixed Zone | -1,84 | -0,31 |
| 219 | RN1.C13 R9 | Dissected-displaced | Footwall Mixed Zone | -2,69 | -0,67 |
| 220 | RN1.C13 R10 | Dissected-displaced | Footwall Mixed Zone | -2,01 | -0,38 |
| 221 | RN.C13 C1 | Dissected-displaced | Footwall Mixed Zone | -2,20 | -0,51 |
| 222 | RN.C13 C2 | Dissected-displaced | Footwall Mixed Zone | -2,04 | -0,56 |
| 223 | RN.C13 C3 | Dissected-displaced | Footwall Mixed Zone | -2,03 | -0,68 |
| 224 | RN.C13 C4 | Dissected-displaced | Footwall Mixed Zone | -2,07 | -0,59 |
| 225 | RN.C13 C5 | Dissected-displaced | Footwall Mixed Zone | -2,27 | -0,66 |
| 226 | RN.C13 C6 | Dissected-displaced | Footwall Mixed Zone | -2,53 | -0,37 |
| 227 | RN.C13 C7 | Dissected-displaced | Footwall Mixed Zone | -2,12 | -0,43 |
| 228 | RN.C13 C8 | Dissected-displaced | Footwall Mixed Zone | -1,71 | -0,40 |
| 229 | RN.C13 C9 | Dissected-displaced | Footwall Mixed Zone | -2,82 | -1,01 |
| 230 | RN.C13 C10 | Dissected-displaced | Footwall Mixed Zone | -2,30 | -0,75 |
| 231 | RN1.C14 R1 | Dissected-displaced | Fault Core | -3,67 | -1,54 |
| 232 | RN1.C14 R2 | Dissected-displaced | Fault Core | -3,88 | -1,52 |
| 233 | RN1.C14 R3 | Dissected-displaced | Fault Core | -4,40 | -1,29 |
| 234 | RN1.C14 R4 | Dissected-displaced | Fault Core | -3,29 | -1,38 |
| 235 | RN1.C14 R5 | Dissected-displaced | Fault Core | -3,34 | -1,08 |
| 236 | RN1.C14 R6 | Dissected-displaced | Fault Core | -3,45 | -1,20 |
| 237 | RN1.C14 C1 | Dissected-displaced | Fault Core | -3,75 | -1,37 |

| | | | | | |
|---|---|---|---|---|---|
| 238 | RN1.C14 C2 | Dissected-displaced | Fault Core | -3,76 | -1,32 |
| 239 | RN1.C14 C3 | Dissected-displaced | Fault Core | -3,23 | -1,41 |
| 240 | RN1.C14 C4 | Dissected-displaced | Fault Core | -2,92 | -1,46 |
| 241 | RN1.C15 R1 | Deformed fault-parallel | Fault Core | -3,67 | -1,32 |
| 242 | RN1.C15 R2 | Deformed fault-parallel | Fault Core | -2,82 | -1,57 |
| 243 | RN1.C15 R3 | Deformed fault-parallel | Fault Core | -2,87 | -1,63 |
| 244 | RN1.C15 R4 | Deformed fault-parallel | Fault Core | -2,88 | -1,25 |
| 245 | RN1.C15 R5 | Deformed fault-parallel | Fault Core | -3,75 | -2,73 |
| 246 | RN1.C15 R6 | Deformed fault-parallel | Fault Core | -2,87 | -1,22 |
| 247 | RN1.C15 R7 | Deformed fault-parallel | Fault Core | -3,16 | -0,49 |
| 248 | RN1.C15 R8 | Deformed fault-parallel | Fault Core | -2,53 | -1,23 |
| 249 | RN1.C15 R9 | Deformed fault-parallel | Fault Core | -2,64 | -1,30 |
| 250 | RN1.C15 R10 | Deformed fault-parallel | Fault Core | -3,62 | -1,70 |
| 251 | RN1.C15 R11 | Deformed fault-parallel | Fault Core | -2,84 | -2,28 |
| 252 | RN1.C15 R12 | Deformed fault-parallel | Fault Core | -3,57 | -1,82 |
| 253 | RN1.C15 R13 | Deformed fault-parallel | Fault Core | -2,79 | -1,71 |
| 254 | RN1.C15 R14 | Deformed fault-parallel | Fault Core | -2,78 | -0,98 |
| 255 | RN1.C15 R15 | Deformed fault-parallel | Fault Core | -2,86 | -0,95 |
| 256 | RN1.C15 R16 | Deformed fault-parallel | Fault Core | -3,35 | -1,17 |
| 257 | RN1.C15 R17 | Deformed fault-parallel | Fault Core | -2,97 | -0,93 |
| 258 | RN1.C15 R18 | Deformed fault-parallel | Fault Core | -2,60 | -1,27 |
| 259 | RN1.C15 R19 | Deformed fault-parallel | Fault Core | -3,08 | -0,60 |
| 260 | RN1.C15 R20 | Deformed fault-parallel | Fault Core | -3,37 | -1,44 |
| 261 | RN1.C15 C1 | Deformed fault-parallel | Fault Core | -3,27 | -1,91 |
| 262 | RN1.C15 C2 | Deformed fault-parallel | Fault Core | -2,33 | -1,40 |
| 263 | RN1.C15 C3 | Deformed fault-parallel | Fault Core | -3,35 | -2,33 |
| 264 | RN1.C15 C4 | Deformed fault-parallel | Fault Core | -3,79 | -2,73 |
| 265 | RN1.C15 C5 | Deformed fault-parallel | Fault Core | -3,64 | -2,56 |
| 266 | RN1.C15 C6 | Deformed fault-parallel | Fault Core | -2,31 | -0,78 |
| 267 | RN1.C15 C7 | Deformed fault-parallel | Fault Core | -2,25 | -0,91 |
| 268 | RN1.C15 C8 | Deformed fault-parallel | Fault Core | -2,48 | -0,86 |
| 269 | RN1.C15 C9 | Deformed fault-parallel | Fault Core | -2,09 | -0,76 |
| 270 | RN1.C1 1 | Tabular fault-parallel | Low-deformation Zone | -6,09 | -12,34 |
| 271 | RN1.C1 2 | Tabular fault-parallel | Low-deformation Zone | -6,19 | -12,83 |
| 272 | RN1.C1 3 | Tabular fault-parallel | Low-deformation Zone | -6,07 | -16,00 |
| 273 | RN1.C1 4 | Tabular fault-parallel | Low-deformation Zone | -6,01 | -15,08 |
| 274 | RN1.C1 5 | Tabular fault-parallel | Low-deformation Zone | -6,16 | -16,23 |
| 275 | RN1.C2 1 | Tabular fault-parallel | Low-deformation Zone | -7,00 | -16,79 |
| 276 | RN1.C2 2 | Tabular fault-parallel | Low-deformation Zone | -5,58 | -19,47 |
| 277 | RN1.C2 3 | Tabular fault-parallel | Low-deformation Zone | -8,45 | -19,49 |
| 278 | RN1.C2 4 | Tabular fault-parallel | Low-deformation Zone | -5,60 | -17,57 |
| 279 | RN1.C2 5 | Tabular fault-parallel | Low-deformation Zone | -5,16 | -16,58 |
| 280 | RN1.C3 1 | Tabular fault-parallel | Low-deformation Zone | -5,74 | -19,79 |
| 281 | RN1.C3 2 | Tabular fault-parallel | Low-deformation Zone | -5,16 | -20,16 |
| 282 | RN1.C3 3 | Tabular fault-parallel | Low-deformation Zone | -5,78 | -23,08 |
| 283 | RN1.C3 4 | Tabular fault-parallel | Low-deformation Zone | -6,02 | -16,67 |
| 284 | RN1.C3 5 | Tabular fault-parallel | Low-deformation Zone | -5,94 | -22,36 |

| | | | | | |
|---|---|---|---|---|---|
| 285 | RN1.C4 1 | Tabular erosive surface | Low-deformation Zone | -5,88 | -9,49 |
| 286 | RN1.C5A 1 | Tabular fault-parallel | Footwall Damage Zone | -2,63 | -1,13 |
| 287 | RN1.C5B 1 | Tabular fault-parallel | Footwall Damage Zone | -1,99 | -1,19 |
| 288 | RN1.C5C 1 | Tabular fault-parallel | Footwall Damage Zone | -2,01 | -0,87 |
| 289 | RN1.C6 1 | Tabular fault-parallel | Footwall Damage Zone | -2,82 | -1,67 |
| 290 | RN1.C6 2 | Tabular fault-parallel | Footwall Damage Zone | -2,27 | -1,29 |
| 291 | RN1.C7A 1 | Deformed fault-parallel | Footwall Mixed Zone | -1,93 | -0,74 |
| 292 | RN1.C7A 2 | Deformed fault-parallel | Footwall Mixed Zone | -3,05 | -1,36 |
| 293 | RN1.C7B 1 | Deformed fault-parallel | Footwall Mixed Zone | -2,02 | -0,72 |
| 294 | RN1.C7B 2 | Deformed fault-parallel | Footwall Mixed Zone | -3,08 | -1,30 |
| 295 | RN1.C8 1 | Deformed fault-parallel | Fault Core | -3,06 | -1,68 |
| 296 | RN1.C8B 1 1 | Deformed fault-parallel | Fault Core | -2,66 | -1,02 |
| 297 | RN1.C8B 1 2 | Deformed fault-parallel | Fault Core | -3,54 | -1,41 |
| 298 | RN1.C8B 2 1 | Deformed fault-parallel | Fault Core | -3,25 | -1,11 |
| 299 | RN1.C8B 2 2 | Deformed fault-parallel | Fault Core | -3,40 | -1,53 |
| 300 | RN1.C9A 1 | Deformed fault-parallel | Fault Core | -3,81 | -3,80 |
| 301 | RN1.C9A 2 | Deformed fault-parallel | Fault Core | -4,71 | -3,39 |
| 302 | RN1.C9A 3 | Deformed fault-parallel | Fault Core | -4,80 | -4,58 |
| 303 | RN1.C9B 1 | Deformed fault-parallel | Fault Core | -5,34 | -7,11 |
| 304 | RN1.C9B 2 | Deformed fault-parallel | Fault Core | -4,71 | -8,09 |
| 305 | RN1.C10 1 | Tabular fault-parallel | Footwall Mixed Zone | -3,26 | -2,99 |
| 306 | RN1.C10 2 | Tabular fault-parallel | Footwall Mixed Zone | -3,64 | -2,30 |
| 307 | RN1.C10 3 | Tabular fault-parallel | Footwall Mixed Zone | -2,94 | -1,85 |
| 308 | RN1.C11 1 | Dissected-displaced | Footwall Damage Zone | -2,91 | -0,90 |
| 309 | RN1.C11 2 | Dissected-displaced | Footwall Damage Zone | -2,99 | -1,14 |
| 310 | RN1.C12A 1 | Tabular fault-parallel | Footwall Damage Zone | -2,41 | -1,18 |
| 311 | RN1.C12A 2 | Tabular fault-parallel | Footwall Damage Zone | -4,12 | -2,91 |
| 312 | RN1.C12B 1 | Tabular fault-parallel | Footwall Damage Zone | -2,75 | -1,91 |
| 313 | RN1.C12B 2 | Tabular fault-parallel | Footwall Damage Zone | -5,35 | -3,37 |
| 314 | RN1.C13A 1 | Dissected-displaced | Footwall Mixed Zone | -2,11 | -0,16 |
| 315 | RN1.C13A 2 | Dissected-displaced | Footwall Mixed Zone | -2,11 | -0,41 |
| 316 | RN1.C13B 1 | Dissected-displaced | Footwall Mixed Zone | -2,24 | -0,22 |
| 317 | RN1.C13B 2 | Dissected-displaced | Footwall Mixed Zone | -2,07 | -0,31 |
| 318 | RN1.C13B 3 | Dissected-displaced | Footwall Mixed Zone | -2,19 | -0,16 |
| 319 | RN1.C13B 4 | Dissected-displaced | Footwall Mixed Zone | -2,02 | -0,23 |
| 320 | RN1.C13B 5 | Dissected-displaced | Footwall Mixed Zone | -1,94 | -0,32 |
| 321 | RN1.C14 1 | Dissected-displaced | Fault Core | -2,86 | -1,60 |
| 322 | RN1.C15A 1 | Deformed fault-parallel | Fault Core | -3,02 | -1,98 |
| 323 | RN1.C15B 1 | Deformed fault-parallel | Fault Core | -7,51 | -2,31 |
| 324 | RN1.C15C 1 | Deformed fault-parallel | Fault Core | -2,44 | -0,74 |

**Table 3.A2.** Complete isotopic data plotted in Fig. 3.11 subdivided between the concretions sampled through the fault zone.

# CHAPTER 4

## Microstructures and Petrophysics of the Rocca di Neto Fault Zone

This chapter is focused on the microstructural characteristics of the deformed sediments along the Rocca di Neto fault zone, Crotone Basin. Deformation bands, gouges and faults are described in detail both at the meso as well as at the micro-scale and their fabric is quantitatively analysed by image analysis techniques. On the basis of the acquired data the deformation mechanism has been constrained (particulate flow vs cataclasis). Petrophysical properties measurement (permeability, grain size and porosity) allowed to evaluate the hydraulic behaviour of the overall fault zone and of the single deforming features.

*Displacement-dependent microstructural and petrophysical properties of deformation bands and gouges within poorly lithified sandstone deformed at shallow burial depth (Crotone Basin, Italy)*

Pizzati, M., Balsamo, F., Storti, F.

This manuscript is currently in preparation for submission to the *Journal of Structural Geology*.

# Displacement-dependent microstructural and petrophysical properties of deformation bands and gouges within poorly lithified sandstone deformed at shallow burial depth (Crotone Basin, Italy)

Mattia Pizzati, Fabrizio Balsamo and Fabrizio Storti

NEXT, Natural and Experimental Tectonics Research Group, Department of Chemistry, Life Sciences, and Environmental Sustainability, University of Parma, 43124 Parma, Italy.

## Abstract

We present here the results of meso and micro-structural analyses conducted on fault-related soft-sediment deformation structures affecting poorly lithified, high-porosity sediments of the Crotone Basin, southern Italy. The investigated fault zone affects a clay and sand stratigraphic succession and has a total displacement between 80-90 m. In the footwall damage zone deformation is achieved by a dense conjugate network of deformation bands, whereas thin gouge layers are developed within the foliated fault core. Permeability of pristine sandstone spans from $5.4 \times 10^4$ to $1.4 \times 10^5$ mD, while inside deformation bands it is reduced 1-2 orders of magnitude and 3-4 orders of magnitude within gouges. Microstructural observation and image analysis technique pointed out a deformation mechanism consisting of a combination of particulate flow during the early stage deformation followed by cataclasis after significant porosity loss. Cataclasis acted selectively on grains according to their mineralogy, with feldspar grains experiencing extensive intragranular fracturing while quartz grains are deformed mainly by abrasion of the asperities. Permeability data show that deformed sediments are barrier to fluid flow, but may behaved as partial conduit in unsaturated conditions as testified by the presence of selective cementation along bands.

### 4.1. Introduction

Petrophysical properties of deformed rocks depend on the overall fault zone structure, deformation mechanism, stress-strain conditions and depth at which deformation occurred (Antonellini and Aydin, 1994; Caine et al., 1996; Evans et al., 1997; Person et al., 2000; Fisher and Knipe, 2001; Ballas et al., 2012; Bense et al., 2013). The hydrological role of fault zone is linked to the lithology and therefore to the mechanical properties of the rocks involved in deformation. Within cohesive rocks, fault zone domains have precise and well-constrained behaviour, with damage zone acting as a preferential conduit and the fault core as an effective barrier (Caine et al., 1996; Faulkner et al., 2010;

Bense et al., 2013). In fault zone developing inside loose sediments this distinction is not always straightforward, since each deformation structure may behave as a barrier in water-saturated conditions and as a partial conduit in unsaturated ones (Rawling et al., 2001; Sigda and Wilson, 2003; Wilson et al., 2003; Balsamo et al., 2012). This peculiar behaviour is dependent on the different kind of structures characterizing high-porosity rocks with respect to the fully lithified counterparts. Within high-porosity rocks, such as poorly lithified sediments or sandstone, deformation typically occurs via deformation bands of various types depending on the kinematic, total displacement and depth of deformation (Friedman and Logan, 1973; Aydin, 1978; Aydin and Johnson, 1983; Olsson, 2000; Wilson et al., 2003; Eichhubl et al., 2010; Exner and Grasemann, 2010; Ballas et al., 2013; Fossen et al., 2017; Cavailhes and Rotevatn, 2018). Deformation bands can develop both as single elements as well as clusters of tens to hundreds bands, followed by localized discrete slip surface during progressive strain-hardening (Aydin and Johnson, 1978; Mair et al., 2000; Soliva et al., 2016; Fossen et al., 2017). Petrophysical properties in faulted high-porosity rocks may be altered by deformation achieved both by particulate flow and cataclasis (Rawling and Goodwin, 2003; Balsamo and Storti, 2011) as constrained by field data (Antonellini and Aydin, 1994; Main et al., 2000; Taylor and Pollard, 2000; Ogilvie and Glover, 2001; Bense et al., 2003; Ballas et al., 2012) as well as by laboratory analyses (Ogilvie et al., 2001; Baud et al., 2012). Such variability in deformation mechanism may cause a significant drop of permeability, from 1 up to 6 orders of magnitude with respect to the undeformed protoliths (Balsamo and Storti, 2010; Ballas et al., 2015; Fossen et al., 2017). Thus, the recognition of fault zone structure and related deformation mechanism is critical to assess the hydrological role of faults in siliciclastic petroleum reservoirs (Bense et al., 2003; Parnell et al., 2004; Fossen and Bale, 2007; Sternlof et al., 2006; Kolyukhin et al., 2010). Many works in the last decades described deformation bands at the micro-scale, to unravel the deformation mechanisms (Antonellini et al., 1994; Cashman and Cashman, 2000; Mair et al., 2002; Balsamo and Storti, 2010; Kaproth et al., 2010; Charalampidou et al., 2011; Fossen et al., 2017). Despite the detailed works, deformation mechanisms have always been constrained mostly qualitatively, by describing the fabric of the deformed sandstone. Nowadays, the main factors controlling the onset of different deformation mechanisms during strain accommodation and the relationship between displacement and petrophysical properties are still under debate and are worth to be studied in detail.

In this contribution, we investigate an extensional fault zone affecting Pleistocene high-porosity sediments, in the Crotone Basin, southern Italy. Fault zone is characterized by the occurrence of deformation bands with different displacement and degree of grain size comminution in the footwall damage zone and gouge layers in the foliated fault core. Structural elements were described both at the meso-scale as well as at the micro-scale. Petrophysical properties of deformed and undeformed sediments (permeability, grain size and porosity) were described both by *in situ* and by laboratory analyses. A quantitative description of deformed fabric

was made with image analysis technique evaluating the shape descriptors of grains and their preferential orientation. This multidisciplinary approach helped to constrain the deformation mechanism composed of particulate flow overprinted by cataclasis and to quantify its effect on petrophysical properties.

### 4.2. Geological Setting

The study area is located in the Crotone Basin, southern Italy (Fig. 4.1a), a small forearc basin developed as a consequence of the subduction of the Adria-Ionian plate below the European-Tyrrhenian plate (Van Dijk et al., 2000; Zecchin et al., 2004; Reitz and Seeber, 2012). The basin formed during the south-eastward migration of the Calabrian Arc, which produced the related accretionary wedge (Polonia et al., 2011; Gutscher et al., 2017). Basin filling began in Middle Miocene times giving rise to a stratigraphic succession as thick as 2500 m, deposited upon the metamorphic basement of the Sila Unit (Zecchin et al., 2004, 2012). The entire basin underwent several subsidence-uplift events during its infilling and was affected by a dominant extensional and subtle transpressional tectonic (Van Dijk and Scheepers, 1995; Van Dijk et al., 2000; Ferranti et al., 2009). The onset of regional uplift since Middle Pleistocene, led to the exposure of the sedimentary succession (Knott and Turco, 1991; Antonioli et al., 2006;

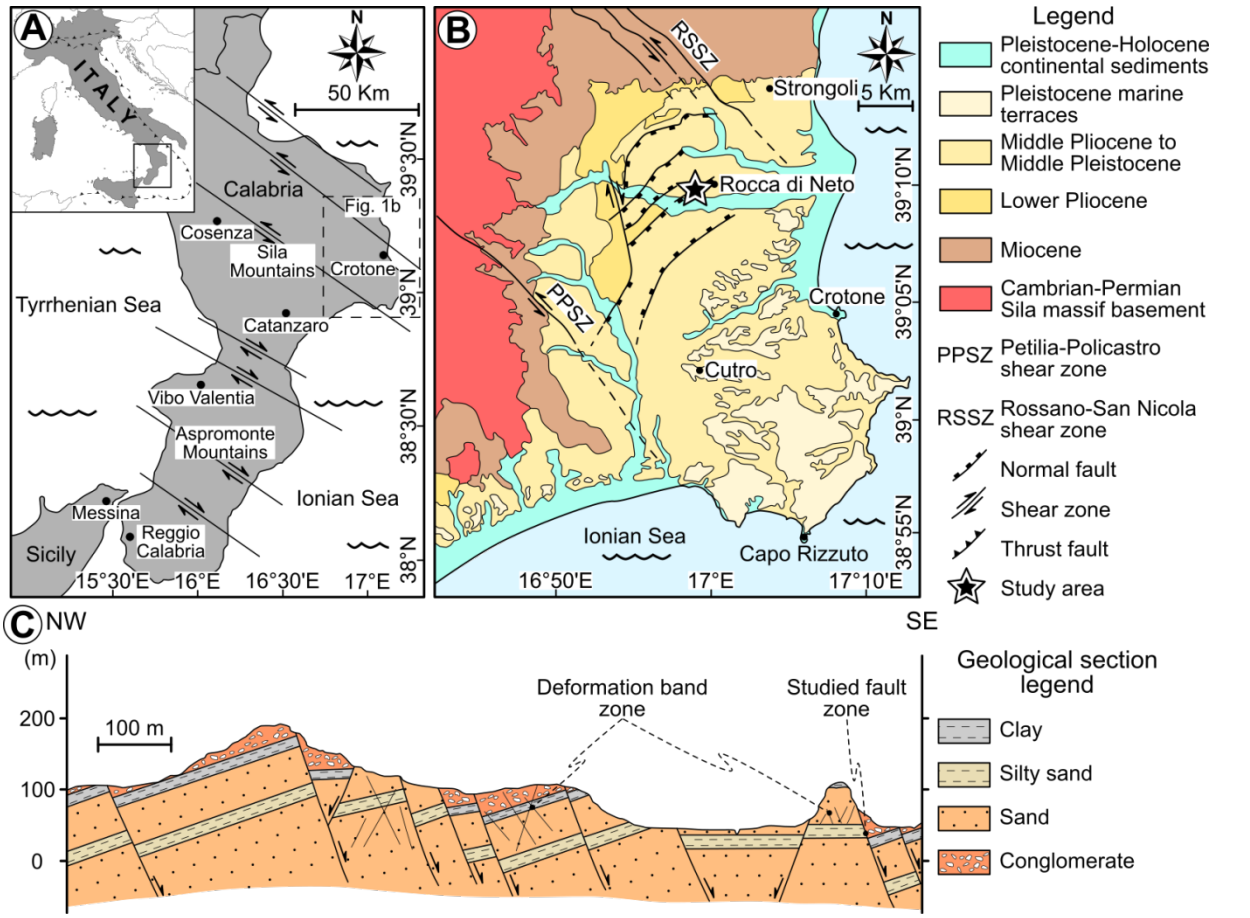


**Fig. 4.1.** (**a**) Geographic position of the Crotone Basin in the framework of the southern Apennines orogenic belt. (**b**) Simplified geological map of the Crotone Basin with the position of the study area along the extensional fault system affecting the middle sector of the basin (modified after Zecchin et al., 2003). (**c**) Detailed geological cross-section of the study area with the position of the Rocca di Neto fault zone (redrawn after Balsamo et al. 2012).

Zecchin et al., 2012; Massari and Prosser, 2013). The present-day structure of the onshore portion of the basin is defined by two major left-lateral shear zones bounding the basin to NE and to SW (Van Dijk, 1994; Zecchin et al., 2004) (Fig. 4.1b). A set of NE-SW-trending extensional faults in the centre of the basin accommodates displacement of several tens to hundreds metres (Balsamo and Storti, 2010) (Fig. 4.1b). The investigated fault zone belongs to the previously described extensional fault system that affects loosely cemented, Pleistocene arkosic sandstone pertaining to the late-stage basin infill (Fig. 4.1c). In particular, the fault zone juxtaposes clayish sediments (Cutro clay) in the hangingwall against silty sands, sandstones and conglomerates in the footwall (Scandale sandstone) (Zecchin et al., 2012). The Cutro clay was deposited in an offshore, shallow marine environment, while the deposition of the Scandale sandstone occurred in a shoreface setting with sediment supply provided by nearby river delta (Zecchin et al., 2012). Due to the loose nature of faulted sediments, the fault zone displays extensive occurrence of soft-sediment deformation.

## 4.3. Analytical Methods

### 4.3.1. Samples and Petrophysical Investigations

To constrain the fault zone structure, porosity evolution, micro-scale deformation mechanisms and petrophysical properties, field and laboratory data were integrated. Field work was aimed to identify the different structural elements and to the collection of samples throughout the fault zone. The overall architecture and evolution of the Rocca di Neto fault system was constrained in a previous manuscript (Pizzati et al. in preparation). Sediment grain size was measured on 68 samples collected from different positions throughout the fault zone with a laser particle analyser Mastersizer 3000 (Malvern Instruments) having an operating range of grain size spanning from 0.01 to 3500 µm. All analyses were performed with a Hydro EV wet dispersion unit, using distilled water as dispersant. Prior to the analysis, all the sediment samples were dried at a constant temperature of 45°C for 48 hours and then sieved at 2000 µm, to remove impurities. Different analytical procedures were developed for each sample type, according to the grain size, accommodated deformation and position with respect to the master fault, thus providing accurate grain size distribution curves. Further details concerning the adopted operating procedures can be found inside the online Supplementary Material. Based on the grain size distribution curves, mean grain size, mode, span (sorting) and the fractal dimension (D-value) were calculated. Span is defined as the width of the grain size distribution, while the D-value is calculated as the slope of the best fit power law distribution between grain size and cumulative frequency of particles per each grain size class in a log-log graph (Blenkinsop, 1991; Rawling and Goodwin, 2003; Balsamo and Storti, 2011). A total of 652 *in situ* permeability measurements were performed across the fault zone using a portable Tiny Perm II air-permeameter (New England Research), which provides accurate data between $10^{-1}$ and $10^{5}$ mD, according to the methodology described by Balsamo et al. (2013). 123 hand samples collected in

different structural domains along the fault zone were cut to obtain 55 polished thin sections impregnated with a blue-dyed resin to ease the 2-D porosity estimation. Petrographic investigation on thin sections was carried out with a petrography microscope (Zeiss Axioplan 2), together with high-resolution scanned thin section images (Nikon SuperCoolScan 5000).

### 4.3.2. Image Analysis Technique

Two-dimensional porosity calculation was performed on 240 selected images acquired with the petrographic microscope at 1.25X magnification, both on the undeformed as well as on faulted sediments, using ImageJ open-source image analysis software. A multi-scale image analysis technique was adopted, aimed to quantitatively describe the shape descriptors of clasts, such as aspect ratio, circularity and solidity, both in the undeformed as well as in the deformed domains. Aspect ratio (AR) is defined as:

$$Aspect\ Ratio = \frac{Major\ axis}{Minor\ axis} \quad (1),$$

where *Major axis* indicates the segment connecting the two farthest points along the perimeter of the grain, while *Minor axis* is the segment having as tips the nearest points on the perimeter. Circularity (C) is given by:

$$Circularity = \frac{4\pi A}{p^2} \quad (2),$$

where *A* is the total area of the grain and *p* is the perimeter. Circularity spans from 0 (extremely elongate and irregular shape) to 1 (perfect circle). Solidity (S) is defined as:

$$Solidity = \frac{A}{A_{conv}} \quad (3),$$

where *A* is the total area of the grain and $A_{conv}$ is the convex area delimited by the convex hull. Solidity varies from 0 (grain with extremely rough surface) to 1 (grain with very smooth surface). Additionally, grain preferred orientation was measured evaluating the angle described by the major axis with a horizontal reference plane. Different magnifications were adopted (1.25, 2.5, 5 and 10X) to better characterize a wide range of grain sizes. With this approach, it was possible to describe the shape of grains with size falling between ~ 10 and 500 µm. Different magnifications were specifically used to describe distinct grain size intervals. In particular, grains with equivalent diameter between 95 and 500 µm were investigated with 1.25X magnification, from 35 to 95 µm with 2.5X magnification, from 25 to 35 µm with 5X magnification and those ones between 10 and 25 µm with 10X magnification. Particles finer than 10 µm were not taken into account because of their size below the lower limit of resolution of the highest used magnification. Particles above 500 µm are rare due to the medium-fine grain size of the analyzed samples. Grains were manually digitized at each magnification to prevent any bias and inaccuracy induced by the auto-tracing methods. Five grain size classes were adopted from 0 to 250 µm, with 50 µm bin size; all the shape descriptors (AR, C and S) extracted from faulted samples were compared with the corresponding undeformed counterparts. Typically, more than 30 data were collected and averaged for each grain size class to grant statistical significance of the shape descriptors. Detailed photomicrographs of microstructures were acquired both with standard petrographic microscope and with a

JEOL JSM 6400 scanning electron microscope (SEM), operating at 240 nA and 20 kV beam current.

## 4.4. Fault Zone Structure

### 4.4.1. Fault Zone Domains

The studied fault zone has a maximum displacement of 80-90 m, juxtaposing the Cutro clay in the hangingwall against the Scandale poorly cemented sandstone in the footwall (Fig. 4.2a, b). The meso-scale fault structure was previously described by Pizzati et al. (in preparation). The footwall exposes four distinct structural domains: (1) a low-deformation zone, with a few, widely spaced, conjugate deformation bands and minor faults; (2) the footwall damage zone, with extensive occurrence of conjugate deformation bands, together with antithetic and synthetic faults; (3) the footwall mixed zone, with a dense network of conjugate and high-strain fault-parallel deformation bands; (4) the fault core, where most of the displacement is accommodated, characterized by foliated sand layers and thin black gouges decorating pod of coarse and medium-grained sand.

### 4.4.2. Deformation Features

In the exposed footwall of the fault zone, the deformation of loose sandstone is achieved mostly by the development of deformation bands with different displacement and orientation, secondary faults, foliated sand layers and black gouges. The least deformed structures comprise deformation bands having offset < 1 cm. They are preferentially developed inside the low-deformation zone, and to lesser extent in the outer part of the footwall damage zone (Fig. 4.3a). Such deformation bands are arranged in conjugate sets, have positive relief and typically display whitish colour compared to the red-orange one of the undeformed sandstone (Fig. 4.3a). A few secondary faults are present displaying higher offset (> 50 cm) compared to the deformation bands. In the footwall damage zone, deformation bands are arranged in three distinct sets, two of them form an inclined conjugate system (DB1 and DB2 in Fig. 4.3b), while the third one is parallel to subsidiary faults (DB in Fig. 4.3b). Deformation bands and faults were distinguished on the basis of the total displacement and considering the thickness of the structural element. In particular, deformation bands are assumed as discrete deforming features with displacement rarely exceeding 10 cm. On the contrary, faults may accommodate greater amount of displacement and are characterized by several cm-thick shear zones. Deformation bands belonging to the conjugate set have displacement between 1 and 5 cm, while the fault-parallel one display higher offset from 5 to 10 cm. Thick clusters of fault-parallel bands show throw > 10 cm. Within the mixed zone, deformation bands are organized in dense arrays parallel to faults and to lesser extent in conjugate set similar to what found in the damage zone (Fig. 4.3c). Displacement often exceeds 10 cm along single deformation bands. Fault core hosts several mm-thick, black gouge layers developed in pervasively foliated fine and coarse sands. The majority of the gouges are gently folded, while a few show straight pattern (Fig. 4.3d), with displacement between 5 and 10 cm. The foliated sand encasing gouge is highly deformed and tectonically compacted.

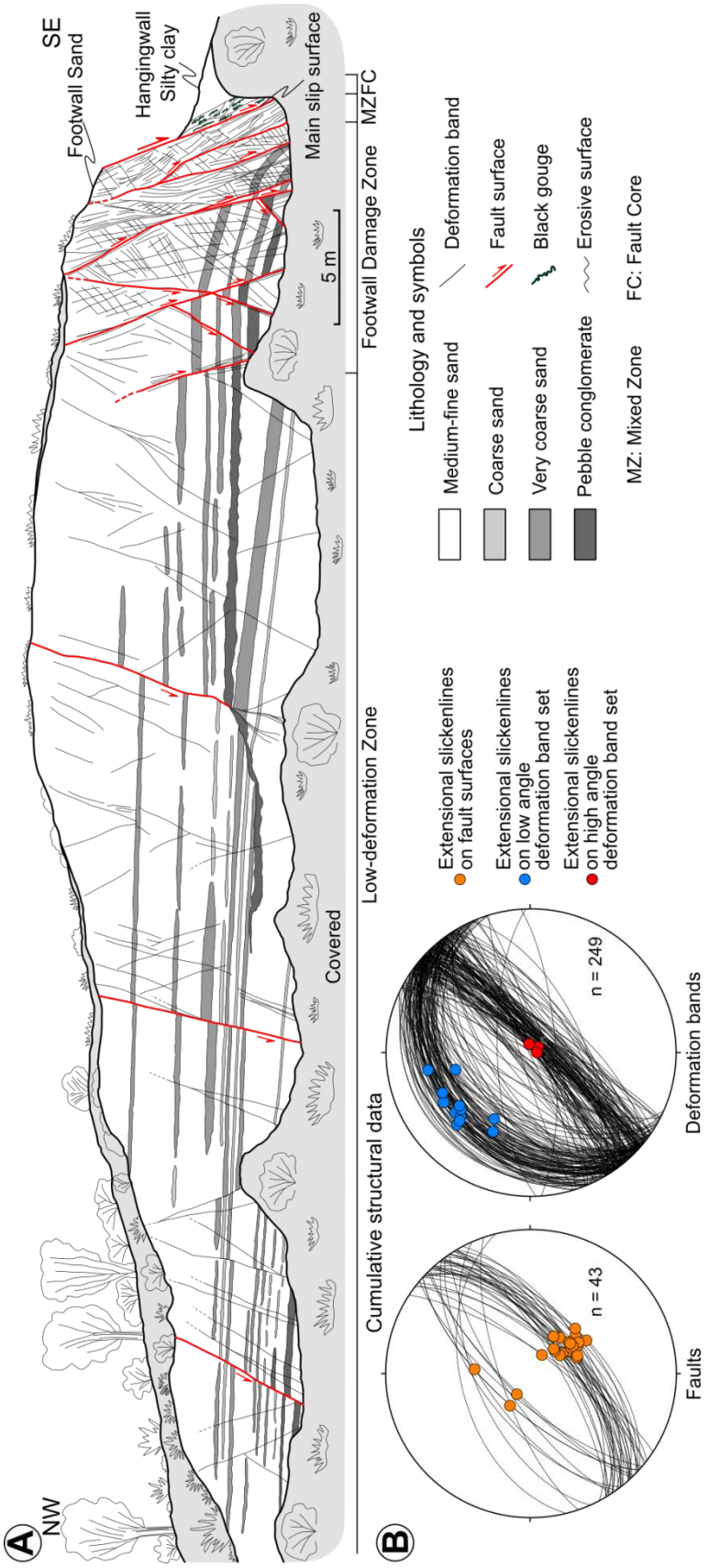


**Fig. 4.2**. Architecture and structural data of the studied fault zone (adapted from Pizzati et al., in preparation). (**a**) Detailed geological section through the footwall of the Rocca di Neto fault, developing inside the Early Pleistocene Scandale poorly lithified sandstone. The hangingwall is almost completely covered and hosts the Middle Pleistocene Cutro clay. (**b**) Cumulative structural data of faults and deformation bands also reporting the extensional slickenlines.

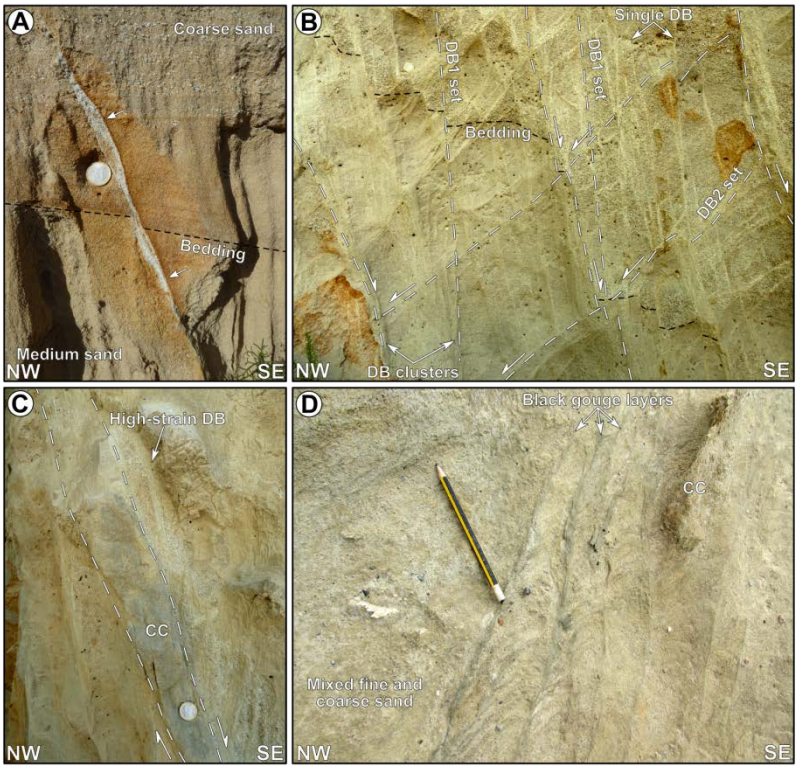


**Fig. 4.3.** Outcrop description of the main deformation elements. (**a**) Low-displacement deformation band (d < 1 cm), inside the low-deformation domain. See the whitish colour of deformed sand within the band contrasting with the marked orange-coloured oxidation front abutting at the contact with the outer part of the band (white arrows). (**b**) Conjugate deformation bands characterizing the footwall damage zone of the fault, organized in two distinct sets synthetic high-angle (DB1) and antithetic low-angle (DB2) with respect to the master fault. A third set is composed of bands parallel to secondary faults (DB). See the coin in the top left corner of the image for scale. (**c**) High-strain deformation band surrounding a secondary fault hosted at the boundary between the footwall damage zone and the mixed zone. The fault is selectively cemented through the precipitation of calcite cement (CC) (see the coin for scale). (**d**) Black gouge layers inside the fault core encased by mixed coarse and fine sand (pencil for scale).

## 4.5. Petrophysical Properties

### 4.5.1. Grain Size Analysis

The grain size of undeformed and faulted samples shows significant variations. In particular, undeformed sediments are mainly composed of well-sorted medium to fine-grained sand with mean grain size of 318 µm, and subordinately medium-coarse sand with mean grain size of 488 µm (Fig. 4.4a). In the footwall damage zone, the medium-fine sand between DBs (interband domain) displays a mean grain size of 233 µm (Fig. 4.4b), while coarse sand has 656 µm mean value (Fig. 4.4c). Low-displacement deformation bands in medium-fine grained sand, display slightly finer grain size compared to the undeformed counterpart (Fig. 4.4d). In particular, these samples show an increase of particles frequency between 10 and 100 µm with respect to the undeformed counterpart (Fig. 4.4d). Inclined conjugate deformation bands have a mean grain size of 125 µm, with decrease in volume density of grain size classes from 100 to 500 µm and relative increase between 0.3 and 70 µm (Fig. 4.4e). The same conjugate bands in coarse sand, have modal value of 230 µm, with a decrease in mean grain size from 656 to 275 µm with respect to the undeformed coarse sand (Fig. 4.4c, f). Subsidiary faults located in the damage zone, have an average grain size of 114 µm, increase in number of particles from 0.3 to 90 µm with respect to the undeformed samples and a modal value of 255 µm (Fig. 4.4g). The foliated sand samples in the mixed zone have mean grain size of 54 µm and display a grain size distribution with three distinct modes at 0.7, 15 and 135 µm, respectively (Fig. 4.4h). Fine sand samples collected inside the fault core have mean grain size of 84 µm, with a slightly bimodal distribution having relative maxima at 0.7 and 43 µm (Fig. 4.4i). Fault core hosts also stretched coarse sand pods with a mean grain size of 376 µm and a modal value of

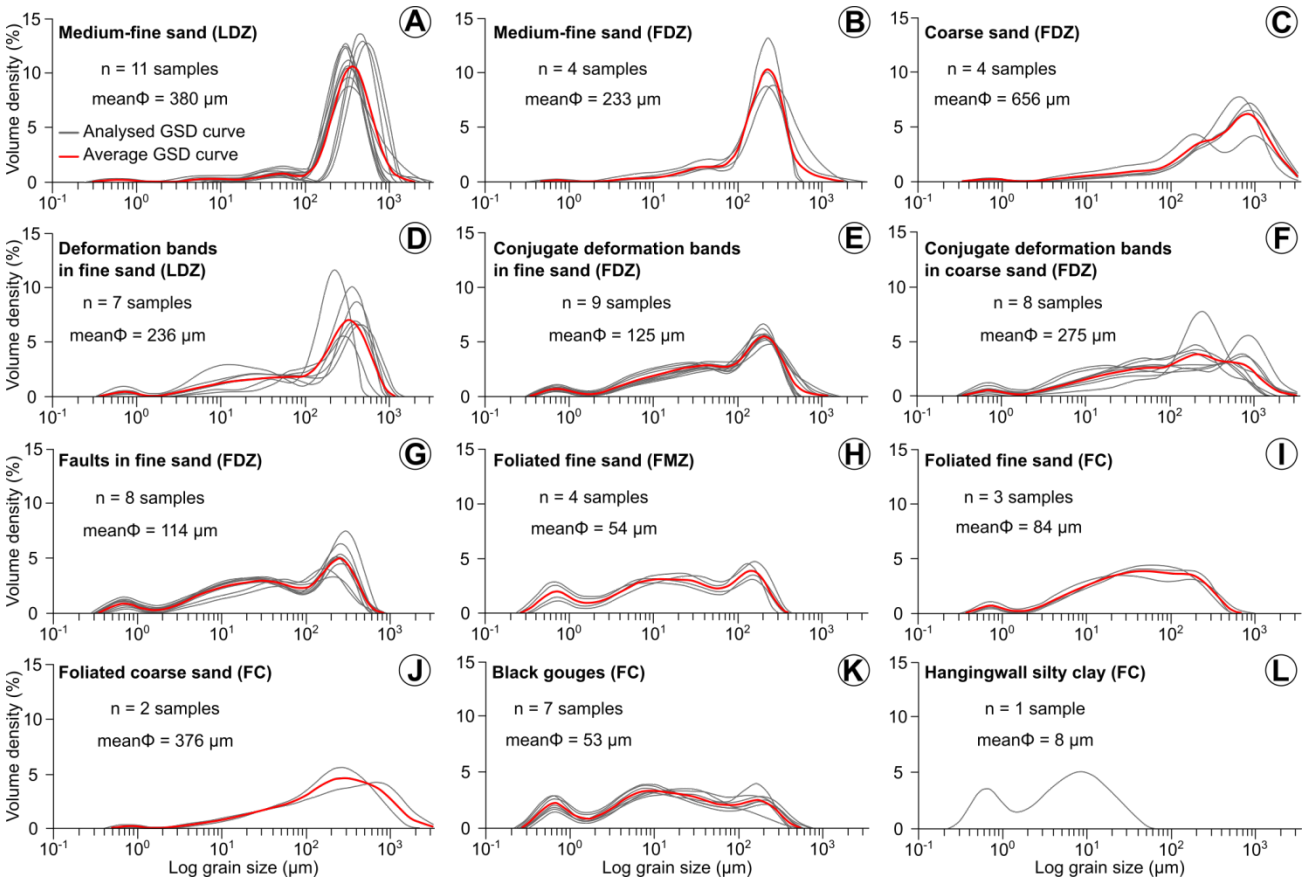


**Fig. 4.4.** Grain size distribution curves of the analysed sediments. (**a**) Medium-fine sand sampled in the low-deformation zone. (**b**) Medium-fine sand from the interband domain inside the footwall damage zone. (**c**) Coarse sand from the interband domain inside the footwall damage zone. (**d**) Low-displacement deformation bands sampled in the low-deformation domain. Conjugate deformation bands deforming medium-fine (**e**) and coarse sand (**f**) within the footwall damage zone. (**g**) Secondary faults inside the footwall damage zone. Foliated fine sand from the mixed zone (**h**) and from the fault core (**i**). (**j**) Foliated coarse sand sampled in the fault core. (**k**) Black gouge from the fault core. (**l**) Silty clay coming from the hangingwall of the fault. LDZ, low-deformation zone; FDZ, footwall damage zone; FMZ, footwall mixed zone; FC, fault core; GSD, grain size distribution.

290 µm (Fig. 4.4j), while black gouges display 53 µm mean grain size and three-modes distribution having maxima at 0.6, 9 and 153 µm, respectively (Fig. 4.4k). Eventually, the only one sample collected in the hangingwall, is composed of a silty clay, with bimodal distribution having maxima at 0.7 and 8 µm (Fig. 4.4l). Black gouges and foliated fine sand inside the fault core, are characterized by mean grain size 7 and 5 times lower than the pristine medium-fine sand, respectively (Fig. 4.5a). Overall, low-displacement deformation bands induce a 1.5 times decrease in grain size, while medium to high-displacement bands may reach mean grain size 3 times lower than the undeformed medium-fine sand (Fig. 4.5a). Span of the granulometric curves is very low (high sorting degree) in undeformed medium-fine (1.7) and medium-coarse sand (1.2) (Fig. 4.5b). Deformed sediment samples, show a gradual increase in span (i.e., sorting decrease). In particular, low-displacement bands inside the low-deformation zone, have a mean span of 3.3, while medium to high-displacement bands in the footwall damage zone range from 3.7 to 8 (Fig. 4.5b). Span is even higher inside the mixed zone, where foliated sand layers and very thin gouges display mean value of 9.2 and 12.8, respectively (Fig. 4.5b). Eventually, black gouge layers in the fault core have mean span of 11.2, while for foliated fine and

coarse sand is 5.4 and 4.3, respectively (Fig. 4.5b). Mean fractal dimension (D value) in the undeformed samples is 2.34 in medium-fine and 2.25 in coarse sand (Fig. 4.5c). Low-displacement bands have a mean D value of 2.55, whereas medium and high-displacement bands have mean D spanning from 2.56 to 2.75 (Fig. 4.5c). Deformed sand inside minor faults with total displacement > 20 cm are characterized by mean D of 2.70. Mixed zone shows consistently higher D value, with foliated fine sands and thin gouges reaching 2.9 and 3.02, respectively. Within the fault core, D values vary because of the presence of different sediment grain size; stretched coarse sand layers have mean D of 2.57, while foliated fine sand has 2.7. Eventually, black gouges display the highest recorded mean D of 3.03, with peak value of 3.19 (Fig. 4.5c).

### 4.5.2. Permeability Measurements

Along the footwall of the fault, air-permeability shows a progressive decrease from the low-deformation zone towards the fault core (Fig. 4.5d). The highest permeability is recorded by medium to fine-grained and coarse sand in the low-deformation domain, with mean values of 5.4 × $10^4$ and 1.4 × $10^5$ mD, respectively. Deformation bands with displacement < 1 cm, have almost half of the permeability shown by undeformed sand (3.1 × $10^4$ mD). Relatively undeformed medium-fine and coarse sand samples inside the footwall damage zone are characterized by mean

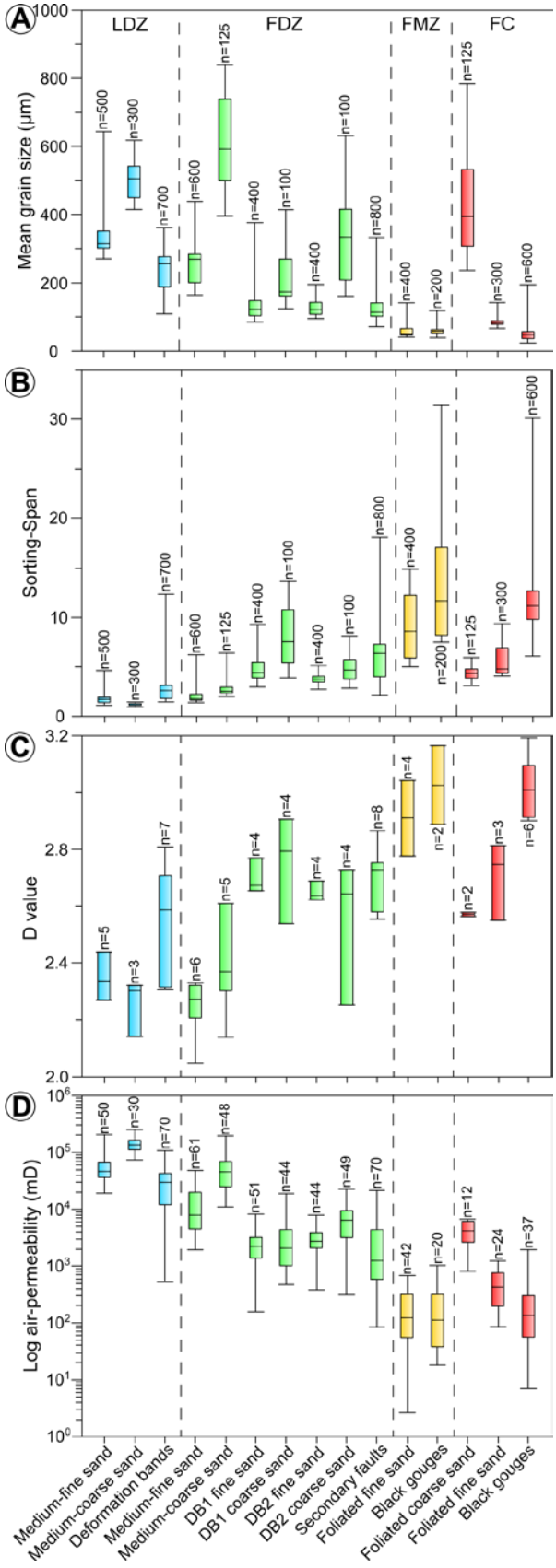


**Fig. 4.5.** Petrophysical characterization of the most recurrent lithologies and deformation elements. (**a**) Mean grain size from the analyses performed with the laser granulometer. (**b**) Sorting-span of the grain size distribution curves. (**c**) D value corresponding to the fractal dimension gained from the grain size analyses. (**d**) Log air-permeability measurements throughout the footwall of the investigated fault zone. LDZ, low-deformation zone; FDZ, footwall damage zone; FMZ, footwall mixed zone; FC, fault core; DB1, synthetic high-angle deformation band; DB2, antithetic low-angle deformation band.

permeability of 1.2 × $10^4$ and 5.3 × $10^4$ mD. Conjugate DB1 and DB2 sets inside the damage zone have permeability spanning from 2.6 × $10^3$ to 7.4 × $10^3$ mD, thus causing a drop from 1 to 1.5 orders of magnitude (Fig. 4.5d). Usually, fault core of subsidiary faults and thick clusters of deformation bands are characterized by permeability drop up to 2 orders of magnitude (Fig. 4.5d). From the inner damage zone to the mixed zone permeability shows an abrupt decrease in foliated sand layers and thin black gouges (mean permeability of 193 and 201 mD, respectively) (Fig. 4.5d). Fault core hosts black gouge layers with mean permeability of 245 mD, with 7 mD as the lower recorded value, featuring an overall permeability decrease of 2.5 to 3 orders of magnitude with respect to the undeformed sand. In the same domain, foliated fine sand and stretched very coarse sand recorded mean permeability of 496 and 4026 mD, respectively (Fig. 4.5d).

### 4.5.3. Two-dimensional Porosity Calculation

Primary porosity was calculated from acquired images neglecting any secondary porosity associated with rare tensile fractures and dissolution of fossil shells. Undeformed sand samples, from fine to coarse-grained, have a mean 2-D porosity of 37.2% with a wide range of variation between 15.8 and 50.6% (Fig. 4.6). Sediment volumes between deformation bands, both in the low-deformation and in the damage zone domains (interband domain in Fig. 4.6), show a mean 2-D porosity of 16.1%. Low-displacement bands (< 1 cm) mainly from the low-deformation zone are characterized by a mean porosity of 5.8% (Fig. 4.6). Medium-displacement bands (1-5 cm) pertaining to the conjugate set have an average 2-D porosity of 2.2%, while high-displacement ones (> 10 cm), mainly sampled in the mixed zone and fault core, reach 1.30% (Fig. 4.6). Eventually, porosity calculation on black gouges sampled from the fault core and from the mixed zone yields a mean value of 0.93% (Fig. 4.6).

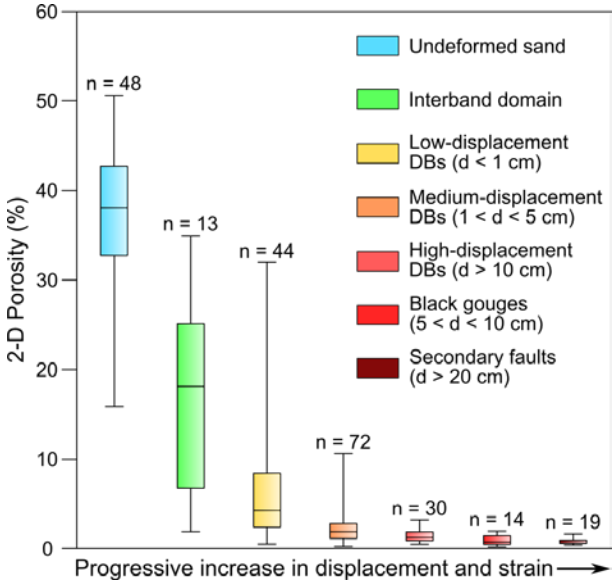


**Fig. 4.6.** Two-dimensional porosity measurements by image analysis technique performed on thin sections. Measurements were made on different samples characterized by increasing displacement. DB, deformation band.

## 4.6. Petrographic and Microstructural Characterization

### 4.6.1. Petrography of Undeformed Sand

The composition of the undeformed sediments was evaluated with the modal analysis preformed on 35 selected thin section images acquired at 1.25X magnification. According to the results, 23 of the pristine sand samples lay in the lithic arkose field, while 12 of them plot in the arkose field in the Q-F-L ternary diagram of Folk, (1974) (Fig. 4.7). In particular, quartz

percentage spans from 50.3 to 67.7%, while feldspar ranges from 19.6 to 36.9% and lithics from 5.3 to 18.2% (Fig. 4.7). Lithics are mainly composed of gneiss or granitic rock fragments, but sedimentary detrital grains also occur in the form of calcite grains and fossil shells. Other less frequent lithics are biotite mica, iron oxides-hydroxides and rare glauconite, muscovite and chlorite.

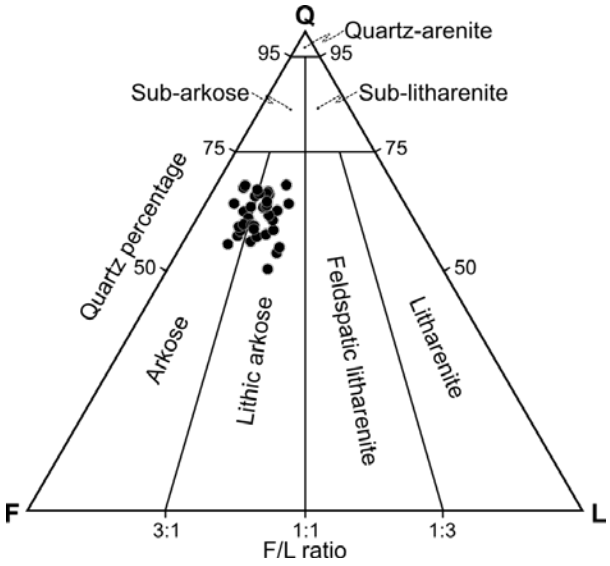


**Fig. 4.7.** Ternary Quartz-Feldspar-Lithics diagram with the modal composition of the pristine sandstone, following classification made by Folk, (1974). Sediment composition was measured on 35 different petrographic images. Q, quartz; F, feldspar; L, lithic fragments.

### 4.6.2. Microstructural Investigation

Deformed sand samples show a variety of microstructures depending on the total displacement accommodated along single discontinuity. At thin section scale, deformation bands in the low-deformation zone, show sharp boundaries with the undeformed sand and can be easily distinguished because of the loss of porosity (Fig. 4.8a). Within such deformation bands, grains do not display any significant reduction of grain size, but show a fabric re-organization in a closer packing. Conjugate deformation bands in the footwall damage zone have a wide range of displacement and consist of tabular structures with a minimum thickness of 1-2 mm, showing mutual cross-cut relationship (Fig. 4.8b). Grains in low-displacement deformation bands are affected by slight decrease in grain size and sorting (Fig. 4.8b). Deformation bands having displacement of a few cm show grain size reduction mainly achieved by fragmentation of coarser feldspar grains and flaking of quartz (Fig. 4.8c). Fault-parallel bands with total displacement above 10 cm, are up to 5-6 mm-thick tabular structures, and display an outer part where grains are comminute, and a ~ 300 µm-thick inner part (core of the band) with greater grain size reduction (Fig. 4.8d). The dark brown matrix in these deformation bands is dominantly composed of crushed feldspar grains together with crushed detrital, calcite cement and fine-grained chips of quartz grains (Fig. 4.8d). Black gouges present complex microstructural features characterized by the presence of ultra-comminute slip zones having thickness > 500 µm encased by less comminute sand volumes (Fig. 4.8e). Frequently, the less deformed sand layers are characterized by the presence of S-C structures, imparted by the preferential orientation of the major axis of clasts and deformed mica flakes (Fig. 4.8e). Eventually, the cores of minor faults form tabular structures as thick as 10 mm and display cataclastic foliation and a wide range of grain size, thus diminishing the overall sample sorting (Fig. 4.8f).

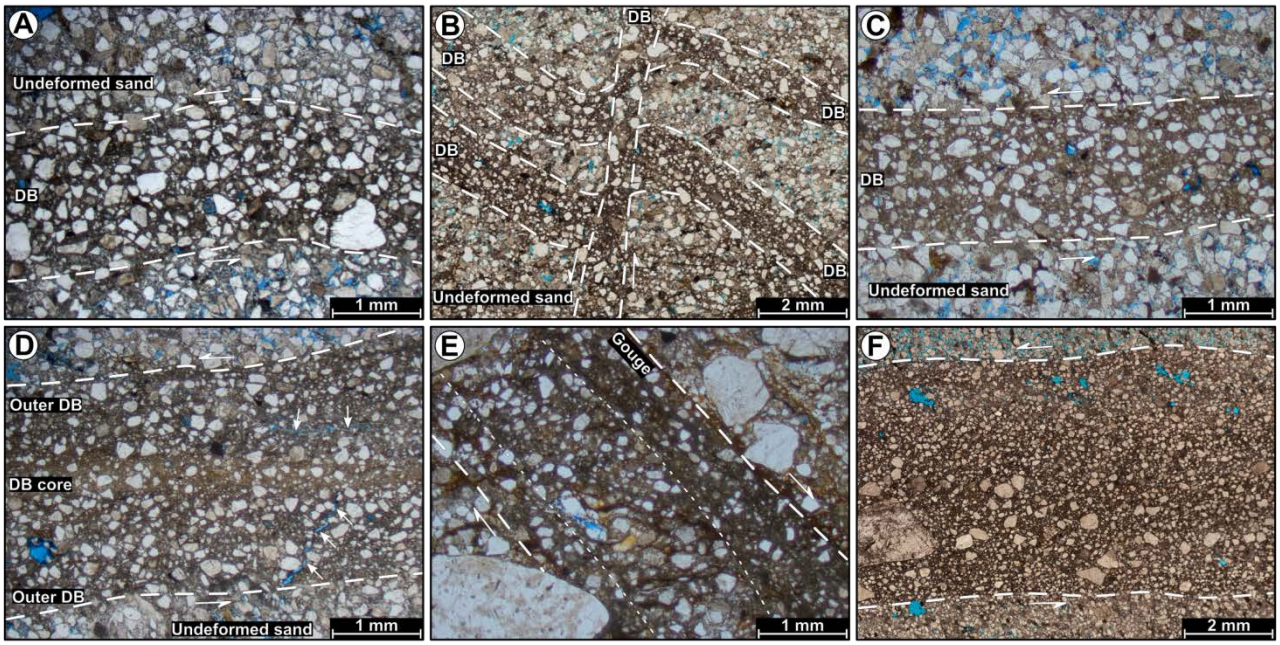


**Fig. 4.8.** Microstructural features of deformation bands and gouges. (**a**) Low-displacement band (DB) within the low-deformation zone showing only grain re-orientation and limited fragmentation and rolling. (**b**) Conjugate mm-scale displacement deformation bands with evidence of grain size reduction and grain fragmentation. (**c**) Fault-parallel deformation band within the footwall damage zone displaying pronounced grain size reduction and rolling of grains. (**d**) High-displacement band close to the master fault, with a well developed ultra-comminute central core showing brownish matrix and an outer part with less enhanced grain size reduction. Tiny tensile fractures may develop both parallel and inclined to the band direction (white arrows). (**e**) Thin black gouge layer with severe comminution of grains in localized shear zone and S-C type structures imparted by the alignment of grains and clay minerals, characterizing the less deformed sediments. (**f**) Secondary fault with cataclastic fabric, highly heterogeneous grain size distribution and poor sorting.

SEM observation allowed to document the breaking mechanism within deformation bands, in which feldspar grains are deformed by several intragranular fractures, leading to the formation of 5-8 clast, while quartz grains show mostly flaking of the asperities (Fig. 4.9a).

High-displacement, fault-parallel deformation bands show a ~ 50 µm-thick slip zone with intense grain size comminution (Fig. 4.9b). This results in an asymmetric gradient of grain size from the slip zone to the opposite side of the deformation band (Fig. 4.9b, c). Deformation bands and gouges sampled in the innermost part of the mixed zone and inside the fault core, host tensile fractures with aperture ranging from 10 to 25 µm (Fig. 4.9a). Fractures are aligned along the shear sense of the band-gouge, or at 40-45° from the direction of the band (Fig. 4.9a).

## 4.7. Particle Shape Data

### 4.7.1. Shape Analysis on Cumulative Data

Grain aspect ratio, circularity and solidity are plotted against grain size in Fig. 4.10. Grains in low-displacement bands are less elongate compared to the undeformed ones, with greater values for smaller particles (Fig. 4.10a). Circularity has almost the same value both in the undeformed as well as in the deformed domain (Fig. 4.10b), and solidity follows the same trend with slightly lower values in the coarse grain size (between 150 and 250 µm) (Fig. 4.10c). From the graphs it

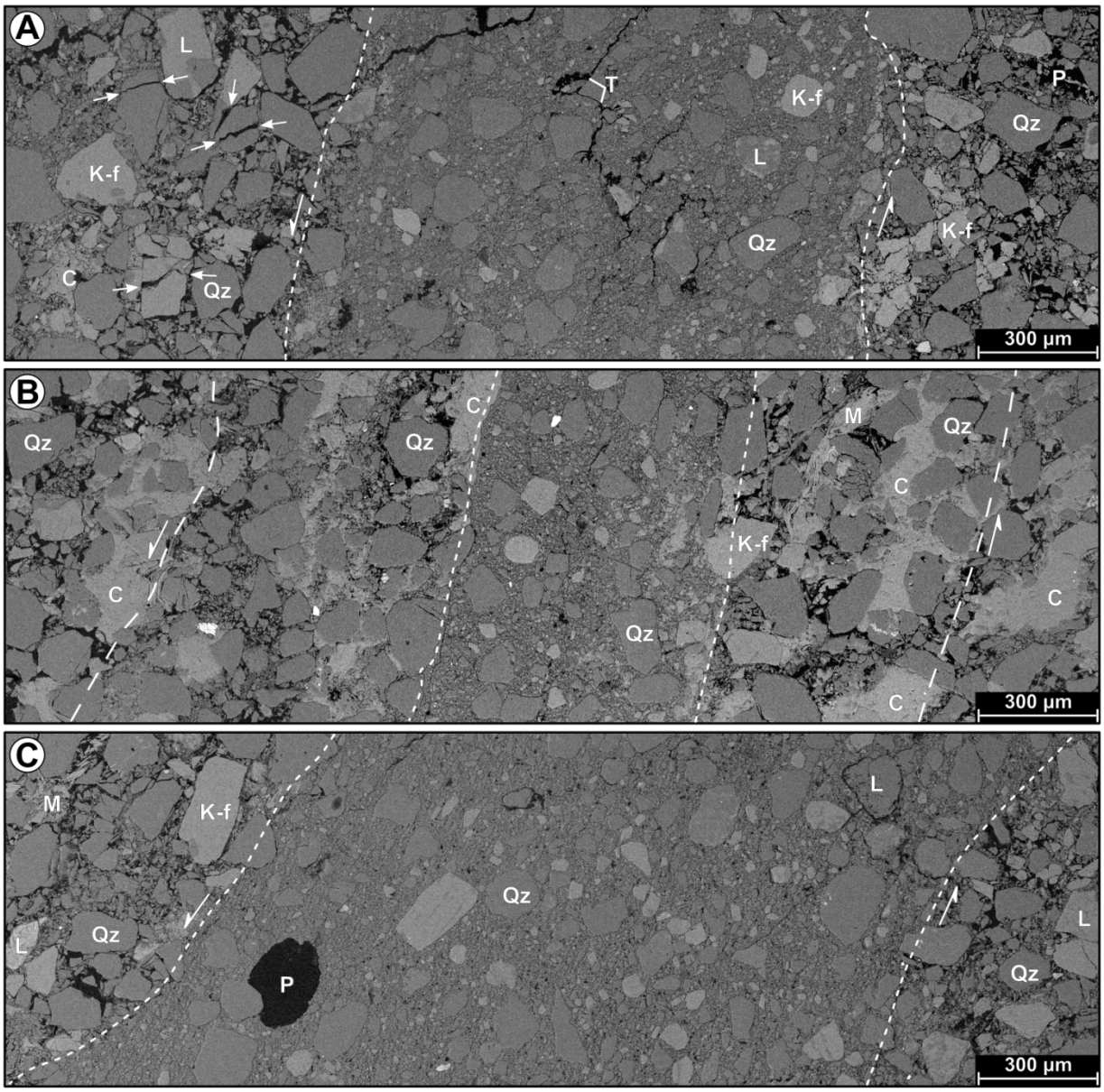


**Fig. 4.9.** Back-scattered SEM microphotographs. (**a**) Medium-displacement deformation band with small-aperture tensile fractures (T) close to the centre. In the outer part of the band, grains, especially feldspar, are affected by intragranular fractures (white arrows). (**b**) High-displacement band close to the fault core, displaying a central core with pronounced grain size reduction, developing a slip surface on one side of the core. Grain size reduction has a decreasing gradient from the slip surface towards the other side of the band. (**c**) Black gouges are characterized by extreme comminution along the slip zone bordering the gouge and by a gradient of grain size reduction moving away from it. Qz, quartz; K-f, feldspar; L, lithic fragments; P, porosity; T, tensile fracture; C, calcite cement; M, muscovite mica.

is evident that finer particles show the highest aspect ratio and the lowest circularity and solidity. Medium-displacement deformation bands are characterized by lower aspect ratio, higher circularity and solidity with respect to the undeformed counterpart (Fig. 4.10d, e, f). Thus, deformed grains are less elongate, more circular and with smoother outer surface than the undeformed ones. The same trend is recorded by high-displacement fault-parallel bands, with a more pronounced difference between the undeformed and deformed samples compared to the previously described bands (Fig. 4.10g, h, i). Black gouges have trends similar to the deformation bands, but aspect ratio has lower values between 100 and 200 µm,

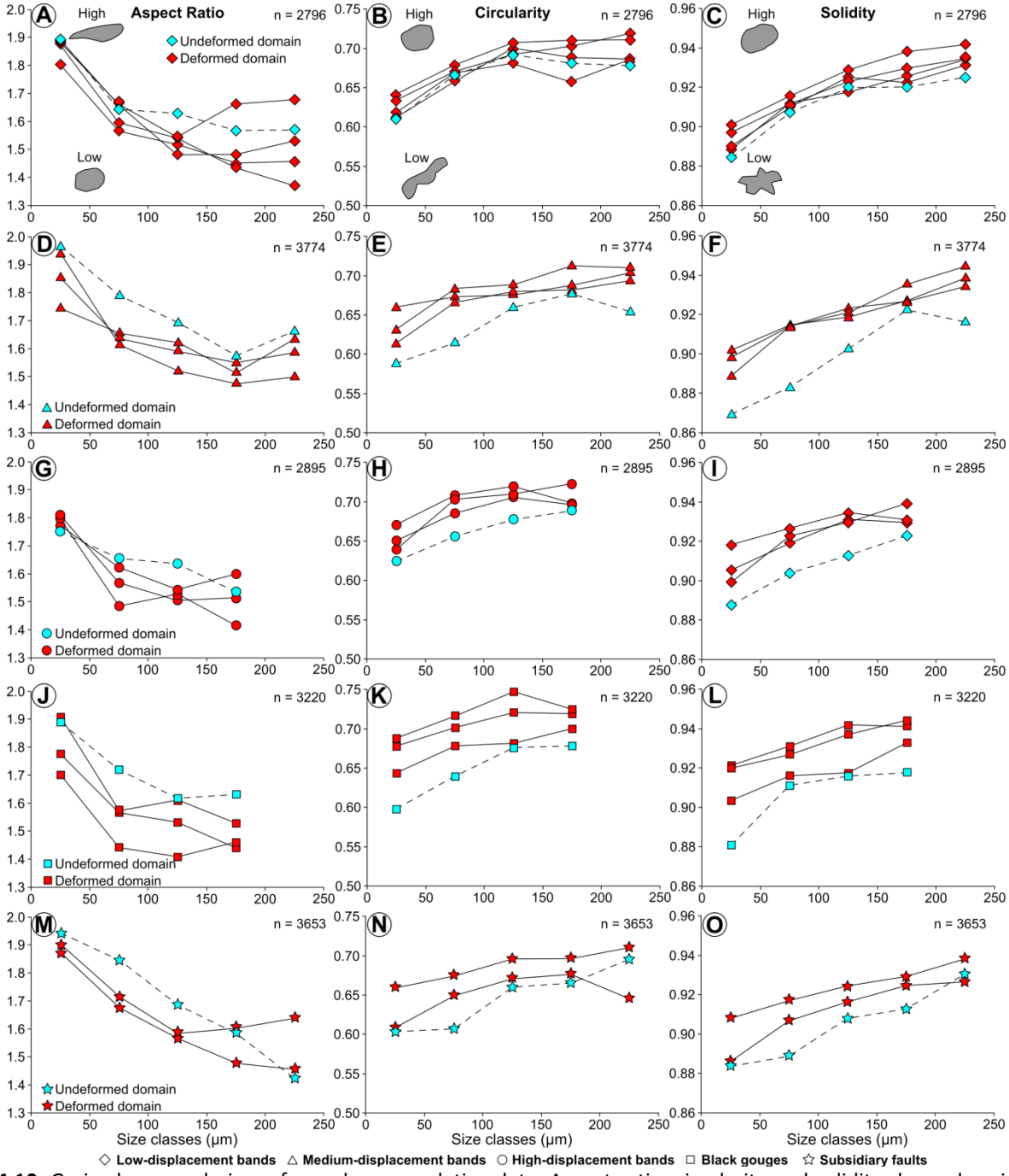


**Fig. 4.10.** Grain shape analysis performed on cumulative data. Aspect ratio, circularity and solidity shape descriptors for low-displacement (**a**, **b**, **c**), medium-displacement (**d**, **e**, **f**), high-displacement bands (**g**, **h**, **i**), black gouges (**j**, **k**, **l**) and subsidiary faults (**m**, **n**, **o**). All data are organized in 5 distinct grain size classes, 50 µm each.

circularity is consistently higher throughout the investigated size classes, while solidity records almost the same values (Fig. 4.10j, k, l). Upon subsidiary faults, aspect ratio of deformed samples is lower compared to the undeformed one, between 0 and 150 µm, while for grain size above 150 µm a faint cross-over occurs with one of the deformed samples (Fig. 4.10m). Circularity values are lower than the ones calculated for gouges and high-displacement bands and are comparable with what recorded by medium-displacement bands (Fig. 4.10n). Solidity has values in line with medium to high-displacement bands (Fig. 4.10o).

### 4.7.2. Quartz-Feldspar-Lithic Grain Shape Analysis

Shape analysis performed on the most recurring mineralogical species, provides much more accurate information with respect to the cumulative analysis. Upon the same deformed samples described above,

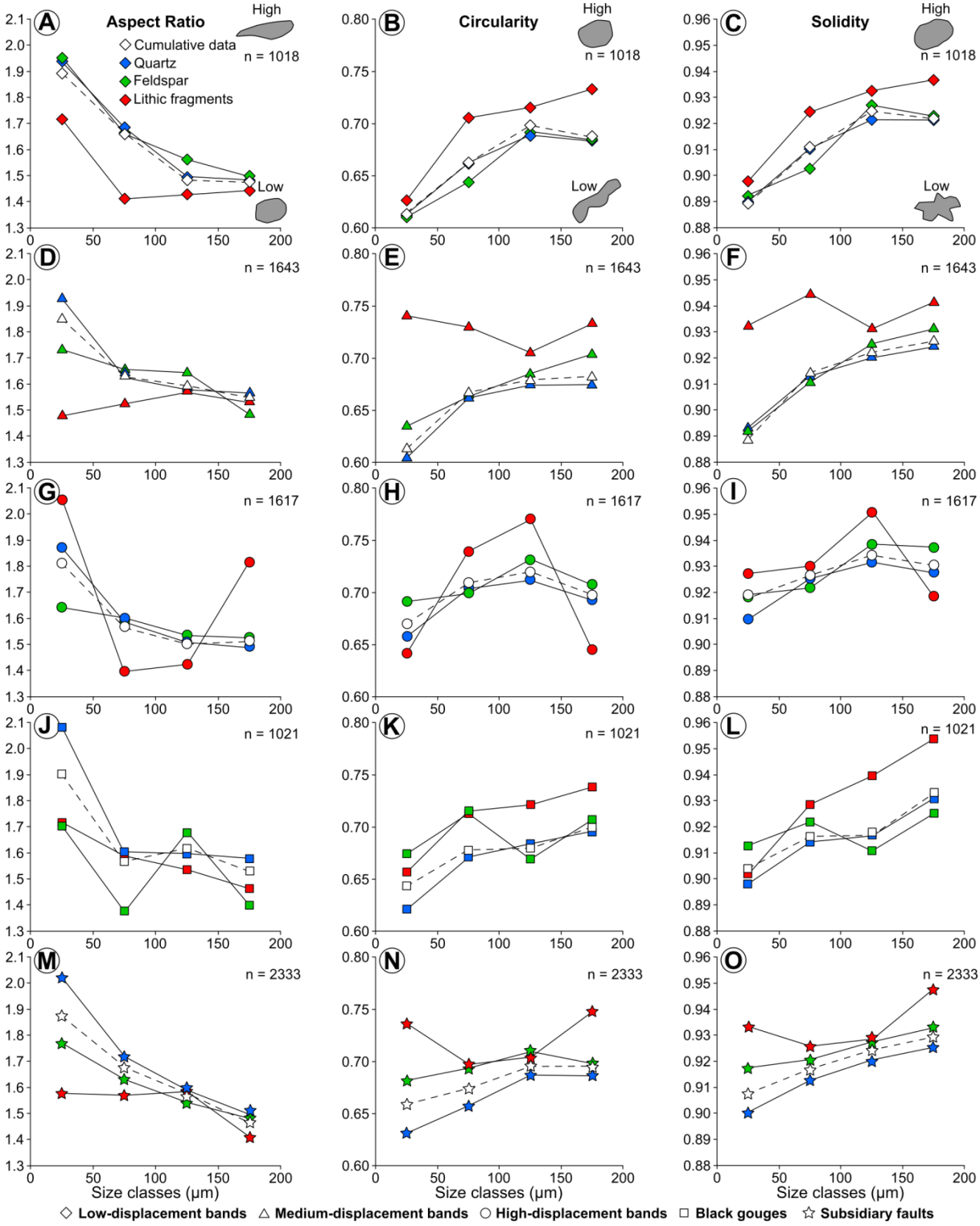


**Fig. 4.11.** Grain shape analysis performed on the three most recurred minerals (quartz, feldspar and lithic fragments). Aspect ratio, circularity and solidity for low-displacement (**a**, **b**, **c**), medium-displacement (**d**, **e**, **f**), high-displacement bands (**g**, **h**, **i**), black gouges (**j**, **k**, **l**) and subsidiary faults (**m**, **n**, **o**). All data are organized in 5 distinct grain size classes, 50 µm each.

shape descriptors were calculated for quartz, feldspar and lithic grains and compared with the cumulative data in Fig. 4.11. Low-displacement bands show similar values of all the three shape descriptors for quartz and feldspar grains (Fig. 4.11a, b, c). Lithic fragments maintain the same trend described by quartz and feldspar, but recorded lower aspect ratio and higher circularity and solidity values. Within medium-displacement deformation bands, quartz grains are more elongate at finer grain size compared to feldspar and lithics, while at coarser grain size all mineralogical phases have similar values (Fig. 4.11d). Conversely, circularity of quartz is consistently lower than the one shown by feldspar, lithic and by cumulative mean data (Fig. 4.11e). Solidity indicates very close values both for feldspar and quartz, the latter recording slightly lower values, whereas lithics plot in the high solidity range (Fig. 4.11f). Inside high-displacement deformation bands the aspect ratio of quartz is higher than the one shown by feldspar at finer grain size (from 0 to 100 μm), while values are almost equivalent for coarse grains (Fig. 4.11g). Lithic fragments have highly varying aspect ratio, with extremely high values from 0 to 50 μm and from 150 to 200 μm, while the lowest values are recorded at intermediate grain size (from 100 to 150 μm) (Fig. 4.11g). Circularity of quartz is lower than feldspar grains, with a cross-over between 50 and 100 μm (Fig. 4.11h). Lithics have less homogeneous trend with the highest circularity between 50 and 150 μm, and the lowest values from 0 to 50 μm and above 150 μm (Fig. 4.11h). Solidity indicates quartz as the least smooth particles, while both feldspar and lithic fragments are smoother (Fig. 4.11i). Inside black gouges, quartz reaches the highest value of aspect ratio (almost 2.1) in the finer grain size class (from 0 to 50 μm) and display values higher than feldspar and lithics until 150 μm where feldspar has relatively higher aspect ratio (Fig. 4.11j). Compared to low and medium-displacement bands, gouges display a pronounced difference of aspect ratio between quartz and feldspar. Both circularity and solidity are lower for quartz grains showing a cross-over with feldspar at coarse grain size (Fig. 4.11k, l). Eventually, secondary faults are characterized by quartz with aspect ratio consistently higher than feldspar and lithics, with a marked difference at lower grain size (from 0 to 100 μm) (Fig. 4.11m). Also circularity and solidity display constant lower values for quartz and relatively higher for feldspar and lithics, those ones having the highest values (Fig. 4.11n, o).

### 4.7.3. Grain Preferential Orientation

Preferential orientation of the major axis of grains, measured both on faulted domains as well as on undeformed samples are shown in Fig. 4.12. In these diagrams, dotted lines represent the direction of the investigated deforming structures on the thin sections. Low-displacement bands display a weak preferential alignment of grains developed parallel to the band direction (dotted line in Fig. 4.12a). Medium-displacement deformation bands show a marked preferred orientation of grains, especially within 50-60° range in clockwise direction from the direction of deformation bands (Fig. 4.12b). Grains in high-displacement bands are strongly aligned along the band direction and the most frequent angular classes fall within 40° in counter-clockwise direction and 10° in clockwise direction to the reference direction

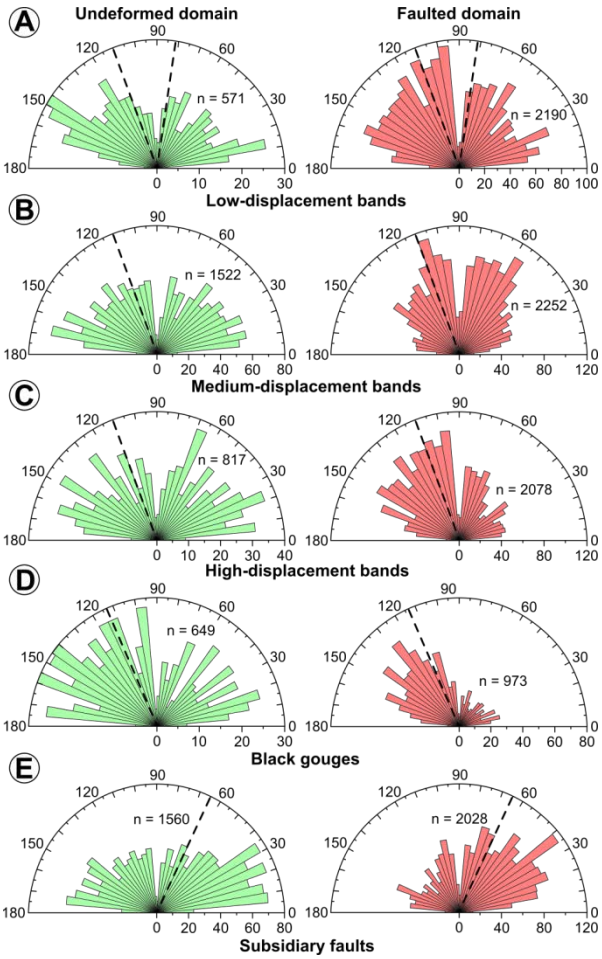


**Fig. 4.12.** Rose plot of the preferential orientation of grains according to the angle between the major axis and a horizontal reference plane. Undeformed control samples are on the left side, while deformed counterparts are on the right side of the figure. Preferential orientation for low-displacement (**a**), medium-displacement (**b**), high-displacement (**c**), black gouges (**d**) and subsidiary faults (**e**). Black dotted lines indicate the orientation of the deformation band, gouge or fault.

of deformation band (Fig. 4.12c). Preferred orientation of grains inside black gouge is even more apparent, with the direction of major axis of grains falling within 35° counter-clockwise from the gouge layer direction (Fig. 4.12d). Secondary faults with displacement > 20-30 cm have the most frequent classes of grain preferential orientation between 30-35° in clockwise direction from the fault (Fig. 4.12e).

Along the deformed domains the influence of the aspect ratio upon the preferential orientation was tested. In particular, grain orientation was plotted by dividing the dataset of faulted samples in three different classes of aspect ratio, namely 1.0-1.5, 1.5-2.0 and 2.0-2.5 (Fig. 4.13). Grains having aspect ratio above the threshold of 2.5 were not taken into account because of the limited number of data not able to provide statistical significance. In all the investigated samples it is evident that grains with aspect ratio falling between 1.0 and 1.5 have a much scattered distribution than the ones with higher values (Fig. 4.13). Samples affected by an overall weak deformation (due to limited displacement), show more randomly oriented clasts at low aspect ratio (Fig. 4.13a, b), while high-strain domains are characterized by more defined anisotropy of orientation (Fig. 4.13c, d, e). Finer grains show a stronger and more defined preferential orientation, with major axis orientation falling within 20° to 30° from the fault or deformation band.

## 4.8. Discussion

### 4.8.1. Deformation Mechanisms (Particulate Flow Followed by Cataclasis)

Deformation occurred at very shallow burial depth as indicated by stratigraphic constraints (Zecchin et al., 2012) and by the very weak compaction affecting the undeformed sandstone, collectively suggesting a maximum burial depth not exceeding 400-500 m. In this framework, deformation bands with displacement < 1 cm (Fig. 4.3a), characterized by grain re-organization and little grain size reduction, are interpreted to develop by particulate flow in highly porous sand (e.g., Rawling and

Goodwin, 2003; Balsamo and Storti, 2010; Rodrigues and Alves da Silva, 2018) (Figs. 4.8a and 4.14a). Particulate flow does not obliterate the original texture of pristine sandstone, but operates a re-organization of fabric leading to a closer packing of grains and to a porosity reduction, which collectively promotes contacts between grains (Antonellini et al., 1994; Kaproth et al., 2010; Soliva et al., 2013; Griffiths et al., 2016) (Figs. 4.6 and 4.14a). In low-displacement samples, the difference between the shape descriptors of deformed and undeformed domains is faint, thus indicating that grains maintain almost the same aspect ratio, circularity and solidity (Fig. 4.10a, b, c). The similar shape descriptors recorded by quartz, feldspar and lithic fragments are interpreted as a further evidence of particulate flow with very limited grain fragmentation, almost preserving the original shape of the pristine sandstone throughout all the investigated size classes (Fig. 4.11a, b, c). Approaching the master fault, deformation bands show a more pronounced reduction of grain size, even for bands with displacement in the order of a few cm (Fig. 4.8b, c). Grains are fractured, most likely during rolling and translation, interpreted as evidence of cataclasis as the main deformation mechanism (Engelder, 1974;

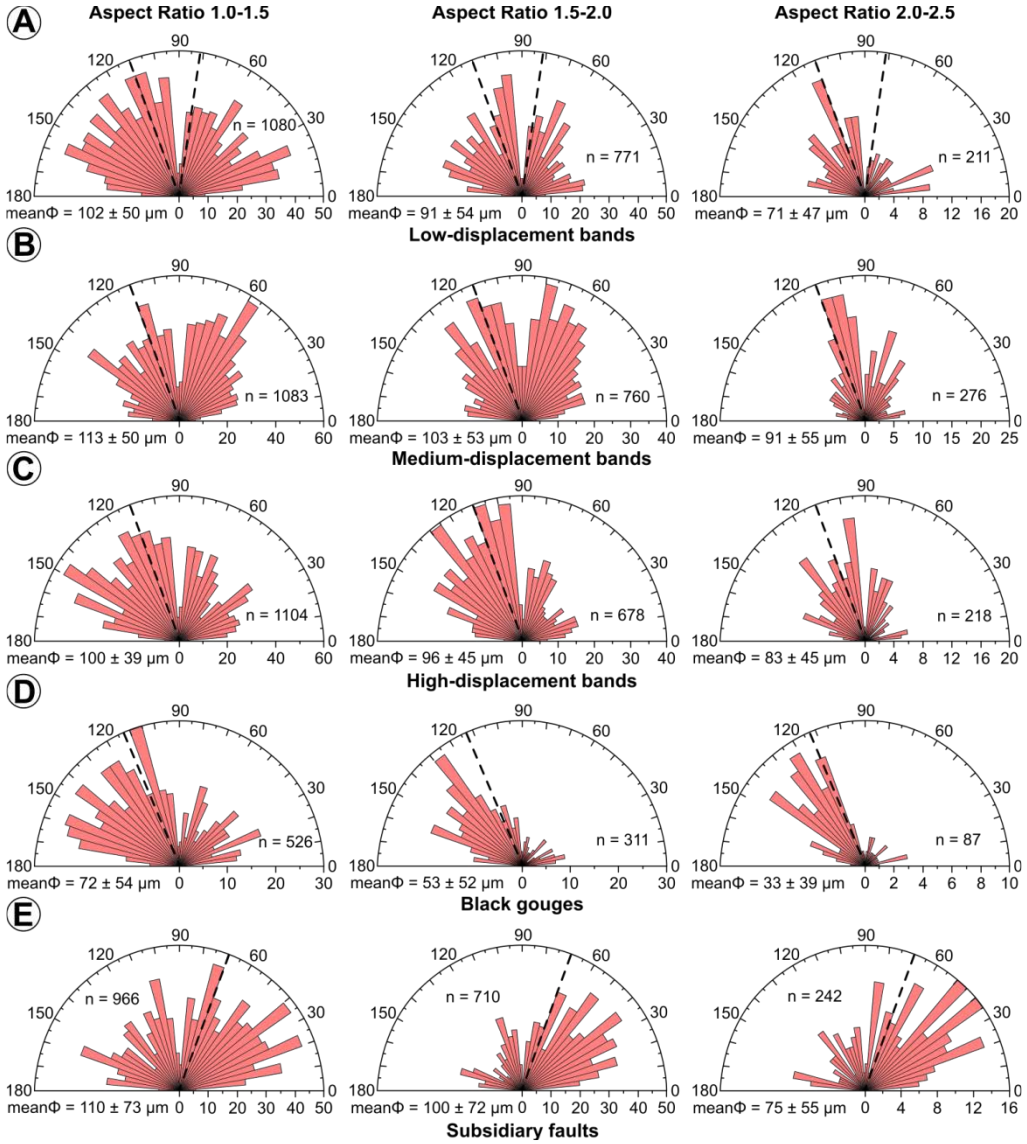


**Fig. 4.13.** Rose plot of the preferential orientation of grains inside the deformed samples according to the aspect ratio and to the grain size. Preferential orientation for low-displacement (**a**), medium-displacement (**b**), high-displacement (**c**), black gouges (**d**) and secondary faults (**e**). Dotted lines indicate the orientation of the band, gouge or fault.

Aydin and Johnson, 1978; Blenkinsop, 1991; Balsamo and Storti, 2010) (Figs. 4.9a and 4.14b, c). Grain breakage leads to a pronounced reduction of interparticle porosity (Fig. 4.6), due to the presence of small grain fragments filling the empty pore space (Antonellini et al., 1994; Kaproth et al., 2010; Skurtveit et al., 2013; Torabi, 2014) (Fig. 4.8c). Cataclasis is responsible for the significant difference of the shape parameters of the three main mineralogical phases involved in the deformation, with quartz grains resulting more elongate and irregular with respect to feldspar and lithics (Fig. 4.11d, e, f). Cataclasis is even more pronounced in deformation bands inside the fault core, leading to the formation of a central core showing strongly comminute grain size and an ultra-fine matrix (Figs. 4.8d and 4.14d). The pronounced difference of shape descriptors between quartz and feldspar provides evidence for severe cataclasis (Fig. 4.11g, h, i). The strongest degree of cataclasis is found in black gouge layers and along the fault core of minor faults, where strain-localization is testified by ultra-comminute layers (Engelder, 1974; Mair et al., 2002b; Balsamo et al., 2014) (Figs. 4.8e, f and 4.14e, f). The strong cataclastic degree is reflected also in the consistent difference of grain shape, particularly enhanced in the finer grain size range (Fig. 4.11j-o).

Cataclasis acts selectively according to the mineralogy of the grains involved in deformation. This feature is evident considering the systematic higher aspect ratio and the lower circularity and solidity values shown by quartz with respect to feldspar, especially at finer grain size range. The fragmentation of grains followed by sliding and rolling, promoted the formation of more equant, smoother and regular shape in the coarse grain size range (Blenkinsop, 1991; Heilbronner and Keulen, 2006; Storti et al., 2007; Balsamo and Storti, 2011) (Fig. 4.10j-o). Conversely at finer grain size, cataclasis produces highly elongate fine quartz sub-grains, while comminution of feldspar leads to more equant particles (Figs. 4.11d, e, f and 4.14b, c, d). This difference in deformation mechanism can be linked to the presence of cleavage and twinning planes along the crystal structures of feldspar, acting as preferential breakage surface (Exner and Tschegg, 2012; Nicchio et al., 2018). The presence of the aforementioned reticular weaknesses, promotes the development of intragranular fractures during incipient cataclasis, leading to the formation of several equant small-sized sub-clasts (Antonellini et al., 1994; Kaproth et al., 2010; Balsamo and Storti, 2011) (Fig. 4.9a). Conversely, quartz grains are less sensitive to the development of intragranular fractures due to the lack of twinning planes and to a higher strength compared to feldspar. This results in deformation achieved mainly by abrasion of the asperities and to lesser extent to intragranular fractures, leading to highly elongate small-sized and rounded-smoothed coarse-sized particles (Balsamo and Storti, 2011).

### 4.8.2. Displacement-Dependent Cataclasis

The deformation mechanism is related to the total amount of displacement accommodated along each deformation structure. While particulate flow is active for displacement < 1 cm, cataclasis settles for displacement > 1 cm and after a porosity loss up to 5-6% (Fig. 4.6). Therefore, a porosity

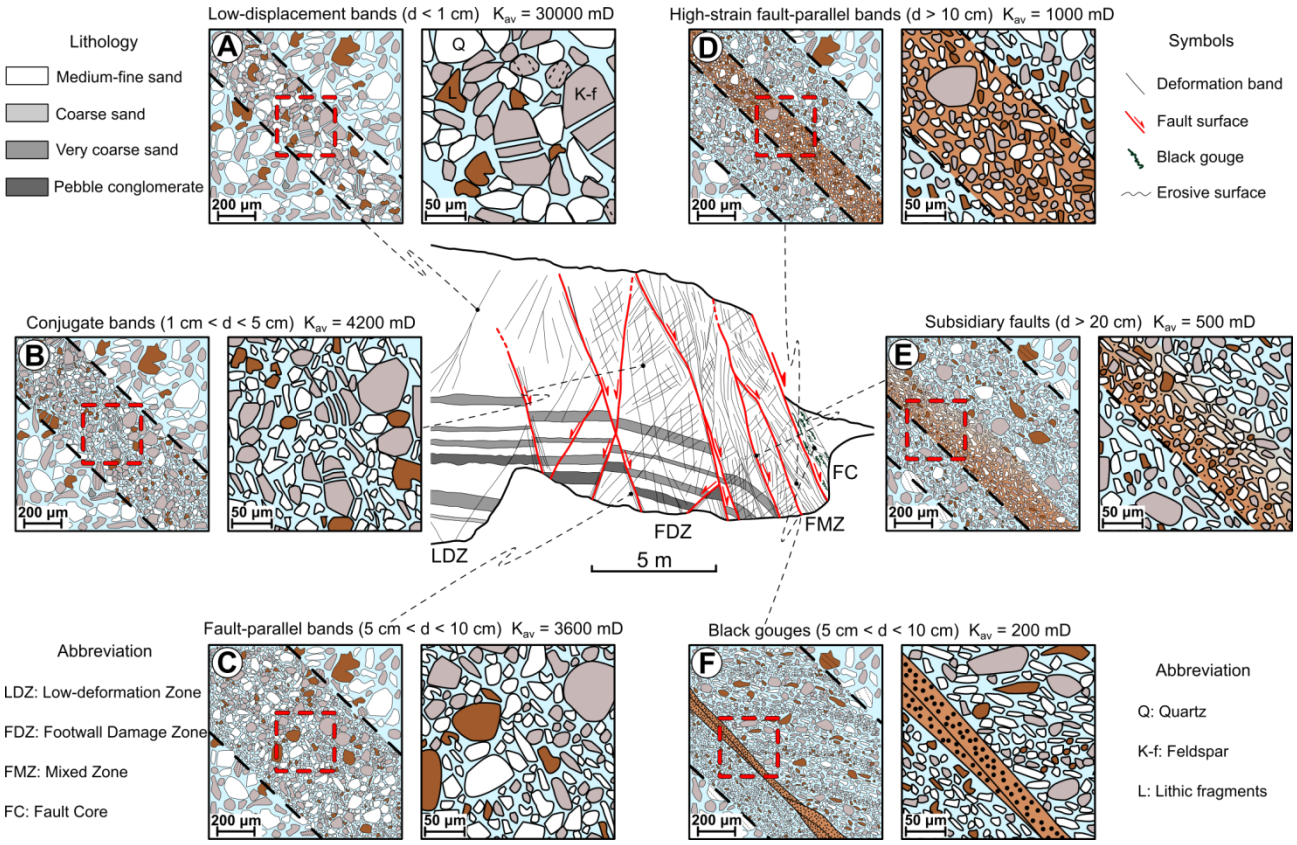


**Fig. 4.14.** Microstructural features according to the identified deformation mechanism. (**a**) Inside the low-deformation zone and the outer damage zone, deformation bands accommodated small-scale displacement (typically < 5 cm). Along these bands deformation is mainly achieved via particulate flow with fabric re-organization and negligible grain fragmentation. This causes a decrease in porosity from 37% of the undeformed sand to 6-7% within bands. (**b**) With slightly higher displacement, grains, especially feldspar, start to break along crystal weakness such as twinning planes. Quartz is less affected by fragmentation via intragranular fracturing and deforms mainly by flaking and chipping of the asperities along the outer surface. (**c**) Inside the footwall damage zone, fault-parallel deformation bands with displacement above 5 cm, are characterized by an immature cataclastic fabric, with evidence of rolling of grains. (**d**) High-displacement bands may develop an inner core with severe grain size reduction, leading to the formation of a brownish matrix composed of crushed feldspar and calcite grains. To the outer part of the band grain size reduction is less pronounced. Eventually, within the mixed zone and fault core are located the most deformed end-members with secondary faults (**e**) displaying an asymmetric structure with a slip surface and a decreasing gradient of grain size reduction moving away from it. Within the fault core black gouges (**f**) display extreme grain crushing leading to the formation of ultra-comminute thin layers, encased by less deformed sand arranged in S-C arrays. The deformation mechanism described above is able to reduce the permeability up to 3.5-4 orders of magnitude with respect to the pristine high-porosity sandstone.

decrease to 5-6% can be assumed as the critical threshold related to the switch from one deformation mechanism to the other. Due to the closer packing, grains are not able to re-organize their position and are forced to deform mostly by the development of intragranular fractures and by abrasion processes. As highlighted by other authors, porosity exerts a strong control upon the deformation mechanism inside porous granular material (Flodin et al., 2003; Shipton et al., 2005; Schultz et al., 2010).

The investigated deforming structures display a different maturity of cataclastic fabric with the increasing displacement (Fig. 4.8). In particular, in low to medium-displacement bands cataclasis is immature as testified by the slight decrease of grain size and sorting of the grain size distribution (Figs. 4.4d, e, f and 4.5). High-displacement deformation bands and fault core of minor faults

accommodating higher offset are characterized by more mature cataclastic fabric as indicated by the pronounced grain size reduction and widening of granulometric curves (i.e., sorting decrease) (Figs. 4.4g, h, i and 4.8d, f). Black gouge layers inside the core of the master fault, are interpreted as the product of extreme cataclasis caused by strain-localization, leading to the formation of thin, ultra-comminute layers (Fig. 4.8e). Cataclasis inside fault gouges is reflected in the extreme grain size reduction and diminishing of sorting (Figs. 4.4k and 4.5). The increasing cataclastic intensity with displacement can be seen also from the shape parameters of grains, in particular by evaluating the difference between quartz and feldspar (Fig. 4.11). Highly cataclastic samples (i.e., black gouges and secondary faults) have more marked difference between the shape descriptors of quartz and feldspar with respect to weakly cataclastic ones (Fig. 4.11). This can be assumed as evidence of different maturity of cataclastic fabric producing highly elongate and irregularly shaped grains at finer grain size and more rounded ones at coarse grain size (Balsamo and Storti, 2011) (Fig. 4.11). Pronounced cataclasis is also responsible for the development of a weak foliation, imparted by the preferential alignment of grains parallel or at low-angle to the orientation of the deformation bands and gouges (Cladouhos, 1999) (Figs. 4.12 and 4.13).

The distribution of the deformation bands, faults and gouges along the fault zone features an increasing displacement gradient approaching the master fault (Figs. 4.2 and 4.3). This is in accordance with the increase of the maturity of cataclastic fabric observed on sampled deformation bands and gouges.

### 4.8.3. Implications on Fluid Flow Through Poorly Lithified Sediments

The deformation mechanism previously described causes a diminishing of petrophysical properties of the deformed sandstone. Even deformation bands affected by low-displacement, accommodated dominantly via particulate flow, may show a permeability drop of half an order of magnitude (Fig. 4.15a). This decrement is mainly achieved by the decrease in porosity, and to lesser extent to grain size and sorting reduction. Deformation bands with higher displacement developing an immature cataclastic fabric, may induce a permeability decrease up to 1.5 orders of magnitude (Fig. 4.15b). This further decrement can be associated with a marked grain size reduction, coupled with a decrease in sorting (wider grain size distribution), thus diminishing the overall effective permeability. High-displacement bands features an effective permeability drop from 3 to 4 orders of magnitude, due to the pronounced cataclastic fabric formed via rolling-translation and abrasion of grains (Fig. 4.15c). In these samples, strain-localization may occur along the boundary between band and undeformed sand thus leading to a gradient of porosity and permeability drop (Fig. 4.15c). Mature cataclasis affecting the core of secondary faults and gouge layers causes a drop of mean permeability up to 4 orders of magnitude due to extreme grain size reduction and to the highest span of the granulometric curves (Fig. 4.15d). As seen before, strain-localization along discrete slip zone may cause an asymmetric drop of porosity and related permeability (Fig. 4.15d). Therefore, early stage particulate

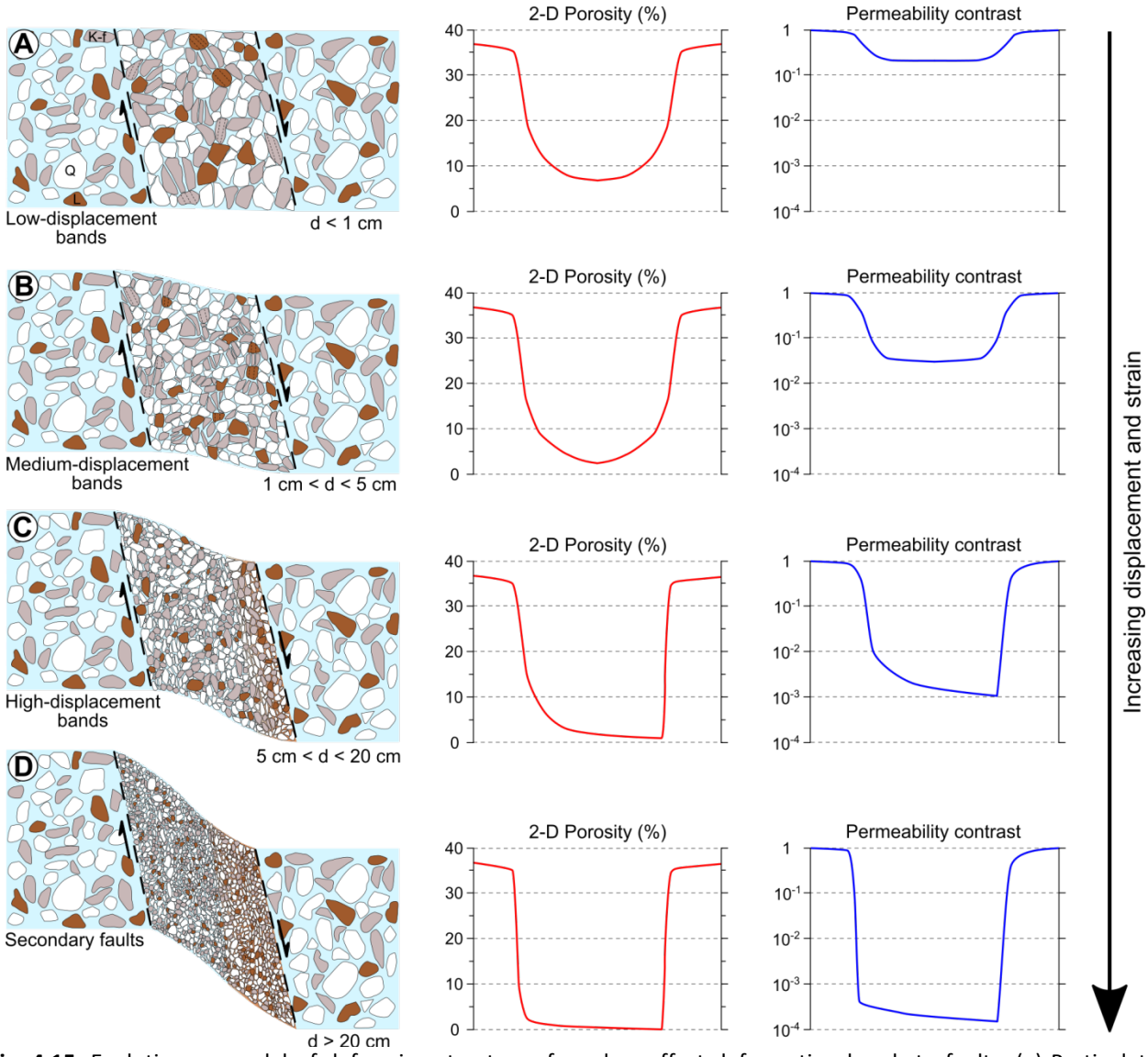


**Fig. 4.15.** Evolutionary model of deforming structures from low-offset deformation bands to faults. (**a**) Particulate flow affecting low-displacement deformation bands provides a weak grain size reduction and a closer packing of grains, leading to a mean porosity of 5-6%. The reduction of porosity features a decrease of permeability of less than one order of magnitude. (**b**) In medium-displacement deformation bands the onset of fragmentation and rolling of grains results in an immature cataclastic fabric, responsible for the reduction of grain size and sorting. Porosity is further reduced (2-3%) as well as permeability (1.5 orders of magnitude less than undeformed sand). (**c**) High-displacement bands are affected by pronounced cataclasis and strain-localization processes inducing an asymmetrical drop of porosity (~ 1%) and permeability (3 orders of magnitude less than the undeformed sand). (**d**) Eventually, along secondary faults with offset > 20 cm, cataclasis is extreme and severe grain size reduction leads to low values of porosity (< 1%) and to a permeability contrast up to 4 orders of magnitude with respect to the pristine sand.

flow followed by cataclasis affecting poorly lithified sand can reduce the effective permeability up to 4 orders of magnitude even with moderate displacement (10-20 cm). Thus, the studied deformation features are likely to have played a barrier role towards fluids orthogonal to the direction of the structural elements (Fig. 4.5). However, the real influence of the deformed features upon fluid flow has to be related also to the lateral continuity and three-dimensional arrangement of deformation bands and gouges (Shipton et al., 2005; Sternlof et al., 2006; Kolyukhin et al., 2010; Ballas et al., 2015). Moreover, lateral variations of thickness of deformation bands can be a critical parameter in decreasing the sealing potential at the scale of the single band

(Rotevatn et al., 2013, 2017). The presence of deformation bands with deformed whitish sand, surrounded by orange-brown stained undeformed sand due to iron oxides precipitation, suggests an effective sealing behaviour even for a few cm displacement (Fig. 4.3a). Even tough, the barrier-conduit role within deformed high porosity sediments is not straightforward as it is in the case of the fully lithified counterpart (Caine et al., 1996; Evans et al., 1997; Fisher et al., 2018). In fact, whereas in lithified rocks the fault core acts as an effective barrier and the damage zone as a preferential conduit, in poorly cemented sediments the sealing behaviour may depend on the hydrological conditions (Sigda and Wilson, 2003; Wilson et al., 2003; Balsamo et al., 2012). In water-saturated conditions deformation bands and gouges display a barrier role, while in unsaturated ones, they may act as partial conduit due to high retention time of fluids within the deformed sediments (Sigda and Wilson, 2003). The Rocca di Neto fault zone has a present day barrier role (as testified by permeability measurement), while during the early phase of deformation, the partial conduit behaviour is witnessed by the presence of selective cementation along deformation bands and faults (Pizzati et al. in preparation). This change in hydrological behaviour is likely due to the different environments and water-saturation conditions experienced by the fault during the deformation history.

## 4.9. Conclusions

We described the meso-scale structural features, microstructural characteristics and petrophysical properties of the extensional Rocca di Neto fault zone, deforming lithic arkosic to arkosic poorly lithified shoreface sandstones at shallow burial conditions (400-500 m). The fault zone accommodated 80-90 m of displacement from Middle Pleistocene to the present day. On the basis of our observations we came to the following conclusions:

1- The deformation mechanisms responsible for the development of deformation bands are non destructive particulate flow producing grain re-arrangement, followed by cataclasis with fragmentation and rolling of grains. Cataclasis becomes dominant after porosity decrease to 5-6% and is more intense with increasing displacement eventually forming gouge layers in the fault core.

2- Cataclasis acts differently according to the mineralogy of the deformed grains: feldspar grains deform mainly by intragranular fractures leading to more equant sub-grains with circular and more regular shape, while quartz grains are less affected by intragranular fractures and deform by flaking of asperities producing more elongated chips. Thus, quartz grains are more elongate, less circular and less smooth with respect to feldspar ones at finer grain size, while the difference is less pronounced at coarser grain sizes.

3- The intensity of cataclasis is more pronounced along deformation bands accommodating high offset. At the scale of the whole fault zone, deforming structures are characterized by an increasing displacement gradient approaching the master fault. This suggests that the degree of cataclasis is displacement-dependent.

4- Along deformation bands and gouge layers the grain size is drastically reduced (7-8 times) with respect to the pristine sandstone, and permeability shows a drop up to 3-4 orders of magnitude.

5- The Rocca di Neto fault zone is characterized by a present day barrier role towards fluids, but the hydrological behaviour depends on different factors such as the water-saturation condition, lateral continuity of deformation bands and gouges and along strike thickness variation. However, the presence of selective cementation preferentially located along bands inside the damage zone suggests a partial conduit role during the early stage deformation.

**Acknowledgements**

The authors would like to thank the technicians of the University of Parma Andrea Comelli for thin section preparation and Luca Barchi for support during SEM image acquisition. Federica Pessina (University of Parma) is also acknowledged for the support during the field work on the Rocca di Neto fault zone and in the Crotone Basin.
Mattia Pizzati collected field samples, interpreted laboratory data and wrote the manuscript, Fabrizio Balsamo, participated to field work, to data interpretation and to manuscript editing, Fabrizio Storti took part to data interpretation and to manuscript correction.

**Supplementary Material 1: Grain Size Analysis**

The grain size analyses were performed with a Mastersizer 3000 (Malvern Instruments) laser granulometer, coupled with the Hydro EV wet dispersion unit with de-ionized water as dispersant fluid. Using a dispersant medium means that the sample has to be completely loose and its introduction inside water may lead to severe bias concerning the real measured grain size, especially in fault rock samples. To avoid any issue related to the analytical technique, we performed several tests aimed to define the proper parameters used during the analysis following the methodology proposed by Storti and Balsamo (2010). Tests were aimed to minimize the sample alteration during the analysis. In particular, 5 main parameters were tested (table 4.A1):

1- The speed of the stirrer at the base of the beaker containing the dispersed sample is a critical parameter to be assess since it governs the speed of the water flux towards the analysis unit. At low speed, water movement inside the beaker is not able to mobilize coarse particles, remaining on the bottom, thus inducing bias on the final grain size analysis. With high stirrer speed, even coarser particles can be measured, but at the same time this can promote a severe fragmentation of grains, especially if they are already damaged or cracked such as fault rock samples. Stirred speed was tested with increment of 100 rpm starting from 500 (lower limit of the instrument) to 3500 rpm (upper limit of the stirrer speed).

2- The measurement time is related to the time required for the laser to efficiently analyse the flux of sample passing through the analysis cell. Usually, measurement time spans from 5 to 20 s, but can be changed according to the nature of the material.

Typically, short measurement times are suitable in the case of well sorted samples, with narrow grain size distribution. On the contrary, poorly sorted samples require longer measurement time to be properly analyzed. Three different configuration were tested with measurement time of 5, 10 and 20 s, respectively.

3- The total number of measurement is again critical because it also determines the residence time of the sample inside the stirring water. We adjusted the number of measurements according to the measurement time described above. Hence, we tested three different configurations, with 100 measurements each of them with a duration of 5s, 50 measurements at 10 s and 25 measurements at 20 s. In this way, the residence time of the sample inside water remained always the same throughout all the three performed tests.

4- Ultrasonication may be used at different intensity. It is helpful to avoid any process linked to the flocculation of clayish material, and related anomalous increase in mean grain size during the analysis. It is also suitable for cleaning grains from dust coating sticking on the outer surface. However, relatively high-intensity of ultrasonication may induce a severe fragmentation of particles affected by micro-cracks and reticular defects. We checked the influence of the ultrasonication at intensity of 2, 5 and 10%.

5- Eventually we tested the repeatability of the analytical procedure by performing 5 analyses on different sub-samples coming from the same sample amount. This test is aimed to check the overall quality of the adopted SOP (Standard Operating Procedure). If the grain size distributions gained from the five tests are comparable, then the SOP is accepted and the analysis of the sample can be performed.

We hereafter describe the different standard operating procedures adopted for the different sediment samples collected along the fault zone.

- Medium-fine sand samples from the low-deformation zone: loose sand samples were just inserted inside the analysis beaker, with a stirrer speed of 2500 rpm, 100 measurements each with 5 s duration, without any ultrasonication. Repeatability test confirmed the adopted parameters.

- Medium-fine sand samples from the footwall damage zone (interband domain): loose samples were inserted inside the analysis beaker, with a stirrer speed of 2600 rpm, 100 measurements each with 5 s duration, without any ultrasonication. Repeatability test confirmed the adopted parameters.

- Coarse sand samples from the footwall damage zone (interband domain): loose samples were put inside the beaker with distilled water, with a stirrer speed of 3000 rpm, 25 measurements each with a duration of 20 s, ultrasonication at intensity of 2% to remove fine dust and iron oxides-hydroxides deposited upon grain surface. Repeatability test confirmed the adopted parameters.

- Low-displacement deformation bands inside the low-deformation zone: slightly cohesive samples were dissolved in distilled water with a bit of mechanical agitation before the analysis. Stirrer speed of 2400 rpm, 100 measurements with duration of 5 s,

ultrasonication at 2%. Repeatability test confirmed the adopted parameters.

- Conjugate deformation bands deforming medium-fine sand inside the footwall damage zone: slightly cohesive samples were dissolved in distilled water with a bit of mechanical agitation before the analysis. Stirrer speed of 2500 rpm, 100 measurements each with duration of 5 s, with 2% ultrasonication. Repeatability test confirmed the adopted parameters.

- Conjugate deformation bands deforming coarse sand inside the footwall damage zone: slightly cohesive samples were dissolved in distilled water with a bit of mechanical agitation before the analysis. Stirrer speed of 2600 rpm, 25 measurements with duration of 20 s each and 2% ultrasonication. Repeatability test confirmed the adopted parameters.

- Fault surfaces inside the footwall damage zone: slightly cohesive samples were dissolved in distilled water with a bit of mechanical agitation before the analysis. Stirrer speed of 2200 rpm, 100 measurements each with duration of 5 s and 2% ultrasonication. Repeatability test confirmed the adopted parameters.

- Foliated fine sand inside the mixed zone: slightly cohesive samples were dissolved in distilled water with a bit of mechanical agitation before the analysis. Stirrer speed of 2000 rpm, 150 measurements with duration of 5 s each, ultrasonication of 5% for the first 50 measurements and then lowered down to 2% for the remaining 100. The analysis was conducted only on the last 100 measurements because the first 50 served to stabilize the mean diameter by ultrasonication. Repeatability test confirmed the adopted parameters.

- Foliated fine sand inside the fault core: slightly cohesive samples were dissolved in distilled water with a bit of mechanical agitation before the analysis. Stirrer speed of 2100 rpm, 150 measurements with duration of 5 s, ultrasonication of 5% for the first 50 measurements and then lowered down to 2% for the remaining 100. The analysis was conducted only on the last 100 measurements because the first 50 served to stabilize the mean diameter by ultrasonication. Repeatability test confirmed the adopted parameters.

- Foliated coarse sand inside the fault core: slightly cohesive samples were dissolved in distilled water with a bit of mechanical agitation before the analysis. Stirrer speed of 2900 rpm, 25 measurements each with a duration of 20 s, no ultrasonication. Repeatability test confirmed the adopted parameters.

- Black gouges from the fault core: samples were left inside distilled water for at least 12 hours prior to the analysis, to allow the completed disaggregation. Stirrer speed of 2000 rpm, 150 measurements each with 5 s duration, ultrasonication of 10% for the first 50 measurements and then 2% for the remaining 100. The analysis was conducted only on the last 100 measurements because the first 50 served to stabilize the mean diameter by ultrasonication. Repeatability test confirmed the adopted parameters.

- Silty clay from the hangingwall: samples were left inside distilled water for at least 12 hours prior to the analysis, to allow the completed disaggregation. Stirrer speed of

1500 rpm, 150 measurements with 5 s duration, ultrasonication of 10% for the first 50 measurements and then 2% for the remaining 100. The analysis was conducted only on the last 100 measurements because the first 50 served to stabilize the mean diameter by ultrasonication. Repeatability test confirmed the adopted parameters.

TABLE 4.A1: PARAMETERS OF THE STANDARD OPERATING PROCEDURES

| Sample type | Structural domain | Stirrer speed (rpm) | Measurement (n°) | Measurement time (s) | Ultrasonication intensity (%) | Sample preparation |
|---|---|---|---|---|---|---|
| Medium-fine sand | (LDZ) | 2500 | 100 | 5 | 0 | - |
| Medium-fine sand (interband) | (FDZ) | 2600 | 100 | 5 | 0 | - |
| Coarse sand (interband) | (FDZ) | 3000 | 25 | 20 | 2 | - |
| Low-displacement bands | (FDZ) | 2400 | 100 | 5 | 2 | Mechanical agitation |
| Conjugate bands (medium sand) | (FDZ) | 2500 | 100 | 5 | 2 | Mechanical agitation |
| Conjugate bands (coarse sand) | (FDZ) | 2600 | 25 | 20 | 2 | Mechanical agitation |
| Fault surfaces | (FDZ) | 2200 | 100 | 5 | 2 | Mechanical agitation |
| Foliated fine sand | (FMZ) | 2000 | 150 | 5 | 5(50 m) + 2(100 m) | Mechanical agitation |
| Foliated fine sand | (FC) | 2100 | 150 | 5 | 5(50 m) + 2(100 m) | Mechanical agitation |
| Foliated coarse sand | (FC) | 2900 | 25 | 20 | 0 | Mechanical agitation |
| Black gouges | (FC) | 2000 | 150 | 5 | 10(50 m) + 2(100 m) | Disaggregation |
| Silty clay | (FC) HW | 1500 | 150 | 5 | 10(50 m) + 2(100 m) | Disaggregation |

**Table 4.A1:** Summary of the parameters used to define the standard operating procedures adopted during grain size analysis. LDZ, low-deformation zone; FDZ, footwall damage zone; FMZ, footwall mixed zone; FC, fault core; HW, hangingwall.

## Supplementary Material 2: Detailed Permeability Measurements

Petrophysical measurements with the position of the sampling spots along the footwall of the fault (Fig. 4.A2). Grain size analysis was carried out with the procedures described in the section above, while air-permeability data were collected and calibrated according to the method described by Balsamo et al. (2012).

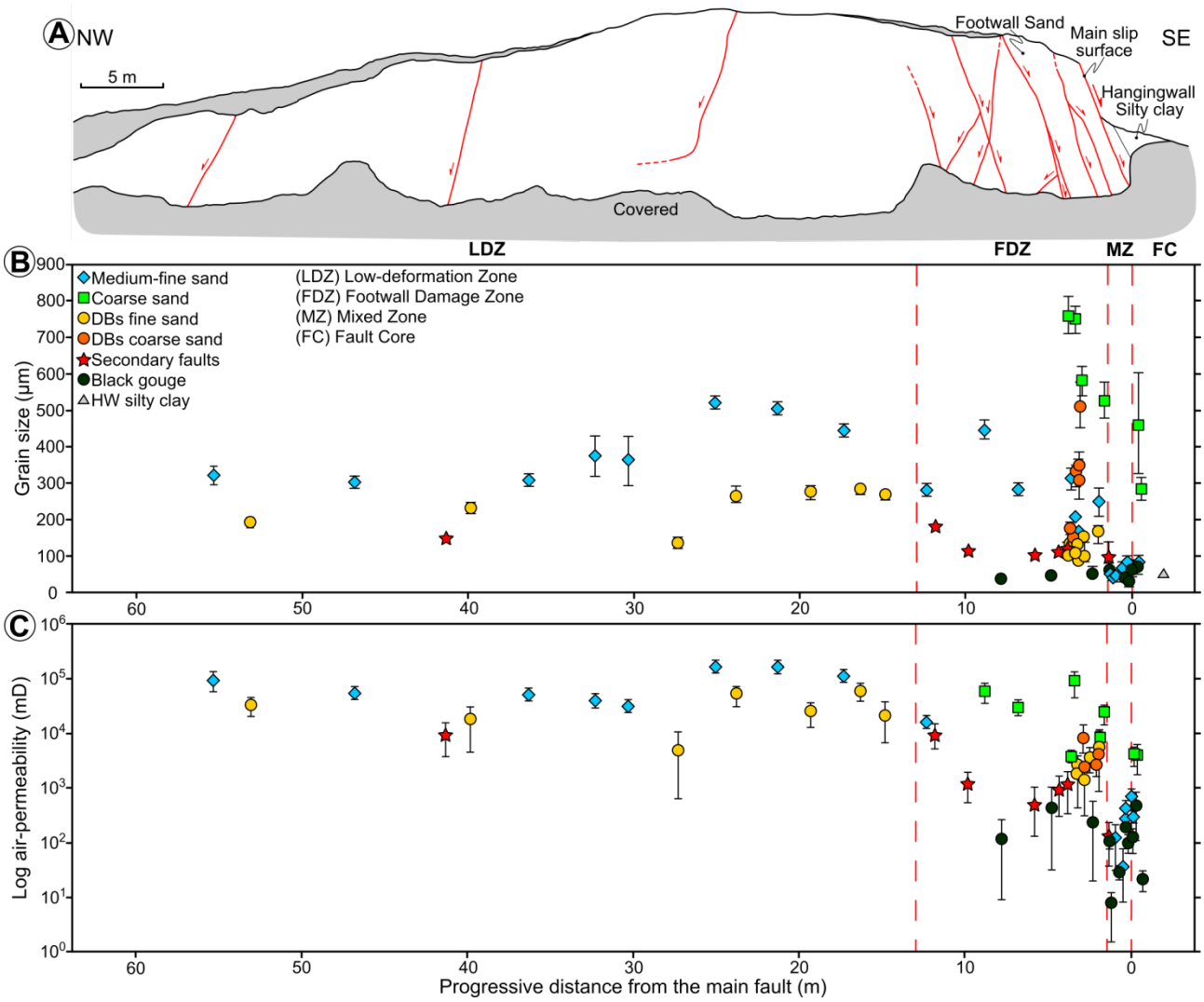


**Fig. 4.A2.** (**a**) Schematic sketch of the footwall side of the fault zone, with the trace of the secondary faults. (**b**) Mean grain size with the exact position of the collected samples. (**c**) *In situ* air-permeability measurements along the same sampling sites.

# CHAPTER 5

# Deformation Bands of the Cotiella Massif

In this chapter is described the occurrence of deformation bands along the footwall of the Cotiella Thrust, Spanish Pyrenees. Deformation bands developed inside calcarenitic rocks with mixed carbonate and siliciclastic component. Due to the depth of deformation (2-3 Km of maximum burial), deformation is achieved by a combination of solution of the carbonate fraction and fragmentation of siliciclastic grains. Thus deformation bands can be defined as shear-enhanced solution and compaction bands.

*Shear-enhanced compaction-solution bands in quartz-rich calcarenites of the Cotiella Massif (Spanish Pyrenees).*

Tavani, S., Granado, P., Balsamo, F., Pizzati, M., Cantarero, I., Corradetti, A., Muñoz, J.A.

Published on the *Journal of Structural Geology,* 114, 274–279. https://doi.org/10.1016/j.jsg.2017.11.018

# Shear-enhanced compaction-solution bands in quartz-rich calcarenites of the Cotiella Massif (Spanish Pyrenees)

Stefano Tavani[1], Pablo Granado[2], Fabrizio Balsamo[3], Mattia Pizzati[3], Irene Cantarero[4], Amerigo Corradetti[1], Josep Anton Muñoz[2]

[1] DISTAR, Università Federico II, Napoli, Italy

[2] Institut de Recerca Geomodels, Departament de Dinàmica de la Terra i de l'Oceà, Universitat de Barcelona, Barcelona, Spain

[3] NEXT, Department of Chemistry, Life Sciences and Environmental Sustainability, Parma University, Parma, Italy

[4] Departament de Mineralogia, Petrologia i Geologia Aplicada, Universitat de Barcelona, Barcelona, Spain

## Abstract

We describe conjugate systems of shear-enhanced compaction bands oriented oblique to the maximum compressive stress and developed in Paleocene quartz-rich calcarenites formed by the interplay between shearing, mechanical compaction, and dissolution. These deformation bands are located in the footwall of the Cotiella Thrust (Spanish Pyrenees), and strike perpendicular to the local tectonic transport direction. Conjugate shear-enhanced compaction bands are mutually perpendicular in cross-section, forming an angle of 45° with the shallow-dipping bedding; no macroscopic evidence of shearing is found along them. These shear-enhanced compaction bands occur together with less abundant bedding-perpendicular compaction bands, which strike perpendicular to the local transport direction. The described shear-enhanced compaction bands consist of mm-thick tabular structures showing higher concentrations of quartz grains with reduced sizes in respect to the surrounding undeformed rock. Optical microscope and SEM investigations show that the high concentration of quartz clasts within the bands was caused by pressure-enhanced dissolution of calcite. Quartz grains fragmentation is also observed within the bands, with no significant clasts rotation and translation. All these features indicate that the described shear-enhanced compaction bands are hybrid structures developed during layer-parallel shortening associated with the Cotiella Thrust and are characterized by localized dissolution of calcite grains and fragmentation of quartz grains.

### 5.1. Introduction

Deformation bands in nature are a roughly tabular mode of deformation localization

that occur in high porosity sandstones (Aydin et al., 2006; Tondi et al., 2006; Wibberley et al., 2007; Fossen et al., 2007, 2011) and poorly consolidated sediments (e.g., Rawling and Goodwin, 2003; Aydin et al., 2006; Tondi et al., 2006; Wibberley et al., 2007; Fossen et al., 2007, 2011). This term includes shear, compaction, and dilation bands, which are kinematically equivalent to faults, solution seams, and joints, respectively, developed in low-porosity rocks (e.g. Fossen et al., 2011). Shear-enhanced compaction bands have been recently documented as a separate type of deformation band, transitional between shear and compaction bands (e.g., Eichhubl et al., 2010; Charalampidou et al., 2011, 2014; Ballas et al., 2013; Soliva et al., 2016). These structures form at about 45° to the maximum principal stress (Eichhubl et al., 2010; Soliva et al., 2013) and, characteristically, displacement along and across the bands is roughly equal (Fossen et al., 2017), making them kinematically similar to slickolites (Carannate and Guzzetta, 1972). Similarly to compaction bands, which occur in porous granular material such as sandstones (Mollema and Antonellini, 1996; Aydin and Ahmadov, 2009; Schultz, 2009; Schultz et al., 2010; Fossen et al., 2011; Deng and Aydin, 2012) and to a lesser extent calcarenites (Baxevanis et al., 2006; Cilona et al., 2012; Rotevatn et al., 2016), shear-enhanced compaction bands occur in contractional regime (Fossen et al., 2017) and they require the occurrence of significant pore space in order to develop (e.g. Fossen et al., 2015). In fact, the processes of grain fragmentation, crushing, and translation, which ensure volume loss and mechanical compaction, occur at the expense of the intergranular porosity, which is progressively reduced during the formation of deformation bands (Mollema and Antonellini, 1996; Fossen et al., 2011; Charalampidou et al., 2014). However, it has been recently documented that hybrid, compaction-solution bands can also occur in low-porosity material, where the space between poorly soluble grains is occupied by relatively highly soluble calcite (Tavani et al., 2016). In these cases, crushing and fragmentation of poorly soluble grains like quartz still produce a certain decrease of the intergranular space, but this reduction is ensured by the stress-enhanced dissolution of the calcite occupying that space, i.e. by the pressure-solution process (Stockdale, 1922; Dunnington, 1954; Gratier et al., 2013). In this work we document shear-enhanced compaction-dissolution bands occurring in low-porosity quartz-rich calcarenites and developed at less than 2–3 km of depth in the Cotiella Massif of the Spanish Pyrenees. The carbonatic and siliciclastic components of the host rock, due to their different solubility and strength at low temperatures, followed different paths during deformation, and in particular during layer parallel shortening. In order to fully characterize this hybrid mode of deformation, outcrop-scale mesostructural analysis is coupled with microstructural investigations, including Optical Microscope, Scanning Electron Microscope (SEM), Cathodoluminescence analyses, and image analysis on selected thin sections.

### 5.2. Geological Background

Deformation bands occur at several places in Paleocene strata exposed in the footwall of the Cotiella Thrust. This thrust is a major structure of the South Pyrenean fold-and-thrust belt (Muñoz, 2002), that display a

gentle foreland-dipping (i.e. South-dipping) attitude, resulting from the imbrication of the underlying Gavarnie Thrust sheets (Cámara and Klimowitz, 1985; Muñoz, 2002). In the study area, the Cotiella Thrust largely preserves its footwall-flat character, juxtaposing the Triassic to Upper Cretaceous succession of the Cotiella extensional basin on top of the Paleogene and Upper Cretaceous rocks of the underlying Gavarnie Thrust sheets (López-Mir et al., 2016) (Fig. 5.1).

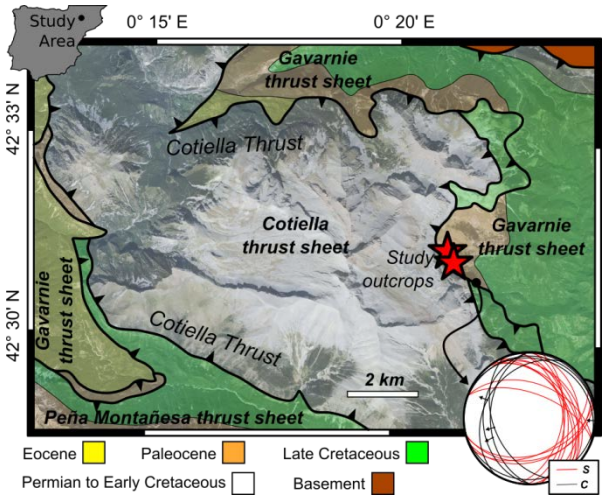


**Fig. 5.1.** Simplified geological map of the Cotiella Massif of Southern Pyrenees (Spain), with location of the study outcrops and stereoplots of S-C structures along the Cotiella Thrust in the vicinity of the outcrops.

The Paleogene sediments hosting the studied deformation bands were deposited in a foreland setting, with the overlying Middle Eocene to Oligocene sequence being in the order of 2–3 km thick (López-Mir et al., 2016). The overall transport direction of the Cotiella Thrust is toward the south (Séguret, 1972; Muñoz et al., 2013), however, local bends and vertical axis rotations occur, resulting in a complex framework of secondary transport directions. In order to evaluate the relationships between the formation of deformation bands and the regional tectonic framework, the data and samples presented here have been collected in an area where the local transport direction of the thrust is well-constrained. There, NNE-striking S-C structures in the Cotiella Thrust footwall provide a top-to-WSW direction of movement (Fig. 5.1), perpendicular to the average strike of the deformation bands presented here.

### 5.3. Outcrops, Samples, and Analyses

The two studied outcrops are located to the south of the Armeña Valley of the Cotiella Massif. These outcrops are about 500 m apart, and located a few tens of meters below the Cotiella Thrust surface. The investigated deformation bands consist of yellowish mm-thick anastomosing bands, showing a spacing of 5–50 cm, and protruding from a greyish calcarenitic host rock (Fig. 5.2). The deformation bands are arranged in two NNW-SSE-striking sets oriented at about 45° and 135° with the bedding surfaces (Fig. 5.2c, f), respectively, thus defining a dihedral angle of nearly 90° (Fig. 5.2b). A few NNW-SSE-striking and bedding-perpendicular deformation bands also occur (Fig. 5.2f). WSWENE-striking veins, oriented perpendicular to both bedding and deformation bands, have been found in both studied outcrops. Small-scale left-lateral bedding-perpendicular brittle faults (which are not shear bands) occur in one of the two outcrops (Fig. 5.2e), forming an angle of about 30° and 60° with the vein set and the deformation bands, respectively (Fig. 5.2f). These brittle strike-slip faults displace the deformation bands, while the same brittle strike slip-faults show ambiguous crosscutting relationships with the veins (meaning that they are broadly coeval).

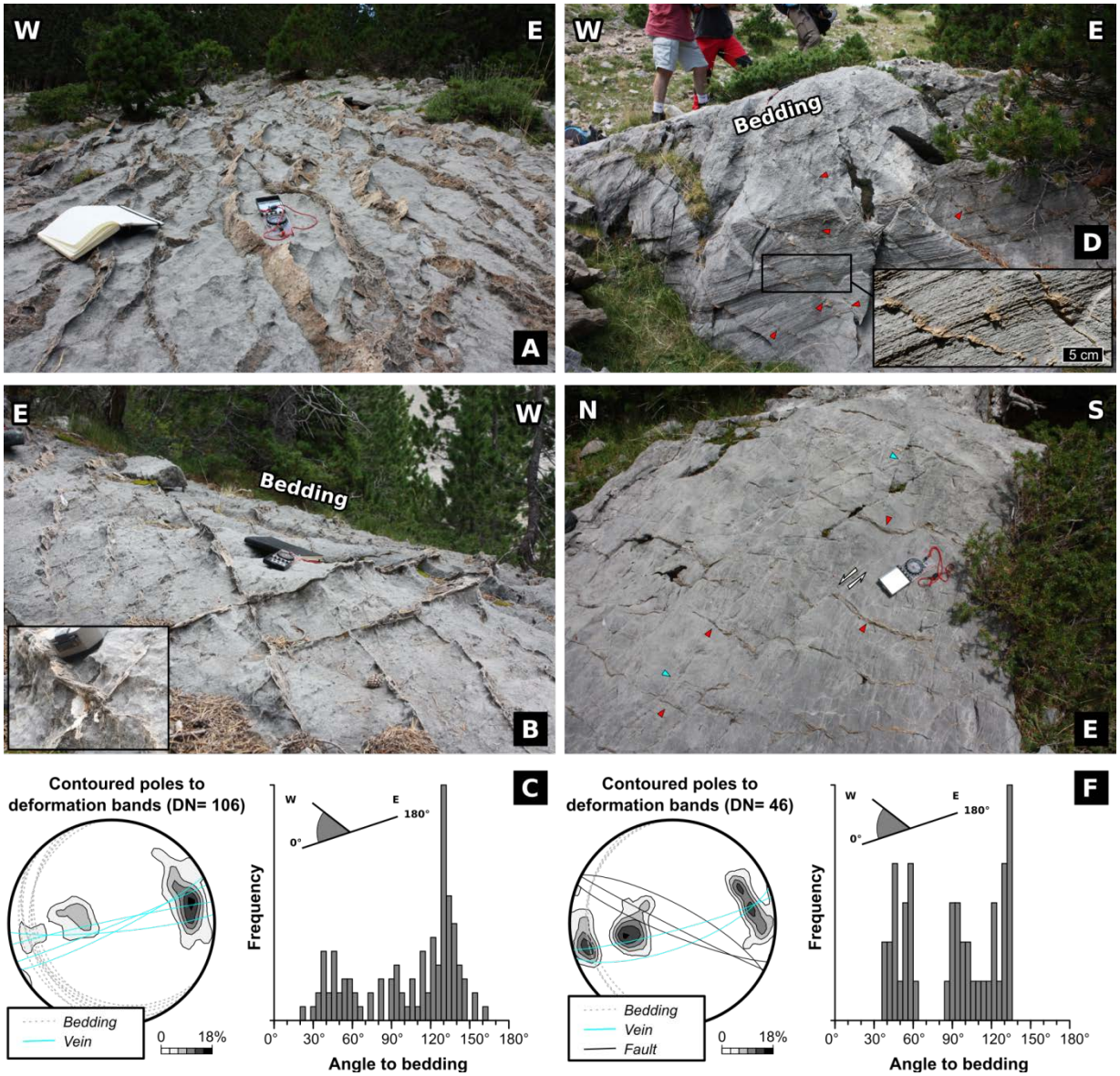


**Fig. 5.2.** Photographs of deformation bands of the northern (**a**–**b**) and southern (**d**–**e**) outcrop, with details showing cross-cutting relationships among different sets of deformation bands and between bands and sedimentary laminations. (**c**) Stereoplots of faults and veins with density contour of poles to deformation bands, and frequency distribution of the angle between deformation band and bedding from the northern (**c**) and southern (**f**) outcrop.

Faults, veins, bedding surfaces, and even laminations, are not displaced by the deformation bands (Fig. 5.2d). Moreover, the deformation bands themselves do not displace each other (Fig. 5.2b). No systematic cross-cutting/abutting relationships among the three sets of deformation bands (i.e. the bedding-perpendicular bands set and the sets including bands forming angles of 45° and 135° with the bedding) have been observed, and the abundant nodes formed by the intersections between the two bedding-oblique sets always form X-type intersections (Mäkel, 2007). These features indicate that these deformation bands do not show any macroscopically detectable evidence of shear (Fig. 5.2b). Samples of host rock and deformation bands have been analysed by means of optical, cathodoluminescence (CL), and scanning electron microscopes (SEM). The host rock consists of a bioclastic calcarenite, with less abundant siliciclastic grains, and intergranular micro-sparry calcite cement (Fig. 5.3a). The carbonate fraction is a

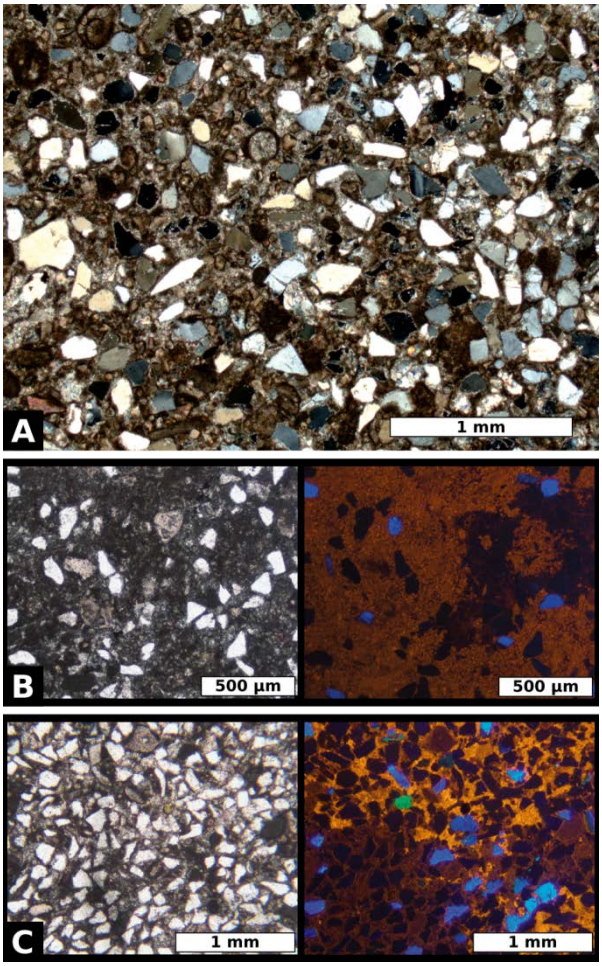


**Fig. 5.3.** Host rock microphotographs. (**a**) Cross-polarised light microphotograph of the quartz-rich calcarenite. (**b–c**) Plane light and cathodoluminescence images of the host rock, with feldspar and plagioclase grains identified by blue and green colour, respectively. Quartz clasts appear white in plane light and dark in cathodoluminescence images, where the calcite is from dull to bright orange.

peloidal grainstone-packstone, with minor echinoderm fragments, red algae and hyaline and agglutinated foraminifera; the non-carbonate fraction is represented by quartz, with a lesser content of K-feldspar, plagioclase and phyllosilicate material (Fig. 5.3). Siliciclastic grains are angular to subangular and their diameter generally does not exceed 0.5 mm (Figs. 5.3 and 5.4). The carbonate fraction colour in cathodoluminescence images ranges from dull to bright orange (Fig. 5.3b–c), indicating a locally pervasive replacement of the host

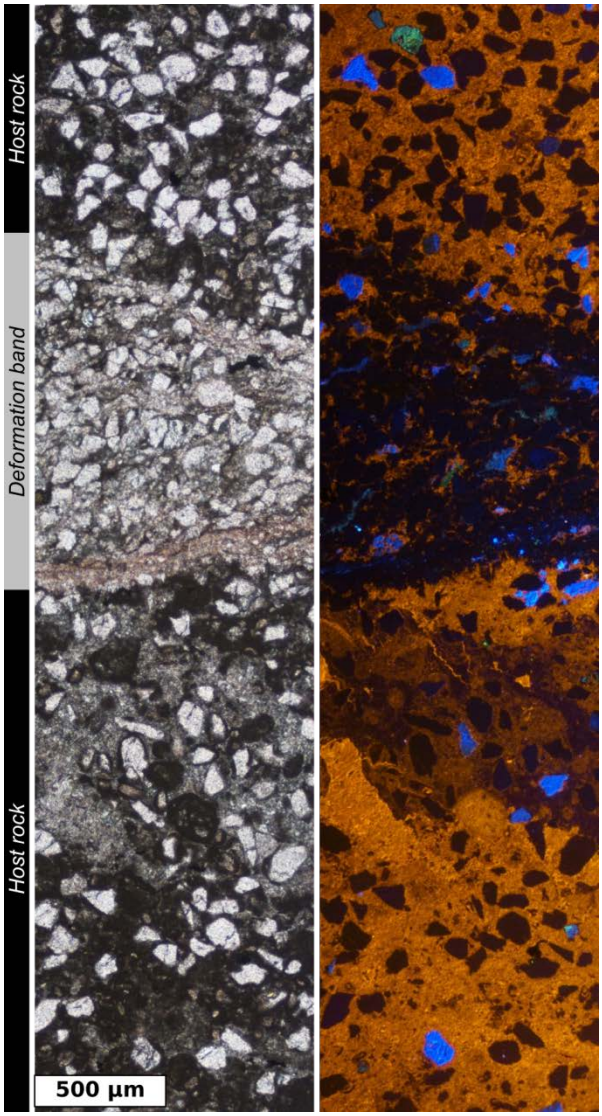


**Fig. 5.4.** Plane light and cathodoluminescence images of a deformation band and surrounding host rock.

rock. Bulk porosity of the host rock is negligible, as the intergranular porosity is occupied by micro-sparry calcite cement. Quartz and feldspar cements have not been observed, neither in the host rock nor within the deformation bands. In thin sections, deformation bands occur as zones of high concentration of siliciclastic grains (Fig. 5.4), with an increased grain fracturing and thin seams of insoluble material accumulation (Fig. 5.4). Image analysis on manually digitised selected images allowed us to compute both (i) the overall carbonate content and (ii) the shape parameter

(calculated as Roundness = 4π·Area/Perimeter2) of siliciclastic grains within and outside the deformation bands (Fig. 5.5). The carbonate content decreases from 60 to 80% within the host rock to 30–40%, and locally less, within the deformation bands (Fig. 5.5). The compactional strain required to obtain such a reduction, in the hypothesis that it is entirely accommodated by dissolution of calcite, is indicated in the green boxes of Fig. 5.5, and it ranges from 30% to 60%. Fracturing of siliciclastic grains within the deformation bands is very heterogeneous, varying from almost no fracturing, to grains split into multiple pieces, leading to a grain size reduction of up to 50% (Fig. 5.5). The increase in fracturing of siliciclastic grains within the deformation bands is accompanied by a very slight, i.e. mostly less than 5%, increase in the roundness of siliciclastic grains. Within the deformation bands, sutured contacts between quartz grains are observed (Fig. 5.6a), indicating pressure-solution at grain contacts. The contact between the host rock and the deformation band is generally sharp, and at places it is delimited by anastomosing stylolites that surround quartz and feldspar grains (Fig. 5.6b). Stylolites are also developed inside the deformation bands and rarely isolated in the host rock. Also, the deformation bands present a higher concentration of insoluble phyllosilicate minerals and iron-titanium oxides than the host rock. Phyllosilicate minerals are represented mainly by illite (Fig. 5.6c, d) and subordinately by montmorillonite and muscovite.

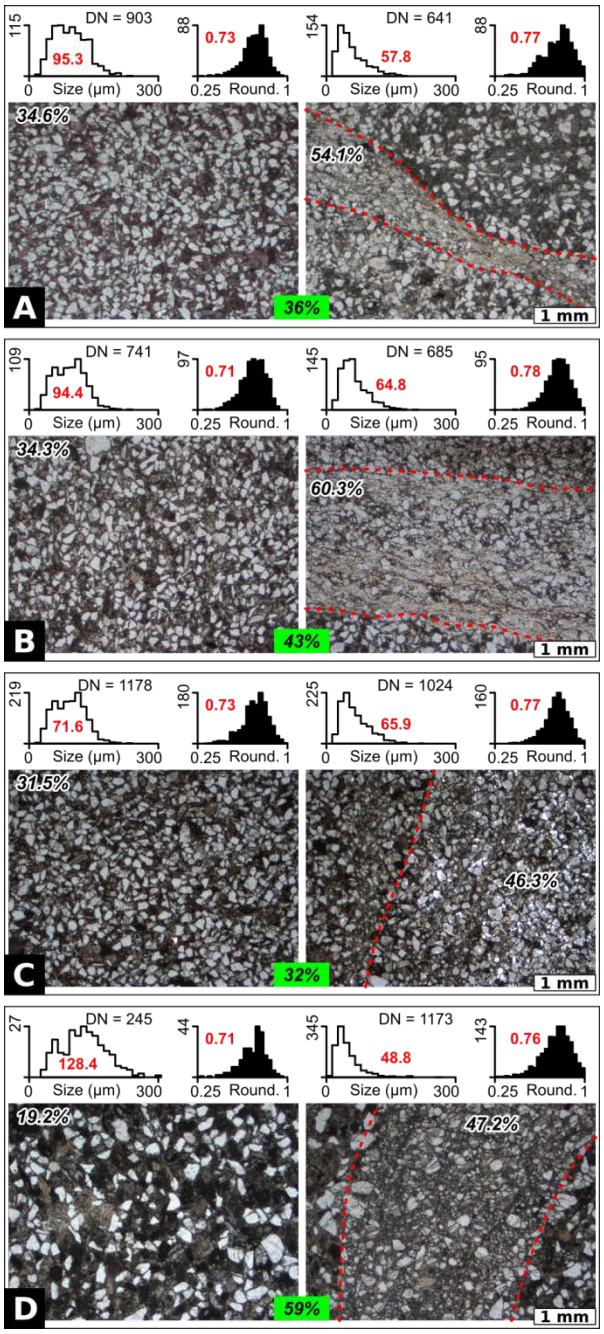


**Fig. 5.5.** Plane light microphotographs of deformation bands (delimited by the red dotted line) along with the corresponding host rock. Siliciclastic content is provided, for both deformation band and host rock, being computed by means of automatic image analysis. Frequency distributions of grain size (equivalent diameter) and roundness (spanning from 1 for a perfect sphere to 0 for clasts with extremely rough and angular borders) in the deformation bands and in the corresponding host rock are also provided, being computed on manually digitised clasts. The average value for both parameters is provided in red. The green boxes provide the amount of shortening required to increase the amount of quartz from that of the host rock to that of the deformation band, by assuming a simple two minerals (i.e. calcite and quartz) composition.

## 5.4. Discussion

At outcrop scale, the studied deformation bands are characterized by the apparent absence of shear displacement along them. Even mm-spaced sedimentary laminations are not displaced across the deformation bands (box in Fig. 5.2d), indicating that the amount of along-band displacement is in the order of less than a few mm. Similarly, a cataclastic fabric has not been recognised in microphotographs of deformation bands. These features evidence the limited role of shearing in the development of the studied deformation bands. The similar shape (i.e. roundness) of siliciclastic particles within and outside the deformation bands also point to a negligible shearing. Shearing in quartz-dominated granular systems, in fact, could lead to chipping and smoothing of rotating clasts (e.g. Balsamo et al., 2010), producing a marked increase in their roundness that has not been observed. On the other hand, our work demonstrates the role of chemical compaction in the development of the studied deformation bands. The reduced amount of calcite within the deformation bands is qualitatively (Fig. 5.4) and quantitatively evident (Fig. 5.5). Stylolites within the deformation bands are coated with insoluble material and hence indicates that the missing carbonate was removed by pressure-enhanced dissolution of the carbonate fraction (Stockdale, 1922; Gratier et al., 2013). Analogously, the occurrence of mechanical compaction along the deformation bands is marked by the reduction of quartz grain size within the bands with respect to that of the host rock (Fig. 5.5), which is a common feature during compaction banding of granular materials (e.g. Mollema and Antonellini, 1996). All these features evidence that the described bands are compaction bands. Bedding-parallel compaction bands developed by coeval chemical and mechanical compaction have recently been documented in a dolomitic limestone by Tavani et al. (2016). These authors report that burial-related calcite dissolution produced a progressive transition from a matrix-supported texture (i.e. calcite) to a grain-supported texture (i.e. dolomite crystal-supported), in which the less soluble dolomite crystals underwent grain-size reduction by fragmentation within compaction bands in response to the progressive closure of the inter-granular space occupied by calcite. A similar process, with coeval dissolution of calcite and fracturing of quartz grains, can be invoked for the compaction bands presented here, consistently with the observed microfabric and clast shape within the deformation bands. The few bedding perpendicular

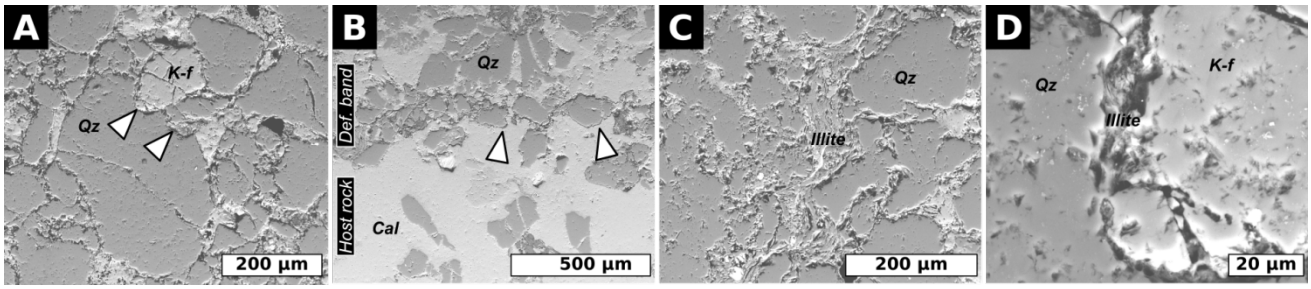


**Fig. 5.6.** Scanning electron microscope images of insoluble material along deformation bands. (**a**) Image showing sutured contacts between siliciclastic grains within deformation bands. (**b**) Solution seam marking the contact between deformation band and host rock. (**c**) Illite accumulation between siliciclastic grains. (**d**) Illite between sutured K-feldspar (K-f) and quartz (Qz) grains.

compaction bands observed in the two studied outcrops, along with bedding-perpendicular veins and the WNW-ESE striking bedding-perpendicular left-lateral faults (Fig. 5.2c, f), define the classical layer-parallel shortening pattern (Tavani et al., 2015). This pattern is consistent with a WSW-ENE directed layer-parallel shortening direction. This direction is perpendicular to the strike of the inclined to bedding compaction bands and lies on the plane bisecting these two sets of compaction bands. Occurrence of compaction in the order of 30–60% in mm-thick bands, indicates that across-band shortening is in the order of a millimetre. Negligible shearing along the deformation bands suggests that displacement across and along the deformation bands is broadly equivalent and small, which is confirmed by the observation that laminations oriented at 45° from the deformation bands are apparently not displaced (inset in Fig. 5.2d). Compaction bands are also arranged in a conjugate pattern, with two mutually perpendicular sets oriented at about 45° to the shortening direction. All these features are diagnostic of shear-enhanced compaction bands (e.g. Eichhubl et al., 2010) as documented in other outcrops world-wide (Ballas et al., 2013; Soliva et al., 2013; Fossen et al., 2015, 2017).

## 5.5. Conclusions

Results presented in this study indicate that in low porosity polymineralic granular systems undergoing layer parallel shortening at shallow burial depth (< 2–3 km), the combination of selective dissolution and mechanical compaction can lead to the development of shear-enhanced deformation bands.

## Acknowledgements

We wish to sincerely thank E. Charalampidou and H. Fossen for their constructive review of the manuscript. This is a contribution of the Institut de Recerca Geomodels and the Geodinàmica i Analisi de Conques research group (2014SGR467SGR) from the Agència de Gestió d'Ajuts Universitaris i de Recerca (AGAUR) and the Secretaria d'Universitats i Recerca del Departament d'Economia i Coneixement de la Generalitat de Catalunya. Financial support from SALTECRES (CGL2014-54118-C2-1-R) project is also acknowledged.

# CHAPTER 6

# General Discussion and Conclusions

This Ph. D Thesis dealt with the study of the relationship between deformation and selective cementation affecting loosely lithified sediments and rocks. This aspect was investigated considering different geological settings and deforming features using a multidisciplinary methodology consisting of meso-structural field data, petrographic and microstructural observations, diagenetic and geochemical analyses. This methodology was first tested on a relatively over-simplified structural setting (Enza River outcrop), and then applied to more complex case studies with extensive occurrence of soft-deformation structures (Rocca di Neto fault zone and Cotiella Thrust). Along the Enza River stratigraphic succession, the selective cementation is provided by shallow meteoric fluids percolating through loose sandstone sequence. The resulting selective cementation led to the formation of concretionary bodies with significant volume and lateral continuity. The only deformation affecting the porous sand strata is given by the tilting along the forelimb of the active Quattro Castella anticline propagating in the periclinal sector during their deposition. Diagenetic bodies developed selectively in medium to fine-grained sand strata, depending on the grain size and permeability structure at the scale of the entire outcrop, and are not constrained to the geometry and internal organization of peculiar sedimentary facies. Concretions recorded the change in fluid flow direction induced by the lateral propagation of the anticline, which promoted a rotation of the hydraulic and topographic gradient. In this framework, concretions can be used as markers of palaeo-fluid flow along folded structures affecting loose sediments in shallow burial conditions. Along the Rocca di Neto fault zone the selective cementation occurred in a structurally complex setting and played an important role in determining the deformation mechanism and the overall fault zone evolution. The presence of deformation structures such as deformation bands and faults affected by sin-kinematic cementation allowed to understand the diagenetic environment in which deformation occurred and helped in constraining the overall fault zone evolution through time. In particular, the shift from a mixed marine and meteoric environment to a markedly meteoric one characterizes the evolution of the fault zone during the uplift history. Along the fault zone, the combination of tectonic compaction and preferential cementation promoted the physical and chemical strain-hardening behaviour, forcing the propagation of the deformation towards the undeformed zone. This aspect is critical to define the timing of deformation involving each structural domain composing the fault zone. The soft-sediment deformation affecting the fault zone displays different characteristics depending on the deformation mechanism. Deformation bands and faults having limited displacement, typically deform by dominant particulate flow, with negligible grain size reduction and fabric re-organization. This leads to a pronounced decrease in porosity, promoting the onset of cataclasis with severe grain fragmentation, crushing and reduction of the overall sediment sorting. The deformation mechanism defines also the petrophysical properties of deformed sediments, which show significant decrease in permeability up to 3-4 orders of

magnitude. The deformed domains are characterized by selective cementation and this would suggest a partial conduit role exerted in under-saturated fluid conditions, despite the reduction of effective permeability. The last case study along the Cotiella Thrust, showed the result of deformation achieved by a combination of solution and compaction on low-porosity rocks with mixed carbonate and siliciclastic composition. Within such calcarenitic rocks, the deformation occurred as deformation bands developed under contractional setting at a maximum burial depth of 2-3 km. Along bands the deformation mechanism is given by the dissolution of the soluble calcite cement and by the fragmentation of quartz and feldspar grains, with limited shear and almost complete absence of cataclasis.

This Ph. D project, using a multidisciplinary study, attempted to describe and characterize the selective cementation occurring inside loosely cemented siliciclastic sediments and to unravel the relationships between deformation and cementation. These aspects have major implications: (i) the evaluation of the hydrological role of folded and faulted siliciclastic rocks and sediments; (ii) understanding the dynamic of selective cementation according to the petrophysical properties of the host granular media; (iii) constrain the structural evolution of fault zones and the deformation mechanism responsible for the occurrence of soft-sediment deformation structures.

These research themes are a matter of interest both for the academic-scientific world and for industrial applications, in particular in the field of exploration and exploitation of petroleum reservoirs as well as for groundwater reserve preservation.

# Future Perspectives

With this Ph. D project were investigated many topics, with particular emphasis on the development of carbonate concretions inside loosely cemented siliciclastic sediments, and upon the relationship between selective cementation and deformation. Despite all the efforts that were made, there still remain several unsolved issues and open questions which require further and more focused study.

- Concerning the development of carbonate concretions, especially from the Enza River Valley case study, it seems that bacterial activity could have played an important role in favouring the cementation. Still, we are not aware of what kind of microbe communities acted during cementation and what conditions they require to consistently take part to the formation of concretions.

- To better describe the process leading to the selective cementation it would be of great interest to evaluate with numerical simulations the growth of concretions, testing the influence of advective vs diffusive mass transfer, oversaturation condition of the cementing fluids and fluid flow pattern through sediments. By following this workflow it could be possible to constrain the time required for concretion cementation.

- In the Rocca di Neto case study we didn't find any direct evidence of bacterial activity inside the most deformed domain. It wasn't the focus and the primary topic to be studied along the fault zone. However, it would be interesting to the check the possible presence of bacteria also along the faults and deformation bands inside loose siliciclastic sediments. This aspect would add a third biological component to the strain-hardening behaviour together with chemical and physical processes.

- The Rocca di Neto fault zone, display features that can be associated with coseismic events and others to slow creep along faults. The detailed study of such features could be of great interest to shed lights on the earthquake dynamics at very shallow burial and near surface conditions.

- Along the Crotone Basin several faults are nicely exposed. Taking in account faults with different displacements and with structural features similar to the one studied in this Thesis, could be helpful to better describe the influence of the kinematic stress field on fault zone development at shallow burial conditions.

# Acknowledgements

During the Ph. D course i benefited from the help of several people, and to me it is essential to thank each of them in this section. First of all i wish to thank my tutor Fabrizio Balsamo, who is a kind friend prior to the Ph. D tutor. He allowed me to work in total independence without any strict control, letting me free to learn from my own errors and mistakes. Sometimes i felt a bit lonely during difficult and problematic moments, but in this way i learned on my skin the importance of being able to solve issues and not just to live them. Now i can say that it was a hard and somehow necessary training, useful not only for the Ph. D course, but also in everyday life. At the end of these fantastic three years i can look back to the difficulties, scientific problems and doubts that were faced and smile thinking that probably those were the moments that made the Ph. D so special and so worth to be lived with enthusiasm and passion, because they represent real chances to grow up. When everything goes in the right direction is always good, but if you have some sort of issue than you are forced to think in a different way, to study more and to push yourself to the limit. Fabrizio Balsamo also introduced me to the beautiful geology of the Crotone Basin, and we spent very nice time on the field. Fabrizio Storti is also acknowledged for constant support, useful and sometimes funny discussions and chats. Without the help of both "Fabrizios" all this would have never been possible.

Prof. Paola Iacumin is warmly thanked for the support and help with the stable isotope analysis and data interpretation. Prof. Roberto Tinterri is kindly acknowledged for the help in facies interpretation and nice chats about siliciclastic rocks, which to me remain the most beautiful rocks in the world. Prof. Rudy Swennen of the Katholieke Universiteit of Leuven (Belgium) is warmly thanked for all the help and support during the visiting period at the Leuven University. It is his merit if now i know something about diagenesis. Prof. Stefano Tavani (University of Naples) is kindly thanked for having involved me in the beautiful Cotiella Massif case study. Prof. Giacomo Prosser (University of Basilicata) is deeply thanked for the accurate and detailed review of the early version of this Thesis.

Then i really wish to thank all the Ph. D students and fellows of the University of Parma for the nice moments and lunch breaks we sheared together. In particular, my most heartfelt thanks are for all the members of NEXT research group, Alessio Lucca, Silvia Cortinovis, Andrea Succo, Luigi Berio, Silvia Brizzi, Matheus Nicchio and Cristian Cavozzi, and also for the former members Mahtab Mozafari, Kei Ogata, Luca Clemenzi, Yago Nestola, Flavio Milazzo and Angelo Borsani. Our group is a very strong one and since i am a great F1 fan, i always believed that a good team is similar to an old-fashion V12 engine used in the early 90's seasons: each member of the team is like a piston and needs to work in perfect harmony and synchrony with the others to provide the maximum horsepower to the engine. Well that is exactly our group, i only have good memories of the three years spent during the Ph. D period. Working with all of them i learned the deepest meaning of the words friendship, loyalty, help, support and passion.

All the technicians of the University of Parma are kindly acknowledged for their support: in particular, Andrea Comelli for this section preparation and Luca Barchi for support during SEM

sessions. Enrico Maria Selmo and Antonietta di Matteo are warmly thanked for having provided the stable isotope analyses and for kind support shown during sample preparation.
All the students that i dealt with are acknowledged and it was a real privilege to show them the few things i learned during these three years and hopefully i managed to transmit them the passion for the research and for geological topics in general. I recommend all the students to study with passion, work as hard as you can and be always humble, positive and willing to learn. Eventually, the most touched thanks are addressed to my family; my dad Pierino and mom Saveria, my brothers Vanni (who is sharing with me the passion for geology) and Davide with his wife Olga and their daughter, the lovely Dalia. Without their support, constant help and comprehension all this would have never been possible. This Thesis is dedicated to all of them, and in particular to my niece Dalia, with the hope that in future she will enjoy the beauty of studying. At the beginning of this Ph. D i was nothing more than a graduate student and now at the end of this journey i grew up as a man and as a geologist, knowing that this will only be the beginning of a new journey.
Dear reader, with these few sentences the very last page unfolds. If this Thesis was a F1 grand prix or a baseball match this would be the last turn of the race, the checkered flag is waving on the finish line... the pitcher steps on the mound grabbing the ball inside the glove and the last pitch of the game is going to be thrown.

# Courses, Publications and other Activities during the Ph. D Course

**Courses and Seminars**

- Workshop entitled "*Geologia del Petrolio*", organized in cooperation between the University of Parma and Eni s.p.a. from the 23rd to 26th February 2016.

- Workshop entitled "*Texture Topics: Texture analysis and orientation imaging*", held by Prof. Renèe Heilbronner, at the University of Basel, Switzerland, from the 31th October to 4th November 2016.

- "*Diagenesis*" Master Degree course held by Prof. Rudy Swennen at the Katholieke Universiteit of Leuven (Belgium), attained during an abroad study period from the 8th November to 20th December 2016. During this period a scientific cooperation was settled.

- Seminar of the Italian Group of Stable Isotopes: "*Espressione dei risultati isotopici, taratura standard interni ed internazionali, accreditamento e metodologie*", organized at the University of Parma the 25th and 26th May 2017.

- Seminar "*The scientific contribution of young researchers in the field of Earth Sciences*", organized in cooperation between the University of Parma and the University of Ferrara, the 7th July 2017.

- Course "*Trattamento dei dati statistici, regressione e taratura*", held by Prof. Giampiero Venturelli, at the University of Parma during November 2017.

- Short Course "*Fault rock microstructures*" held by Prof. Renèe Heilbronner, University of Basel, Switzerland, organized at the University of Parma the 11th and 12th December 2017.

- Short course "*Project design and grant writing*", organized at the University of Parma the 12th 13th March 2018.

**Conference Contributions**

- Pizzati, M., Cavozzi, C., Magistroni, C., Storti F. (2016). Use of integrated analogue and numerical modelling to predict tridimensional fracture intensity in fault-related-folds. *European Geosciences Union, General Assembly, Vienna, 17-22/04/2016 (oral presentation)*.

- Pizzati, M., Balsamo, F., Iacumin, P., Storti, F. (2016) Carbonate concretions in synkinematic Quaternary sediments as markers of paleo-fluid flow induced by the development of the Quattro Castella growth anticline, Northern Apennines, Italy. *European Geosciences Union, General Assembly, Vienna, 17-22/04/2016 (poster presentation)*.

- Pizzati, M., Cavozzi, C., Magistroni, C., Storti, F. (2016). Use of analogue modelling as driver for 3D fracture pattern predictions in fault-related-folds. *88° Congresso della Società Geologica Italiana, Napoli, 7-9/9/2016 (poster presentation)*.

- Pizzati, M., Balsamo, F., Iacumin, P., Storti, F. (2016). Carbonate concretions in loose Quaternary sediments as markers of paleo-fluid flow induced by the development of the Quattro Castella Anticline, Northern Apennines, Italy. *88° Congresso della Società Geologica Italiana, Napoli, 7-9/9/2016 (poster presentation)*.

- Pizzati M., Balsamo F., Iacumin P. Swennen R. and Storti F. (2017) Paleo-fluid flow in folded, poorly lithified Quaternary sediments revealed by diagenetic concretions developed during the growth of Quattro Castella Anticline (Northern Apennines, Italy). *European Geosciences Union, General Assembly, Vienna, 23-29/4/2017 (poster presentation).*

- Pizzati M., Balsamo F., Iacumin P. Swennen R. and Storti F. (2017) Structural architecture and petrophysical properties of the Rocca di Neto extensional fault zone developed in the shallow marine sediments of the Crotone Basin (Southern Apennines, Italy). *European Geosciences Union, General Assembly, Vienna, 23-29/4/2017 (poster presentation).*

**Publications on Peer-Review International Journals**

- Pizzati, M., Balsamo, F., Storti, F., Mozafari, M., Iacumin, P., Tinterri, R., Swennen, R., 2018. From axial parallel to orthogonal groundwater flow during fold amplification: insights from carbonate concretion development during the growth of the Quattro Castella Anticline, Northern Apennines, Italy. *Journal of the Geological Society of London* 175, 806–819. https://doi.org/10.1144/jgs2018-031

- Tavani, S., Granado, P., Balsamo, F., Pizzati, M., Cantarero, I., Corradetti, A., Muñoz, J.A., 2018. Shear-enhanced compaction-solution bands in quartz-rich calcarenites of the Cotiella Massif (Spanish Pyrenees). *Journal of Structural Geology* 114, 274–279. https://doi.org/10.1016/j.jsg.2017.11.018

**Publications about to be Submitted**

- Pizzati, M., Balsamo, F., Storti, F., Iacumin, P. Physical and chemical strain-hardening in faulted poorly lithified sandstones (Crotone Basin, Italy). To be submitted to *Geological Society of America Bulletin*.

- Pizzati, M., Balsamo, F., Storti, F. Petrophysical and microstructural properties of sub-seismic deformation bands and gouges in a fault zone developed in poorly lithified sandstone at shallow burial depth (Crotone Basin, Italy). To be submitted to *Journal of Structural Geology*.

**Other Activities**

- Support during didactic field work of the course Structural Geology, teacher in charge Prof. Fabrizio Storti, 6th May 2016.

- Seminar concerning image analysis techniques, addressed to the students of the course Earthquake Geology, teacher in charge Dott. Fabrizio Balsamo, 9th-12th April 2018.

- Selected reviewer of two submitted manuscripts (Yoshida et al., "*Spherical carbonate concretions formed around decaying organic matter in early diagenesis*", submitted to *Scientific Reports*, and Nemra et al., "*Potpourri of various co-occurring synsedimentary carbonate concretions from the Miocene of NW-Algeria*" submitted to *Facies*).

- Co-tutor of one Thesis of the Bachelor's Degree course in Geological Sciences, University of Parma.

- Notte dei Ricercatori 2016 and 2017, University of Parma.

**Awards**

The poster contribution entitled “Pizzati, M., Balsamo, F., Iacumin, P., Storti, F. (2016). Carbonate concretions in loose Quaternary sediments as markers of paleo-fluid flow induced by the development of the Quattro Castella Anticline, Northern Apennines, Italy”, received an award during the 88° Congress of the Italian Geological Society, Napoli, 7th-9th September 2016, as the best poster of the Session S2: “Structural geology all around on the Earth and other planets: case studies, modelling and industrial applications (session dedicated to the memory of Marco Beltrando)”.

# Reference List


Abdel-Wahab, A., and McBride, E.F., 2001, Origin of giant calcite-cemented concretions, Temple Member, Qasr El Sagha Formation (Eocene), Faiyum Depression, Egypt: Journal of Sedimentary Research, v. 71, p. 70–81, doi: 10.1306/031700710070.

Ahlgren, S.G., 2001, The nucleation and evolution of Riedel shear zones as deformation bands in porous sandstone: Journal of Structural Geology, v. 23, p. 1203–1214, doi: 10.1016/S0191-8141(00)00183-8.

Aiello, I.W., Garrison, R.E., Moore, J.C., Kastner, M., and Stakes, D.S., 2001, Anatomy and origin of carbonate structures in a Miocene cold-seep field: Geology, v. 29, p. 1111–1114, doi: 10.1130/0091-7613(2001)029<1111:AAOOCS>2.0.CO;2.

Alfaro, P., Gibert, L., Moretti, M., Garcìa-Tortosa, F.J., Sanz de Galdeano, C., Galindo-Zaldívar, J., and Lopez-Garrido, A.C., 2010, The significance of giant seismites in the Plio-Pleistocene Baza palaeo-lake (S Spain): Terra Nova, v. 22, p. 172–179, doi: 10.1111/j.1365-3121.2010.00930.x.

Angeletti, L., Canese, S., Franchi, F., Montagna, P., Reitner, J., Walliser, E.O., and Taviani, M., 2015, The “chimney forest” of the deep Montenegrin margin, south-eastern Adriatic Sea: Marine and Petroleum Geology, v. 66, p. 542–554, doi: 10.1016/j.marpetgeo.2015.04.001.

Antonellini, M., and Aydin, A., 1994, Effect of faulting on fluid flow in porous sandstones: petrophysical properties: American Association of Petroleum Geologists Bulletin, v. 78, p. 355–377, doi: 10.1306/8D2B1B60-171E-11D7-8645000102C1865D.

Antonellini, M., Aydin, A., and Orr, L., 1999, Outcrop-Aided Characterization of a Faulted Hydrocarbon Reservoir, Arroyo Grande Oil Field, California, USA, *in* Haneberg, W.C., Mozley, P.S., Moore, J.C., and Goodwin, L.B., eds., Faults and Subsurface Fluid Flow in the Shallow Crust: Washington D.C., USA, Geophysical Monograph 113, American Geophysical Union, p. 7–26.

Antonellini, M., Aydin, A., and Pollard, D.D., 1994, Microstructure of deformation bands in porous sandstones at Arches National park, Utah: Journal of Structural Geology, v. 16, p. 941–959.

Antonellini, M., Petracchini, L., Billi, A., and Scrocca, D., 2014, First reported occurrence of deformation bands in a platform limestone, the Jurassic Calcare Massiccio Fm., northern Apennines, Italy: Tectonophysics, v. 628, p. 85–104, doi: 10.1016/j.tecto.2014.04.034.

Antonioli, F., Ferranti, L., Lambeck, K., Kershaw, S., Verrubbi, V., and Dai Pra, G., 2006, Late Pleistocene to Holocene record of changing uplift rates in southern Calabria and northeastern Sicily (southern Italy, Central Mediterranean Sea): Tectonophysics, v. 422, p. 23–40, doi: 10.1016/j.tecto.2006.05.003.

Arribas, M.E., Rodriguez-Lopez, J.P., Meléndez, N., Soria, A.R., and de Boer, P.L., 2012, Giant calcite concretions in aeolian dune sandstones; sedimentological and architectural controls on diagenetic heterogeneity, mid-Cretaceous Iberian Desert System, Spain: Sedimentary Geology, v. 243–244, p. 130–147, doi: 10.1016/j.sedgeo.2011.10.011.

Aydin, A., 1978, Small faults formed as deformation bands in sandstone: Pageoph, v. 116, p. 913–930.

Aydin, A., and Ahmadov, R., 2009, Bed-parallel compaction bands in aeolian sandstone: Their identification, characterization and implications: Tectonophysics, v. 479, p. 277–284, doi: 10.1016/j.tecto.2009.08.033.

Aydin, A., Borja, R.I., and Eichhubl, P., 2006, Geological and mathematical framework for failure modes in granular rock: Journal of Structural Geology, v. 28, p. 83–98, doi: 10.1016/j.jsg.2005.07.008.

Aydin, A., and Johnson, A.M., 1983, Analysis of faulting in porous sandstones: Journal of Structural Geology, v. 5, p. 19–31, doi: 10.1016/0191-8141(83)90004-4.

Aydin, A., and Johnson, A.M., 1978, Development of faults as zones of deformation bands and as slip surfaces in sandstone: Pageoph, v. 116, p. 931–942.

Ballas, G., Fossen, H., and Soliva, R., 2015, Factors controlling permeability of cataclastic deformation bands and faults in porous sandstone reservoirs: Journal of Structural Geology, v. 76, p. 1–21, doi: 10.1016/j.jsg.2015.03.013.

Ballas, G., Soliva, R., Benedicto, A., and Sizun, J.P., 2014, Control of tectonic setting and large-scale faults on the basin-scale distribution of deformation bands in porous sandstone (Provence, France): Marine and Petroleum Geology, v. 55, p. 142–159, doi: 10.1016/j.marpetgeo.2013.12.020.

Ballas, G., Soliva, R., Sizun, J.P., Benedicto, A., Cavailhes, T., and Raynaud, S., 2012, The importance of the degree of cataclasis in shear bands for fluid flow in porous sandstone Provence, France: AAPG Bulletin, v. 96, p. 2167–2186, doi: 10.1306/04051211097.

Ballas, G., Soliva, R., Sizun, J., Fossen, H., and Benedicto, A., 2013, Shear-enhanced compaction bands formed at shallow burial conditions; implications for fluid flow (Provence, France): Journal of Structural Geology, v. 47, p. 3–15, doi: 10.1016/j.jsg.2012.11.008.

Balsamo, F., Aldega, L., De Paola, N., Faoro, I., and Storti, F., 2014, The signature and mechanics of earthquake ruptures along shallow creeping faults in poorly lithified sediments: Geology, v. 42, p. 435–438, doi: 10.1130/G35272.1.

Balsamo, F., Bezerra, F.H.R., Vieira, M.M., and Storti, F., 2013, Structural control on the formation of iron-oxide concretions and Liesegang bands in faulted, poorly lithified Cenozoic sandstones of the Paraìba Basin, Brazil: Bulletin of the Geological Society of America, v. 125, p. 913–931, doi: 10.1130/B30686.1.

Balsamo, F., and Storti, F., 2010, Grain size and permeability evolution of soft-sediment extensional sub-seismic and seismic fault zones in high-porosity sediments from the Crotone basin, southern Apennines, Italy: Marine and Petroleum Geology, v. 27, p. 822–837, doi: 10.1016/j.marpetgeo.2009.10.016.

Balsamo, F., and Storti, F., 2011, Size dependent comminution, tectonic mixing and sealing behavior of a “structurally oversimplified” fault zone in poorly lithified sands: Evidence for a coseismic rupture? Bulletin of the Geological Society of America, v. 123, p. 651–668, doi: 10.1130/B30099.1.

Balsamo, F., Storti, F., and Gröcke, D., 2012, Fault-related fluid flow history in shallow marine sediments from carbonate concretions, Crotone basin, south Italy: Journal of the Geological

Society, London, v. 169, p. 613–626, doi: 10.1144/0016-76492011-109.

Balsamo, F., Storti, F., Salvini, F., Silva, A.T., and Lima, C.C., 2010, Structural and petrophysical evolution of extensional fault zones in low-porosity, poorly lithified sandstones of the Barreiras Formation, NE Brazil: Journal of Structural Geology, v. 32, p. 1806–1826, doi: 10.1016/j.jsg.2009.10.010.

Barnaby, R.J., and Rimstidt, J.D., 1989, Redox conditions of calcite cementation interpreted from Mn and Fe contents of authigenic calcites: Geological Society of America Bulletin, v. 101, p. 795–804, doi: 10.1130/0016-7606(1989)101<0795:RCOCCI>2.3.CO;2.

Baud, P., Meredith, P., and Townend, E., 2012, Permeability evolution during triaxial compaction of an anisotropic porous sandstone: Journal of Geophysical Research: Solid Earth, v. 117, p. 1–23, doi: 10.1029/2012JB009176.

Baxevanis, T., Papamichos, E., Flornes, O., and Larsen, I., 2006, Compaction bands and induced permeability reduction in Tuffeau de Maastricht calcarenite: Acta Geotechnica, v. 1, p. 123–135, doi: 10.1007/s11440-006-0011-y.

Beitler, B., Parry, W.T., and Chan, M.A., 2005, Fingerprints of Fluid Flow: Chemical Diagenetic History of the Jurassic Navajo Sandstone, Southern Utah, U.S.A.: Journal of Sedimentary Research, v. 75, p. 547–561, doi: 10.2110/jsr.2005.045.

Bense, V.F., Van den Berg, E.H., and Van Balen, R.T., 2003, Deformation mechanisms and hydraulic properties of fault zones in unconsolidated sediments; the Roer Valley Rift System, The Netherlands: Hydrogeology Journal, v. 11, p. 319–332, doi: 10.1007/s10040-003-0262-8.

Bense, V.F., Gleeson, T., Loveless, S.E., Bour, O., and Scibek, J., 2013, Fault zone hydrogeology: Earth-Science Reviews, v. 127, p. 171–192, doi: 10.1016/j.earscirev.2013.09.008.

Billi, A., Salvini, F., and Storti, F., 2003, The damage zone-fault core transition in carbonate rocks: Implications for fault growth, structure and permeability: Journal of Structural Geology, v. 25, p. 1779–1794, doi: 10.1016/S0191-8141(03)00037-3.

Bjorkum, P.A., and Walderhaug, O., 1990, Geometrical arrangement of calcite carbonate concretions within shallow marine sandstones: Earth Science Reviews, v. 29, p. 145–161.

Bjorkum, P.A., and Walderhaug, O., 1993, Isotopic composition of a calcite-cemented layer in the Lower Jurassic Birdport Sands, southern England; implications for formation of laterally extensive calcite-cemented layers: Journal of Sedimentary Research, v. 63, p. 678–682, doi: 10.1306/D4267BB3-2B26-11D7-8648000102C1865D.

Blenkinsop, T.G., 1991, Cataclasis and Processes of Particle Size Reduction: Pageoph, v. 136, p. 59–86.

Boccaletti, M., Corti, G., and Martelli, L., 2011, Recent and active tectonics of the external zone of the Northern Apennines (Italy): International Journal of Earth Sciences, v. 100, p. 1331–1348, doi: 10.1007/s00531-010-0545-y.

Boccaletti, M., Elter, P., and Guazzone, G., 1971, Plate Tectonic Models for the Development of the Western Alps and Northern Apennines: Nature, v. 234, p. 108–111.

Boles, J.R., Landis, C.A., and Dale, P., 1985, The Moeraki Boulders—Anatomy of Some Septarian Concretions: Journal of Sedimentary Petrology, v. 55, p. 398–406, doi: 10.1306/212F86E3-2B24-11D7-8648000102C1865D.

Boukhedimi, M.A., Louni-Hacini, A., Bouhadad, Y., Ritz, J.F., Machane, D., Benhamouche, A., and Bourenane, H., 2017, Evidence of seismites in coastal Quaternary deposits of western Oranie (northwestern Algeria): Journal of Seismology, v. 21, p. 539–549, doi: 10.1007/s10950-016-9616-2.

Boutt, D.F., Plourde, K.E., Cook, J., and Goodwin, L.B., 2014, Cementation and the hydromechanical behavior of siliciclastic aquifers and reservoirs: Geofluids, v. 14, p. 189–199, doi: 10.1111/gfl.12062.

Bretan, P., 2016, Trap Analysis: an automated approach for deriving column height predictions in fault-bounded traps: Petroleum Geoscience, v. 23, p. 56–69, doi: 10.1144/10.44petgeo2016-022.

Budd, D.A., and Land, L.S., 1990, Geochemical imprint of meteoric diagenesis in Holocene Ooid Sands, Schooner Cays, Bahamas: Correlation of calcite cement geochemistry with extant groundwaters: Journal of Sedimentary Research, v. Vol. 60, p. 361–378, doi: 10.1306/212F919C-2B24-11D7-8648000102C1865D.

Caine, J.S., Bruhn, R.L., and Forster, C.B., 2010, Internal structure, fault rocks, and inferences regarding deformation, fluid flow, and mineralization in the seismogenic Stillwater normal fault, Dixie Valley, Nevada: Journal of Structural Geology, v. 32, p. 1576–1589, doi: 10.1016/j.jsg.2010.03.004.

Caine, J.S., Evans, J.P., and Forster, C.B., 1996, Fault zone architechture and permeability structure: Geology, v. 24, p. 1025–1028, doi: 10.1130/0091-7613(1996)024<1025.

Caine, J.S., and Forster, C.B., 1999, Fault Zone Architecture and Fluid Flow: Insights From Field Data and Numerical Modeling, *in* Haneberg, W.C., Mozley, P.S., Moore, J.C., and Goodwin, L.B., eds., Faults and Subsurface Fluid Flow in the Shallow Crust: Washington D.C., USA, Geophysical Monograph 113, American Geophysical Union, p. 101–127.

Caine, J.S., and Minor, S.A., 2009, Structural and geochemical characteristics of faulted sediments and inferences on the role of water in deformatiion, Rio Grande Rift, New Mexico: Bulletin of the Geological Society of America, v. 121, p. 1325–1340, doi: 10.1130/B26164.1.

Cámara, P., and Klimowitz, J., 1985, Interpretación geodinámica de la vertiente centro-occidental surpirenaica (cuencas del Jaca-Tremp): Estudio Geologico, v. 41, p. 391–404.

Carannate, G., and Guzzetta, G., 1972, Stilotiti e sliccoliti come meccanismo di deformazione delle masse rocciose: Bollettino della Società dei Naturalisti Napoli, v. 81, p. 157–170.

Cashman, S., and Cashman, K., 2000, Cataclasis and deformation-band formation in unconsolidated marine terrace sand, Humboldt County, California: Geology, v. 28, p. 111–114, doi: 10.1130/0091-7613(2000)28<111:CADFIU>2.0.CO;2.

Cavailhes, T., and Rotevatn, A., 2018, Deformation bands in volcaniclastic rocks – Insights from the Shihtiping tuffs, Coastal Range of Taiwan: Journal of Structural Geology, v. 113, p. 155–175, doi: 10.1016/j.jsg.2018.06.004.

Cavazza, W., Braga, R., Reinhardt, E.G., and Zanotti, C., 2009, Influence of host-rock texture on the morphology of carbonate concretions in a meteoric diagenetic environment: Journal of Sedimentary Research, v. 79, p. 377–388, doi: 10.2110/jsr.2009.047.

Chafetz, H.S., Mcintosh, A.G., and Rush, P.F., 1988, Freshwater phreatic diagenesis in the marine realm of recent Arabian Gulf carbonates: Journal of Sedimentary Petrology, v. 58, p. 433–440.

Chan, M.A., Ormo, J., Park, A.J., Stich, M., Souza-Egipsy, V., and Komatsu, G., 2007, Models of iron oxide concretion formation: Field, numerical, and laboratory comparisons: Geofluids, v. 7, p. 356–368, doi: 10.1111/j.1468-8123.2007.00187.x.

Chan, M.A., Parry, W.T., and Bowman, J.R., 2000, Diagenetic hematite and manganese oxides and fault-related fluid flow in Jurassic sandstones, Southeastern Utah: AAPG Bulletin, v. 84, p. 1281–1310, doi: 10.1306/A9673E82-1738-11D7-8645000102C1865D.

Chan, M. a, Potter, S.L., Bowen, B.B., Parry, W.T., Barge, L.M., Seiler, W., Petersen, E.U., and Bowman, J.R., 2012, Characteristics Of Terrestrial Ferric Oxide Concretions And Implications For Mars: Sedimentary Geology of Mars: SEPM Special Publication, v. 102, p. 253–270, doi: 10.2110/pec.12.102.0229.

Charalampidou, E.M., Hall, S.A., Stanchits, S., Lewis, H., and Viggiani, G., 2011, Characterization of shear and compaction bands in a porous sandstone deformed under triaxial compression: Tectonophysics, v. 503, p. 8–17, doi: 10.1016/j.tecto.2010.09.032.

Charalampidou, E.M., Hall, S.A., Stanchits, S., Viggiani, G., and Lewis, H., 2014, Shear-enhanced compaction band identification at the laboratory scale using acoustic and full-field methods: International Journal of Rock Mechanics and Mining Sciences, v. 67, p. 240–252, doi: 10.1016/j.ijrmms.2013.05.006.

Choi, J.-H., Edwards, P., Ko, K., and Kim, Y.-S., 2015, Definition and classification of fault damage zones: A review and a new methodological approach: Earth Science Reviews, v. 152, p. 70–87, doi: 10.1016/j.earscirev.2015.11.006.

Cibin, U., Cavazza, W., Fontana, D., Milliken, K.., and McBride, E.F., 1993, Comparison of composition and texture of calcite-cemented concretions and host sandstones, Northern Apennines, Italy: SEPM Journal of Sedimentary Research, v. Vol. 63, p. 945–954, doi: 10.1306/D4267C4E-2B26-11D7-8648000102C1865D.

Cilona, A., Baud, P., Tondi, E., Agosta, F., Vinciguerra, S., Rustichelli, A., and Spiers, C.J., 2012, Deformation bands in porous carbonate grainstones: Field and laboratory observations: Journal of Structural Geology, v. 45, p. 137–157, doi: 10.1016/j.jsg.2012.04.012.

Cladouhos, T.T., 1999, Shape preferred orientations of survivor grains in fault gouge: Journal of Structural Geology, v. 21, p. 419–436, doi: 10.1016/S0191-8141(98)00123-0.

Dale, A., John, C.M., Mozley, P.S., Smalley, P.C., and Muggeridge, A.H., 2014, Time-capsule concretions: Unlocking burial diagenetic processes in the Mancos Shale using carbonate clumped isotopes: Earth and Planetary Science Letters, v. 394, p. 30–37, doi: 10.1016/j.epsl.2014.03.004.

Davatzes, N.C., Eichhubl, P., and Aydin, A., 2005, Structural evolution of fault zones in sandstone by multiple deformation mechanisms: Moab fault, southeast Utah: Bulletin of the Geological

Society of America, v. 117, p. 135–148, doi: 10.1130/B25473.1.

Davis, J.M., 1999, Oriented carbonate concretions in paleoaquifer: Insights into geologic controls on fluid flow.: Water Resourches Research, v. 35, p. 1705–1711.

Davis, G.H., Bump, A.P., García, P.E., and Ahlgren, S.G., 2000, Conjugate Riedel deformation band shear zones: Journal of Structural Geology, v. 22, p. 169–190, doi: 10.1016/S0191-8141(99)00140-6.

Davis, G.H., Reynolds, S.J., and Kluth, C.F., 2012, Structural geology of rocks and regions: New York, USA, Wiley, 839 p.

Davis, J.M., Roy, N.D., Mozley, P.S., and Hall, J.S., 2006, The effect of carbonate cementation on permeability heterogeneity in fluvial aquifers: An outcrop analog study: Sedimentary Geology, v. 184, p. 267–280, doi: 10.1016/j.sedgeo.2005.11.005.

De Boever, E., Huysmans, M., Muchez, P., Dimitrov, L., and Swennen, R., 2009, Controlling factors on the morphology and spatial distribution of methane-related tubular concretions - Case study of an Early Eocene seep system: Marine and Petroleum Geology, v. 26, p. 1580–1591, doi: 10.1016/j.marpetgeo.2008.11.004.

Demirdag, S., Yavuz, H., and Altindag, R., 2009, The effect of sample size on Schmidt rebound hardness value of rocks: International Journal of Rock Mechanics and Mining Sciences, v. 46, p. 725–730, doi: 10.1016/j.ijrmms.2008.09.004.

Deng, S., and Aydin, A., 2012, Distribution of compaction bands in 3D in an aeolian sandstone: The role of cross-bed orientation: Tectonophysics, v. 574–575, p. 204–218, doi: 10.1016/j.tecto.2012.08.037.

Dickson, J.A.D., 1966, Carbonate identification and genesis as revealed by staining: Journal of Sedimentary Petrology, v. 36, p. 491–505.

Dix, G.R., and Mullins, H.T., 1987, Shallow, subsurface growth and burial alteration of Middle Devonian calcite concretions: Journal of Sedimentary Petrology, v. 57, p. 140–152, doi: 10.1306/212F8ACB-2B24-11D7-8648000102C1865D.

Doglioni, C., 1991, A proposal for the kinematic modelling of W-dipping subductions - possible applications to the Tyrrhenian-Apennines system: Terra Nova, v. 3, p. 423–434, doi: 10.1111/j.1365-3121.1991.tb00172.x.

Dunnington, H.V., 1954, Stylolites development post-date rock induration: Journal of Sedimentary Petrology, v. 24, p. 27–49.

Dutton, S.P., White, C.D., Willis, B.J., and Novakovic, D., 2002, Calcite cement distribution and its effect on fluid flow in deltaic sandstone, Frontier Formation, Wyoming: American Association of Petroleum Geologist Bulletin, v. 86, p. 2007–2021.

Eichhubl, P., Hooker, J.N., and Laubach, S.E., 2010, Pure and shear-enhanced compaction bands in Aztec Sandstone: Journal of Structural Geology, v. 32, p. 1873–1886, doi: 10.1016/j.jsg.2010.02.004.

Eichhubl, P., Taylor, W.L., Pollard, D.D., and Aydin, A., 2004, Paleo-fluid flow and deformation in

the Aztec Sandstone at the Valley of Fire, Nevada - Evidence for the coupling of hydrogeologic, diagenetic, and tectonic processes: Bulletin of the Geological Society of America, v. 116, p. 1120–1136, doi: 10.1130/B25446.1.

Engelder, J.-T., 1974, Cataclasis and the generation of Fault Gouge: Geological Society of America Bulletin, v. 85, p. 1515, doi: 10.1130/0016-7606(1974)85<1515:catgof>2.0.co;2.

Evans, J.P., Forster, C.B., and Goddard, J. V, 1997, Permeability of fault-related rocks, and implications for hydraulic structure of fault zones: Journal of Structural Geology, v. 19, p. 1393–1404.

Exner, U., and Grasemann, B., 2010, Deformation bands in gravels: displacement gradients and heterogeneous strain: Journal of the Geological Society, v. 167, p. 905–913, doi: 10.1144/0016-76492009-076.

Exner, U., and Tschegg, C., 2012, Preferential cataclastic grain size reduction of feldspar in deformation bands in poorly consolidated arkosic sands: Journal of Structural Geology, v. 43, p. 63–72, doi: 10.1016/j.jsg.2012.08.005.

Fagereng, Å., Hillary, G.W.B., and Diener, J.F.A., 2014, Brittle-viscous deformation, slow slip, and tremor: Geophysical Research Letters, v. 41, p. 4159–4167, doi: 10.1002/2014GL060433.

Farrell, N.J.C., Healy, D., and Taylor, C.W., 2014, Anisotropy of permeability in faulted porous sandstones: Journal of Structural Geology, v. 63, p. 50–67, doi: 10.1016/j.jsg.2014.02.008.

Faulkner, D.R., Jackson, C.A.L., Lunn, R.J., Schlische, R.W., Shipton, Z.K., Wibberley, C.A.J., and Withjack, M.O., 2010, A review of recent developments concerning the structure, mechanics and fluid flow properties of fault zones: Journal of Structural Geology, v. 32, p. 1557–1575, doi: 10.1016/j.jsg.2010.06.009.

Ferranti, L., Santoro, E., Mazzella, M.E., Monaco, C., and Morelli, D., 2009, Active transpression in the northern Calabria Apennines, southern Italy: Tectonophysics, v. 476, p. 226–251, doi: 10.1016/j.tecto.2008.11.010.

Fisher, Q.J., Haneef, J., Grattoni, C.A., Allshorn, S., and Lorinczi, P., 2018, Permeability of fault rocks in siliciclastic reservoirs: Recent advances: Marine and Petroleum Geology, v. 91, p. 29–42, doi: 10.1016/j.marpetgeo.2017.12.019.

Fisher, Q.J., and Knipe, R.J., 2001, The permeability of faults within siliciclastic petroleum reservoirs of the North Sea and Norwegian Continental Shelf: Marine and Petroleum Geology, v. 18, p. 1063–1081, doi: 10.1016/S0264-8172(01)00042-3.

Flodin, E., Prasad, M., and Aydin, A., 2003, Petrophysical constraints on deformation styles in Aztec sandstone, Southern Nevada, USA: Pure and Applied Geophysics, v. 160, p. 1589–1610, doi: 10.1007/s00024-003-2377-1.

Folk, R.L., 1974, Petrology of sedimentary rocks: Austin, Texas, USA, Hemphill Publishing Company, 170 p.

Folk, R.L., 1993, SEM imaging of bacteria and nannobacteria in carbonate sediments and rocks: Journal of Sedimentary Petrology, v. 63, p. 990–999, doi: 10.1306/D4267C67-2B26-11D7-8648000102C1865D.

Fossen, H., 2010a, Deformation bands formed during soft-sediment deformation: Observations from SE Utah: Marine and Petroleum Geology, v. 27, p. 215–222, doi: 10.1016/j.marpetgeo.2009.06.005.

Fossen, H., 2010b, Structural Geology: New York, USA, Cambridge University Press, 463 p.

Fossen, H., and Bale, A., 2007, Deformation bands and their influence on fluid flow: AAPG Bulletin, v. 91, p. 1685–1700, doi: 10.1306/07300706146.

Fossen, H., Schultz, R. a., Shipton, Z.K., and Mair, K., 2007, Deformation bands in sandstone: a review: Journal of the Geological Society, London, v. 164, p. 755–769, doi: 10.1144/0016-76492006-036.

Fossen, H., Schultz, R.A., and Torabi, A., 2011, Conditions and implications for compaction band formation in the Navajo Sandstone, Utah: Journal of Structural Geology, v. 33, p. 1477–1490, doi: 10.1016/j.jsg.2011.08.001.

Fossen, H., Soliva, R., Ballas, G., Trzaskos, B., Cavalcante, C., and Schultz, R.A., 2017, A review of deformation bands in reservoir sandstones: geometries, mechanisms and distribution: Geological Society, London, Special Publications, v. 459, p. SP459.4, doi: 10.1144/SP459.4.

Fossen, H., Zuluaga, L.F., Ballas, G., Soliva, R., and Rotevatn, A., 2015, Contractional deformation of porous sandstone: Insights from the Aztec Sandstone, SE Nevada, USA: Journal of Structural Geology, v. 74, p. 172–184, doi: 10.1016/j.jsg.2015.02.014.

Friedman, M., and Logan, J.M., 1973, Lüders' bands in experimentally deformed sandstone and limestone: Bulletin of the Geological Society of America, v. 84, p. 1465–1476, doi: 10.1130/0016-7606(1973)84<1465:LBIEDS>2.0.CO;2.

Friedman, I., and O'Neil, J.R., 1977, Compilation of stable isotope fractionation factors of geochemical interest: Geological Survey Professional Paper, v. 440, p. 1–117, doi: 10.1016/S0016-0032(20)90415-5.

Galli, P., and Scionti, V., 2006, Two unknown M > 6 historical earthquakes revealed by palaeoseismological and archival researches in eastern Calabria (southern Italy). Seismotectonic implications: Terra Nova, v. 18, p. 44–49, doi: 10.1111/j.1365-3121.2005.00658.x.

Giustini, F., Brilli, M., and Patera, A., 2016, Mapping oxygen stable isotopes of precipitation in Italy: Journal of Hydrology: Regional Studies, v. 8, p. 162–181, doi: 10.1016/j.ejrh.2016.04.001.

Goldstein, R.H., and Reynolds, T.J., 1994, Systematics of fluid inclusions in diagenetic minerals: SEPM, Short Course 31, 199 p.

Gratier, J.P., Dysthe, D., and Renard, F., 2013, The role of pressure solution creep in the ductility of the Earth's upper crust: Advances in Geophysics, v. 54, p. 47–179.

Gratier, J.P., Richard, J., Renard, F., Mittempergher, S., Doan, M.L., Di Toro, G., Hadizadeh, J., and Boullier, A.M., 2011, Aseismic sliding of active faults by pressure solution creep: Evidence from the San Andreas fault observatory at Depth: Geology, v. 39, p. 1131–1134, doi: 10.1130/G32073.1.

Griffiths, J., Faulkner, D.R., Edwards, A.P., and Worden, R.H., 2016, Deformation band development as a function of intrinsic host-rock properties in Triassic Sherwood Sandstone: Geological Society, London, Special Publications, v. 435, doi: 10.1144/SP435.11.

Gunderson, K.L., Pazzaglia, F.J., Picotti, V., Anastasio, D.A., Kodama, K.P., Rittenour, T., Frankel, K.F., Ponza, A., Berti, C., Negri, A., and Sabbatini, A., 2014, Unraveling tectonic and climatic controls on synorogenic growth strata (Northern Apennines, Italy): Bulletin of the Geological Society of America, v. 126, p. 532–552, doi: 10.1130/B30902.1.

Gutscher, M.A., Kopp, H., Krastel, S., Bohrmann, G., Garlan, T., Zaragosi, S., Klaucke, I., Wintersteller, P., Loubrieu, B., Le Faou, Y., San Pedro, L., Dominguez, S., Rovere, M., Mercier de Lepinay, B., et al., 2017, Active tectonics of the Calabrian subduction revealed by new multi-beam bathymetric data and high-resolution seismic profiles in the Ionian Sea (Central Mediterranean): Earth and Planetary Science Letters, v. 461, p. 61–72, doi: 10.1016/j.epsl.2016.12.020.

Habermann, D., Neuser, R.D., and Richter, D.K., 1998, Low limit of Mn2+-activated cathodoluminescence of calcite: state of the art: Sedimentary Geology, v. 116, p. 13–24, doi: 10.1016/S0037-0738(97)00118-8.

Habermann, D., Neuser, R.D., and Richter, D.K., 1996, REE-activated cathodoluminescence of calcite and dolomite: high-resolution spectrometric analysis of CL emission (HRS-CL): Sedimentary Geology, v. 101, p. 1–7, doi: 10.1016/0037-0738(95)00086-0.

Hall, J.S., Mozley, P., Davis, J.M., and Roy, N.D., 2004, Environments of formaton and controls on spatial distribution of calcite cenentation in Plio-Pleistocene fluvial deposits, New Mexico, U.S.A: Journal of Sedimentary Research, v. 74, p. 643–653, doi: 10.1306/020904740643.

Hancock, P.L., 1985, Brittle microtectonics principles and practice: Journal of Structural Geology, v. 7, p. 437–457.

Hays, P.D., and Grossman, E.L., 1991, Oxygen isotopes in meteoric calcite cements as indicators of continental paleoclimate: Geology, v. 19, p. 441–444, doi: 10.1130/0091-7613(1991)019<0441:OIIMCC>2.3.CO.

Heilbronner, R., and Keulen, N., 2006, Grain size and grain shape analysis of fault rocks: Tectonophysics, v. 427, p. 199–216, doi: 10.1016/j.tecto.2006.05.020.

Hendry, J.P., Pearson, M.J., Trewin, N.H., and Fallick, A.E., 2006, Jurassic septarian concretions from NW Scotland record interdependent bacterial, physical and chemical processes of marine mudrock diagenesis: Sedimentology, v. 53, p. 537–565, doi: 10.1111/j.1365-3091.2006.00779.x.

Hendry, J.P., and Poulsom, A.J., 2006, Sandstone-hosted concretions record evidence for syn-lithification seismicity, cavitation processes, and Palaeocene rapid burial of Lower Cretaceous deep-marine sandstones (Outer Moray Firth, UK North Sea): Journal of the Geological Society, London, v. 163, p. 447–460, doi: 10.1144/0016-764905-033.

Heynekamp, M.R., Goodwin, L.B., Mozley, P.S., and Haneberg, W.C., 1999, Controls on Fault-Zone Architecture in Poorly Lithified Sediment, Rio Grande Rift, New Mexico: Implications for Fault-Zone Permeability and Fluid Flow, *in* Haneberg, W.C., Mozley, P.S., Moore, J.C., and Goodwin,

L.B., eds., Faults and Subsurface Fluid Flow in the Shallow Crust: Washington D.C., USA, Geophysical Monograph 113, American Geophysical Union, p. 27–49.

Hiatt, E.., and Pufhal, P.K., 2014, Cathodoluminescence petrography of carbonate rocks.: Mineralogical Association of Canada, Short Courses, 45, p. 75–96.

Houseknecht, D.W., 1987, Assessing the relative importance of compaction processes and cementation to reduction of porosity in sandstone: American Association of Petroleum Geologist Bulletin, v. 71, p. 633–642.

Hudson, J.D., 1977, Stable isotopes and limestone lithification: Journal of the Geological Society, London, v. 133, p. 637–660.

Hudson, J.D., Coleman, M.L., Barreiro, B.A., and Hollingworth, N.T.J., 2001, Septarian concretions from the Oxford Clay (Jurassic, England, UK): Involvement of original marine and multiple external pore fluids: Sedimentology, v. 48, p. 507–531, doi: 10.1046/j.1365-3091.2001.00374.x.

Imanishi, K., Ando, R., and Kuwahara, Y., 2012, Unusual shallow normal-faulting earthquake sequence in compressional northeast Japan activated after the 2011 off the Pacific coast of Tohoku earthquake: Geophysical Research Letters, v. 39, p. 1–7, doi: 10.1029/2012GL051491.

Jacob, A.F., 1973, Elongate concretions as paleochannel indicators, tongue river formation (Paleocene), North Dakota: Bulletin of the Geological Society of America, v. 84, p. 2127–2132, doi: 10.1130/0016-7606(1973)84<2127:ECAPIT>2.0.CO;2.

Johansen, T.E.S., Fossen, H., and Kluge, R., 2005, The impact of syn-faulting porosity reduction on damage zone architecture in porous sandstone: An outcrop example from the Moab Fault, Utah: Journal of Structural Geology, v. 27, p. 1469–1485, doi: 10.1016/j.jsg.2005.01.014.

Johnson, M.R., 1989, Paleographic significance of oriented calcareous concretions in the Triassic Katberg Formation, South Africa: Journal of Sedimentary Petrology, v. 59, p. 1008–1010, doi: 10.1306/212F90D9-2B24-11D7-8648000102C1865D.

Kaproth, B.M., Cashman, S.M., and Marone, C., 2010, Deformation band formation and strength evolution in unlithified sand: The role of grain breakage: Journal of Geophysical Research: Solid Earth, v. 115, p. 1–11, doi: 10.1029/2010JB007406.

Katz, O., and Reches, Z., 2000, Evaluation of mechanical rock properties using a Schmidt: International Journal of Rock Mechanics and Mining Sciences, v. 37, p. 723–728.

Katz, Y., Weinberger, R., and Aydin, A., 2004, Geometry and kinematic evolution of Riedel shear structures, Capitol Reef National Park, Utah: Journal of Structural Geology, v. 26, p. 491–501, doi: 10.1016/j.jsg.2003.08.003.

Kim, Y.S., Peacock, D.C.P., and Sanderson, D.J., 2004, Fault damage zones: Journal of Structural Geology, v. 26, p. 503–517, doi: 10.1016/j.jsg.2003.08.002.

Klein, J.S., Mozley, P.S., Campbell, A., and Cole, R., 1999, Spatial distribution of carbon and oxygen isotopes in laterally extensive carbonate-cemented layers: Implications for mode of growth and subsurface identification: Journal of Sedimentary Research, v. 69, p. 184–201, doi: 10.1306/D42689AA-2B26-11D7-8648000102C1865D.

Knott, S.D., and Turco, E., 1991, Late Cenozoic kinematics of the Calabrian Arc, southern Italy: Tectonics, v. 10, p. 1164–1172, doi: 10.1029/91TC01535.

Kodaira, S., No, T., Nakamura, Y., Fujiwara, T., Kaiho, Y., Miura, S., Takahashi, N., Kaneda, Y., and Taira, A., 2012, Coseismic fault rupture at the trench axis during the 2011 Tohoku-oki earthquake: Nature Geoscience, v. 5, p. 646–650, doi: 10.1038/ngeo1547.

Kolyukhin, D., Schueller, S., Espedal, M.S., and Fossen, H., 2010, Deformation band populations in fault damage zone-impact on fluid flow: Computational Geosciences, v. 14, p. 231–248, doi: 10.1007/s10596-009-9148-8.

Lash, G.G., 2015, Authigenic barite nodules and carbonate concretions in the Upper Devonian shale succession of western New York - A record of variable methane flux during burial: Marine and Petroleum Geology, v. 59, p. 305–319, doi: 10.1016/j.marpetgeo.2014.09.009.

Li, Z., Goldstein, R.H., and Franseen, E.K., 2017, Meteoric calcite cementation: diagenetic response to relative fall in sea-level and effect on porosity and permeability, Las Negras area, southeastern Spain: Sedimentary Geology, v. 348, p. 1–18, doi: 10.1016/j.sedgeo.2016.12.002.

Li, Y., Zhang, W., Aydin, A., and Deng, X., 2018, Formation of calcareous nodules in loess–paleosol sequences: Reviews of existing models with a proposed new “per evapotranspiration model”: Journal of Asian Earth Sciences, v. 154, p. 8–16, doi: 10.1016/j.jseaes.2017.12.002.

Logan, J.M., Friedman, M., Higgs, N., Dengo, C., and Shimamoto, T., 1979, Experimental studies of simulated gouge and their application to studies of natural fault zones: Open File Report United States Geological Survey, v. 79, p. 305–343, doi: 10.2466/02.PR0.116k22w7.

López-Mir, B., Muñoz, J.A., and García-Senza, J., 2016, 3D Geometries reconstruction of Upper Cretaceous passive diapirs and salt withdrawal basin in the Cotiella Basin (southern Pyrenees): Journal of the Geological Society of London, v. 173, p. 616–627.

Loveless, S., Bense, V., and Turner, J., 2011, Fault architecture and deformation processes within poorly lithified rift sediments, Central Greece: Journal of Structural Geology, v. 33, p. 1554–1568, doi: 10.1016/j.jsg.2011.09.008.

Loyd, S.J., and Berelson, W.M., 2016, The modern record of “concretionary” carbonate: Reassessing a discrepancy between modern sediments and the geologic record: Chemical Geology, v. 420, p. 77–87, doi: 10.1016/j.chemgeo.2015.11.009.

Maestrelli, D., Benvenuti, M., Bonini, M., Carnicelli, S., Piccardi, L., and Sani, F., 2018, The structural hinge of a chain-foreland basin: Quaternary activity of the Pede-Apennine Thrust front (Northern Italy): Tectonophysics, v. 723, p. 117–135, doi: 10.1016/j.tecto.2017.12.006.

Main, I., Kwon, O., Ngwenya, B., and Elphick, S., 2000, Fault sealing during deformation band growth in porous sandstone: Geology, v. 28, p. 1131–1134.

Mair, K., Elphick, S., and Main, I., 2002, Influence of confining pressure on the mechanical and structural evolution of laboratory deformation bands: Geophysical Research Letters, v. 29, p. 49-1-49–4, doi: 10.1029/2001GL013964.

Mair, K., Frye, K.M., and Marone, C., 2002, Influence of grain characteristics on the friction of

granular shear zones: Journal of Geophysical Research: Solid Earth, v. 107, p. 1–9, doi: 10.1029/2001JB000516.

Mair, K., Main, I., and Elphick, S., 2000, Sequential growth of deformation bands in the laboratory: Journal of Structural Geology, v. 22, p. 25–42, doi: 10.1016/S0191-8141(99)00124-8.

Mäkel, G.H., 2007, The modelling of fractured reservoirs: constraints and potential for fracture network geometry and hydraulics analysis: Geological Society London Special Publication, v. 292, p. 375–403.

Mandl, G., 2000, Faulting in Brittle Rocks. An Introduction to the Mechanics of Tectonic Faults. Berlin, Springer: 434 p.

Massari, F., and Prosser, G., 2013, Late Cenozoic tectono-stratigraphic sequences of the Crotone Basin: Insights on the geodynamic history of the Calabrian arc and Tyrrhenian Sea: Basin Research, v. 25, p. 26–51, doi: 10.1111/j.1365-2117.2012.00549.x.

McBride, E.F., 1988, Contrasting Diagenetic Histories of Concretions Vs Host Rocks, Lion Mountain Member, Riley Formation (Upper Cambrian), Texas: Geological Society of America Bulletin, v. 100, p. 1803–1810.

McBride, E.F., and Milliken, K.L., 2006, Giant calcite-cemented concretions, Dakota Formation, central Kansas, USA: Sedimentology, v. 53, p. 1161–1179, doi: 10.1111/j.1365-3091.2006.00813.x.

McBride, E.F., and Parea, G.C., 2001, Origin of highly elongate, calcite-cemented concretions in some Italian coastal beach and dune sands: Journal of Sedimentary Research, v. 71, p. 82–87, doi: 10.1306/041900710082.

McBride, E.F., Picard, M.D., and Folk, R.L., 1994, Oriented concretions, Ionian Coast, Italy: Evidence of groundwater flow direction: Journal of Sedimentary Research, v. A64, p. 535–540.

Menéndez, B., Zhu, W., and Wong, T.F., 1996, Micromechanics of brittle faulting and cataclastic flow in Berea sandstone: Journal of Structural Geology, v. 18, p. 1–16, doi: 10.1016/0191-8141(95)00076-P.

Mollema, P.N., and Antonellini, M.A., 1996, Compaction bands: A structural analog for anti-mode i cracks in aeolian sandstone: Tectonophysics, v. 267, p. 209–228, doi: 10.1016/S0040-1951(96)00098-4.

Montenat, C., Barrier, P., Ott dEstevou, P., and Hibsch, C., 2007, Seismites: An attempt at critical analysis and classification: Sedimentary Geology, v. 196, p. 5–30, doi: 10.1016/j.sedgeo.2006.08.004.

Moore, C.H., 1989, Carbonate diagenesis and porosity: Amsterdam, Elsevier, 338 p.

Morad, S., 1998, Carbonate cementation in sandstones: Special Pubblication Association Sedimentologists, v. 26, p. 1–26.

Morad, S., Ketzer, J.M., and DeRos, F., 2000, Spatial and temporal distribution of diagenetic alterations in siliciclastic rocks: implication for mass transfer in sedimentary basins: Sedimentology, v. 47, p. 95–120, doi: 10.1046/j.1365-3091.2000.00007.x.

Mozley, P.S., 1996, The internal structure of carbonate concretions in mudrocks: a critical evaluation of the conventional concentric model of concretion growth: Sedimentary Geology, v. 103, p. 85–91, doi: 10.1016/0037-0738(95)00087-9.

Mozley, P.S., and Davis, J.M., 2005, Internal structure and mode of growth of elongate calcite concretions: Evidence for small-scale, microbially induced, chemical heterogeneity in groundwater: Bulletin of the Geological Society of America, v. 117, p. 1400–1412, doi: 10.1130/B25618.1.

Mozley, P.S., and Davis, J.M., 1996, Relationship between oriented calcite concretions and permeability correlation structure in an alluvial aquifer, Sierra Ladrones Formation, New Mexico: Journal of Sedimentary Research, v. 66, p. 11–16, doi: 10.1306/D4268293-2B26-11D7-8648000102C1865D.

Mozley, P.S., and Goodwin, L.B., 1995, Patterns of cementation along a Cenozoic normal fault: a record of paleoflow orientations: Geology, v. 23, p. 539–542, doi: 10.1130/0091-7613(1995)023<0539:POCAAC>2.3.CO;2.

Mozley, P.S., and Wersin, P., 1992, Isotopic composition of siderite as an indicator of depositional environment: Geology, v. 20, p. 817–820, doi: 10.1130/0091-7613(1992)020<0817.

Msharrafieh, M., and Sultan, R., 2006, Dynamics of a complex diffusion-precipitation-re-dissolution Liesegang pattern: Chemical Physics Letters, v. 421, p. 221–226, doi: 10.1016/j.cplett.2006.01.054.

Muchez, P., Nielsen, P., Sintubin, M., and Lagrou, D., 1998, Conditions of meteoric calcite formation along a Variscan fault and their possible relation to climatic evolution during the Jurassic-Cretaceous: Sedimentology, v. 45, p. 845–854, doi: 10.1046/j.1365-3091.1998.00182.x.

Muñoz, J.A., 2002, The Pyrennes. In Gibbons, W., Moreno, T. The geology of Spain: 370-385 p.

Muñoz, J.A., Beamud, E., Fernández, O., Arbués, P., Dinarès-Turell, J., and Poblet, J., 2013, The Ainsa Fold and thrust oblique zone of the central Pyrenees: Kinematics of a curved contractional system from paleomagnetic and structural data: Tectonics, v. 32, p. 1142–1175, doi: 10.1002/tect.20070.

Nelson, C.S., and Smith, A.M., 1996, Stable oxygen and carbon isotope compositional fields for skeletal and diagenetic components in New Zealand Cenozoic nontropical carbonate sediments and limestones: A synthesis and review: New Zealand Journal of Geology and Geophysics, v. 39, p. 93–107, doi: 10.1080/00288306.1996.9514697.

Nicchio, M.A., Nogueira, F.C.C., Balsamo, F., Souza, J.A.B., Carvalho, B.R.B.M., and Bezerra, F.H.R., 2018, Development of cataclastic foliation in deformation bands in feldspar-rich conglomerates of the Rio do Peixe Basin, NE Brazil: Journal of Structural Geology, v. 107, p. 132–141, doi: 10.1016/j.jsg.2017.12.013.

Nicol, A., Childs, C., Walsh, J.J., and Schafer, K.W., 2013, A geometric model for the formation of deformation band clusters: Journal of Structural Geology, v. 55, p. 21–33, doi: 10.1016/j.jsg.2013.07.004.

Nyman, S.L., Nelson, C.S., and Campbell, K.A., 2010, Miocene tubular concretions in East Coast

Basin, New Zealand: Analogue for the subsurface plumbing of cold seeps: Marine Geology, v. 272, p. 319–336, doi: 10.1016/j.margeo.2009.03.021.

Ogilvie, S.R., and Glover, P.W.J., 2001, The petrophysical properties of deformation bands in relation to their microstructure: Earth and Planetary Science Letters, v. 193, p. 129–142, doi: 10.1016/S0012-821X(01)00492-7.

Ogilvie, S.R., Orribo, J.M., and Glover, P.W.J., 2001, The influence of deformation bands upon fluid flow using profile permeametry and positron emission tomography: Geophysical Research Letters, v. 28, p. 61–64, doi: 10.1029/2000GL008507.

Okubo, C.H., and Schultz, R.A., 2007, Compactional deformation bands in Wingate Sandstone; additional evidence of an impact origin for Upheaval Dome, Utah: Earth and Planetary Science Letters, v. 256, p. 169–181, doi: 10.1016/j.epsl.2007.01.024.

Olsson, W.A., 2000, Origin of Lüders' bands in deformed rock: Journal of Geophysical Research, v. 105, p. 5931–5938, doi: 10.3109/17453674.2010.492765.

Olsson, W.A., Lorenz, J.C., and Cooper, S.P., 2004, A mechanical model for multiply-oriented conjugate deformation bands: Journal of Structural Geology, v. 26, p. 325–338, doi: 10.1016/S0191-8141(03)00101-9.

Oppo, D., Capozzi, R., and Picotti, V., 2013, A new model of the petroleum system in the Northern Apennines, Italy: Marine and Petroleum Geology, v. 48, p. 57–76, doi: 10.1016/j.marpetgeo.2013.06.005.

Oppo, D., Capozzi, R., Picotti, V., and Ponza, A., 2015, A genetic model of hydrocarbon-derived carbonate chimneys in shelfal fine-grained sediments: The Enza River field, Northern Apennines (Italy): Marine and Petroleum Geology, v. 66, p. 555–565, doi: 10.1016/j.marpetgeo.2015.03.002.

Ozawa, S., Nishimura, T., Suito, H., Kobayashi, T., Tobita, M., and Imakiire, T., 2011, Coseismic and postseismic slip of the 2011 magnitude-9 Tohoku-Oki earthquake.: Nature, v. 475, p. 373–376, doi: 10.1038/nature10227.

Parnell, J., Watt, G.R., Middleton, D., Kelly, J., and Baron, M., 2004, Deformation Band Control on Hydrocarbon Migration: Journal of Sedimentary Research, v. 74, p. 552–560, doi: 10.1306/121703740552.

Parry, W.T., 2011, Composition, nucleation, and growth of iron oxide concretions: Sedimentary Geology, v. 233, p. 53–68, doi: 10.1016/j.sedgeo.2010.10.009.

Person, M., Goodwin, L.B., Rawlings, G., and Connell, S., 2000, The evolution of fault-zone permeability and groundwater flow patterns within the Albuquerque Basin of the Rio Grande Rift, NM: Journal of Geochemical Exploration, v. 69–70, p. 565–568, doi: 10.1016/S0375-6742(00)00061-3.

Philit, S., Soliva, R., Castilla, R., Ballas, G., and Taillefer, A., 2018, Clusters of cataclastic deformation bands in porous sandstones: Journal of Structural Geology, v. 114, p. 235–250, doi: 10.1016/j.jsg.2018.04.013.

Philit, S., Soliva, R., Labaume, P., Gout, C., and Wibberley, C., 2015, Relations between shallow

cataclastic faulting and cementation in porous sandstones: First insight from a groundwater environmental context: Journal of Structural Geology, v. 81, p. 89–105, doi: 10.1016/j.jsg.2015.10.001.

Piazza, A., Artoni, A., and Ogata, K., 2016, The Epiligurian wedge-top succession in the Enza Valley (Northern Apennines): evidence of a syn-depositional transpressive system: Swiss Journal of Geosciences, v. 109, p. 17–36, doi: 10.1007/s00015-016-0211-x.

Pirrie, D., 1987, Orientated calcareous concretions from James Ross Island, Antarctica: British Antarctic Survey Bulletin, v. 75, p. 41–50.

Polonia, A., Torelli, L., Mussoni, P., Gasperini, L., Artoni, A., and Klaeschen, D., 2011, The Calabrian Arc subduction complex in the Ionian Sea: Regional architecture, active deformation, and seismic hazard: Tectonics, v. 30, p. 1–28, doi: 10.1029/2010TC002821.

Ponza, A., Pazzaglia, F.J., and Picotti, V., 2010, Thrust-fold activity at the mountain front of the Northern Apennines (Italy) from quantitative landscape analysis: Geomorphology, v. 123, p. 211–231, doi: 10.1016/j.geomorph.2010.06.008.

Potter, S.L., Chan, M.A., Petersen, E.U., Dyar, M.D., and Sklute, E., 2011, Characterization of Navajo Sandstone concretions: Mars comparison and criteria for distinguishing diagenetic origins: Earth and Planetary Science Letters, v. 301, p. 444–456, doi: 10.1016/j.epsl.2010.11.027.

Raiswell, R., and Fisher, Q.J., 2004, Rates of carbonate cementation associated with sulphate reduction in DSDP/ODP sediments: Implications for the formation of concretions: Chemical Geology, v. 211, p. 71–85, doi: 10.1016/j.chemgeo.2004.06.020.

Rawling, G.C., and Goodwin, L.B., 2003, Cataclasis and particulate flow in faulted, poorly lithified sediments: Journal of Structural Geology, v. 25, p. 317–331, doi: 10.1016/S0191-8141(02)00041-X.

Rawling, G.C., and Goodwin, L.B., 2006, Structural record of the mechanical evolution of mixed zones in faulted poorly lithified sediments, Rio Grande rift, New Mexico, USA: Journal of Structural Geology, v. 28, p. 1623–1639, doi: 10.1016/j.jsg.2006.06.008.

Rawling, G.C., Goodwin, L.B., and Wilson, J.L., 2001, Internal architecture, permeability structure, and hydrologic significance of contrasting fault-zone types: Geology, v. 29, p. 43–46, doi: 10.1130/0091-7613(2001)029<0043:IAPSAH>2.0.CO;2.

Reitz, M.A., and Seeber, L., 2012, Arc-parallel strain in a short rollback-subduction system: The structural evolution of the Crotone basin (northeastern Calabria, southern Italy): Tectonics, v. 31, p. 1–23, doi: 10.1029/2011TC003031.

Remitti, F., Vannucchi, P., Bettelli, G., Fantoni, L., Panini, F., and Vescovi, P., 2011, Tectonic and sedimentary evolution of the frontal part of an ancient subduction complex at the transition from accretion to erosion: The case of the Ligurian wedge of the Northern Apennines, Italy: Bulletin of the Geological Society of America, v. 123, p. 51–70, doi: 10.1130/B30065.1.

Rodrigues-Pascua, M.A., Calvo, J.P., De Vicente, G., and Gomez-Gras, D., 2000, Soft-sediment deformation structures interpreted as seismites in lacustrine sediments of the Prebetic Zone, SE Spain, and their potential use as indicators of earthquake magnitudes during the Late Miocene: Sedimentary Geology, v. 135, p. 117–135, doi: 10.1016/S0037-0738(00)00067-1.

Rodrigues, R. de S., and Alves da Silva, F.C., 2018, Deformation bands and associated structures in the Tucano Basin, NE Brazil: A multiscale analysis: Marine and Petroleum Geology, v. 96, p. 202–213, doi: 10.1016/j.marpetgeo.2018.05.035.

Rotevatn, A., Fossmark, H.S., Bastesen, E., Thorsheim, E., and Torabi, A., 2017, Do deformation bands matter for flow? Insights from permeability measurements and flow simulations in porous carbonate rocks: Petroleum Geoscience, v. 23, p. 104–119, doi: 10.1144/petgeo2016-038.

Rotevatn, A., Sandve, T.H., Keilegavlen, E., Kolyukhin, D., and Fossen, H., 2013, Deformation bands and their impact on fluid flow in sandstone reservoirs: The role of natural thickness variations: Geofluids, v. 13, p. 359–371, doi: 10.1111/gfl.12030.

Rotevatn, A., Thorsheim, E., Bastesen, E., Fossmark, H.S.S., Torabi, A., and Sælen, G., 2016, Sequential growth of deformation bands in carbonate grainstones in the hangingwall of an active growth fault: Implications for deformation mechanisms in different tectonic regimes: Journal of Structural Geology, v. 90, p. 27–47, doi: 10.1016/j.jsg.2016.07.003.

Sample, J.C., Reid, M.R., Tobin, H.J., and Moore, J.C., 1993, Carbonate cements indicate channeled fluid flow along a zone of vertical faults at the deformation front of the Cascadia accretionary wedge (northwest U.S. coast): Geology, v. 21, p. 507–510, doi: 10.1130/0091-7613(1993)021<0507:CCICFF>2.3.CO;2.

Sample, J.C., Woods, S., Bender, E., and Loveall, M., 2006, Relationship between deformation bands and petroleum migration in an exhumed reservoir rock, Los Angeles Basin, California, USA: Geofluids, v. 6, p. 105–112, doi: 10.1111/j.1468-8123.2005.00131.x.

Scholz, C.H., 1998, Earthquakes and friction laws: Nature, v. 391, p. 37–42, doi: 10.1038/34097.

Schueller, S., Braathen, A., Fossen, H., and Tveranger, J., 2013, Spatial distribution of deformation bands in damage zones of extensional faults in porous sandstones: Statistical analysis of field data: Journal of Structural Geology, v. 52, p. 148–162, doi: 10.1016/j.jsg.2013.03.013.

Schultz, R.A., 2009, Scaling and paleodepth of compaction bands, Nevada and Utah: Journal of Geophysical Research, v. 114, p. 1–13, doi: 10.1029/2008JB005876.

Schultz, R.A., Okubo, C.H., and Fossen, H., 2010, Porosity and grain size controls on compaction band formation in Jurassic Navajo Sandstone: Geophysical Research Letters, v. 37, p. 1–5, doi: 10.1029/2010GL044909.

Sefton-Nash, E., and Catling, D.C., 2008, Hematitic concretions at Meridiani Planum, Mars: Their growth timescale and possible relationship with iron sulfates: Earth and Planetary Science Letters, v. 269, p. 365–375, doi: 10.1016/j.epsl.2008.02.009.

Séguret, M., 1972, Étude tectonique des nappes et séries dvcollés de la partie centrale du versant sud est Pyrénves-caractére synsédimentaire, rôle de la compression et de la gravité. Série géologique structurale, 2, France. Publications de l?universite des Sciences at Tech: 155 p.

Seilacher, A., 2001, Concretion morphologies reflecting diagenetic and epigenetic pathways: Sedimentary Geology, v. 143, p. 41–57, doi: 10.1016/S0037-0738(01)00092-6.

Sellés-Martínez, J., 1996, Concretion morphology, classification and genesis: Earth-Science

Reviews, v. 41, p. 177–210, doi: 10.1016/S0012-8252(96)00022-0.

Shipton, Z.K., and Cowie, P.A., 2003, A conceptual model for the origin of fault damage zone structures in high-porosity sandstone: Journal of Structural Geology, v. 25, p. 333–344, doi: 10.1016/S0191-8141(02)00037-8.

Shipton, Z.K., and Cowie, P.A., 2001, Damage zone and slip-surface evolution over μm to km scales in high-porosity Navajo sandstone, Utah: Journal of Structural Geology, v. 23, p. 1825–1844, doi: 10.1016/S0191-8141(01)00035-9.

Shipton, Z.K., Evans, J.P., and Thompson, L.B., 2005, The geometry and thickness of deformation-band fault core and its influence on sealing characteristics of deformation-band fault zones: Aapg Memoir, v. 85, p. 181–195, doi: 10.1306/1033723M853135.

Sigda, J.M., Goodwin, L.B., Mozley, P.S., and Wilson, J.L., 1999, Permeability Alteration in Small-Displacement Faults in Poorly Lithified Sediments: Rio Grande Rift, Central New Mexico, *in* Haneberg, W.C., Mozley, P.S., Moore, J.C., and Goodwin, L.B., eds., Faults and Subsurface Fluid Flow in the Shallow Crust: Washington D.C., USA, Geophysical Monograph 113, American Geophysical Union, p. 51–68.

Sigda, J.M., and Wilson, J.L., 2003, Are faults preferential flow paths through semiarid and arid vadose zones? Water Resources Research, v. 39, p. 1–14, doi: 10.1029/2002WR001406.

Skurtveit, E., Torabi, A., Alikarami, R., and Braathen, A., 2015, Fault baffle to conduit developments: reactivation and calcite cementation of deformation band fault in aeolian sandstone: Petroleum Geoscience, v. 21, p. 3–16, doi: 10.1144/petgeo2014-031.

Skurtveit, E., Torabi, A., Gabrielsen, R.H., and Zoback, M.D., 2013, Experimental investigation of deformation mechanisms during shear-enhanced compaction in poorly lithified sandstone and sand: Journal of Geophysical Research: Solid Earth, v. 118, p. 4083–4100, doi: 10.1002/jgrb.50342.

Soliva, R., Ballas, G., Fossen, H., and Philit, S., 2016, Tectonic regime controls clustering of deformation bands in porous sandstone: Geology, v. 44, p. 423–426, doi: 10.1130/G37585.1.

Soliva, R., Schultz, R.A., Ballas, G., Taboada, A., Wibberley, C., Saillet, E., and Benedicto, A., 2013, A model of strain localization in porous sandstone as a function of tectonic setting, burial and material properties; new insight from Provence (southern France): Journal of Structural Geology, v. 49, p. 50–63, doi: 10.1016/j.jsg.2012.11.011.

South, D.L., and Talbot, M.R., 2000, The sequence stratigraphic framework of carbonate diagenesis within transgressive fan-delta deposits: Sant Llorenç del Munt fan-delta complex, SE Ebro Basin, NE Spain: Sedimentary Geology, v. 138, p. 179–198, doi: 10.1016/S0037-0738(00)00149-4.

Sternlof, K.R., Chapin, J.R., Pollard, D.D., and Durlofsky, L.J., 2004, Permeability effects of deformation band arrays in sandstone: American Association of Petroleum Geologists Bulletin, v. 88, p. 1315–1329, doi: 10.1306/032804.

Sternlof, K.R., Karimi-Fard, M., Pollard, D.D., and Durlofsky, L.J., 2006, Flow and transport effects of compaction bands in sandstone at scales relevant to aquifer and reservoir management: Water Resources Research, v. 42, p. 1–16, doi: 10.1029/2005WR004664.

Stockdale, P.B., 1922, Stylolites their nature and origin: Indiana University Study, p. 1–97.

Storti, F., and Balsamo, F., 2010, Particle size distributions by laser diffraction: sensitivity of granular matter strength to analytical operating procedures: Solid Earth, v. 1, p. 25–48, doi: 10.5194/se-1-25-2010.

Storti, F., Balsamo, F., Cappanera, F., and Tosi, G., 2011, Sub-seismic scale fracture pattern and in situ permeability data in the chalk atop of the Krempe salt ridge at Lägerdorf, NW Germany: Inferences on synfolding stress field evolution and its impact on fracture connectivity: Marine and Petroleum Geology, v. 28, p. 1315–1332, doi: 10.1016/j.marpetgeo.2011.03.014.

Storti, F., Balsamo, F., and Salvini, F., 2007, Particle shape evolution in natural carbonate granular wear material: Terra Nova, v. 19, p. 344–352, doi: 10.1111/j.1365-3121.2007.00758.x.

Sylvester, A.G., 1988, Strike-slip faults: Geological Society of America Bulletin, v. 100, p. 1666–1703.

Tavani, S., Storti, F., Lacombe, O., Corradetti, A., Muñoz, J.A., and Mazzoli, S., 2015, A review of deformation pattern templates in foreland basin systems and fold-and-thrust belts: Implications for the state of stress in the frontal regions of thrust wedges: Earth-Science Reviews, v. 141, p. 82–104, doi: 10.1016/j.earscirev.2014.11.013.

Tavani, S., Vitale, S., Grifa, C., Iannace, A., Parente, M., and Mazzoli, S., 2016, Introducing dolomite seams: Hybrid compaction-solution bands in dolomitic limestones: Terra Nova, v. 28, p. 195–201, doi: 10.1111/ter.12210.

Taylor, K.G., Gawthorpe, R.L., Curtis, C.D., Marshall, J.D., and Awwiller, D.N., 2000, Carbonate cementation in a sequence-stratigraphic framework: Upper Cretaceous sandstones, Book Cliffs, Utah-Colorado: Journal of Sedimentary Research, v. 70, p. 360–372, doi: 10.1306/2DC40916-0E47-11D7-8643000102C1865D.

Taylor, K.G., Gawthorpe, R.L., and Van Wagoner, J.C., 1995, Stratigraphic control on laterally persistent cementation, Book Cliff, Utah: Journal of the Geological Society, London, v. 152, p. 225–228.

Taylor, L.W., and Pollard, D.D., 2000, Estimation of in situ permeability of deformation bands in porous sandstone, Valley of Fire, Nevada: Water Resources Research, v. 36, p. 2595–2606.

Theakstone, W.H., 1981, Concretions in glacial sediments at Seglvatnet, Norway: Journal of Sedimentary Research, v. 51, p. 191–196, doi: 10.1306/212F7C43-2B24-11D7-8648000102C1865D.

Tindall, S., and Eckert, A., 2015, Geometric and mechanical-stiffness controls on jointing in cataclastic deformation bands: Journal of Structural Geology, v. 77, p. 126–137, doi: 10.1016/j.jsg.2015.05.008.

Tinterri, R., Muzzi Magalhaes, P., Tagliaferri, A., and Cunha, R.S., 2016, Convolute laminations and load structures in turbidites as indicators of flow reflections and decelerations against bounding slopes. Examples from the Marnoso-arenacea Formation (northern Italy) and Annot Sandstones (south eastern France): Sedimentary Geology, v. 344, p. 382–407, doi: 10.1016/j.sedgeo.2016.01.023.

Todd, J.E., 1903, Concretions and their geological effects: Geological Society of America Bulletin, v. 14, p. 353–368.

Tondi, E., Antonellini, M., Aydin, A., Marchegiani, L., and Cello, G., 2006, The role of deformation bands, stylolites and sheared stylolites in fault development in carbonate grainstones of Majella Mountain, Italy: Journal of Structural Geology, v. 28, p. 376–391, doi: 10.1016/j.jsg.2005.12.001.

Tondi, E., Cilona, A., Agosta, F., Aydin, A., Rustichelli, A., Renda, P., and Giunta, G., 2012, Growth processes, dimensional parameters and scaling relationships of two conjugate sets of compactive shear bands in porous carbonate grainstones, Favignana Island, Italy: Journal of Structural Geology, v. 37, p. 53–64, doi: 10.1016/j.jsg.2012.02.003.

Torabi, A., 2014, Cataclastic bands in immature and poorly lithified sandstone, examples from Corsica, France: Tectonophysics, v. 630, p. 91–102, doi: 10.1016/j.tecto.2014.05.014.

Torabi, A., Braathen, A., Cuisiat, F., and Fossen, H., 2007, Shear zones in porous sand: Insights from ring-shear experiments and naturally deformed sandstones: Tectonophysics, v. 437, p. 37–50, doi: 10.1016/j.tecto.2007.02.018.

Torabi, A., and Fossen, H., 2009, Spatial variation of microstructure and petrophysical properties along deformation bands in reservoir sandstones: AAPG Bulletin, v. 93, p. 919–938, doi: 10.1306/03270908161.

Tueckmantel, C., Fisher, Q.J., Knipe, R.J., Lickorish, H., and Khalil, S.M., 2010, Fault seal prediction of seismic-scale normal faults in porous sandstone: A case study from the eastern Gulf of Suez rift, Egypt: Marine and Petroleum Geology, v. 27, p. 334–350, doi: 10.1016/j.marpetgeo.2009.10.008.

Ujiie, K., and Kimura, G., 2014, Earthquake faulting in subduction zones: insights from fault rocks in accretionary prisms: Progress in Earth and Planetary Science, v. 1, p. 1–30, doi: 10.1186/2197-4284-1-7.

Van Den Bril, K., and Swennen, R., 2009, Sedimentological control on carbonate cementation in the Luxembourg Sandstone Formation: Geologica Belgica, v. 12, p. 3–23.

Van Dijk, J.P., 1994, Late Neogene kinematics of intra-arc oblique shear zones: The Petilia-Rizzuto Fault Zone (Calabrian Arc, Central Mediterranean): Tectonics, v. 13, p. 1201–1230, doi: 10.1029/93TC03551.

Van Dijk, J.P., Bello, M., Brancaleoni, G.P., Cantarella, G., Costa, V., Frixa, A., Golfetto, F., Merlini, S., Riva, M., Torricelli, S., Toscano, C., and Zerilli, A., 2000, A regional structural model for the northern sector of the Calabrian Arc (southern Italy): Tectonophysics, v. 324, p. 267–320, doi: 10.1016/S0040-1951(00)00139-6.

Van Dijk, J.P., and Scheepers, P.J.J., 1995, Neotectonic rotations in the Calabrian Arc; implications for a Pliocene-Recent geodynamic scenario for the Central Mediterranean: Earth Science Reviews, v. 39, p. 207–246, doi: 10.1016/0012-8252(95)00009-7.

Viola, I., Oppo, D., Franchi, F., Capozzi, R., Dinelli, E., Liverani, B., and Taviani, M., 2015, Mineralogy, geochemistry and petrography of methane-derived authigenic carbonates from Enza River, Northern Apennines (Italy): Marine and Petroleum Geology, v. 66, p. 566–581,

doi: 10.1016/j.marpetgeo.2015.03.011.

Wanas, H.A., 2008, Calcite-cemented concretions in shallow marine and fluvial sandstones of the Birket Qarun Formation (Late Eocene), El-Faiyum depression, Egypt: Field, petrographic and geochemical studies: Implications for formation conditions: Sedimentary Geology, v. 212, p. 40–48, doi: 10.1016/j.sedgeo.2008.09.003.

Wibberley, C.A.J., Gonzalez-Dunia, J., and Billon, O., 2017, Faults as barriers or channels to production-related flow: insights from case studies: Petroleum Geoscience, v. 23, p. 134–147, doi: 10.1144/petgeo2016-057.

Wibberley, C.A.J., Petit, J.P., and Rives, T., 2007, The mechanics of fault distribution and localization in high-porosity sands, Provence, France: Geological Society of London Special Publication, v. 164, p. 599–608.

Wilkinson, M., 1993, Concretions of the Valtos Sandstone Formation of Skye: geochemical indicators of palaeo-hydrology: Journal of the Geological Society, v. 150, p. 57–66, doi: 10.1144/gsjgs.150.1.0057.

Williams, R.T., Goodwin, L.B., and Mozley, P.S., 2016, Diagenetic controls on the evolution of fault-zone architecture and permeability structure: Implications for episodicity of fault-zone fluid transport in extensional basins: Bulletin of the Geological Society of America, v. 129, p. 464–478, doi: 10.1130/B31443.1.

Wilson, J.E., Goodwin, L.B., and Lewis, C.J., 2003, Deformation bands in nonwelded ignimbrites: Petrophysical controls on fault-zone deformation and evidence of preferential fluid flow: Geology, v. 31, p. 837–840, doi: 10.1130/G19667R.1.

Wong, T., and Zhu, W., 1999, Brittle Faulting and Permeability Evolution: Hydromechanical Measurement, Microstrucutral Observation, and Network Modeling, *in* Haneberg, W.C., Mozley, P.S., Moore, J.C., and Goodwin, L.B., eds., Faults and Subsurface Fluid Flow in the Shallow Crust: Washington D.C., USA, Geophysical Monograph 113, American Geophysical Union, p. 83–99.

Yamaguchi, A., Sakaguchi, A., Sakamoto, T., Iijima, K., Kameda, J., Kimura, G., Ujiie, K., Chester, F.M., Fabbri, O., Goldsby, D., Tsutsumi, A., Li, C.F., and Curewitz, D., 2011, Progressive illitization in fault gouge caused by seismic slip propagation along a megasplay fault in the Nankai Trough: Geology, v. 39, p. 995–998, doi: 10.1130/G32038.1.

Yoshida, H., Ujihara, A., Minami, M., Asahara, Y., Katsuta, N., Yamamoto, K., Sirono, S.I., Maruyama, I., Nishimoto, S., and Metcalfe, R., 2015, Early post-mortem formation of carbonate concretions around tusk-shells over week-month timescales: Scientific Reports, v. 5, p. 1–7, doi: 10.1038/srep14123.

Zamanian, K., Pustovoytov, K., and Kuzyakov, Y., 2016, Pedogenic carbonates: Forms and formation processes: Earth-Science Reviews, v. 157, p. 1–17, doi: 10.1016/j.earscirev.2016.03.003.

Zattin, M., Picotti, V., and Zuffa, G.G., 2002, Fission-track reconstruction of the front of the Northern Apennine thrust wedge and overlying Ligurian unit: American Journal of Science, v. 302, p. 346–379, doi: 10.2475/ajs.302.4.346.

Zecchin, M., Caffau, M., Civile, D., Critelli, S., Di Stefano, A., Maniscalco, R., Muto, F., Sturiale, G., and Roda, C., 2012, The Plio-Pleistocene evolution of the Crotone Basin (southern Italy): Interplay between sedimentation, tectonics and eustasy in the frame of Calabrian Arc migration: Earth-Science Reviews, v. 115, p. 273–303, doi: 10.1016/j.earscirev.2012.10.005.

Zecchin, M., Massari, F., Mellere, D., and Prosser, G., 2004, Anatomy and evolution of a Mediterranean-type fault bounded basin: The Lower Pliocene of the northern Crotone Basin (Southern Italy): Basin Research, v. 16, p. 117–143, doi: 10.1111/j.1365-2117.2004.00225.x.

Zhang, J., Wong, T.F., and Davis, D.M., 1990, Micromechanics of pressure induced grain crushing in porous rocks: Journal of Geophysical Research, v. 95, p. 341–352, doi: 10.3324/haematol.2011.043265.

Zhu, W., and Wong, T., 1997, The transition from brittle faulting to cataclastic flow: Permeability evolution: Journal of Geophysical Research: Solid Earth, v. 102, p. 3027–3041, doi: 10.1029/96JB03282.